Thèse n° 9943

# Fat navigators based retrospective motion correction strategies for brain magnetic resonance imaging

Présentée le 18 septembre 2020

à la Faculté des sciences de base
Laboratoire Leenaards-Jeantet d'imagerie fonctionnelle et métabolique
Programme doctoral en physique

pour l'obtention du grade de Docteur ès Sciences

par

**Frédéric GRETSCH**

Acceptée sur proposition du jury

Prof. F. Mila, président du jury
Prof. R. Gruetter, Dr D. Gallichan, directeurs de thèse
Dr D. Atkinson, rapporteur
Dr S. Malik, rapporteur
Prof. D. Van De Ville, rapporteur

École
polytechnique
fédérale
de Lausanne

2020

# Acknowledgements

Many people contributed to this work, either directly or indirectly. Here are a few words to try and express my deep gratitude.

First and foremost, I would like to deeply thank Daniel Gallichan for giving me the opportunity to accomplish this work. His guidance, advice and open-mindedness were invaluable, and I can only hope some glimpses of it can be found in this manuscript. Many thanks to my other thesis advisor, Rolf Gruetter, for integrating me into such a pleasant work environment.

To my fellow PhD students: Antoine, Veronika, Guillaume, Yohan, João, Emma, Sarah, Elise, Masoumeh, and more generally all the people of the LIFMET lab. For the shared hardships of PhD studies and great memories, it is my honor that even though I may leave you as colleagues, you shall remain dear friends.

Many thanks as well to the great researchers and even better persons: Olivier, José, Ileana , Hikari. Also to Lillian, whom I thank for her diligent and efficient administrative prowess and kindness. To Tobias Kober, for his straightforwardness, jolly nature and help for collaboration with Siemens. At the CHUV, many thanks to Jean-Baptiste for the scans, and to Jessica, Prof. Stuber and Prof. Hagmann for their interest and help in trying out the project in clinical conditions.

On the personal side, my largest thanks go to my sister Cécile, for proving that hope and tenacity do succeed. Many thanks to Aude as well. To my parents, Catherine and Pierre, for their continuous encouragement and always being here for me.

To my friends, especially François, Grégoire and Nicolas, for the welcome stress relief they gifted me. Also, to the Hapkido group led by Sidi, for the many physical and mental training lessons. Finally, a big thank you to Sasha for the ever interesting and mind opening discussions.

# Abstract

Magnetic resonance resonance (MRI) is a widely used modality to obtain in vivo tissue information. Clinical applications are near countless, and almost all body parts can be examined using an MR scanner. As the method is non invasive, does not use ionizing radiation and provides excellent soft tissue contrast, it also appears as an excellent tool for neuroscience research. The major drawback of MRI remains the relatively long acquisition times, of the order of several minutes. During the measurement, the subject must stay still and avoid moving at all costs, as otherwise image artefacts will appear and potentially render the acquired data (partially) unusable. As higher image resolution imply longer acquisition time, probing finer anatomical details imply ultimately requires dealing with said motion. While some research goes in the way of reducing the acquisition time, it necessarily comes at the price of lower sensitivity and hence inherently diminishes the achievable gain for high-resolution imaging as the signal is weaker to start with.

In this work, the focus is to try and compensate for motion during brain imaging using a navigator method. This amounts to measure not only the desired image, but also other MR based information, called navigator, at regular intervals during the scan. A modeling step then establishes a link between the navigators samples and the head position change. Incorporating the motion information into the main image reconstruction framework helps to retrospectively reduce the impact of said motion and the associated incoherences which would appear during the standard reconstruction. Brain imaging is probably the easiest case of motion correction in MRI, as the motion can readily be well approximated as rigid.

The navigator methods developed and investigated in this work, called FatNavs, are based on the fat signal, which in head imaging is very sparse in space and therefore can be imaged rapidly. They also present the advantage of reduced impact on the main image water signal.

Several implementation strategies were tested as, due to the versatility of MRI, all image contrasts cannot be ideally navigated using a single general implementation. Applications to inversion recovery based sequences (MP2RAGE) used a well separated navigator and image acquisition scheme. This method being routinely acquired, comparison to Moiré Phase Tracking, the current gold standard for motion tracking and correction, was also performed in collaboration with Hendrik Mattern from the Magdeburg University.

For gradient-echo imaging sequences (GRE), on which time-of-flight angiography and susceptibility induced contrasts are based, both separate and mixed acquisition schemes were tested. Furthermore, for imaging protocols using long echo time, the fluctuation of the magnetic field during the scan can also induce severe artefacts. Therefore, extension of the FatNavs to a dual-echo field-mapping version was also explored.

Finally, combination of FatNavs with FID navigators, which lack spatial information but have much higher temporal resolution, was investigated for both motion and field fluctuation retrospective correction.

**Keywords:** MRI, Ultra-high field, Navigators, Motion correction, Field fluctuation correction, Structural Imaging

# Résumé

L'imagerie par résonance magnétique (IRM) est une technologie couramment utilisée pour obtenir des informations sur des tissus en condition in vivo. Ses applications cliniques sont nombreuses, et quasiment toutes les parties du corps peuvent être examinées par un scanner IRM. C'est également un excellent outil de recherche pour les neurosciences, car la méthode est non-invasive, n'utilise pas de rayonnement ionisant et procure un excellent contraste entre les différents tissus. Le point faible principal de l'IRM reste le temps d'acquisition relativement long, de l'ordre de plusieurs minutes. Durant la mesure, le sujet doit rester stable et éviter au maximum de bouger, car autrement des artefacts apparaissent sur l'image et peuvent la rendre potentiellement inutilisable. Comme une plus haute résolution d'image implique des temps d'acquisition plus long, explorer les fins détails anatomique requiert une véritable gestion du mouvement. Il est possible de diminuer le temps d'acquisition, mais uniquement au prix d'une sensibilité plus faible, ce qui présente un avantage limité pour la haute résolution où le signal est bas.

Dans ce travail, le but est d'essayer de compenser le mouvement ayant lieu durant l'acquisition d'images du cerveau en utilisant une méthode basée sur des navigateurs. Cela consiste à mesurer non seulement l'image désirée, mais également d'autres signaux IRM à intervalles réguliers, appelés navigateurs. Une étape de modélisation permet ensuite d'établir un lien entre les navigateurs et le changement de position de la tête. En incorporant cette information dans la reconstruction de l'image, l'impact du mouvement et des artefacts qui y sont liés est réduit de manière rétrospective. La correction du mouvement pour des images du cerveau est probablement le cas le plus simple en IRM car le mouvement peut être bien approximé comme étant rigide.

Les méthodes de navigateurs développées et étudiées ici, appelées FatNavs, sont basées sur le signal du gras qui lors de l'imagerie de la tête est un signal spatialement épars, ce qui permet de l'acquérir très rapidement. Elles présentent également l'avantage d'avoir un impact réduit sur le signal de l'eau, qui est le signal d'intérêt lors de l'imagerie du cerveau,

Plusieurs stratégies d'implémentation ont été testées pour être compatibles avec la versatilité des images IRM, qui ne permet pas d'implémenter une stratégie unique et générale pour tous les contrastes d'image. Les applications aux séquences basées sur une inversion (type MP2RAGE) utilisent une acquisition du navigateur bien séparée de celle de l'image. Cette méthode ayant été régulièrement employée, elle fut comparée à la méthode de référence actuelle pour la correction du mouvement (MPT) lors d'une collaboration avec Hendrik Mattern de l'université de Magdeburg.

Pour les séquences d'imagerie de type écho de gradients, dont l'angiographie temps-de-vol et les contrastes basés sur la susceptibilité magnétique font parties, des acquisitions de FatNavs séparée et mixte on été testées. De plus, pour les protocoles utilisant un long temps d'écho, les fluctuations du champ magnétique durant le scan peuvent également induire des artefacts sévères sur l'image. Ainsi, une extension des FatNavs permettant la mesure du champ a également été étudiée.

Enfin, la combinaison de FatNavs avec des navigateurs FID, qui manquent d'informations spatiales mais ont une bien plus grande résolution temporelle, a été explorée pour la correction rétrospective du mouvement et des fluctuations du champ magnétique.

# Contents

**Acknowledgements** **3**

**Abstract** **5**

**1 Introduction** **21**
- 1.1 Context of the thesis . . . 21
- 1.2 The physics of MRI: overview . . . 22
  - 1.2.1 The NMR signal and its dynamics . . . 22
  - 1.2.2 A crash course in MRI Signal detection . . . 23
- 1.3 Basics of image reconstruction . . . 25
  - 1.3.1 Cartesian acquisition and reconstruction . . . 25
  - 1.3.2 Parallel imaging . . . 26
  - 1.3.3 Metrics of image quality . . . 27
- 1.4 MR signal and motion in brain imaging . . . 27
- 1.5 Literature review . . . 31
  - 1.5.1 Prospective and Retrospective correction . . . 31
  - 1.5.2 External sensor based motion tracking . . . 31
  - 1.5.3 MR navigators motion tracking . . . 32
  - 1.5.4 Auto-focusing methods . . . 36
- 1.6 FatNavs . . . 37
  - 1.6.1 Fat in head MR imaging . . . 37
    - Signal sources . . . 37
    - Fat selection . . . 38
  - 1.6.2 Standard FatNavs implementation . . . 39
  - 1.6.3 Limitations and impacts . . . 45
    - Limitations . . . 45
    - Impacts . . . 46
- 1.7 Structure of the thesis . . . 48

**2 Comparison to Moiré phase tracking** **49**
- 2.1 Pre-print . . . 50
  - 2.1.1 Introduction . . . 50
  - 2.1.2 Methods . . . 51
    - Moiré phase tracking . . . 51
    - FatNavs . . . 52
    - Experiment 1: Motion estimates . . . 52
    - Experiment 2: Retrospective motion correction using MPT and FatNavs . . . 53
  - 2.1.3 Results . . . 54
    - Direct motion estimates experiment . . . 54

Retrospective motion correction comparison . . . 58
2.1.4 Discussion . . . 65
Experiment 1: direct comparison of voluntary motion patterns . . . 65
Experiment 2: Comparison of retrospective correction of involuntary motion . 65
2.1.5 Conclusions . . . 66
2.1.6 Acknowledgments . . . 66

**3 Block FatNavs for first order $B_0$ fluctuation retrospective correction 67**
3.1 Post-print . . . 67

**4 EPI-like FatNavs 89**
4.1 Definition, acquisition and corrections . . . 89
4.1.1 Calibration and correction . . . 91
4.2 Comparison to standard FatNavs . . . 95
4.3 Applications and proof of concept . . . 99

**5 Segmented FatNavs 103**
5.1 Segmented FatNavs . . . 103
5.1.1 Definition . . . 103
5.1.2 Implementation details . . . 104
5.1.3 Acquisition ordering schemes . . . 104
5.1.4 Artefacts and correction procedure . . . 105
5.2 Application: Time-of-Flight . . . 108
5.2.1 Sequence description . . . 108
5.2.2 Motion correction at 7T: ascending ordering . . . 109
Acquisition . . . 109
Results and discussion . . . 110
5.2.3 Motion correction of centric acquisitions . . . 116
Acquired protocols . . . 116
Results . . . 116
5.2.4 SegFatNavs for inducing magnetization transfer . . . 119
SegFatNavs flip angle impact . . . 119
Comparison to default MT pulse . . . 119
Discussion and concluding remarks . . . 121
5.2.5 Transfer to clinical field strength . . . 121
5.3 Summary and outlook . . . 123

**6 Combining segmented FatNavs and FID navigators 125**
6.1 FID Navigators . . . 125
6.1.1 Description and relation to motion . . . 125
6.1.2 Implementation . . . 126
6.1.3 Artefacts . . . 127
6.1.4 SegFatNavs as prior knowledge to the FID motion model . . . 130
6.2 Example applications . . . 132
6.2.1 $B_0$ fluctuation correction . . . 132
Methods . . . 132
Results and discussion . . . 133
6.2.2 Link to physiological processes . . . 138
Methods . . . 138

Results . . . 138
Discussion . . . 142
6.2.3 Sudden intentional motion as a limitations demonstration . . . 143
Methods . . . 143
Results . . . 144
Discussion . . . 148
6.3 Summary and outlook . . . 149

**7 Thesis summary and outlook 151**
7.1 Summary of the results . . . 151
7.2 Outlook . . . 152

**References 153**

**Publications 165**

**CV 167**

# List of Figures

1.1 Possible impacts of motion during acquisition (simulation). Raw data used for simulation were downloaded from `https://people.eecs.berkeley.edu/~mlustig/Software.html` . . . 30
1.2 Setups for some marker based motion tracking modalities. . . . 32
1.3 Examples of **k**−space based motion navigators trajectories. . . . 35
1.4 Examples of image-space based navigators. . . . 36
1.5 Orthogonal views of water (top) and fat (bottom) signal sources standardly found in head MRI. . . . 37
1.6 Normalized excitation profile of the $1-\bar{2}-1$ binomial pulse. Low and high flip angle curves are normalized to exhibit the non linear behavior. . . . 39
1.7 Resolution comparison of FatNavs. . . . 40
1.8 Kernels used for CAIPI and GRAPPA reconstruction of Figure 1.9. Blue dots represent acquired data and red crosses target points to estimate. PE1 corresponds to the left-right direction and PE2 the anterior-posterior one. . . . 41
1.9 Fully sampled, GRAPPA and CAIPI ($R = 4 \times 4$, $\Delta = 2$ ) reconstructions for 2mm FatNavs. Reconstructions are basically indistinguishable. . . . 42
1.10 Fully sampled, GRAPPA and CAIPI ($R = 6 \times 6$, $\Delta = 3$ ) reconstructions for 2mm FatNavs. The CAIPI recon shows somewhat less noise-amplification. . . . 43
1.11 $L_1$ constrained reconstructions after three iterations of non-linear adaptive step size conjugate gradient. Shown is the sum-of-squares of channels wise reconstructions performed after GRAPPA **k**−space completion. . . . 44
1.12 Top: $T_1$ histograms extracted from MP2RAGE acquisition with 2mm FatNavs inclusion for different navgiator parameters, as well as FatNavs free result. Bottom: relative different the reference scan. See text for details. . . . 47

2.1 Example volumes of both FatNav protocols acquired in the first experiment. . . . 55
2.2 Representative time-courses of both slow motion (left column) and faster motion (right column) acquired in the first experiment. Red crosses represent FatNavs and blue line represents MPT estimates. Temporal resolution of estimates: 1.5 / 0.37 s for 2mm / 4 mm FatNavs and 0.012 s for MPT. . . . 56
2.3 RMSE between the FatNavs and the MPT estimates for all the motion patterns acquired during the first experiment. The translation and rotation ranges and rates are indicated in the plots. The values in brackets are for the 4mm FatNavs scans. 2mm FatNavs outperform 4mm FatNavs for slow motion patterns, and inversely for faster patterns. . . . 57
2.4 Example views of the raw and motion corrected reconstruction using the 2mm FatNavs motion information (volunteer 2 first scan). The MPT corrected image also showed considerable improvement, but was inferior to the FatNavs one in this case, see Figure 2.7. 58

2.5 Case of superior MPT correction compared to FatNavs (Volunteer 8 first scan). Notably, ringing artefact above the cerebellum and blurring in the frontal cortex present in the FatNavs correction are nicely suppressed by MPT. . . . . . . . . . . . . . . . . 60

2.6 Zoomed-in view of the three reconstructions for volunteer 8 first scan. While the FatNavs image is sharper than the raw reconstruction, ringing is also more visible. . . 61

2.7 Case of superior FatNavs correction compared to MPT (volunteer 2 first scan), as can be seen by the overall better delineation of structures within the cerebellum. The yellow arrow indicates such a difference. . . . . . . . . . . . . . . . . . . . . . . . . . 62

2.8 Zoomed-in view of the three reconstructions for volunteer 2 second scan. The MPT-corrected image is arguably of slightly lesser quality than the raw reconstruction (this was the only such case observed). . . . . . . . . . . . . . . . . . . . . . . . . . . 63

2.9 Normalized gradient squared metric for both motion tracking modalities, and both inversion images produced by MP2RAGE. Graphed is the relative change of the metric compared to the raw reconstruction, in percent. . . . . . . . . . . . . . . . . . . . 63

2.10 Top: slices of the $T_1$ maps obtained for three high-resolution imaging protocols: without navigators, with 4mm or with 2mm FatNavs. Bottom: the histograms of $T_1$ values obtained after brain masking. The two clear peaks correspond to white-matter and grey-matter voxels. . . . . . . . . . . . . . . . . . . . . . . . . . . . . . . 64

3.1 Bloch simulation of the water signal during the high-resolution GRE protocol with FatNav inclusion. Dashed lines represent the steady state in absence of FatNavs. The green line is the white to gray matter contrast. The point-spread functions associated to these signals are found by zero-padding and shifting before taking the Fourier transform to account for the host sequence partial Fourier. They show a resolution loss of less than 2.2%. . . . . . . . . . . . . . . . . . . . . . . . . . . . . . . . . 73

3.2 FatNavs without gradient offsets or partial Fourier were acquired. Field change coefficients were estimated using either all the measured data, or after partial Fourier simulation (in x and y). The RMSE between fully-sampled and partial Fourier reconstructions are 0.1 Hz for the 0th order term, and 1.8 / 2.5 / 4 Hz/m for the x / y / z directions. The higher value on z is probably due to breathing during sampling, which is almost twice as long for this protocol than for the one used in the rest of the study (which uses partial Fourier). . . . . . . . . . . . . . . . . . . . . . . . . . . 74

3.3 Example data from a single subject with a 5 Hz/m offset in the x direction every other volume. (A) Mean $B_0$ difference between breathing peaks and troughs in the fat layer, after masking for fat signal. (B) Mean $B_0$ field across entire fat signal mask vs time. Markers represent the peaks and troughs of respiration, used to derive the plot (A). (C) Spectra of the time-courses of the estimated linear field change in z derived from both consecutive volume difference (CVD) and double linear interpolation difference (DLID) methods, in arbitrary units [a.u.].
75

3.4 Gradient offsets measured across volunteers. Error bars show +- 1 standard deviation. 76

3.5 Representative reconstructions example for the high-resolution scan while deep-breathing. Abbreviations stand for: raw reconstruction (Raw), motion correction only (MC), motion and zeroth order $B_0$ corrections, and motion and first order $B_0$ corrections. The bottom right is the absolute difference between both $B_0$ order corrections, multiplied by 5. All images use the same color-map. Red arrows highlight regions where improvements can be most clearly observed with increasing levels of correction. . . . . 78

3.6 Estimated motion and field parameters for the scans of Figure 3.5 , where the volunteers were asked to breathe deeply. . . . . . . . . . . . . . . . . . . . . . . . . . . . 79
3.7 Representative reconstructions example for the high-resolution scan while subject breathed naturally. Figure organization is as in Figure 3.5. . . . . . . . . . . . . . . 80
3.8 Estimated motion and field parameters for the scan of Figure 3.7 (volunteer 1), where the volunteer was asked to breathe normally. . . . . . . . . . . . . . . . . . . . . . . 81
3.9 Representative motion and first-order $B_0$ corrected images in the deep-breathing scan. First column is using both echoes from the FatNavs to estimate the field changes, whereas the second column uses only the first echo. The third column is the absolute difference times 5. Red arrows indicate regions where slight depreciative change of image quality can be found compared to the image without the red arrow. . . . . . 82
3.10 Difference between the dual-echo and first echo field coefficient estimates. The scans shown are those where the volunteers moved the most (both during the natural breathing scan). Both the raw difference and the first-order motion-regressed difference are shown. The horizontal black lines represent the constant zero value. . . . . . . . . . 83
3.11 Bar plots showing the relative reduction of image gradient entropy between the raw images and the different corrected images for both deep breathing and natural breathing scans. . . . . . . . . . . . . . . . . . . . . . . . . . . . . . . . . . . . . . 83

4.1 Kernel for the multiple-readout per $T_R$ FatNavs. This example shows six bipolar readouts. . . . . . . . . . . . . . . . . . . . . . . . . . . . . . . . . . . . . . . . 90
4.2 $\mathbf{k}-$space acquisition order for $n = 6$. The blip gradient is played on the segmented direction, and each color is associated to one of the readouts during the kernel. . . . 90
4.3 Simulation of the alteration of the point-spread function due to signal relaxation for the standard consecutive ordering and the one used by the EPI-like FatNavs. . . . . 91
4.4 Raw and corrected reconstructions for a five readouts-per-kernel acquisition . . . . . 92
4.5 Examples of the EPI-like FatNavs correction parameters found by the proposed method. . . . . . . . . . . . . . . . . . . . . . . . . . . . . . . . . . . . . . . . 94
4.6 Corrected reconstructions of 2mm EPI-like FatNavs for different numbers of readout-per-kernel. . . . . . . . . . . . . . . . . . . . . . . . . . . . . . . . . . . . . . 96
4.7 Example of $n = 6$ EPI-like FatNavs motion parameters time-courses comparison to the equivalent standard FatNavs. . . . . . . . . . . . . . . . . . . . . . . . . . . . . 97
4.8 RMSE of the direct comparison experiment of 2mm FatNavs to 2mm EPI-like FatNavs. . . . . . . . . . . . . . . . . . . . . . . . . . . . . . . . . . . . . . . . . . 98
4.9 Top: raw reconstruction. Bottom: motion correction using 2 mm EPI-like FatNavs ($n = 5$). . . . . . . . . . . . . . . . . . . . . . . . . . . . . . . . . . . . . . . 100
4.10 Motion parameters estimated from 2mm EPI-like FatNavs with $n = 5$. Retrospective correction based on these motion parameters is shown in Figure 4.9. . . . . . . . . . 101
4.11 EPI-like 1.5mm FatNavs reconstruction with $n = 4$. Top: uncorrected. Bottom: corrected. . . . . . . . . . . . . . . . . . . . . . . . . . . . . . . . . . . . . . . . 101

5.1 Ascending cartesian GRE imaging acquisition scheme with included SegFatNavs. An extra loop over slabs can be easily added above the iPhaseEncode one for multi-slabs imaging protocols. . . . . . . . . . . . . . . . . . . . . . . . . . . . . . . . . . . 103
5.2 $\mathbf{k}-$space acquisition ordering. Left is ascending and right is centric. The black cross represents the $\mathbf{k}-$space center, and the color line links successive acquisitions. . . . . 105

5.3 Several examples of the motion parameters spectra for different scanning parameters. Translations and rotations are combined using sum-of squares and scaled for visual convenience. The dashed black lines represent the inverse of the least common multiple of the SegFatNavs period and the inner loop length, as well as multiples thereof. . . 107
5.4 Puzzling example where the artefact appears only at the fifth harmonic of the least common multiple of the SegFatNavs period and inner loop period. . . . . . . . . . . 107
5.5 Homemade TOF sequence sequence kernel including venous signal suppression, flow-compensated GRE kernel and SegFatNavs acquisition. . . . . . . . . . . . . . . . . . 108
5.6 Example of the 4 mm SegFatNavs acquired during the 0.25 mm TOF. . . . . . . . . 110
5.7 Brain masked sagittal MIP of raw (top) and motion corrected (bottom) reconstructions for the 0.4 mm TOF. Associated motion parameters can be found in Figure 5.8. 112
5.8 Motion parameters of the 0.4 mm scan presented in Figure 5.7. . . . . . . . . . . . . 113
5.9 Focus on the Circle of Willis for a 0.25 mm scan (volunteer 2). Raw (left) and motion corrected (right) reconstructions. Figure 5.10 shows the estimated motion parameters for this scan. . . . . . . . . . . . . . . . . . . . . . . . . . . . . . . . . . . . . . . 113
5.10 Motion parameters of the 0.25 mm scan presented in Figure 5.9. . . . . . . . . . . . 113
5.11 Small motion 0.25 mm scan MIPs. Top: volunteer 1, bottom: volunteer 2. . . . . . 114
5.12 Motion parameters of the 0.25mm scans presented in Figure 5.11. Top: volunteer 1, bottom: volunteer 2. . . . . . . . . . . . . . . . . . . . . . . . . . . . . . . . . . . 115
5.13 Raw (top) and motion corrected (bottom) 0.5 mm centric cycle-matched acquisition. Motion parameters are plotted on Figure 5.14. . . . . . . . . . . . . . . . . . . . . 117
5.14 Estimated motion during the 0.5 mm centric cycle-matched scan shown in Figure 5.13. 118
5.15 Zooms on raw (left) and motion corrected (right) reconstruction of a 0.5 mm centric cycle-unmatched acquisition. Yellow arrows indicate regions of signal enhancement and blurring reduction. Associated motion parameters are presented in Figure 5.16. . 118
5.16 Filtered motion parameters associated to Figure 5.15. Notice the very small range of motion. . . . . . . . . . . . . . . . . . . . . . . . . . . . . . . . . . . . . . . . . 118
5.17 1mm isotropic images with low (left) and high (right) SegFatNavs flip angle. The images are displayed on the same windowing scale. The higher SegFatNavs flip angle induces lower brain tissues (and fat) signals in the TOF image. . . . . . . . . . . . 119
5.18 1mm isotropic acquisitions for comparing standard MT module to MT induced by SegFatNavs. The left side of the vertical white line is using the Siemens MT module, and the right side high flip angle SegFatNavs. White / gray matter contrast is visibly identical in both acquisitions. . . . . . . . . . . . . . . . . . . . . . . . . . . . . 120
5.19 Siemens MT module image divided by high SegFatNavs flip angle image after 2mm 3D tukey filtering. The ratio being very close to one indicates equivalent MT effects in both acquisitions. . . . . . . . . . . . . . . . . . . . . . . . . . . . . . . . . . 120
5.20 Raw (left) and motion corrected (right) 3T TOF 0.5×0.5×1 mm protocol, with a deliberate nodding motion during the scan. . . . . . . . . . . . . . . . . . . . . . . 122
5.21 SegFatNavs during a 3T TOF 0.5×0.5×1 mm protocol, with a deliberate nodding motion during the scan. . . . . . . . . . . . . . . . . . . . . . . . . . . . . . . . . 122
5.22 Example of 4mm SegFatNavs incorporated in the clinical TOF protocol at 3T. . . . 122

6.1 Magnitude of the mean FID signal across all acquisitions. Six receive channels are displayed. The initial fluctuations are discarded. . . . . . . . . . . . . . . . . . . . 127
6.2 Default ascending **k**−space acquisition order (left) and modified smoother version (right). . . . . . . . . . . . . . . . . . . . . . . . . . . . . . . . . . . . . . . . . 128
6.3 FIDNavs signal for both trajectories of Figure 6.2 without SegFatNavs. . . . . . . . 128

6.4 FIDNavs signal of the smoother trajectory when changing the repetition time (top) or the slice resolution (bottom). The signal is smoothed in the resolution comparison for visual convenience. . . . . . 129
6.5 FIDNavs signal for both trajectories of Figure 6.2 with SegFatNavs (nSegments = 2). 130
6.6 Schematic of the sequence. Host imaging sequence is drawn blue and navigators green. Flow compensation gradients are omitted for simplicity. While the spoiling direction is consistent between host and SegFatNavs, the physical ($xyz$) axis represented by readout, phase and slice are different in practice, but are drawn on the same line here. 132
6.7 Example of superior image quality obtained by the FID based correction (right) compared to the SegFatNavs based correction (left) (volunteer 1). The difference stems from the field fluctuation correction, see Figure 6.8. . . . . . 133
6.8 Field fluctuation parameters (top: SegFatNavs, bottom: FIDs) associated to the reconstructions of Figure 6.7. . . . . . 134
6.9 Slices of the raw reconstruction of very compliant subject (volunteer 2). . . . . . 135
6.10 Field and motion parameters of volunteer 2, as estimated by the FIDs. . . . . . 136
6.11 Relative change of the gradient squared metric to the raw reconstruction for all corrections (MC = Motion correction). . . . . . 137
6.12 RMS of the residual errors of the FIDNavs to SegFatNavs parameters calibration. . 137
6.13 Reconstructions where SegFatNavs sample deep breathing adequately. From top to bottom: raw, SegFatNavs-based correction, FIDNavs-based correction. All corrections include motion and first order $B_0$ compensation. . . . . . 140
6.14 $Z$ translation as estimated by the FIDNavs, after Tukey filtering (1 Hz constant window and 2 Hz passband). In green is the physiological data: breathing (top) and cardiac trace peaks (bottom). . . . . . 141
6.15 Histogram of the FIDNavs motion parameters during the cardiac cycle. . . . . . 141
6.16 Color-coded $\mathbf{k}-$space trajectory (from red to black to blue), with yellow markers representing when the nodding instruction was presented to the subject. Single nod scans are on the left and the periodic instruction scan on the right. . . . . . 144
6.17 Axial MIP of the FIDNavs based motion corrected reconstructions for the rest and single-nod scans. . . . . . 146
6.18 Axial MIP of the SegFatNavs (left) and FIDNavs based motion corrected reconstructions for the periodic nod scan. . . . . . 147
6.19 Relative metrics change to the raw reconstruction: AES (left) and gradient squared (right). . . . . . 147

# List of Tables

4.1 Acquisition times of 2mm EPI-like FatNavs protocols on the 7T CIBM scanner. . . . 95

5.1 Parameters of the high-resolution TOF protocols and of the included SegFatNavs. . . 110
5.2 Motion range, defined as the difference between the maximum and the minimum value, for all presented 0.4 mm and 0.25 mm scans. . . . . . . . . . . . . . . . . . . . . . . . . 111

6.1 Gradient squared metric percentage increase compared to the raw reconstruction. . . 138
6.2 RMS of the residual errors of the FIDNavs to SegFatNavs calibration. . . . . . . . . . 139
6.3 Motion range for all scans as estimated from the SegFatNavs. . . . . . . . . . . . . . . 144

# Glossary

**NMR** Nuclear magnetic resonance.

**MRI** Magnetic resonance imaging.

**High-field** Refers to acquisitions at $B_0 > 3$ T.

**RF** Radiofrequency

**MT** Magnetization transfer.

**k−space** Conjugate space of the 3D material world coordinates by Fourier transformation.

**FOV** Field of view.

**Gradients** Short name for the gradient coils of the scanner.

**Readout** Means either the signal acquisition, in the sense of digital sampling or the direction of the associated gradient during **k**−space sampling.

**GRE** Gradient recalled echo sequence , where the signal is measured without refocusing RF pulses

**TSE** Turbo spin echo sequence, during which refocusing RF pulses induce partial rephasing the magnetization during readout.

$T_E$ Echo time. Time between the excitation and when the center of **k**−space along the readout direction is is sampled.

$T_R$ Repetition time, generally the time between two imaging excitation pulses.

**MPT** Moiré Phase Tracking

# Chapter 1

# Introduction

## 1.1 Context of the thesis

From the early steps of nuclear magnetic resonance (NMR) in the 1930's by Rabbi [1] and the 1940's by Purcell and Bloch among others [2, 3], NMR became a reference tool in analytical chemistry for substance identification using spectroscopy, but also found other diverse applications, such as probing protein dynamics [4]. The potential for medical imaging applications was realized in the 1970's by Mansfield and Lauterbur [5, 6], and by Damadian in parallel works [7].

Magnetic resonance imaging is now a widely used imaging modality both in clinical practice and in neuroscience research. Its non-invasive and non ionizing radiation coupled with excellent soft tissue contrast makes it a reference technology for many medical imaging exams. According to the Swiss Federal Statistic Office, over $601,000$ MRI exams were performed in Swiss hospitals in 2016. The safety of MRI, especially without contrast agents, makes it a fundamental tool for brain study or diagnostics, as both anatomical and functional information [8] can be extracted using MRI.

With increasing magnetic field strength comes the possibility to achieve very-high resolution images, however the technique suffers from relatively long acquisition times. The MRI examination itself is far from comfortable. This is due to the general stress of a medical examination, but also the loud noise of the MR scanner and closed surroundings (claustrophobia). While parallel imaging [9, 10] helped to reduce the scan-time tremendously, thick slab acquisitions are typically at least several minutes in duration. For example, a whole brain 1 $mm$ isotropic MP2RAGE scan with 3 fold acceleration takes over 6 minutes [11]. High resolution ($\leq 0.7$ $mm$ in-plane) scans are diagnostically very important, but also imply longer acquisition. This increases the probability of motion during the scan, and diminishes the feasibility of reacquisition in case of non-diagnostic image quality. While it is expected of the exact proportion of motion corrupted scans to vary according to the subject age and medical condition, it was shown [12] that around 15% of all brain, head and neck exams had motion artefacts making the image unusable, and an additional 30% presented mild artefacts. Having to repeat a scan costs time and money to hospitals without guarantee of success. Mild artefacts were defined as not *likely* to bias the diagnostic, however they also give an indication of the proportion of higher resolution scans which would present comparable or worse artefacts levels.

This work will focus on a MRI based motion correction method called fat navigators. The rest of this chapter briefly introduces the basics of MRI physics, image acquisition and reconstruction in sections §1.2 and §1.3 respectively. The reader familiar with these concepts is encouraged to jump to §1.4 onwards, where the impact of motion on brain imaging is described, followed by a summary of existing motion correction methods for brain imaging from the literature. Finally, the goals of the thesis will be formulated.

## 1.2 The physics of MRI: overview

### 1.2.1 The NMR signal and its dynamics

The nuclear magnetic resonance (NMR) signal originates from the interaction of nuclear spin with an external magnetic field $\mathbf{B}$. Spin is one of the fundamental properties of particles, like mass and electric charge, and is often referred to as intrinsic angular momentum. The strength with which a particle couples to the classical external magnetic field is determined by its gyromagnetic ratio $\gamma$, such that the energy of interaction $U$ in the Hamiltonian is given by the Zeeman term

$$\hat{U} = -\gamma \mathbf{B} \cdot \hat{\mathbf{S}} \tag{1.2.1}$$

where $\hat{\mathbf{S}}$ is the spin operator. This is the usual scalar product of the magnetic field with the nuclear magnetic moment $\hat{\mathbf{m}}$

$$\hat{\mathbf{m}} = \gamma \hat{\mathbf{S}}. \tag{1.2.2}$$

The spin operators satisfy the algebra

$$[\hat{S}_i, \hat{S}_j] = i\hbar \sum_k \epsilon_{ijk} \hat{S}_k \tag{1.2.3}$$

where $\epsilon_{ijk}$ stands for the Levi-Civita symbol. (1.2.3) implies that spin is fully determined by a multiple of $\hbar/2$, which by transitivity is called spin as well and will be written as $S$. Each component of the spin operator ($\hat{S}_z$ for example) then has eigenvalues $\{-S, -S+1, ..., S\}$. By the Ehrenfest theorem, the temporal evolution of the magnetization expectation value is given by

$$\frac{\mathrm{d}}{\mathrm{d}t} \langle \hat{\mathbf{m}} \rangle = \gamma \langle \hat{\mathbf{m}} \times \mathbf{B} \rangle . \tag{1.2.4}$$

In modern applications of NMR and in MRI, the magnetic field is constant for most of the experiment, and is written as $\mathbf{B} = B_0 \mathbf{e_z}$ by convention. (1.2.4) disregards all other interactions involving the spins, such as spin-spin couplings. It does not include any mechanism allowing the magnetization of the sample to reach thermal equilibrium. The local, irreversible fluctuations of the magnetic field at the nucleus sites induced by molecular tumbling are also not accounted for. This process is however the source of most of the NMR signal dynamics. For example it allows transitions between the energy levels of (1.2.1) and thus establishment of thermal equilibrium. Hydrogen is the main source of the MRI signal, has a spin $1/2$ and its gyromagnetic ratio is given by

$$\frac{\gamma_{H^1}}{2\pi} = 42.58 \text{ MHz/T}. \tag{1.2.5}$$

The associated Larmor frequency $\nu$ is defined from the energy levels difference and the Planck constant by

$$\nu = \frac{\Delta E}{h} = \frac{\gamma}{2\pi} B_0 = \bar{\gamma} B_0. \tag{1.2.6}$$

At room temperature (20 °C), the ratio of the Zeeman energy levels difference to the thermal energy is very small

$$\frac{\hbar \gamma B_0}{k_B T} \approx 6.97 \cdot 10^{-6} B_0[T] \tag{1.2.7}$$

so that, on average, only a few spins over a 100 thousand are polarized at field strengths in the range of MRI scanners.

In the scope of this thesis, the detailed description of microscopic interactions betweens spins is not directly relevant to the design and interpretation of the experiments, and the interested reader is encouraged to consult specialized textbooks [13, 14]. Macroscopically, the dynamics of the total nuclear magnetization $\mathbf{M}$ is given by the Bloch equation (1.2.8).

$$\begin{aligned}\frac{\mathrm{d}}{\mathrm{d}t}M_z =&\gamma\left(\mathbf{M}\times\mathbf{B}\right)_z+\frac{M_0-M_z}{T_1}\\ \frac{\mathrm{d}}{\mathrm{d}t}M_{x,y} =&\gamma\left(\mathbf{M}\times\mathbf{B}\right)_{x,y}-\frac{M_{x,y}}{T_2^*}\end{aligned} \tag{1.2.8}$$

This law was originally established empirically through experiments, and sees the introduction of two characteristic times: $T_1$ which describes the return to the thermal equilibrium magnetization $M_0$ and $T_2^*$ which describes the coherence time of the transverse magnetization. The relaxation mechanisms depend on the underlying mobility and environment of the molecules. Therefore, mobile water, which is the signal measured in MRI, will exhibit different relaxation rates depending on the tissue and its condition, leading to contrast generation. Neglecting relaxation, the solution to Bloch equation has the simple geometrical interpretation that the magnetization rotates around the magnetic field.

It should be noted that $T_2^*$ includes the coherence loss due to intra-voxel field inhomogeneity, which can be explained both by the variety of magnetic susceptibilities and structures inside the voxel (intrinsic to the material), and by large-scale field inhomogeneity left over after shimming. By applying two RF pulses (see §1.2.2) in succession with a time interval $\Delta T$, it is possible to create transverse magnetization and then flip (part of) it like an omelette. Doing so reverses the phase accumulated in between pulses and hence will completely refocus the transverse magnetization after an additional phase evolution time $\Delta T$. This is called a spin-echo and leads to the definition of a separate transverse relaxation time $T_2$, which is larger than $T_2^*$ as it stems only from irreversible processes.

Finally, another mechanism affecting the NMR signal, called magnetization transfer (MT) [15], should be mentioned. It applies as a general term to explain spin exchange between two molecules, when the final spin states of the nuclei have been reversed either by direct coupling or by chemical exchange. A well accepted model is a two pools model. One of mobile water, imaged by MRI, and one of motion restricted magnetization, such as that found in macromolecules. Due to the much shorter $T_2^*$ of the latter and when saturated (i.e. $M_z \approx 0$), magnetization transfer tends to pump available magnetization from the mobile water pool to drive the system back towards equilibrium. This induces a lower available signal for imaging and allows the probing of microscopic dynamics between pools, which in itself can be considered as a contrast.

### 1.2.2 A crash course in MRI Signal detection

The following describes briefly the main components of the MR scanner and their functions, as well as to how to acquire imaging data. An MRI scanner has three major components: the static $B_0$ main magnet, the gradient field inserts, and the RF chain. Additionally, static coils named shimming coils produce low order spherical harmonics in order to maximize the field homogeneity in the region of interest.

The gradient insert allows control over the spatial variation of the $z$ component of the magnetic field by creating gradients $\mathbf{G}$ such that

$$B_z = B_0 + \mathbf{G}\cdot\mathbf{x}. \tag{1.2.9}$$

Introducing a magnetic field $B_1$ in the $x$–$y$ plane allows the magnetization vector to be tilted away from thermal equilibrium. This can be achieved if $B_1$ oscillates close to the Larmor frequency.

Introducing the complex parametrization $B_\perp = B_x + iB_y$ and $M_\perp = M_x + iM_y$ , the Bloch equations become

$$\begin{aligned}\frac{\mathrm{d}}{\mathrm{d}t}M_z =& \frac{i}{2}\gamma\left(M_\perp\overline{B_\perp} - \overline{M_\perp}B_\perp\right) + \frac{M_0 - M_z}{T_1} \\ \frac{\mathrm{d}}{\mathrm{d}t}M_\perp =& i\gamma\left(B_\perp M_z - M_\perp B_z\right) - \frac{M_\perp}{T_2^*}\end{aligned}. \tag{1.2.10}$$

The detected signal is picked up by the RF receive coil. If the magnetization has a non-zero transverse component, it will rotate at the Larmor frequency and hence produces an electromotive force in the coil by induction. Mathematically, expressing the Bloch equation in a reference frame rotating around $z$ in a counter-clockwise direction with angular velocity $\Omega$ leads to the same formulation, but with an effective magnetic field defined as

$$\gamma B_z \to \gamma B_z - \Omega \tag{1.2.11}$$

and with all vector-components (such as $m_\perp$ and $B_\perp$) understood as coordinates in the rotating frame. From here onwards, everything is assumed to be in the rotating reference frame and let

$$\gamma B_z = \Omega + \gamma \Delta B_0. \tag{1.2.12}$$

On resonance ($\Delta B_0 = 0$) and neglecting relaxation, the application of a constant purely real transverse field to the equilibrium magnetization $\mathbf{M} = M_0\mathbf{e_z}$ implies

$$\begin{aligned}M_\perp(t) &= iM_0 \sin\left(\gamma B_\perp t\right) \\ M_z(t) &= M_0 \cos\left(\gamma B_\perp t\right)\end{aligned} \tag{1.2.13}$$

which has the simple interpretation of rotating the magnetization by a flip angle $\alpha$

$$\alpha(t) = \gamma B_\perp t. \tag{1.2.14}$$

Therefore, introducing a circular polarized field in the transverse plane allows to manipulate both components of the magnetization. Creating this field is the role of the RF transmit antenna. From (1.2.10), and in the limit of small flip-angle defined as $M_z \approx$ constant, the general law of the final magnetization state for an arbitrary pulse $B_\perp(t)$ of duration $T$ is given by

$$M_\perp(T) = iM_z e^{-i\gamma\Delta B_0 T}\int_0^T \gamma B_\perp(\tau)e^{i\gamma\Delta B_0\tau}\mathrm{d}\tau. \tag{1.2.15}$$

Under a centered time parametrization shifted by $T/2$ and with the associated $B_\perp$ function redefinition, one gets

$$M_\perp(T) = iM_z e^{-i\frac{\gamma}{2}\Delta B_0 T}\int_{-T/2}^{T/2} \gamma B_\perp(\tau)e^{i\gamma\Delta B_0\tau}\mathrm{d}\tau \tag{1.2.16}$$

which reads as: the response of the magnetization to an RF pulse is the Fourier transform of the $B_\perp$ pulse evaluated at the magnetization off-resonance. For arbitrary $B_\perp$ waveform and for large flip angle, no analytical solution exists and numerical methods must be performed to establish the magnetization response.

By convention and because it is an experimental parameter, $B_\perp$ is often noted $B_1$, and both notations may be found in this work.

The following describes spatial encoding, generated by additional instructions to the gradient coils. The measured signal $y$ is

$$y(t) \propto \int M_{\perp}(\mathbf{x},t) \exp\left(\int_0^t -i\gamma B_z(\mathbf{x},\tau)\mathrm{d}\tau\right) \mathrm{d}V. \tag{1.2.17}$$

Defining $\mathbf{k}$ as

$$\mathbf{k}(t) = \gamma \int_0^t \mathbf{G}(\tau)\mathrm{d}\tau \tag{1.2.18}$$

and for static off-resonance, it becomes

$$y(t) \propto \int M_{\perp}(\mathbf{x},t) e^{-i\gamma\Delta B_0(\mathbf{x})t} e^{-i\mathbf{k}(t)\cdot\mathbf{x}}\mathrm{d}V. \tag{1.2.19}$$

Measuring during a short time in which the magnetization does not undergo significant relaxation allows sampling of the spatial Fourier transform of the transverse magnetization. The representative sampling time is the echo time $T_E$, defined as $\mathbf{k}(T_E) = \mathbf{0}$. How to obtain a discrete image from the sampling is briefly explained in §1.3. In practice, the measured signal of the induced electromotive force has to be demodulated around the frequency $\Omega$ in order to correspond to (1.2.19).
Combining gradient instructions and RF pulses, it becomes possible to select either a slab for 3D $\mathbf{k}-$space encoding or a thin slice for 2D encoding. For example, combining a cardinal sine RF pulse with frequency $f$ with a constant gradient $G_s$ allows the excitation of a slab (or slice) of width

$$\Delta s = \frac{f}{\bar{\gamma} G_s} \tag{1.2.20}$$

along the direction of $\mathbf{G_s}$, which follows directly from (1.2.16).
Finally, it should be mentioned that the transverse components of the magnetic field cannot be zero by Maxwell laws

$$\nabla \cdot \mathbf{b} = 0 \qquad \text{and} \qquad \nabla \times \mathbf{b} = \mathbf{0}. \tag{1.2.21}$$

The transverse components of the field are called the concomitant field, but can be safely neglected at high-field.

## 1.3 Basics of image reconstruction

### 1.3.1 Cartesian acquisition and reconstruction

The following and additional discussions can be found in all reference MRI textbooks, such as [16].
A standard MRI acquisition is to sample a Cartesian grid of $\mathbf{k}-$space. The following one dimensional encoding scheme can immediately be generalized to encoding in two or three dimensions. The measured signal $y$ is given by

$$y_n = \int m(x) \exp\left(-ixn\Delta k\right) \mathrm{d}x \tag{1.3.1}$$

where $\Delta k$ is the experimental parameter relating to difference of the $x$ gradient moment at sampling time, and $n \in \{-N, -N+1, \dots, N-1\}$. The hardware dependent gain factor is assumed to be equal to one for simplicity. The image $I$ is reconstructed by discrete Fourier transform

$$I(x) = \sum_{m=-N}^{N-1} y_m \exp\left(ixm\Delta k\right). \tag{1.3.2}$$

A direct computation shows the usual Nyquist criteria

$$I(x+L) = I(x) \qquad \text{with } L = \frac{2\pi}{\Delta k}. \tag{1.3.3}$$

With $\Delta x = \dfrac{L}{2N}$ the voxel value is given by

$$I(x) = \int m(x')\mathrm{sinc}\left(\frac{\pi}{\Delta x}(x'-x)\right) \frac{2Ne^{-i\dfrac{\pi}{L}(x'-x)}}{\mathrm{sinc}\left(\dfrac{\pi}{L}(x'-x)\right)}\mathrm{d}x'. \tag{1.3.4}$$

The voxel signal is therefore directly linked to the magnetization value via a convolution with a so-called point-spread function (PSF). $\Delta x$ is the voxel resolution in the $x$ direction, and nicely coincides with the more formal definition of the resolution given by

$$\text{resolution} = \frac{\int \mathrm{PSF}(x)\mathrm{d}x}{\mathrm{PSF}(0)}. \tag{1.3.5}$$

### 1.3.2 Parallel imaging

While a full **k**−space sampling is required to reconstruct the complex image, additional spatial discrimination to that of the gradient coils exists in the acquired data if multiple receive coils are used. For each receive channel the reconstructed image is weighted by the associated sensitivity profile. Parallel imaging amounts to exploit this weighting as a way to speed up the image acquisition by acquiring only part of the **k**−space. Many under-sampling patterns have been proposed, and the theoretical description of the main Cartesian sampling scheme will be presented here. Application of said schemes to FatNavs is discussed in §1.6.
Measuring one **k**−space point every $R$ points in one direction leads to an effect called aliasing, where the $n$-th voxel value is given by

$$m_R(n) = \sum_{k|R=0} y(k)e^{i2\pi\frac{kn}{2N}} = \frac{1}{R}\sum_{r=0}^{R-1} m(n+\frac{2Nr}{R}). \tag{1.3.6}$$

The aliasing will appear due to the violation of the Nyquist condition for each receive channel, as can be observed from

$$m_R(n) = m_R(n+\frac{2N}{R}). \tag{1.3.7}$$

The aliased images of each channel relate to underlying magnetization image $m$ by

$$\begin{pmatrix} m_{R,1}(n) \\ \vdots \\ m_{R,n_c}(n) \end{pmatrix} = \begin{pmatrix} S_1(n) & \dots & S_1(n+\dfrac{(R-1)2N}{R}) \\ \vdots & \ddots & \vdots \\ S_{n_c}(n) & \dots & S_{n_c}(n+\dfrac{(R-1)2N}{R}) \end{pmatrix} \begin{pmatrix} m(n) \\ \vdots \\ m(n+\dfrac{(R-1)2N}{R}) \end{pmatrix} = S\mathbf{m}. \tag{1.3.8}$$

If the number of receive channels $n_c$ exceeds the acceleration factor $R$, and if the sensitivity maps are different from one another, then (1.3.8) can be directly solved by inverting the $S$ matrix. This method is called SENSE [9], and as expected it leads to the same result as the least square solution of the MRI signal forward problem:

$$\underset{\mathbf{m}}{\arg\min} \parallel \mathbf{y} - ES\mathbf{m} \parallel^2 \tag{1.3.9}$$

where $\mathbf{y}$ is the measured under-sampled data, $S$ the sensitivity maps and $E$ the Fourier encoding operator.
Another established reconstruction, dubbed GRAPPA [10], fills up the non-acquired data $y_c(\mathbf{k})$ directly in $\mathbf{k}-$space by a linear combination of the acquired neighboring data from all channels:

$$y_c(\mathbf{k}) = \sum_{c',j} w_{c,c',j} y_{c'}(\mathbf{k} + \delta_{\mathbf{j}}\mathbf{k}) \tag{1.3.10}$$

where the weights $w_{c,c',j}$ are estimated on fully sampled data. GRAPPA bypasses the sensitivity maps estimation by assuming (1.3.10), which in image space is equivalent to the hypothesis that on the spatial signal domain $(m(\mathbf{x}) \neq 0)$

$$S_c(\mathbf{x}) = \sum_{c',j} w_{c,c',j} S_{c'}(\mathbf{x}) e^{i\delta_{\mathbf{j}}\mathbf{k}\cdot\mathbf{x}}. \tag{1.3.11}$$

### 1.3.3 Metrics of image quality

This short text aims to clarify the notion of a good brain image. What makes a general image good ? The logical and probably most accurate answer is an image which represents what it should. In the case of a brain image, the anatomy should be represented accurately, under the limits of the acquired contrast and resolution. For example, this implies undeniably visible boundaries of structures and no signal outside of the head.
MRI is prone to artefacts, among which motion artefacts are a common example. In a clinical setting, the notion of diagnostic image quality arises. It qualifies whether the artefacts of the image (if any) exclude or hinder establishing a diagnostic. The final image is meant to be interpreted by a radiologist, therefore a sensible image comparison metric of two similar images is to ask several radiologists if one provides different information compared to the other. For example it might be that some slight ringing, while clearly visible, does not critically hinder the diagnosis. However for high-resolution imaging in a research oriented context, said ringing would likely be unacceptable. Also, in said context, accurate radiologic expertise may not be needed, as the ringing is readily identifiable by an observer without clinical training.
It becomes natural to try and look for a measure of image quality, which would correlate to ringing and blurring reduction. Among the many proposed [17], two often used and reliable metrics are the gradient entropy and the normalized gradient squared. In this work, the gradient is understood as the Euclidean norm of the 3D discrete gradient.

## 1.4 MR signal and motion in brain imaging

The working assumptions of this text are that concomitant field, timing errors, field inhomogeneity, gradient non-linearity and eddy currents are all negligible. Consider a magnetization packet, of trajectory $\mathbf{x}(t)$, and of weight $m(t)$. This weight intrinsically includes relaxation effects ($T_2$ or $T_2^*$) and previous excitation history, i.e. it depends on $T_1$ and $T_R$. It is proportional to the transverse magnetization of the sample, where the proportionality constant is hardware dependent. Also, perfect spoiling between excitations is assumed. The MR signal $y_c$ of a receive coil $c$ as a function of time is then

$$y_c(t) = \int_V s_c(\mathbf{x}(t)) m(t) \exp\left(-i\phi\left[t, \mathbf{x}\right]\right) \mathrm{d}V \tag{1.4.1}$$

where $s_c$ is the receiver spatial sensitivity profile. The exponential factor represents the spatial encoding

$$\phi\left[t, \mathbf{x}\right] = \gamma \int_0^t \mathbf{G}(\tau) \cdot \mathbf{x}(\tau) \mathrm{d}\tau \tag{1.4.2}$$

with $\mathbf{G}$ the $z$ magnetic field gradients.

In the stationary case $\mathbf{x}$ is time independent, and the object image is obtained by inverse Fourier transform of the measured signal. The position in Fourier space, or $\mathbf{k}-$space, is given by

$$\mathbf{k}(t) = \gamma \int_0^t \mathbf{G}(\tau) \mathrm{d}\tau.$$

The total MR signal will be a sum of the signals for all the “magnetization packets” of the sample. Several motion types should be distinguished at this stage:

1. Flow: Blood is intrinsically a moving signal source. The position of some blood molecules is always changing between the RF excitation pulse, the phase (and slice) encoding gradient(s), and the signal acquisition. This typically leads to flow artefacts in the image, coming from the inconsistency in the encoding because of the $x(\tau)$ term. Gradient moment nulling techniques [18] allow rewinding of the non-zero velocity induced phase contribution, and therefore localize the blood signal more accurately (in practice, only a first moment nulling is usually implemented).

2. Diffusion: Water molecules diffuse in tissue. This means that, inevitably, all sequence signals have some diffusion weighting [19]. The scale of motion associated to diffusion is much smaller than the imaging resolution, hence this type of motion is to be understood as a signal weighting process and not an artefact source.

3. Elasticity: Blood flow is not constant over-time, but periodic. This implies that blood vessels, at every length scale, follow contraction/dilatation periods. Ultimately, acquiring brain at fixed time points in the cardiac cycle, allows construction of deformation maps. It was found that the maximal displacement does not exceed 0.2 $mm$ [20]. State-of-the-art estimates of cardiac induced bulk motion estimates are of the same order [21].

4. Bulk motion: It is the motion of the head as a whole. Its causes are many, among them are nodding, shifting due to an uncomfortable body position, muscle relaxation and breathing. This is the motion one aims to quantify and then correct for.

From here onward, the term motion refers to bulk motion. A major advantage in brain MRI compared to other body parts it that the brain is, to a very good approximation, a rigid body (keeping in mind the elasticity and flow phenomena). This means its motion can be fully determined with only six parameters: three for translations and three for rotations. Obviously there are pitfalls to this approximation. For example, if the lower jaw or the tongue is in the excited volume, the hypothesis breaks down, as they are physically not rigidly connected to the brain. The eyes also follow a different motion than the head. However, either by a clever choice of the phase encoding direction(s) and/or of the excited volume, the artefacts produced by these parts can usually be pushed outside of the brain. Mathematically, rigid motion is defined as

$$\mathbf{x}(t) = R(t)\mathbf{x}(0) + \mathbf{d}(t) \tag{1.4.3}$$

where $R(t)$ and $\mathbf{d}(t)$ are the rotation matrix and translation vector respectively.
Now to model the brain MR signal in presence of motion. If $m(\mathbf{x})$ now denotes the full object at time equal 0 in (1.4.3), and if no motion takes place during the measurement of $\mathbf{k}$, that is $R$ and $d$ are constant during the measurement, then the signal becomes

$$y_c(\mathbf{k}) = \exp\left(-i\mathbf{k}\cdot\mathbf{d}\right)\int_V s_c(R\mathbf{x}+\mathbf{d})m(\mathbf{x})\exp\left(-iR^T\mathbf{k}\cdot\mathbf{x}\right)\mathrm{d}V \tag{1.4.4}$$

As for nearly all motion correction techniques, the change of the receiver sensitivities induced by motion was neglected. Most often, thanks to tight foam padding of the subject head which restricts the range of motion and the slow spatial variation of the sensitivities, this assumption is justified. Notice that, in the event of several readouts per excitation, such as in TSE sequences, motion in between refocusing pulses is not adequately modeled by (1.4.4). A derivation based on the general equation (1.4.2) should be used instead .
The main implications of the motion induced signal changes are:

- While somewhat hidden in the notation of (1.4.4), spin history will potentially not be consistent across the whole image acquisition. Indeed for spatially selective excitations, motion will generally imply that the excited brain region during the scan is not the same before and after moving. Furthermore, the steady-state of the newly excited region is not yet established when acquired, adding further undesirable signal modulation. Large slabs are by definition less sensitive to these effects, as most of the signal represents the constantly excited regions. In all standard acquisitions, the flip angle does not vary enough on the motion range to induce inconsistency in the signal. On the other hand, 2D acquisitions are the worst case scenario for these spin history effects.

- As seen in (1.4.4), rotations imply that the $\mathbf{k}-$space is sampled at a rotated version of the targeted position. For translations, the well known equivalence to phase ramps in $\mathbf{k}-$space is explicit. The strength of the motion artefacts on the image depends both on the motion parameters, and when motion takes place, i.e. where in $\mathbf{k}-$space. Simulated examples are shown in Figure 1.1.

It was shown [22] that the most prevalent motion in clinical data larger than 0.5 mm or ° is the pitch rotation (around the left-right axis) and the head-foot translation. Motion of lower amplitude is generally expected to be unavoidable.

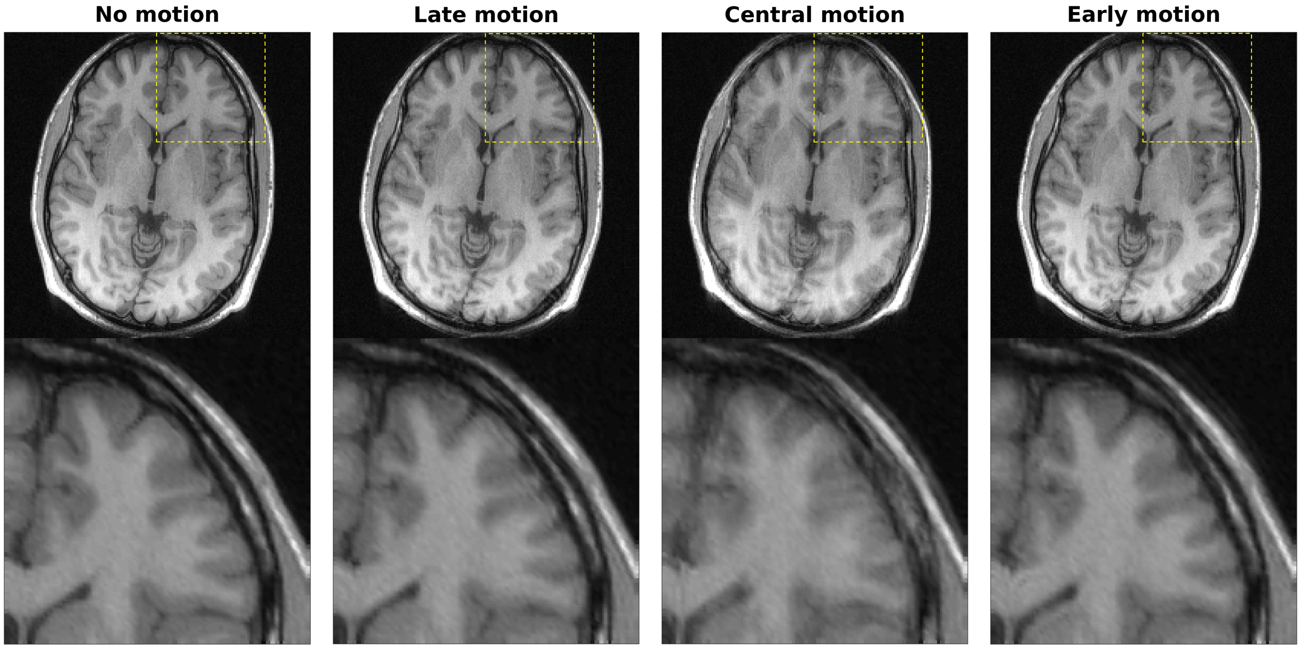
No motion
Late motion
Central motion
Early motion

(a) Simulation of a 5°in-plane rotation.

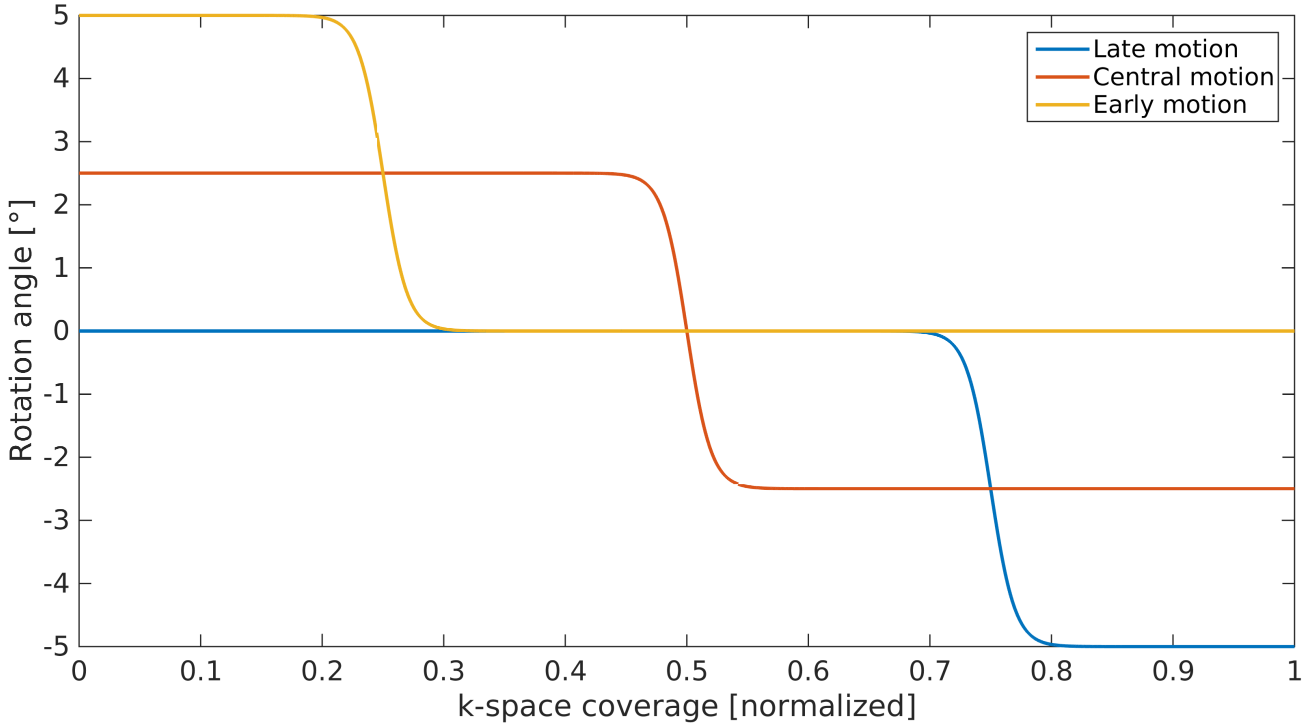

(b) In-plane rotation angle during $\mathbf{k}-$space acquisition.

Figure 1.1 – Possible impacts of motion during acquisition (simulation). Raw data used for simulation were downloaded from `https://people.eecs.berkeley.edu/~mlustig/Software.html` .

## 1.5 Literature review

### 1.5.1 Prospective and Retrospective correction

In order to correct for motion, one must first estimate the six motion parameters. If this is feasible sufficiently often, one can feed the information back to the scanner to update the geometrical parameters used for scanning, so that the scanner follows the subject motion. This procedure is called prospective motion correction (PMC). It is important to understand that typically no extrapolation is done when applying PMC, so that in reality it is slightly lagging behind the true motion. This delay is larger if some filtering of the motion parameters is applied. PMC can also produce unwanted image artifacts when the motion parameter estimations fall far from their true values, for example if the marker becomes loose or changes its position relative to the brain. PMC has the advantage that, when precise motion estimates are available, all major motion induced problems disappear (for typical ranges of motion). No unwanted spin history alteration takes place and the image reconstruction can be carried exactly like in a scan without motion. For Cartesian sampling that means very fast algorithms can be readily applied.

Retrospective motion correction (RMC) involves correcting for motion only after data acquisition. In practice, one extrapolates the motion state during the whole $\mathbf{k}-$space acquisition from some punctuated motion parameter estimates. Translations are compensated by applying the appropriate phase-ramp correction. The correction of rotations is more involved, as it means finding the image $m$ such that $y_c = F s_c m$ where $F_c$ is the Fourier operator defined by the measured $\mathbf{k}-$space trajectory, i.e. locally rotated compared to the intended trajectory. Formally this problem should be solved iteratively, and several alternatives exist to combine the receiver channels. In practice, especially for high-resolution imaging, only the first step of the iteration is carried out (channel-wise), and then the motion corrected images are combined. For each channel, the motion corrected image is given by $m_c = \tilde{F}^\dagger y_c$ with $\tilde{F}^\dagger$ the adjoint of a fast non-uniform Fourier transform (nuFFT) operator [23]. The main disadvantages of RMC are the following. It can only be robust for 3D excitation based sequences because of through plane motion. Spin history effects can however be present in case of through plane/slab motion depending on said motion amplitude and the specific excitation pulses used. It also is much more computationally expensive for Cartesian trajectory based sequences compared to the non corrected reconstruction.

RMC can also be used for retrospective motion de-correction of PMC data, thereby producing a motion corrupted image, without spin history related artefacts, allowing comparison of corrected and de-corrected images [24]. RMC could theoretically also be used to enhance the timing of motion estimates applied during PMC, thereby mitigating the effects of PMC's intrinsic delays. However, current PMC methods have a high update frequency ($> 10$ Hz), making such combination only likely to be useful in very specific applications.

### 1.5.2 External sensor based motion tracking

Here external sensors solutions will be summarized. These sensors can be MR based or rely on other mechanisms. The idea is to attach one or several markers to the subject's head, and track these markers motion. The brain motion is then assumed to be the same as that of the marker. First non-MR based methods, such as optical tracking, will be discussed. If the marker has no specific pattern, like a homogeneous sphere, then several markers (and potentially cameras) will be needed to fully quantify the motion parameters. On the other hand, a single marker and camera setup can be sufficient for complete motion quantification if the marker encodes enough information, such as checkerboards [25] and Moiré patterns [21]. Marker-less optical tracking using structured light has also been proposed [26]. Advantages of these methods are that they are completely independent of

the MRI sequence, and fast data processing allows for PMC at a high refresh rate (50 Hz). Because of the high refresh rate, sequence independence and high accuracy, they are regarded as the current gold-standard for motion tracking and have found diverse applications, such as very-high resolution scans [27], functional MRI [28] and quantitative MRI [29]. However, they also come with disadvantages. First and foremost, the marker is required to be in the line-of-sight of the camera. Due to the generally closed or grid-like RF head coil geometries, this is not always possible. Specific solutions, such as attaching the marker to a mouthpiece reaching outside of the RF coil have been implemented. However such methods require patient specific devices.
Non-MR based methods require a cross-calibration step which links the reference frames of the camera, in which motion is quantified, to the scanner coordinate system. Suboptimal calibration necessarily produces wrong patient motion estimates, and visible artefacts can emerge under moderate motion ($\sim 8^\circ$) with a one degree calibration error [30].
Sensors using the MR scanner have also been investigated. These methods usually require some dedicated module in the imaging sequence to acquire the marker MR information, often based on 1D projections. A noticeable exception [31] uses a magnetometer and an accelerometer and, assuming $\mathbf{B_0}$ and gravitational field $\mathbf{g}$ to be orthogonal, it can estimate rotations without any sequence change. Such methods have the advantage to be defined directly in the scanner coordinates system, so that cross-calibration is not needed. The latest methods rely on local RF transmit coils [32–34]. These local coils allow for higher SNR. It has been shown that using concentric shells in $\mathbf{k}-$space allows for both translation and rotation estimates [35]. Figure 1.2 shows some hardware setup examples.
A variation of the method called gradient tones [36] uses rapidly oscillating gradient waveforms and allows to super-impose the marker and the image encoding gradients without penalty. It was implemented using local transmit and receive RF coils. Using a different nucleus than $^{1}$H for the marker ($^{19}$F in this case) highly reduces any interaction with the water signal studied in MRI. Processing the phase of the marker signal yields its coordinates. It was more recently shown that the logic of the gradient tones can also be used using only native sequence elements, without additional oscillating gradients [37].

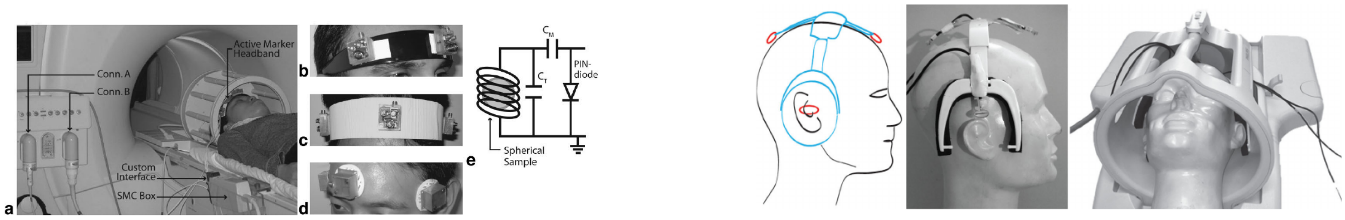

(a) Water based markers setup, taken from [32].

(b) Gradient tones setup, taken from [36].

Figure 1.2 – Setups for some marker based motion tracking modalities.

### 1.5.3 MR navigators motion tracking

MR navigation attempts to establish the subject motion using the signal model (1.4.4). An imaging sequence can be self-navigated (which requires some redundancy in the signal acquisition), or external navigator instructions can be added to the sequence, such as RF pulses and/or gradients followed by signal acquisition. The mapping from navigators to motion can be done in several ways. One approach is to compare each navigator to a reference navigator of the same kind. Another possibility is to compare the navigator data to a more complete reference signal.

Depending on the navigator module, the signal may not come from the whole head, but only from the excited slice, which restricts the available motion information. Acquiring data after a 2D slice excitation will naturally fail to properly quantify any through-slice motion, that is one translation and 2 rotations. Accessing the six motion parameters intrinsically requires more data. For example, neglecting rotations implies that the three central axis-lines of $\mathbf{k}-$space give the projections of the signal on each axis, and translations can therefore be inferred. The following describes representative navigation methods proposed in the literature.

It is possible to find motion directly from the $\mathbf{k}-$space data. From the magnitude one can first estimate rotations. Once these have been taken into account the phase of the signal is used to infer translations. To estimate rotations precisely, it is necessary (and sufficient) to sample a sphere surface densely. This acquisition can be done once and serve as reference for future navigators, like for the so-called cloverleaf navigators [38], or for every navigator, such as in the spherical navigators (sNavs) approach [39, 40]. Figure 1.3 shows the trajectories of these navigators. Other trajectories, such as spirals, have been proposed. The advantage of such methods is the very short acquisition time. However, they have yet to demonstrate the capacity to correctly quantify small, involuntary motion. Also, unlike image magnitude based estimates, they are more sensitive to system imperfections (gradient delays, eddy currents) and $B_0$ inhomogeneity.

Low resolution images can be used as navigators. However they also take a significant time for signal acquisition, which is why they have mainly been included in imaging sequences with some intrinsic dead time, such at MP(2)RAGE or TSE. EPI volumetric navigators (vNavs) (8 $mm$ with $\frac{3}{4}$ partial Fourier) have been used with PMC [41–43], but application to high-resolution imaging is still under investigation [44].

PROMO (PROspective MOtion correction) [45] acquires three orthogonal thick (1 cm) slices during a parent sequence's dead-time (such as inversion recovery or turbo spin-echo). As these acquisitions use spiral $\mathbf{k}-$space trajectories, they were called SP-Nav. An example can be found in Figure 1.4b. Motion is estimated in real-time and allows prospective correction. During the dead-time, several SP-Navs are acquired and using the extended Kalman filter algorithm, the current motion estimate is updated each SP-Nav, allowing a finer final estimate to be used for the imaging part of the parent sequence. Due to the large field of view of each plane, a region of interest assumed to follow rigid motion is defined in each navigator after registered to a brain atlas, which allows the suppression of the neck and jaws to the motion estimates. The reference SP-Nav is the last of the dummy scans acquired at the beginning, before the effective image acquisition.

Fat navigators (FatNavs) have also been proposed. They have the added advantage of limited impact on the water signal and greatly benefit from parallel imaging techniques thanks to the natural spatial sparsity of the fat signal. Proposed FatNavs include: one 2D EPI sagittal slice [46], 3D excitation followed by three 2D EPI projections [47] and highly accelerated 3D GRE [48]. The former two methods allow PMC and show image quality improvement for large motion, while the latter is currently restricted to RMC approaches, but has been proved beneficial even for microscopic involuntary motion.

As mentioned previously, imaging sequences can also be self-navigated, at the price of acquisition redundancy. Radial trajectories have many desirable properties for motion correction, but are ill-adapted to high-resolution imaging as they rapidly become prohibitively time-consuming (this is because the Nyquist criteria is $\frac{\pi}{2}$ times greater in two dimensions, and even worse in three dimensions). The $\mathbf{k}-$space center oversampling on its own leads to less pronounced large scale motion artefacts by pure averaging. Additionally, the rigid body model allows for motion estimates. In PROPELLER (Periodically Rotated Overlapping ParallEL Lines with Enhanced reconstruction)[49], blades (originally called strips) are standard Cartesian acquisitions passing through the $\mathbf{k}-$space center. Several blades are acquired at different angles, leading to a circular

area at the center of $\mathbf{k}-$space sampled for every blade. A graphical representation of the acquisition is shown in Figure 1.4a. Therefore motion between blades can be estimated at this lower resolution. This method is used in two dimensional acquisitions. The corrected blades with worst correlation scores to the the mean corrected signal in the circular area are down-weighted in the final reconstruction. This in turn reduces through-plane motion artefacts.
One can also estimate motion by using the first moments of the acquired spokes. Two dimensional motion correction was proposed [50]. The center of mass can be found from the zeroth and first moments, and gives the translations between the spokes acquisitions. The in-plane rotation is computed from the second moments of translation corrected spokes. Using a gridding approach, finding the rotation first and then the in-plane translation was implemented on segmented acquisitions [51]. It was also shown that the segments acquisition ordering is important to reduce gaps in the corrected $\mathbf{k}-$space, and bit-reversed ordering is preferable in that respect (the bit reversed ordering of the sequence 1 2 3 4 5 6 7 8 is 1 5 3 7 2 6 4 8). Three dimensional motion correction is also possible. It was proposed [52] to divide a pseudo-random acquisition scheme into motion-free data subsets, detected by change of the center of mass. Each subset covering enough directions (thanks to the "isotropic" acquisition order), it allows low resolution images reconstruction and registration, leading to the full motion estimates. This method proved efficient for step-like motion. Data which cannot be corrected for is simply discarded, without creating gaps in $\mathbf{k}-$space and hence only inducing lower final SNR. Another 3D approach [53] acquires rotated Cartesian planes in $\mathbf{k}-$space after a 3D excitation. Using bit-reversed ordering of the plane angle, successive planes are orthogonal and the parallel imaging technique GROWL is used to complete $\mathbf{k}-$space in a central cylinder, using successive plane pairs. Each plane pair therefore leads to fully sampled central cylinders, from which three dimensional motion (relative to a reference pair) is estimated.
Using the free induction decay (FID) signals, it is still possible to detect motion thanks to the combination of the receiver spatial inhomogeneity [54] and the high coherence of the FID signal. This signal is sensitive not only to motion, but also to field drifts, breathing-induced $B_0$ changes and eddy-currents (non-constant during imaging sequences !) for example. It has been demonstrated as useful for detection of motion events, and can be used to decide whether another motion specific navigator should be acquired[55].
Finally, additional assumptions can lead to motion quantification and/or correction without acquisition redundancy. A few of such methods are presented below.
An original use of data consistency arises from parallel imaging. The SMASH hypothesis is such that the sensitivity maps can be combined such that

$$\sum_c w_{c,m}(x) s_c(x,y) = \exp(-im\Delta k_y) \quad \forall x, \quad m \in \mathbb{N}. \tag{1.5.1}$$

Finding the phase factors applied to fully sampled data such that the condition is best satisfied is called SMASH Navigators [56], and was used for retrospective correction of in-plane translations . It is a cumulative correction, growing from a reference line and using the SMASH condition with $m = 1$ (growing right) or $m = -1$ (growing left).
In segmented acquisitions, where the subject position is assumed constant during each segment, it is possible to retrieve the translation induced phase from correlation of highly under-sampled (one segment only) based images [57, 58]. This works better if the acquisition field-of-view is larger than the object.
Although not truly navigated, Projection Onto Convex Sets (POCS) reconstruction allows the detection of inconsistent data, arguably due to motion. This data is then discarded before the final reconstruction [59]. This logic, applied to a randomized $\mathbf{k}-$space acquisition scheme allowed

reduction of motion artefacts in 2 dimensional imaging. It is also capable of reducing artefacts due to pulsatile motion. However, motion is not quantified.

In summary, navigator methods have mostly been implemented in imaging sequences with sufficient dead-time. Prospective and retrospective correction have been proposed, the former uses coarser navigator resolution but showed good image improvement in case of large deliberate motion. Sequences without dead-time can be self navigated, but rely on some radial-like $\mathbf{k}-$space trajectory. They are therefore highly inefficient for very-high resolution imaging. Data reacquisition allows for more uniform $\mathbf{k}-$space sampling at the price of unpredictable additional scan-time.

The different navigators have not been directly compared as implementing them simultaneously is most often not possible, or even contradictory, and repeating the same motion pattern during a long scan is qualitative at best. Furthermore, not all navigators track the same motion parameters, making comparison not always sensible.

Little work has been done to compare navigator methods to sensors-based ones. Most relevant is perhaps the PROMO comparison to Moiré-Phase Tracking [60] where large ($\geq 0.5$ mm / °) differences were observed.

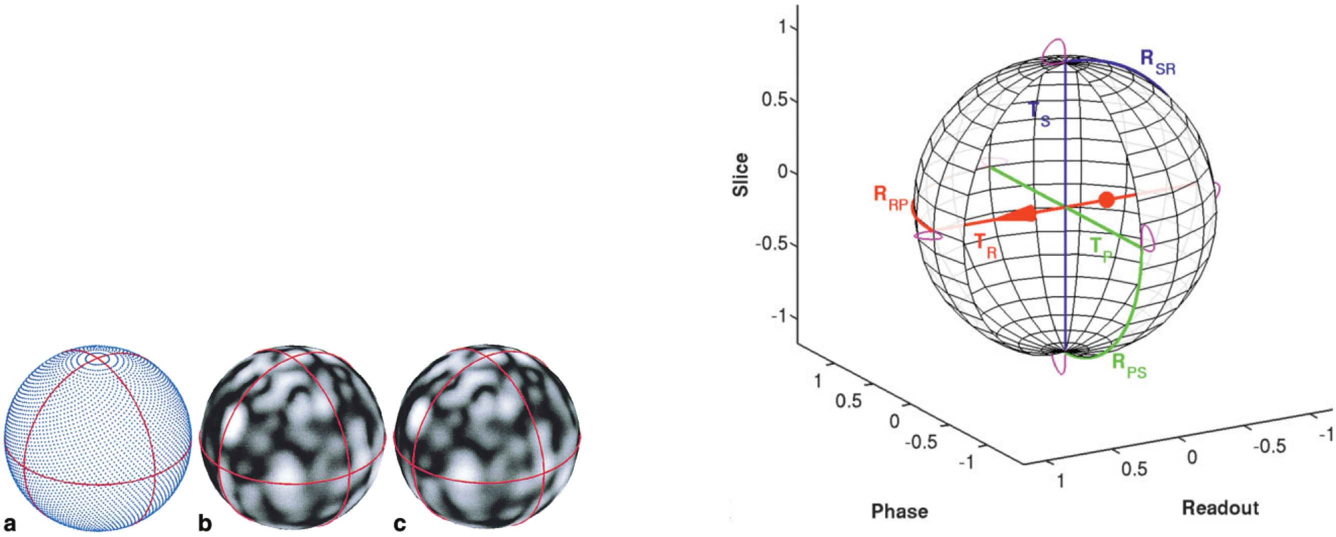

(a) Spherical navigator, taken from [39]. **b** and **c** shows the change in the signal magnitude after rotation.

(b) Cloverleaf navigator, taken from [38].

Figure 1.3 – Examples of $\mathbf{k}-$space based motion navigators trajectories.

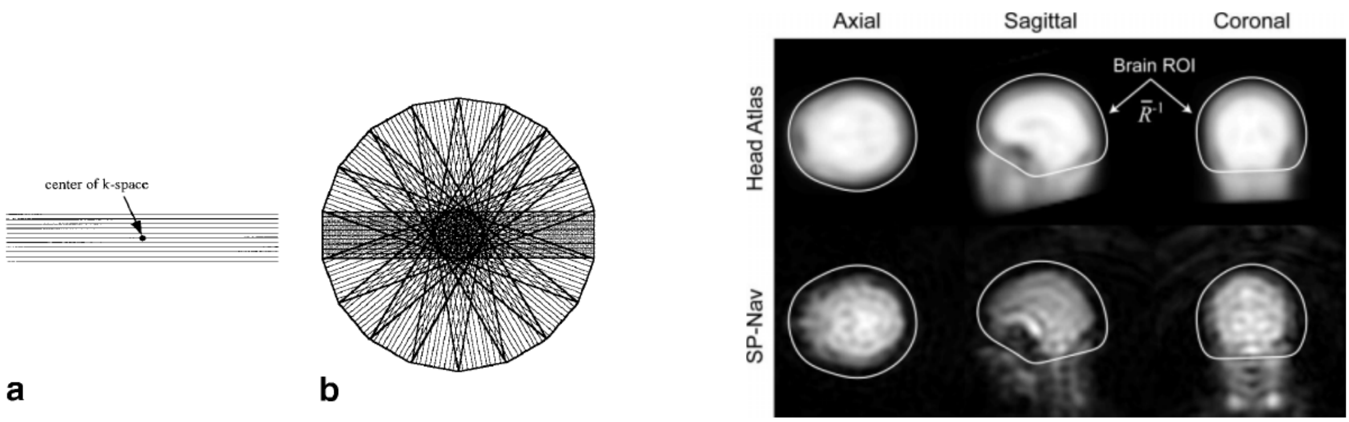

(a) PROPELLER trajectories, **a)** a single strip , **b)** all acquired data (multiple strips), taken from [49].

(b) SP-Nav example from the PROMO approach, taken from [45]

Figure 1.4 – Examples of image-space based navigators.

### 1.5.4 Auto-focusing methods

Auto-focusing methods involve a fully model-based correction. The idea is to find motion parameters which minimize some cost function $C(m)$. This cost function has the general form

$$C = \text{artefact metric} + \text{regularization terms}.$$

For a current trial estimate of the motion parameters $p$, one computes the correction operator $F_p^\dagger$ and the cost function value is given by

$$C(F_p^\dagger y)$$

with $y$ the measured data. This non linear problem is solved iteratively. Proposed metrics include image and gradient entropies [61, 62]. The regularization terms try to enforce some prior knowledge, such as relatively smooth motion during the scan. While these methods, by construction, only apply motion-like correction, it is unclear to what extent the resulting image can be trusted due to their implicit dependence on the choice of the metric. For example, the metric value will intuitively be contrast dependent and hence introduce bias between different tissues. Their main advantage is full blindness, making them a priori applicable to any acquired data, without the need for additional motion-tracking hardware or sequence modifications.
Other variations of the logic exist. For example, the search space can be both the image and the motion parameters [63]. For such methods, it was shown [64] that the acquisition order matters for the reconstruction to converge to a satisfactory final image.

## 1.6 FatNavs

The goal of this section is to introduce the technical basis used by fat navigators in their original form. It will focus on snapshot-like FatNavs, meaning the navigators are acquired as blocks inserted into the host imaging sequence. Their general limitations and impacts shall be discussed.

### 1.6.1 Fat in head MR imaging

**Signal sources**

The sources of fat signal observed during head MRI are the bone marrow fat, the subcutaneous fat layer and the fat present in the ocular orbits .

The following descriptions and numbers are summarized from [65]. At the molecular level, fat is a general name covering several families: saturated , monounsaturated and diunsaturated (i.e. with zero, one or two double bonds between carbon atoms, respectively). These constitute roughly 30%, 45% and 25% of the fat contents in the bone marrow and the subcutaneous fat.

Many hydrogens atoms enter the composition of the fatty acid chain. The dominant signal comes from the $CH_2$ methylene hydrogens, at 1.3 ppm from Tetramethylsilane (TMS). In a head imaging experiment, the water signal is the dominant signal, and hence it is convenient to consider its resonance peak as the reference, at 4.5 ppm from TMS. Therefore, from now, all chemical shifts should be understood away from the water peak, meaning fat resonates at around -3.2 ppm. At 7T, this implies that fat mostly resonates roughly 1000 Hz slower than water. A comparison of both water and fat images is shown in Figure 1.5.

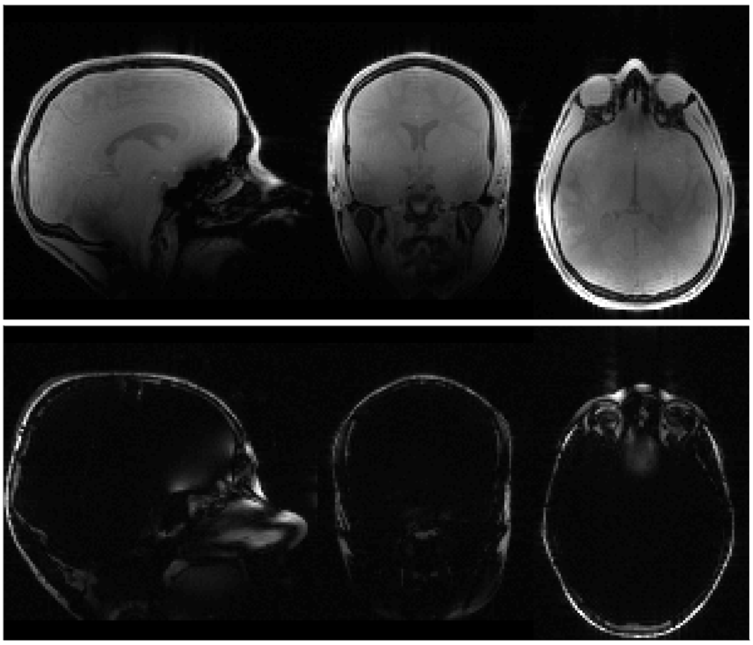

Figure 1.5 – Orthogonal views of water (top) and fat (bottom) signal sources standardly found in head MRI.

Still focusing on the methylene resonance at 7T, measurement showed fast $T_1$ relaxation of 0.55 $s$. This is significantly lower than gray and white matter ($\sim$ 1.9 $s$ and 1.15 $s$ respectively [11]). The $T_2$ value is approximately 66 ms.

### Fat selection

Let us first focus on purely spectral, i.e. spatially unlocalized, selectivity. The goal is to excite one pool (fat) and leave the other pool (water) unperturbed. The simplest RF pulse strategy achieving this is to use so-called binomial pulses. The idea is to apply several short ($\sim$100 $\mu s$) square pulses with a time delay $\tau$ between them. Assuming the RF frequency is the target frequency one wants to excite, the idea is to fix $\tau$ such that each short pulse cancels (in part) the effect of the previous ones on the undesired magnetization pool at chemical shift $\delta$. An easy way to insure that is to fix the phase-evolution time so that each pulse produces a rotation in the exact opposite direction of the previous one, i.e. after the undesired pool rotated by $\pi$. The phase evolution is related to the magnetization frequency offset $f$ and the sub-pulses separation time $\tau$ by

$$\phi = 2\pi f \tau. \tag{1.6.1}$$

This implies

$$\tau = \frac{1}{2\delta\bar{\gamma}B_0}. \tag{1.6.2}$$

With each pulse (labeled with index $i$ ranging from 1 to $N$) having a positive amplitude $A_i$, this leads to the condition

$$\sum_{i=1}^{N}(-1)^{i+1}A_i = 0. \tag{1.6.3}$$

Equation (1.6.3) is satisfied if the pulses amplitudes follow a binomial expansion, that is

$$A_i = C\frac{(N-1)!}{(i-1)!(N-i)!} \tag{1.6.4}$$

for some constant $C$. Such pulses are simply noted $1-1$, $1-2-1$ , $1-3-3-1$ for $N = 1, 2, 3, 4$ respectively. In practice, implementation is easier with water as the reference frequency. Fat selection is thereby simply established by adding a $\pi$ phase offset to every other pulse, represented by a bar above the amplitude. From now on the short square pulses will be called sub-pulses and the word pulse is reserved for the complete sub-pulses chain. The more sub-pulses are added, the sharper the frequency selectivity profile, but also the longer the total duration.

For a $1-\bar{2}-1$ binomial pulse, the transverse magnetization obtained from thermal equilibrium is

$$|M_\perp| = M_0\frac{\alpha}{2}\sqrt{\Big(\sin(2\phi) - 2\sin(\phi)\Big)^2 + \Big(2\cos(\phi)\,\big(\cos(\phi) - 1\big)\Big)^2} \tag{1.6.5}$$

in the low flip angle (noted $\alpha$) regime, for a phase evolution $\phi$ between sub-pulses. This analytical result, which neglects relaxation and assumes instantaneous sub-pulses, is readily obtained using Bloch equations. By construction, the maximal signal is obtained for $\phi = \pi$ and the minimal one for $\phi = 0$. The result is $2\pi$ periodic, but in practice this periodicity in $\phi$ is generally not important, due to the absence of magnetization further off-resonance.

Figure 1.6 shows the non-linearity of the binomial pulse for large flip angles. However, both low and high flip angle regimes show the same desired property of smooth evolution. The stop-band in the low flip angle regime is however larger, as seen by remarking that the low flip angle curve is always below the high flip angle one. Experimentally, this pulse is sufficient at 7T for fat/water separation, as Figure 1.5 shows.

Finally, let us mention there also exist pulses which combine both spatial and spectral selectivity, dubbed spatial-spectral pulses. At 7T, the $1-\bar{2}-1$ binomial pulse is roughly 1 ms long, whereas spatial-spectral pulses would be around 10 ms long [66]. Combined with other considerations, this makes such pulse very challenging for motion correction, see §1.6.3.

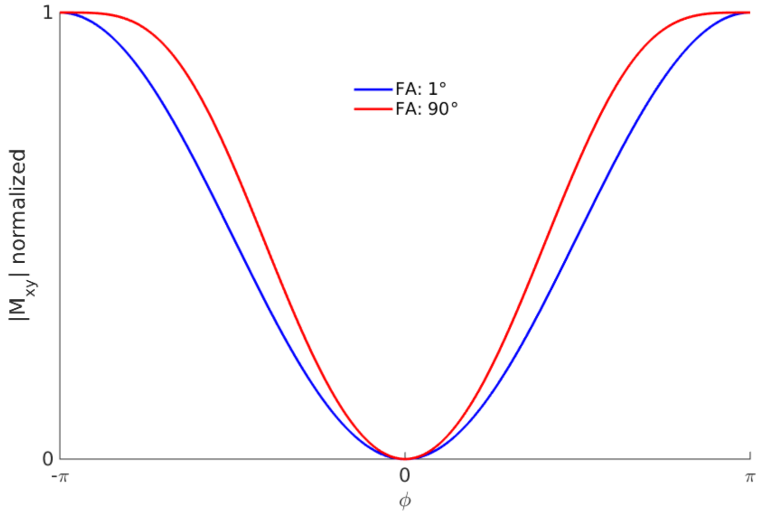

Figure 1.6 – Normalized excitation profile of the $1-\bar{2}-1$ binomial pulse. Low and high flip angle curves are normalized to exhibit the non linear behavior.

### 1.6.2 Standard FatNavs implementation

Standard FatNavs consist of a 3D GRE acquisition using a fat selective excitation. The experimental scanning parameters are chosen as follows. Due to the non spatially selective excitation, the readout direction is chosen as head-to-foot in order to minimize scan time, as this direction is one along which the fat signal is the most spread out. The readout oversampling also opens the possibility to reduce the contribution of the neck area to the final navigator image. Echo and repetition times are chosen as short as possible.

Acquiring the navigator "in one go" minimizes motion during its measurement, leading to expected better navigator quality and higher consistency between volumes. This snapshot-approach is used by standard FatNavs.

Figure 1.7 shows MRI images obtainable for different voxel sizes. Clear accuracy gain is visible between 4 mm to 2 mm, and to a lesser extent from 2 to 1.5 mm. The acquisition time of a 2mm image covering the whole head is 1.4 s, with 4 × 4 undersampling and ¾ partial Fourier in two directions. It is therefore very improbable that such a FatNavs with voxel size $\lesssim 1.5$ mm can be implemented into an imaging sequence, as the acquisition time would be around 6 seconds for a 1 mm navigator ! However, enhancing the acquisition scheme can lead to higher resolution navigator acquisition, as will be presented in §4.

As a side note, the keen observer will spot two shell like objects above the skull (especially visible in the coronal plane of the 1 mm image). These are actually signals coming from some components of the RF coil used (Nova 32Ch). However, their small size and low signal intensity do not impact registration between volumes in any significant way. Therefore, they shall entirely be neglected from now on.

The reason why high undersampling still leads to accurate FatNavs images finds itself in the signal sparsity in space. Indeed, grossly speaking, the domain of support from fat is basically a thin shell, compared to a filled ovoid for water. This intrinsic smallness compared to RF wavelength and imaging FOV implies that the GRAPPA hypothesis (see (1.3.11)) is more easily satisfied under standard experimental conditions. Conversely, this sparsity makes using a receive-coil sensitivity maps based approach much more complex for equivalent undersampling factor. Indeed, using GRAPPA automatically includes the signal domain of support information, whereas this has to be actively constrained during a SENSE reconstruction for example, which is not straightforward and

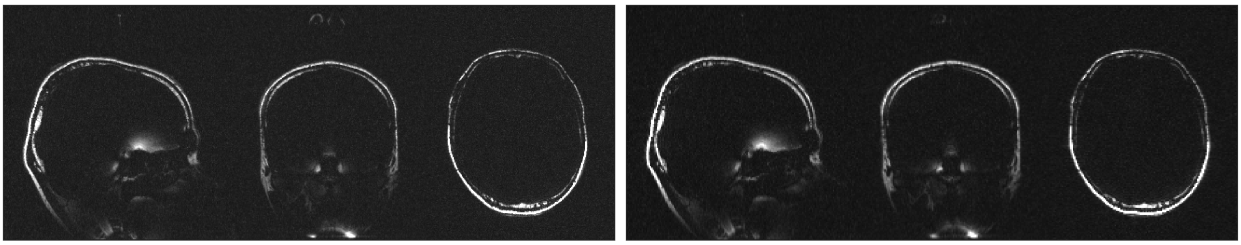

(a) 1 mm (b) 1.5 mm

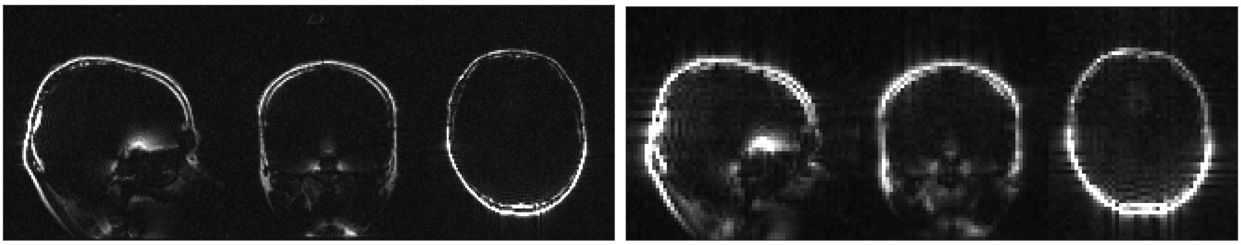

(c) 2 mm (d) 4 mm

Figure 1.7 – Resolution comparison of FatNavs.

requires significant (and often time-consuming) fine-tuning.

**k**−space can be undersampled in many ways. Figure 1.8 shows two established undersampling patterns, GRAPPA and CAIPI [10, 67]. The associated reconstructions are shown in Figure 1.9. These were obtained after undersampling of a fully sampled dataset. In the case of FatNavs, the expected gain (if any) from a CAIPI approach compared to naive GRAPPA is un-noticeable for $R = 4 \times 4$ undersampling. The windowing on this figure is very sharp to allow to notice the small differences in low signal regions and in the reconstruction artefacts. It seems clear that both reconstructions lead to the same navigator quality. Going to higher ($R = 6 \times 6$) undersampling one can spot slightly lower noise amplification in the CAIPI case, as can be seen in the posterior bone marrow region in Figure 1.10. On the practical side, implementing a CAIPI pattern in the sequence file which runs on the Siemens scanner is not a straightforward implementation process if one desires to make it robust and flexible. Given the low gain of this approach, FatNavs use naive GRAPPA undersampling patterns.

More generally, given a host imaging sequence one tries to correct motion for, going for the highest acceleration possible for FatNavs is not necessarily the best thing to do, as any undersampling leads to SNR loss, so a trade-off between acquisition time (both for the snapshot hypothesis and the timing of the host imaging sequence), resolution and SNR has to be considered. As will be shown in §5.2, even 4 mm FatNavs can correct motion in very high-resolution (0.25 mm isotropic) angiography imaging, suggesting the need for combined higher-acceleration and high-resolution FatNavs is questionable.

Finally, it is tempting to try to further exploit the sparsity in space of the fat signal using a more involved image reconstruction framework. It is well known [68] that constrained reconstruction methods can enforce desired properties (also called prior-knowledge) of the reconstructed image. The $L_1$ norm, usually noted $\| \cdot \|_1$, is a constraint which promotes sparsity. With the navigator **k**−space data noted $y$ and the Fourier encoding operator noted $E$, the reconstructed image $\hat{x}$ is given by

$$\hat{x} = \arg\min_{x} \|Ex - y\|_2 + \lambda_1 \|x\|_1 \tag{1.6.6}$$

where $\lambda_1$ is the relative weight of the sparsity constraint term to the first term, which enforces data consistency. The problem becomes non-linear with such constraints, and iterative methods such as conjugate gradient become necessary to find an estimate of the solution. Comparing to the

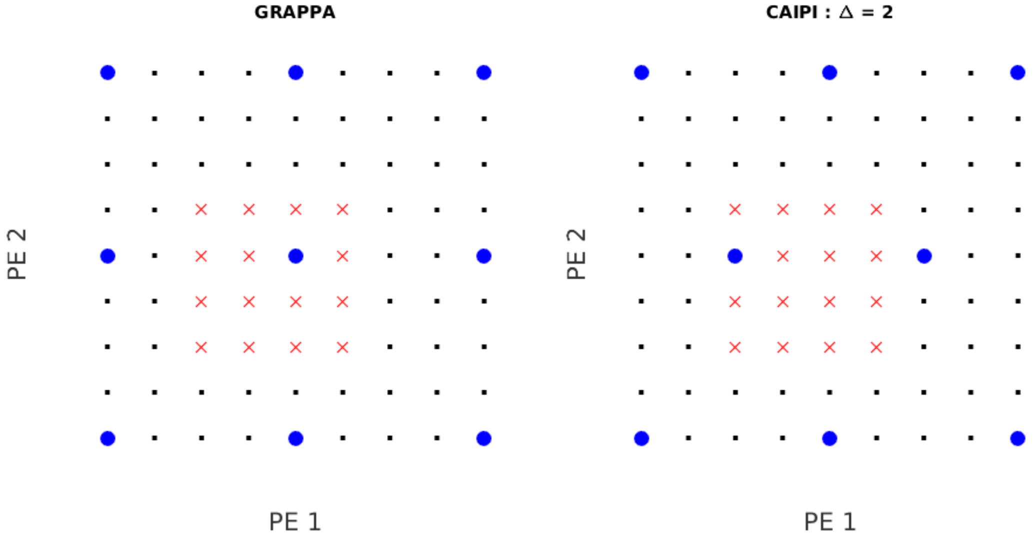

Figure 1.8 – Kernels used for CAIPI and GRAPPA reconstruction of Figure 1.9. Blue dots represent acquired data and red crosses target points to estimate. PE1 corresponds to the left-right direction and PE2 the anterior-posterior one.

unconstrained solution, it was found that no visible gain apart from background noise suppression were achieved, see Figure 1.11. The trade-off dilemma mentioned above has to be kept in mind, adding to it the downside of the increased computation time necessary for solving (1.6.6).

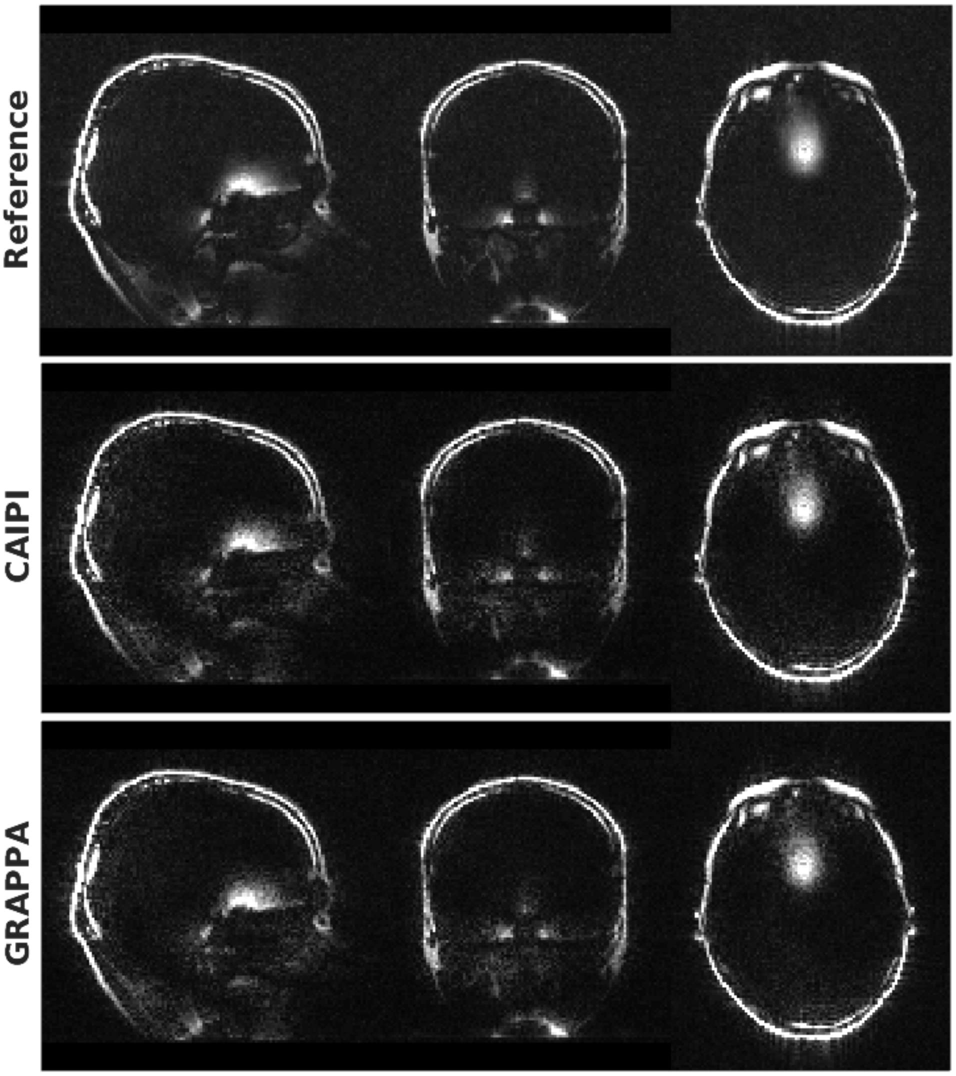
Reference
CAIPI
GRAPPA

Figure 1.9 – Fully sampled, GRAPPA and CAIPI ($R = 4 \times 4$, $\Delta = 2$ ) reconstructions for 2mm FatNavs. Reconstructions are basically indistinguishable.

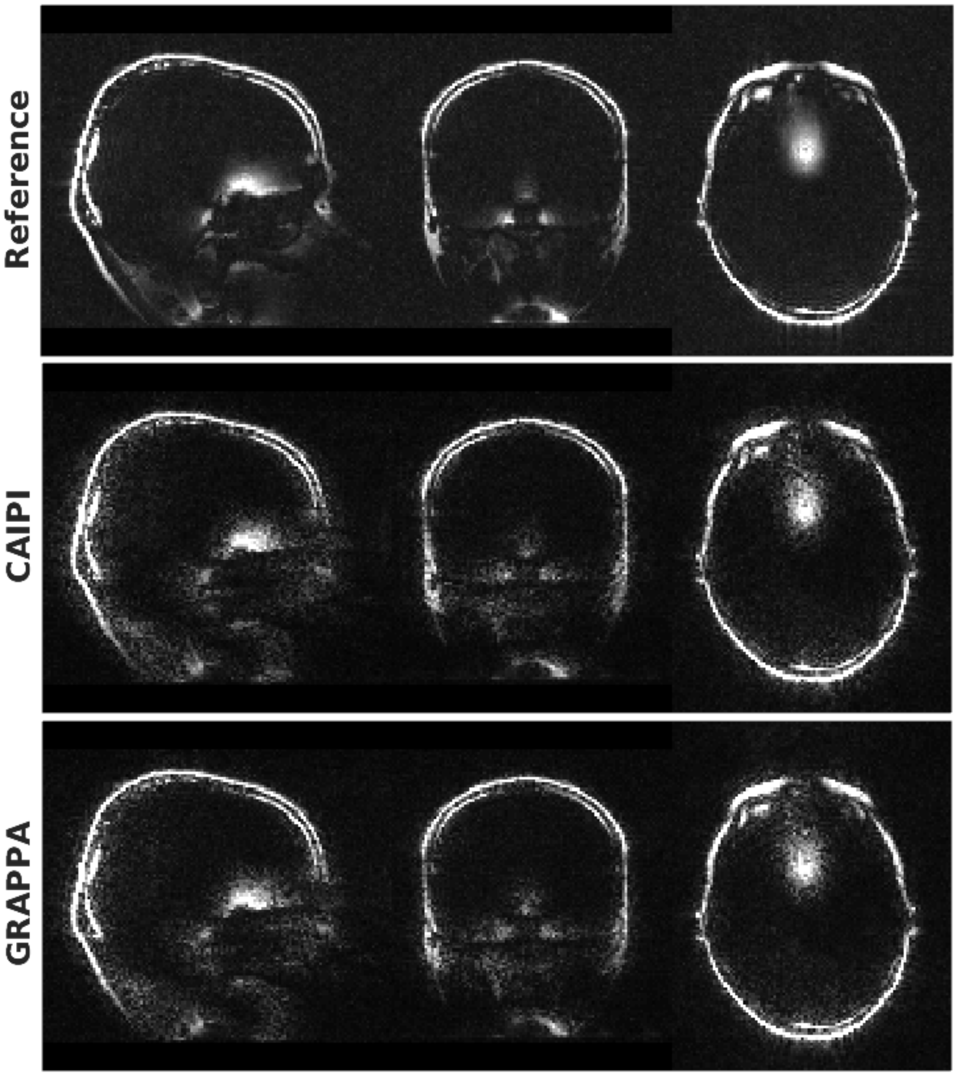
Reference
CAIPI
GRAPPA

Figure 1.10 – Fully sampled, GRAPPA and CAIPI ($R = 6 \times 6$, $\Delta = 3$ ) reconstructions for 2mm FatNavs. The CAIPI recon shows somewhat less noise-amplification.

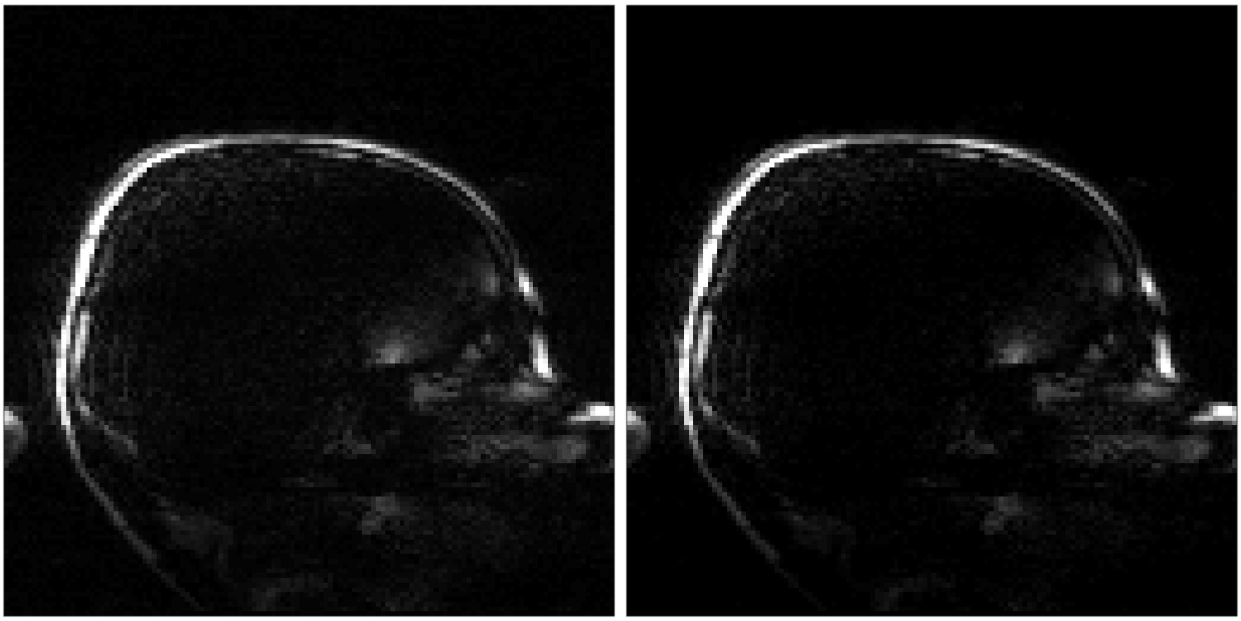

(a) $R = 4 \times 4$, low $\lambda_1$ (b) $R = 4 \times 4$, high $\lambda_1$

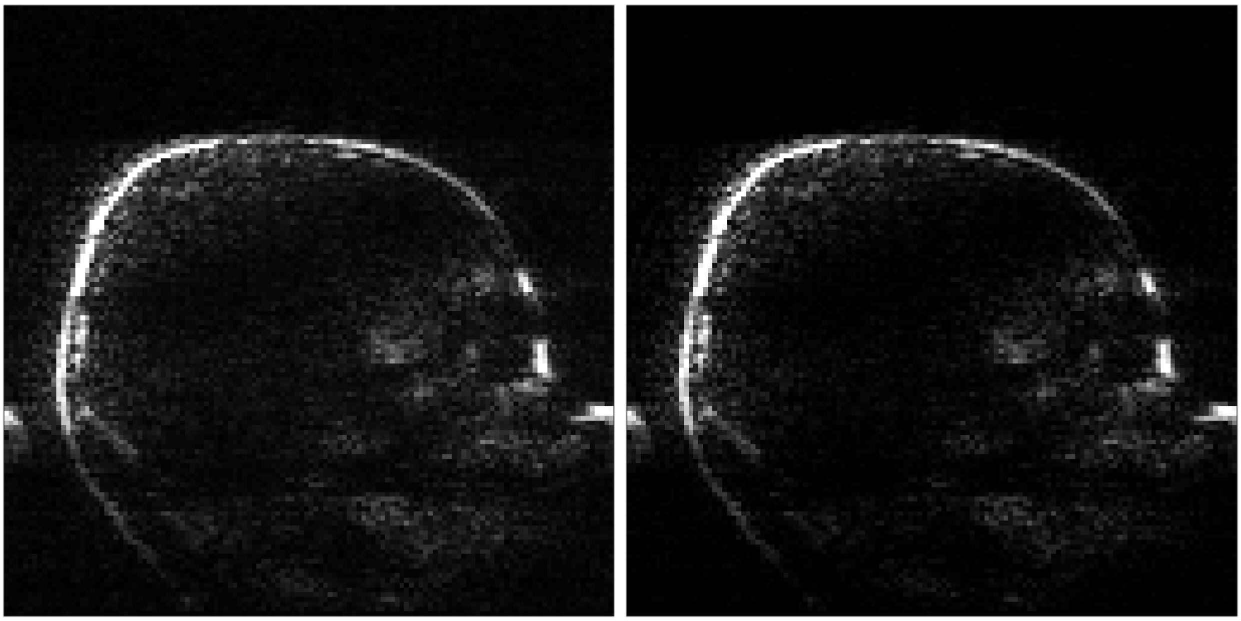

(c) $R = 8 \times 8$, low $\lambda_1$ (d) $R = 8 \times 8$, high $\lambda_1$

Figure 1.11 – $L_1$ constrained reconstructions after three iterations of non-linear adaptive step size conjugate gradient. Shown is the sum-of-squares of channels wise reconstructions performed after GRAPPA $\mathbf{k}-$space completion.

### 1.6.3 Limitations and impacts

**Limitations**

The original FatNavs approach ideally fits in sequences with dead-time, such as MP2RAGE or turbo-spin echo. This does not fit with many routinely used sequences, based on 3D GRE, where the available “dead-time” would be of the order of milliseconds. While it is possible to include the block FatNavs into GRE, this comes at the cost of of increased scan duration and disruption of the water steady-state. Results of such an inclusion are presented in §3.

The temporal resolution of the navigator is also lacking. In a standard MP2RAGE implementation it would amount to one navigator every six seconds. Therefore, the motion one can hope to correct has to be either relatively slow compared to this frequency, such as drifts mainly due to muscle relaxation. Changing from a still pose to another can be approximately captured assuming the subject changes poses at most once in between FatNavs, and only a few times during the entire scan. Faster or cyclic motion, such as breathing induced motion, is not resolved at all.

As the motion is corrected retrospectively and has poor temporal resolution, the host imaging sequence should follow a 3D excitation. The larger the excited slab the better, as only a fraction of the signal source (i.e. of excited magnetization) changes by through-slab motion, thereby leading to a reduced violation of the reconstruction model assumption of imaging the same object in different poses. The extreme opposite case of 2D slice-by-slice imaging could be correctable if motion takes place only in-plane, which is very unlikely for long scans.

The fundamental working hypothesis is that the fat signal exhibits the same motion as the brain. However, included in the navigator are the lower jaw and upper-back of the neck. It may also happen that the subject yawns, swallows, or otherwise makes a chewing motion during navigator acquisition. This breaks the rigid motion hypothesis and introduces some bias into the motion estimates. As can be glimpsed from the FatNavs images, the number of voxels affected by this is not entirely negligible. A rough estimate is that the lower jaw represents around 10% of the total number of fat voxels. This region is therefore not expected to drive most of the registration. As the registration tries to match every volume to a reference one, the worst case is when the reference is significantly different than all other FatNavs. It would be possible to implement an automated test to check how geometrically similar FatNavs are to each other, and deal with outliers accordingly. However, in practice during this work, no subjects scanned presented non-rigid mouth motion significant enough to motivate the implementation of such checks. Some tests were made where only the receive channels closest to the superior posterior part of the head were considered during reconstruction. These tests showed visually identical motion correction quality when significant jaw motion was suspected to have an influence. They also showed slightly lower performance in absence of such motion, presumably due to the lower number of high signal voxels leading to overall lower available SNR.

Gradient non-linearity induces geometrical distortions far from the magnet isocenter, leading to a warped image. This is clearly visible in the lower neck region where the fat bends towards the anterior direction. This affects every volume, and as long as motion keeps the head in a region where the distortion field does not vary significantly the motion parameters obtained without unwarping the images are, for all practical purposes, identical the ones one gets after unwarping. In our experience, padding the subject head with foam inserts allows to restrict motion to a point where only the most severe motion patterns would make warping a relevant issue.

Finally, it has been reported that the fat contents from which the MRI signal comes can be reduced and sometimes completely lost in emaciated patients [69]. This *de facto* renders FatNavs unusable for these subjects.

### Impacts

Up to now, the assumption of the navigator having no impact on the water signal was not questioned. As is clear from previous images, no water signal is observable in the FatNavs, apart from the region close to the paranasal sinuses. These are due to the presence of air in the cavities, thereby inducing a localized resonance frequency inhomogeneity which falls into the passband of the fat-selective binomial pulse. However, the water magnetization is rotated during the fat-selective pulse, it simply goes back to its original position. This is true as long as the pulse is much shorter than the relaxation time of the magnetization. However, the brain contains many structures, including some called semi-solid, consisting of macromolecules. Due to their size and lower mobility, the magnetization of the hydrogen atoms contained by these molecules present a very high relaxation rate, with a characteristic time of approximately 10 $\mu$s [70]. This implies that the magnetization of such isochromats is actually reduced during the binomial pulse, as the phase-evolution time (at 7T) of the binomial pulse is around 500 $\mu$s. This effectively leads to a decrease of the semi-solid longitudinal magnetization. Via magnetization transfer (MT), part of the imaged water magnetization will be recruited to counteract this loss [15]. This implies lower imaged signal in regions where the magnetization transfer takes place significantly.

To see an example of the potential impact FatNavs can therefore have, the $T_1$ histograms obtained from the MP2RAGE sequence will be briefly discussed. The following results do not account for inhomogeneous $B_1$. However, as all experimental conditions are the same, qualitative comparison is still valid. The tested FatNavs parameters were different flip angles as well as the delay between the end of the second inversion readout of the MP2RAGE and the navigator acquisition.

Figure 1.12 shows that reducing said delay lowers the difference to a FatNavs free acquisition. This is expected as magnetization has more time to reach thermal equilibrium before the next inversion pulse, thereby allowing MT effect to dissipate and be significantly reduced. Similarly, the lower the flip angle the lower the impact on the quantitative estimates. A more careful, quantitative analysis and additional results for different FatNavs resolutions (i.e. varying the number of RF pulses) are included in §2.

In time-of-flight angiography, MT can be expected to actually be beneficial to reduce the static tissue signal, thereby augmenting the vessels-to-brain contrast. This possibility was explored and the results are discussed in §5.2.

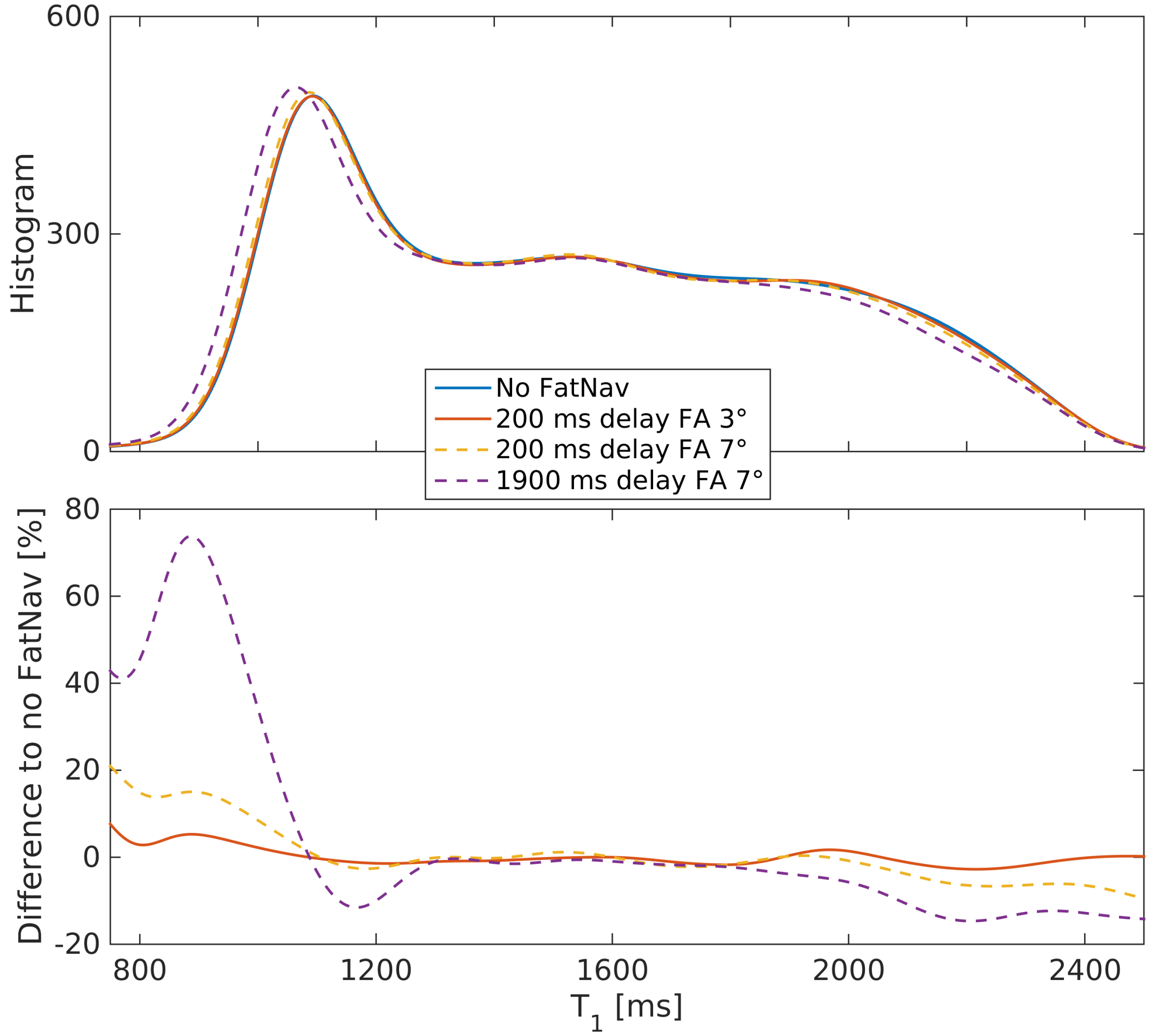

Figure 1.12 – Top: $T_1$ histograms extracted from MP2RAGE acquisition with 2mm FatNavs inclusion for different navgiator parameters, as well as FatNavs free result.
Bottom: relative different the reference scan. See text for details.

## 1.7 Structure of the thesis

Three dimensional fat navigators (FatNavs) have shown great results in cooperative subjects, and present the added advantage of reduced interference with the water signal of interest for brain imaging. The goal of this work is to compare FatNavs to other motion correction methods, to expand the applicability of this method to more sequence types, to add modularity, and if possible bypass its limited temporal resolution. The thesis is structured as follows:

- Chapter §2 directly compares 3D FatNavs to Moiré Phase tracking, the currently recognized gold standard motion tracking modality. Motion parameters for different motion patterns and retrospective corrections based on both methods are compared.
- Chapter §3 explores an extension to a dual-echo version and its ability to track low spatial order temporal $B_0$ fluctuations.
- Chapter §4 describes a faster acquisition scheme allowing for implementation on lower performance gradient hardware and for a wider range of imaging protocols.
- Chapter §5 proposes an alternative acquisition scheme requiring much less dead-time ($\sim$ 4 ms) than the original implementation ($\sim$ 1 s). It demonstrates the motion correction ability of the scheme in an in-house implementation time-of-flight angiography sequence.
- Chapter §6 explores the combination of the method from chapter §5 with FID navigators in order to enhance the temporal resolution of the motion estimates. Combination with the dual-echo navigators is also presented.

Chapter §2 gives qualitative and quantitative answers to both accuracy estimation and comparison to other motion tracking methods, which are fundamental to better establish FatNavs as a valid alternative for motion correction in anatomical neuroimaging. Chapter §3 tackles a whole different problem in compensating field fluctuation, which is a source of significant artefacts when acquiring long echo time $T_2^*$ contrast protocols, especially so at ultra-high field. Chapter §4 pushes extensively the limits of the original FatNavs implementation, while keeping equivalent motion correction abilities. Jointly, chapters §5 and §6 open wide the range of imaging sequences into which FatNavs can be included, possibly with higher temporal resolution than previous implementation schemes, for both motion and field fluctuation correction.

Unless stated otherwise, all experiments of this work were performed at the CIBM (Lausanne) using a 7T Siemens scanner with a head-only gradient insert, using a 32 channel receive RF coil.

# Chapter 2

# Comparison to Moiré phase tracking

Direct comparison of different motion correction techniques is primordial to exhibit their respective advantages and limitations. In this spirit, FatNavs were directly compared to the current gold standard motion tracking modality, Moiré Phase Tracking (MPT).
The following chapter follows a pre-print manuscript submitted to MRM on April 1st 2019. It is a collaboration work with Dr. Oliver Speck's lab in Magdeburg, Germany. Contributions are as follows:

- Frédéric Gretsch (thesis author): Experiment design, data processing, results analysis, manuscript redaction.
- Hendrik Mattern: Experiment design and data acquisition, results discussion, comments on the manuscript and MPT technical part redaction.
- Daniel Gallichan: Results discussion and manuscript review.
- Olivier Speck: Manuscript review.

The article was accepted without significant changes (DOI: 10.1002/mrm.27908).
As a chapter summary, FatNavs and MPT showed equivalent retrospective corrections of high-resolution structural images for the studied cohort of compliant subjects. In fringe cases (2 out of 18), differences were found: MPT proved superior if the subject breathed deeply and FatNavs were the better choice in a scan when most likely the MPT marker did not stay properly attached to the subject's head. For a subject at rest, the RMSE between both modalities was below 0.1 mm/°.

## 2.1 Pre-print

### Fat navigators and Moiré phase tracking comparison for motion estimation and retrospective correction

Frédéric Gretsch,[1] Hendrik Mattern[2], Daniel Gallichan[3] and Oliver Speck[2,4,5,6]

[1] *Laboratory for Functional and Metabolic Imaging, École Polytechnique Fédérale de Lausanne, Lausanne, Switzerland*
[2] *Department of Biomedical Magnetic Resonance, Institute of Experimental Physics, Otto-von-Guericke-University, Magdeburg, Germany*
[3] *CUBRIC, School of Engineering, Cardiff University, UK*
[4] *German Center for Neurodegenerative Disease, Magdeburg, Germany*
[5] *Center for Behavioral Brain Sciences, Magdeburg, Germany*
[6] *Leibniz Institute for Neurobiology, Magdeburg, Germany*

**Purpose:** To compare motion tracking by two modern methods (fat navigators - FatNavs and Moiré phase tracking - MPT) as well as their performance for retrospective correction of very high resolution acquisitions.
**Methods:** A direct comparison of FatNavs and MPT motion parameters was performed for several motion patterns to estimate the agreement between methods. In addition, two different navigator resolution were applied. 0.5 mm isotropic MP2RAGE images with simultaneous MPT and FatNavs tracking were acquired in nine cooperative subjects. Retrospective motion corrections based on both tracking modalities were compared qualitatively and quantitatively. The FatNavs impact on quantitative $T_1$ maps was also investigated.
**Results:** Both methods showed good agreement within a 0.3 mm/° margin in subjects that moved very little. Higher resolution FatNavs (2mm) showed overall better agreement with MPT than 4mm resolution ones, except for fast and large motion. The retrospective motion corrections based on MPT or FatNavs were at par in 33 cases out of 36, and visibly improved image quality compared to the uncorrected images. In separate fringe cases, both methods suffered from their respective potential shortcomings: unreliable marker attachment for MPT and poor temporal resolution for FatNavs. The magnetization transfer induced by the navigator RF pulses had a visible impact on the $T_1$ values distribution, with a shift of the gray and white matter peaks of 12 ms at most.
**Conclusion:** This work confirms both FatNavs and MPT as excellent retrospective motion correction methods for very high resolution imaging of cooperative subjects.

### 2.1.1 Introduction

Along with the increasing availability of ultra-high field MRI, in vivo, sub-millimeter imaging can be achieved at reasonable SNR and scan time. However, subject motion remains a major challenge [71] because with higher imaging resolution and correspondingly longer scan durations, both the sensitivity to subject motion and the likelihood of motion occurring increase. At sub-millimeter resolution unintentional subject motion is on the order of the imaging resolution, thus, even small-scale motion such as slow head drifts and breathing can degrade the image quality [27, 72]. Several solutions to address motion have been proposed [73], especially in the case of brain imaging, where bulk motion can be reasonably well modeled as rigid.
Moiré phase tracking (MPT) is an optical method to track subject motion with a single in-bore camera and a single marker (attached to the subject) in six degrees-of-freedom. Using the motion

estimates provided by this external hardware, the MR imaging volume's position and orientation can be updated during scanning, thus, correcting motion prospectively. This technique allowed the highest resolution whole brain in vivo data acquisition [27], with up to 250 µm and 150 µm isotropic resolution for anatomical [74] and vascular [75] data respectively. Due to its accuracy and short latency, MPT is often regarded as a gold standard [21].

Another approach to motion compensation is to use MR navigators [38, 41]. Among these, fat selective navigators (FatNavs) were proposed [46] and showed [48] successful application to retrospective motion correction of very high-resolution protocols for $T_1$/T2/T2* imaging with up to 350 µm isotropic resolution. The main advantages of FatNavs are that the fat signal in the head is sparse, allowing very high acceleration for the navigators themselves, that they require no additional hardware and that they have only minimal impact on the water signal. A hybrid hardware/MR based-method, dubbed 'field probes', was recently compared to MPT [76] and showed good agreement, but direct comparison to modern navigator methods is lacking. In this work, we compared MPT and FatNavs motion estimates, as well as their application to retrospective motion correction of very-high resolution acquisitions. To this end, motion estimates of different FatNav protocols were compared to simultaneously recorded MPT estimates for various motion patterns. Subsequently, unintentional motion in high resolution MP2RAGE was corrected retrospectively on the basis of the FatNavs or MPT estimates. Results were analyzed qualitatively and quantitatively to compare FatNavs to MPT.

Finally, the bias of FatNav magnetization transfer effects on $T_1$ mapping was analyzed in a single subject experiment. More generally, this work explores relevant advantages and disadvantages of current navigator-based and hardware-based methods for retrospective motion correction.

### 2.1.2 Methods

All experiments were performed on a 7T whole-body MRI scanner (Siemens Healthineers, Erlangen, Germany) using a 32-channel RF head coil (Nova Medical, Wilmington, Massachusetts, USA). All eleven subjects were healthy and compliant volunteers who are regularly scanned at 7T. Furthermore, all volunteers gave written consent prior to participation in this study, which was approved by the local ethics committee. Two experiments were performed to (1) compare the motion estimates of MPT against FatNavs and (2) to analyse the image reconstruction quality using estimates from both methods for retrospective motion correction.

#### Moiré phase tracking

MPT (Metria Innovation, Milwaukee, Wisconsin, USA) consist of an in-bore camera, a single 15x15 $\text{mm}^2$ marker, and a tracking PC. The marker is attached to the subjects' teeth of the upper jaw via custom-made mouthpieces (based on individual dental impressions). Tracking in six degrees of freedom with this single-marker, single-camera setup is realized by lithographically printing layers on the transparent marker to generate Moiré patterns. Under rotation these patterns change and by fitting sinusoidal functions to the gray levels along the pattern the out-of-plane-rotation can be estimated. Standard photogrammetric techniques are used to estimate the remaining four degrees of freedom.

Tracking is performed with 86 frames per second and the precision of the motion estimates was previously reported as 0.01mm and 0.01 ° [21]. A detailed description and validation of the motion correction system can be found elsewhere [21, 27]. Finally, motion estimates acquired by MPT need to be transformed from the camera to the scanner coordinate system, using a process called cross-calibration.

### FatNavs

FatNavs aim to acquire the fat signal of the head, mainly the subcutaneous fat, and exploit the signal sparsity (in space) to highly accelerate the whole image acquisition using parallel imaging [77]. The excitation consists of a binomial pulse, and a 1-2-1 implementation scheme is sufficient at 7T to almost exclusively measure fat and leave the brain signal mostly undetectable in the navigator image.

Different implementations have been proposed, including 2D [46], 3D collapsed [47] and full 3D [48] versions. The full 3D version was used in this study and shall be called FatNavs for simplicity. Approximately 1.5 s are required to acquire a 2mm isotropic navigator. As with almost all navigators, dedicated scan-time in the imaging sequence is required for the navigator acquisition, making inversion recovery based sequences such as MP2RAGE natural candidates due to their inherent dead-time. If no dead-time is present in the imaging sequence, alternatives can be considered at the price of addition scan-time [78].

Unlike MPT, FatNavs do not require any additional hardware or cross-calibration. Due to the computational load of reconstructing each accelerated FatNav and the additional latency this would incur for real-time correction, motion correction is typically applied retrospectively for 3D FatNavs. Finally, even with perfect fat selectivity, the navigator acquisition does have an impact on the brain signal, mainly due to magnetization transfer (MT) effects. These effects can be reduced by using a low excitation flip angle as the short $T_1$ of fat allows for sufficient navigator signal, but depending on the total duration of each section of dead-time, the influence of the MT effect may still be directly observed.

### Experiment 1: Motion estimates

During the first experiment FatNavs were acquired successively while monitoring the subject's motion using the MPT setup. This allowed direct comparison of rigid motion parameters with maximal scan-time efficiency as only navigators were acquired without any parent imaging sequence. The volunteer was asked to perform predefined motion patterns during the acquisitions. These six patterns were: rest (no intentional motion, TA=10 min), coughing (TA=30 s, single intentional coughing after approximately 15s of scanning, repeated three times), foot motion (dorsal plantar flexion, TA=60s), swallowing (TA=60s, swallowing twice during scanning), deep breathing (TA=60s), drawing a figure eight with the nose (TA=2min 30s), once slowly and once faster. For each motion pattern two different FatNavs protocols were acquired back-to-back, namely a 2 mm protocol ($T_E/T_R$ 1.68/3.8 ms, TA=1.65 s) and a 4mm one ($T_E/T_R$ 1.43/3.4 ms, TA=0.37 s), leading to motion-estimate frequencies of 0.6 Hz and 2.7 Hz respectively. Other parameters were identical for both scans: 1950 Hz/pixel readout bandwidth, 7° FA, 4x4 under-sampling and $\frac{3}{4}$ partial Fourier in both phase encoding directions (left-right and anterior-posterior).

The auto-calibration signal needed for the FatNavs GRAPPA reconstruction was acquired before each scan ( 4 s) without intentional motion. These protocols were chosen as they proved efficient in previous work [48, 78] and allow exploration of the tradeoff between spatial vs temporal resolution. MPT and navigator data were synchronized by an optical trigger sent at every FatNav and stored in the MPT log files. The FatNavs were co-registered using SPM [77], and the time closest to acquisition of the $\mathbf{k}-$space center of each navigator was defined as their measurement time-point. The method used to quantify differences between modalities was as follows. Similarly to a retrospective motion correction approach, the acquired FatNavs motion parameters were interpolated linearly to the MPT measurements time-points, in a range restricted to values between the first and last FatNavs measurements. The root mean squared of the difference between the MPT motion parameters and the interpolated FatNavs parameters defined the FatNavs error to

MPT, called hereafter RMSE for brevity, It was computed separately for each of the six motion parameters.

The motion parameters ranges during FatNavs acquisition were defined as the difference between maximum and minimum MPT estimates. Translation and rotation ranges were then defined as the mean of the three associated motion parameters ranges, and shall serve as basis for motion amplitude comparison. The rate of motion was estimated as follows. The root mean squared of the temporal derivative of the MPT motion parameters were computed, then combined into the translation (or rotation) rate by taking the mean of the three associated parameters. For the coughing pattern, all computations were restricted to a 5 seconds window centered at the cough peak.

### Experiment 2: Retrospective motion correction using MPT and FatNavs

The second experiment, performed on nine volunteers, consisted of acquiring two 0.5 mm isotropic MP2RAGE [11] scans (each MP2RAGE scan acquires two inversion images and generates a combined uniform contrast which aims to maximize the gray and white matter contrast). The volunteers were asked to stay still. Parameters were: $T_{I1}/T_{I2}/T_R$ 800/2700/6000 ms, $\alpha_1/\alpha_2$ 7/5 °, two-fold acceleration in anterior-posterior direction and $\frac{3}{4}$ partial Fourier in left-right direction. The total acquisition time of a scan was 23 min 34 s.

FatNavs were measured directly after the second inversion readout train[48], using the 2mm protocol from the first experiment, but with a 3° nominal flip angle. Another difference to the first experiment had to be made for the sequence timing to be feasible by the hardware. In order to fit the FatNavs in the available dead-time, the center of the excitation passband of the 1-2-1 binomial pulse was put at -7 ppm, instead of -3.3. ppm which would be fat-centered. This leads to a roughly 50% shorter excitation duration but also makes the nominal flip angle higher than the effective fat excitation. However, the short $T_1$ of fat and lower value of the pulse's passband at the water frequency allow for very sharp fat images. Again the GRAPPA calibration signal for the navigators was acquired at the very beginning of the scan.

The MP2RAGE sequence is an excellent candidate to measure $T_1$ maps at 7T [79]. In order to investigate the impact of the FatNavs on the quantitative $T_1$ maps computed from the uniform contrast of the MP2RAGE, single scans without navigators, with 2mm FatNavs, and with 4mm FatNavs were consecutively acquired on one additional volunteer. The $T_1$ histograms were computed after brain masking and no motion correction was performed in order to remove bias from the correction method. Due to the lack of $b_1$ maps, a global $b_1$ efficiency for all three scans was estimated on the navigator free acquisition to center the white matter $T_1$ peak around previously reported values [11]. The histogram of the scan without FatNavs was statistically compared to both others using a Kolmogorov–Smirnov test. The peak values of each scan were estimated by fitting the histograms with a sum of two Gaussians. Direct visual comparison of $T_1$ maps was also performed.

The retrospective motion correction followed the same reconstruction pipeline after interpolation of the chosen motion data (MPT or FatNavs) to the times of measurement of all readout-events. This was done as follows: the motion estimates for each $\mathbf{k}-$space readout event were linearly interpolated from the neighboring acquired time points (i.e. every 6 s for FatNavs and 0.011 s for MPT). No temporal filtering was applied at any step. Motion correction consisted of multiplication by a pure phase factor (for translations) of the $\mathbf{k}-$space data followed by a nuFFT [23] operator (for rotations), and was applied channel-wise. A similar reconstruction pipeline is freely available online [80]. Each measurement was reconstructed without motion correction, with FatNav motion estimates, and with MPT motion estimates, thus, three datasets were created.

Qualitatively the uniform contrast image of the raw (no motion correction) and motion corrected images (FatNavs based or MPT based) were directly compared. Quantitatively, the normalized gradient squared of the images was computed, as it was shown to be an excellent metric candidate for autofocusing-based motion correction [17]. Increase of the metric generally correlates with better image quality / lower artefacts. Both inversion images were considered as their contrast is unbounded (unlike the uniform contrast image). The MPT system is most commonly used with real-time updates of the scanner coordinate system. Within this study we chose to disable the real-time update feature so that motion-estimates from the MPT could be directly compared with those from the FatNavs within the same scan without additional bias. The difference to prospective correction with MPT is expected to be small (for small-scale head motion) as the spatially non-selective excitation used in the whole-head MP2RAGE protocol should be largely insensitive to through-slab motion and incoherent spin-history artefacts.

### 2.1.3 Results

**Direct motion estimates experiment**

An example of the acquired FatNavs is presented in Figure 2.1. Figure 2.2 presents example time-courses of the motion parameters extracted from both tracking methods. Generally, visual inspection reveals similar trends for MPT and FatNavs, especially for slower motion. The scale of the estimates varied between modalities, potentially explaining the offset visible at the beginning of the 2mm rest scan. As expected, in the case of faster motion such as coughing and swallowing, the navigators failed to track accurately the subject pose. Larger differences were observed for the figure eight patterns.

The RMSE values between the MPT and the FatNavs motion parameters are presented in Figure 2.3 as well as the translation and rotation ranges and rates during the scans. The RMSE were less than 0.3 mm (and °) except for deep breathing ($< 0.35$ for 2mm FatNavs and $< 0.5$ for the 4mm FatNavs) and figure eight pattern ($\gtrsim 1$) . Lower spatial resolution (4mm) FatNavs performed worse than the 2mm navigators for smaller motion range patterns(rest, feet and swallowing). They show similar performance for deep breathing and coughing, presumably because of a tradeoff between the temporal and spatial resolutions of the FatNavs. The figure eight pattern was better captured by the 4mm FatNavs. The continuous, large motion of this pattern and its higher motion rate compared to the other patterns are expected to be the primary sources of this difference, as the 4mm FatNavs have a higher temporal resolution than the 2mm Fatnavs, effectively rendering the subject pose closer to being constant during a navigator acquisition. The temporal interpolation during metric computation also cannot be expected to properly capture the true pose change between navigator measurements (i.e. every 1.65 s for the 2mm navigators).

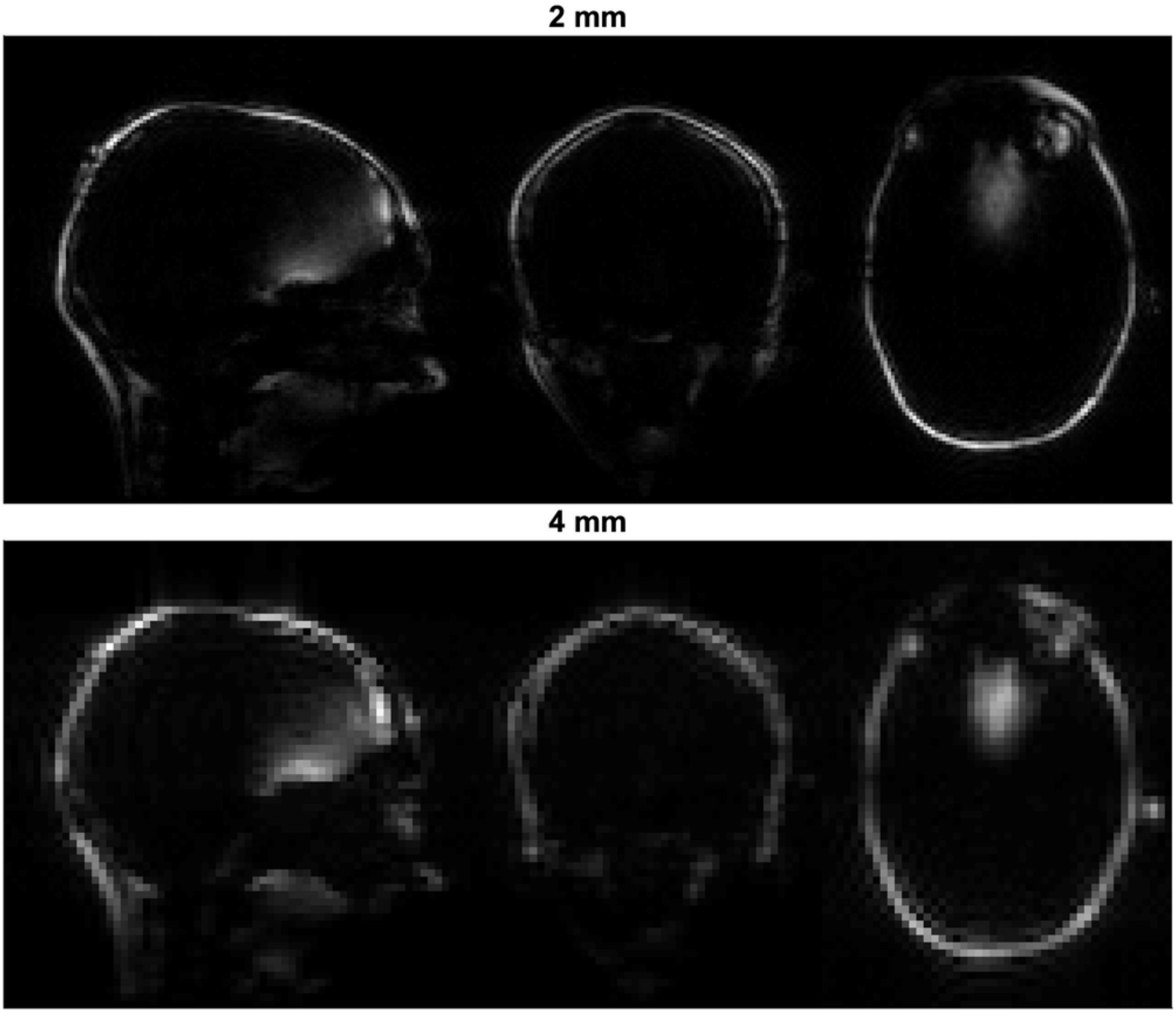

Figure 2.1 – Example volumes of both FatNav protocols acquired in the first experiment.

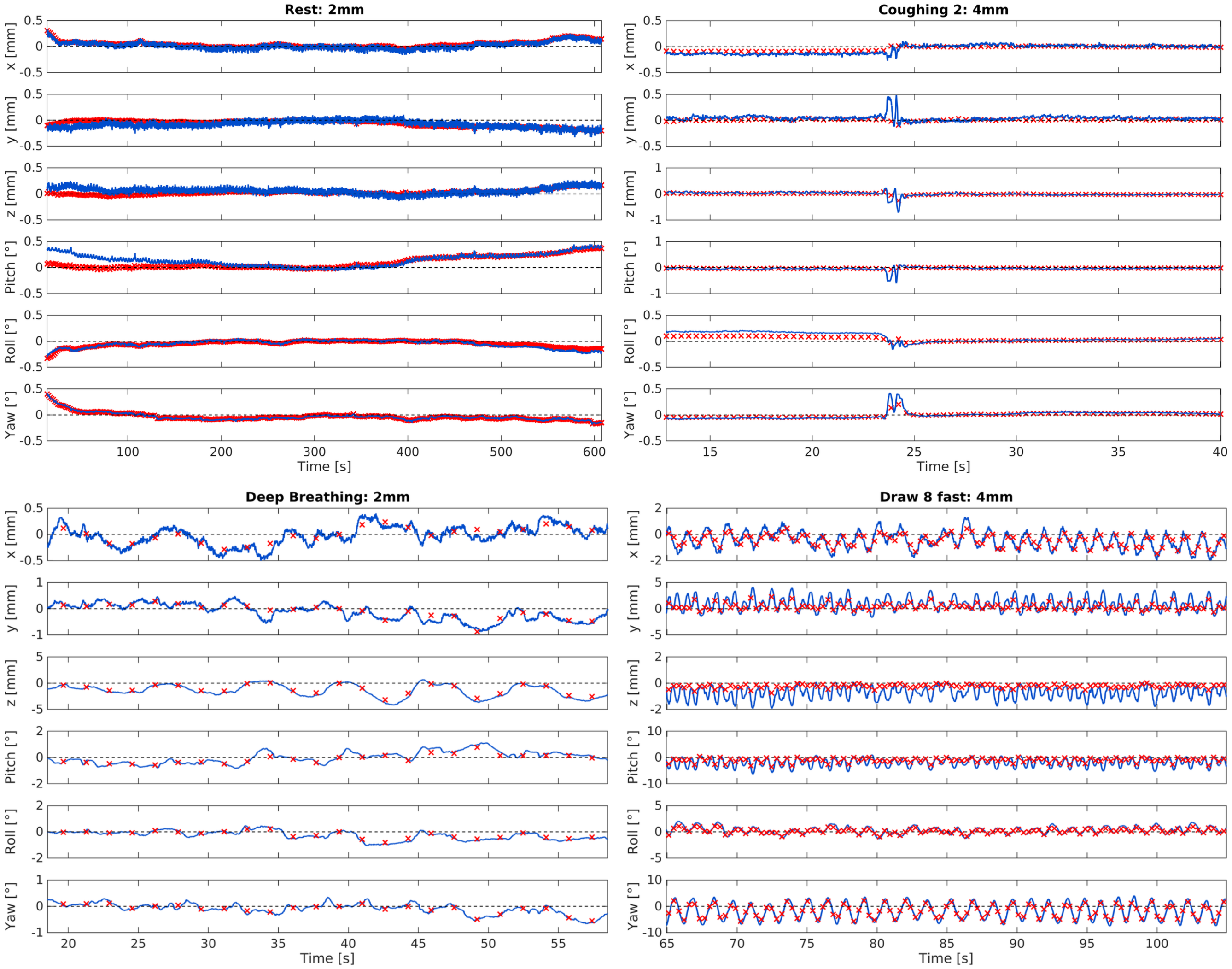

Figure 2.2 – Representative time-courses of both slow motion (left column) and faster motion (right column) acquired in the first experiment. Red crosses represent FatNavs and blue line represents MPT estimates. Temporal resolution of estimates: 1.5 / 0.37 s for 2mm / 4 mm FatNavs and 0.012 s for MPT.

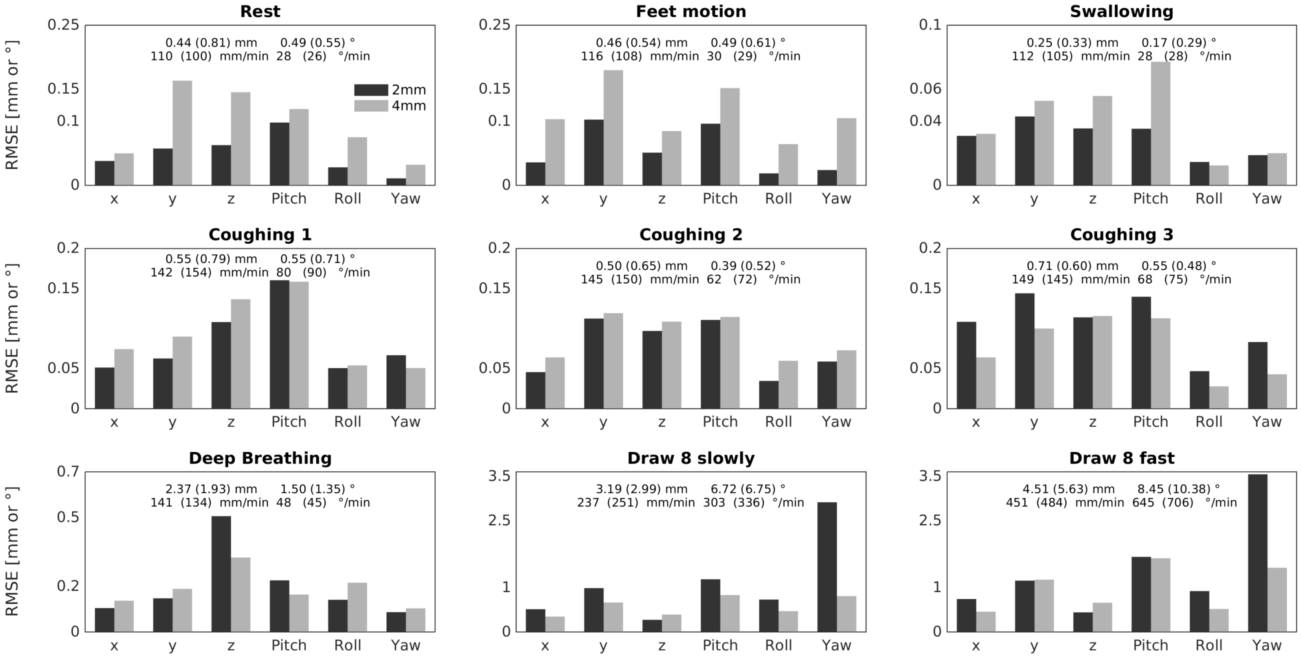

Figure 2.3 – RMSE between the FatNavs and the MPT estimates for all the motion patterns acquired during the first experiment. The translation and rotation ranges and rates are indicated in the plots. The values in brackets are for the 4mm FatNavs scans. 2mm FatNavs outperform 4mm FatNavs for slow motion patterns, and inversely for faster patterns.

### Retrospective motion correction comparison

Visual inspection showed in 33 out of 36 cases motion corrected images were sharper and had overall reduced blurring and ringing artifacts compared to the uncorrected versions. Figure 2.4 shows an example of the improvements of FatNavs-based reconstruction compared to the raw reconstruction. Neither of the correction types (i.e. FatNavs or MPT based) showed consistently superior quality compared to the other across volunteers.

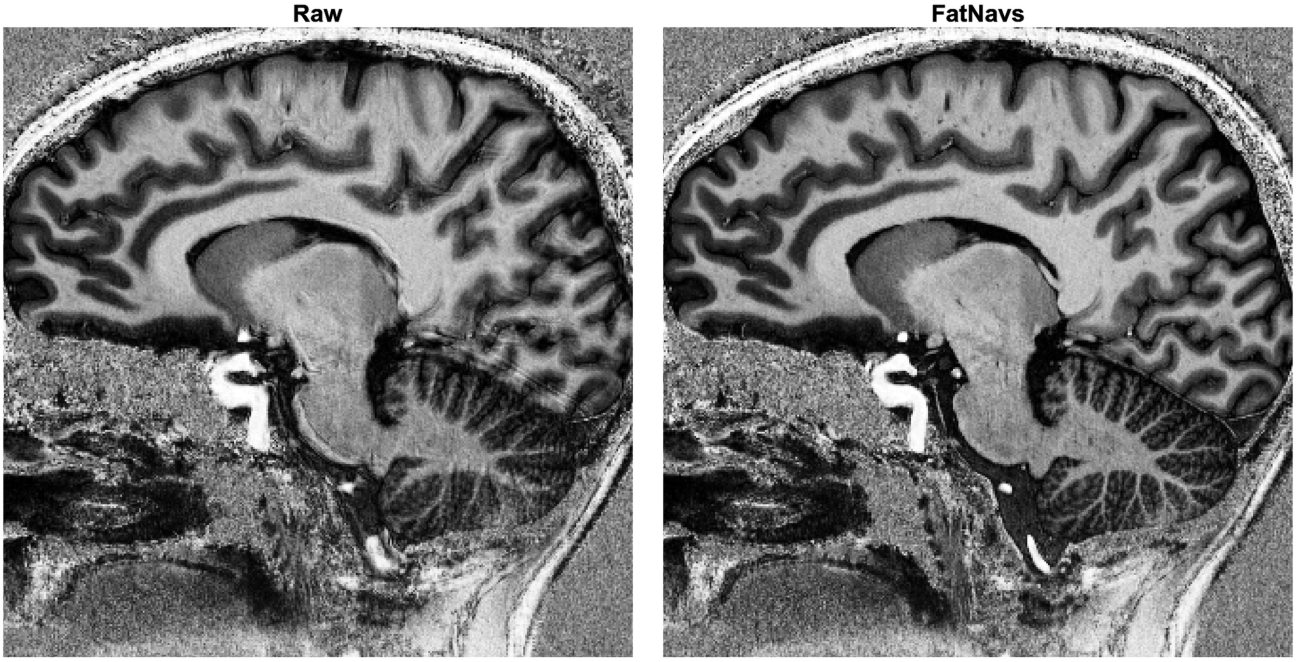

Figure 2.4 – Example views of the raw and motion corrected reconstruction using the 2mm FatNavs motion information (volunteer 2 first scan). The MPT corrected image also showed considerable improvement, but was inferior to the FatNavs one in this case, see Figure 2.7.

We noted only two cases where the corrected images were slightly worse than the raw reconstruction. These were: both scans of volunteer 8 for FatNavs and the second scan of volunteer 2 for the MPT (slight additional blurring). It was asserted that volunteer 8 breathed deeply during the scan and has a high BMI. Figure 2.5 shows both motion corrections for volunteer 8 (first scan). The oscillating motion during acquisition was entirely missed by the FatNavs but captured by the MPT. The ringing, notably above the cerebellum and in the upper frontal cortex, is nicely suppressed in the MPT correction but was still present in the FatNavs correction. The FatNavs correction was however still sharper than the raw reconstruction. Figure 2.6 shows the three reconstructions side-by-side for the interested reader.

By contrast, the FatNavs-based correction proved superior to the MPT correction for volunteer 2, see Figure 2.7. The motion parameters of MPT and FatNavs for this volunteer showed a similar trend but were different in amplitudes (scan 1) and abrupt motion in the MPT estimates occurred compared to FatNavs (scan 2). Figure 2.8 also shows the raw reconstruction for a more complete visual impression of this fringe case.

The normalized gradient metric confirmed the visual observation previously described, and is presented in Figure 2.9. However, it is our observation that changes of less than 2% did not correspond to visually perceived image degradation. Disagreement between the metrics of the first and second inversion images occurred once for FatNavs (volunteer 8 scan 2) and twice for MPT (volunteer 6 scan 1, volunteer 9 scan 1). The FatNavs case may be linked to inconsistent interpolation of the motion between FatNavs compared to true motion, as the low temporal resolution of the navigators did not capture the breathing-induced motion. In the MPT cases, the values are small and no difference on the images could actually be found, corroborating the metric limits mentioned above.

Slice images and histograms of the $T_1$ values extracted from the single subject experiment without, with 4mm, and 2mm FatNavs inclusion are presented in Figure 2.10. While $T_1$ maps were visually very similar, the histogram analysis shows the 4mm FatNavs $T_1$ values to be significantly closer to the original protocol (without navigator) than with 2mm FatNavs inclusion, but slight bias can be still noted. This is corroborated by the Kolmogorov–Smirnov test statistics which were 0.0035 and 0.0122 for the 4mm and 2mm FatNavs respectively. The peaks of the fitted Gaussians were always centered at lower $T_1$ values than in the navigator free scan. For white matter, the offset was 1.7 ms and 7.7 ms for the 4mm and 2mm FatNavs scans respectively. For gray matter it was 2.8 ms and 11.5 ms. It is interesting to note that the $T_1$ bias differed approximately by a factor 4 between both navigated scans, which matches the ratio of the number of RF pulses between the 2mm and 4mm FatNavs. The same approximate ratio can be seen between the K-S statistics. As expected, the lower number of RF pulses of the 4mm FatNavs, combined with the longer relaxation period before the next inversion pulse, lowered the impact of magnetization transfer on the $T_1$ maps of the water signal compared to the 2mm navigator. While some brain signal was visible in the frontal area of the navigator for the direct comparison experiment (see Figure 2.1), it was not the case for the MP2RAGE experiments as the passband of the navigator excitation pulse was twice farther from water, making magnetization transfer the dominating source of disruption of the water signal. The approximate ad hoc $b_1$ correction seems reasonable enough as the $T_1$ values from the grey matter peak are in the range of reported values in the literature.

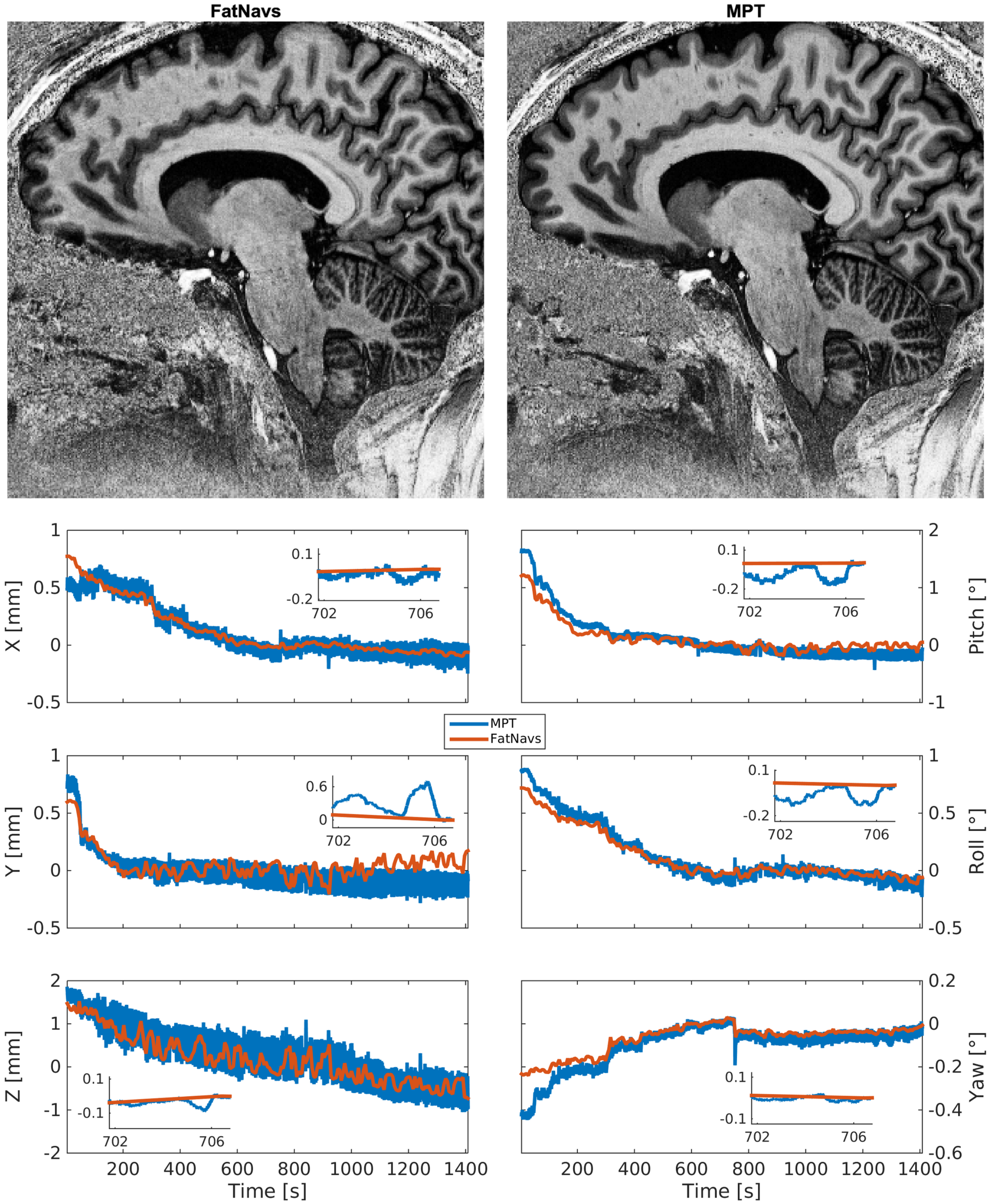
FatNavs
MPT
X [mm]
Y [mm]
Z [mm]
Pitch [°]
Roll [°]
Yaw [°]
MPT
FatNavs
Time [s]
Time [s]
200
400
600
800
1000
1200
1400
702
706
0.1
-0.2
0.6
0
-0.1
1
0.5
0
-0.5
2
-1
-2
0.2
-0.2
-0.4
-0.6

Figure 2.5 – Case of superior MPT correction compared to FatNavs (Volunteer 8 first scan). Notably, ringing artefact above the cerebellum and blurring in the frontal cortex present in the FatNavs correction are nicely suppressed by MPT.

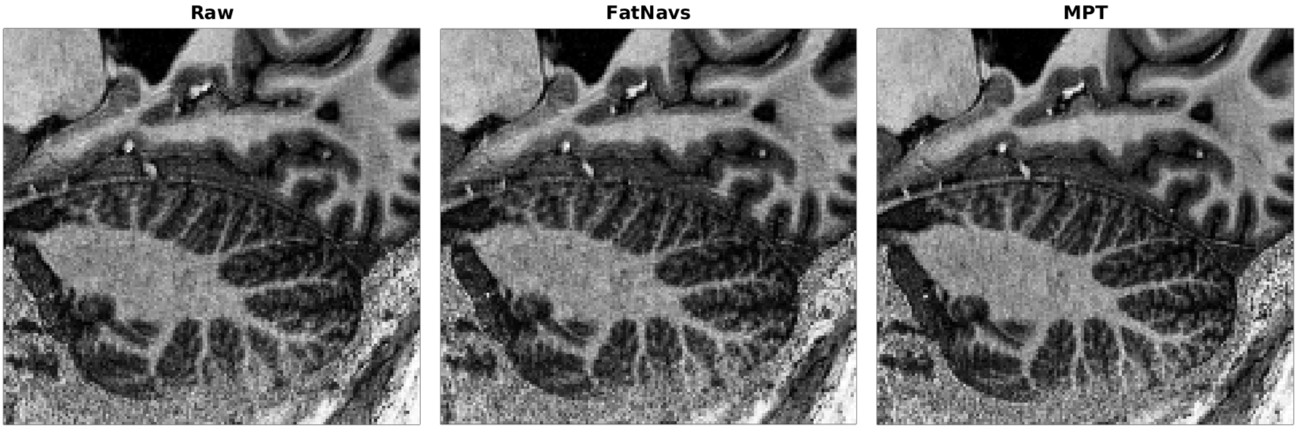

Figure 2.6 – Zoomed-in view of the three reconstructions for volunteer 8 first scan. While the FatNavs image is sharper than the raw reconstruction, ringing is also more visible.

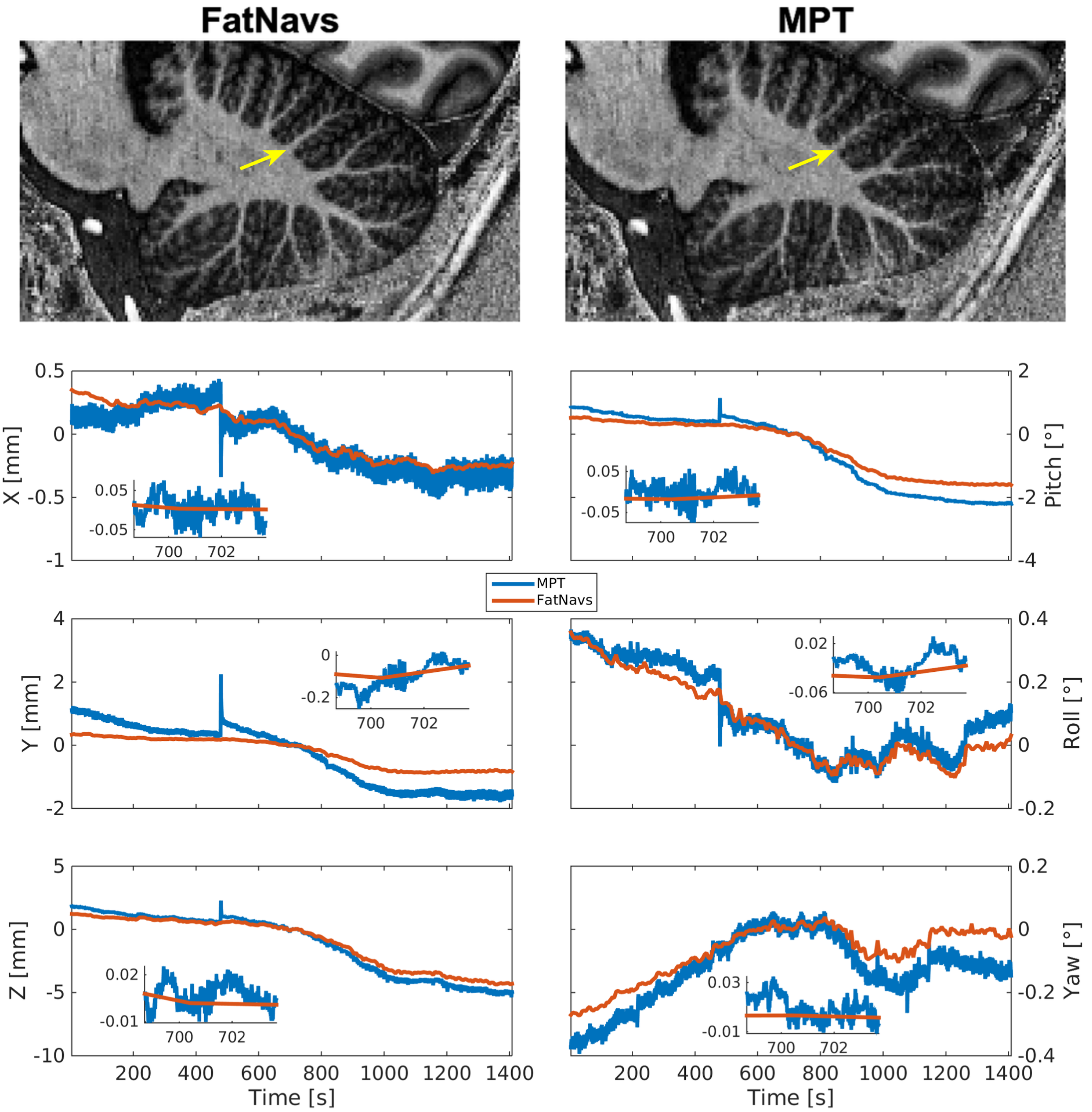

Figure 2.7 – Case of superior FatNavs correction compared to MPT (volunteer 2 first scan), as can be seen by the overall better delineation of structures within the cerebellum. The yellow arrow indicates such a difference.

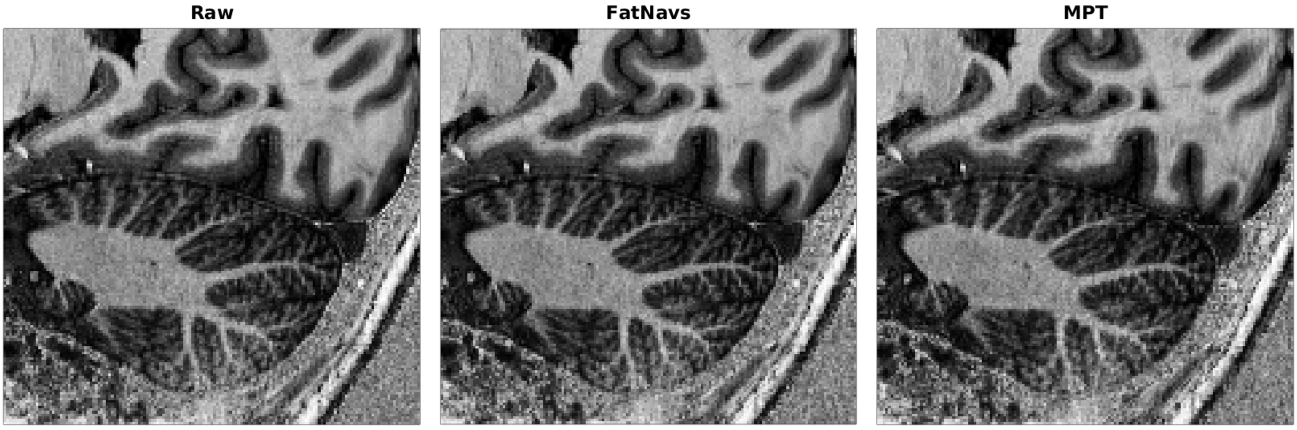

Figure 2.8 – Zoomed-in view of the three reconstructions for volunteer 2 second scan. The MPT-corrected image is arguably of slightly lesser quality than the raw reconstruction (this was the only such case observed).

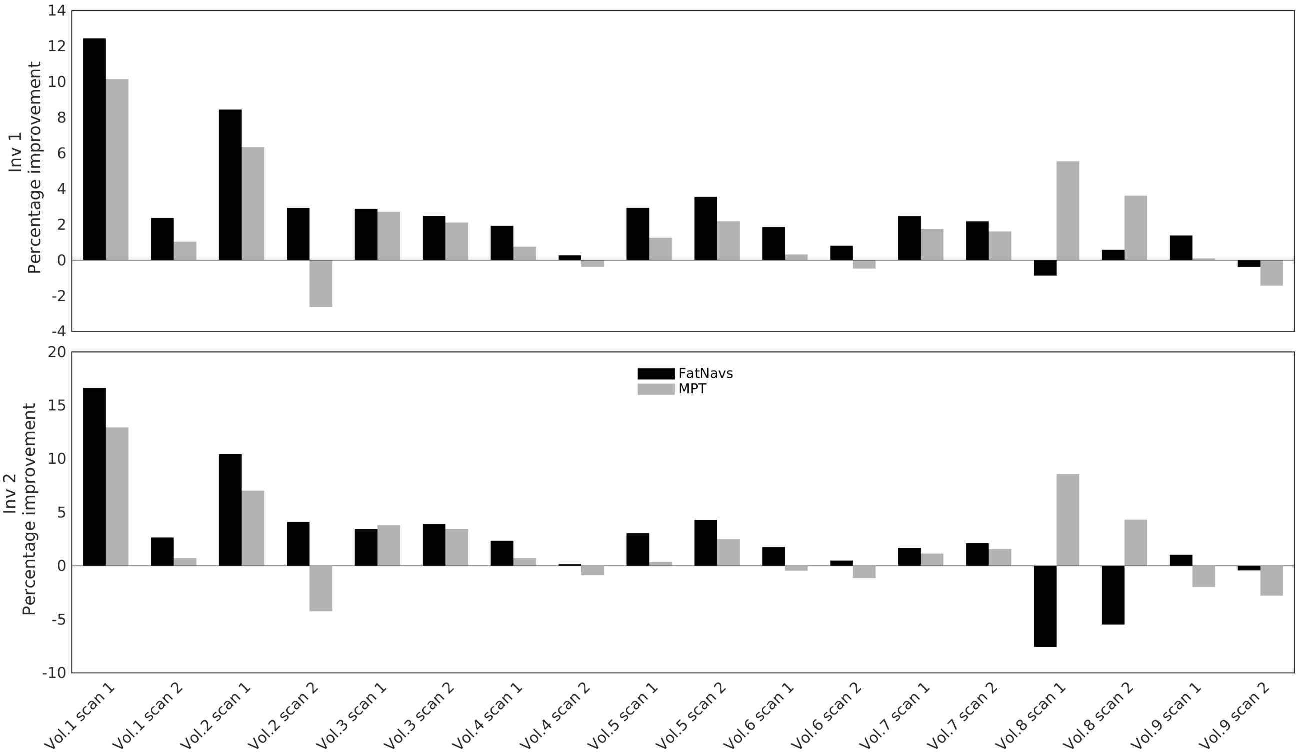

Figure 2.9 – Normalized gradient squared metric for both motion tracking modalities, and both inversion images produced by MP2RAGE. Graphed is the relative change of the metric compared to the raw reconstruction, in percent.

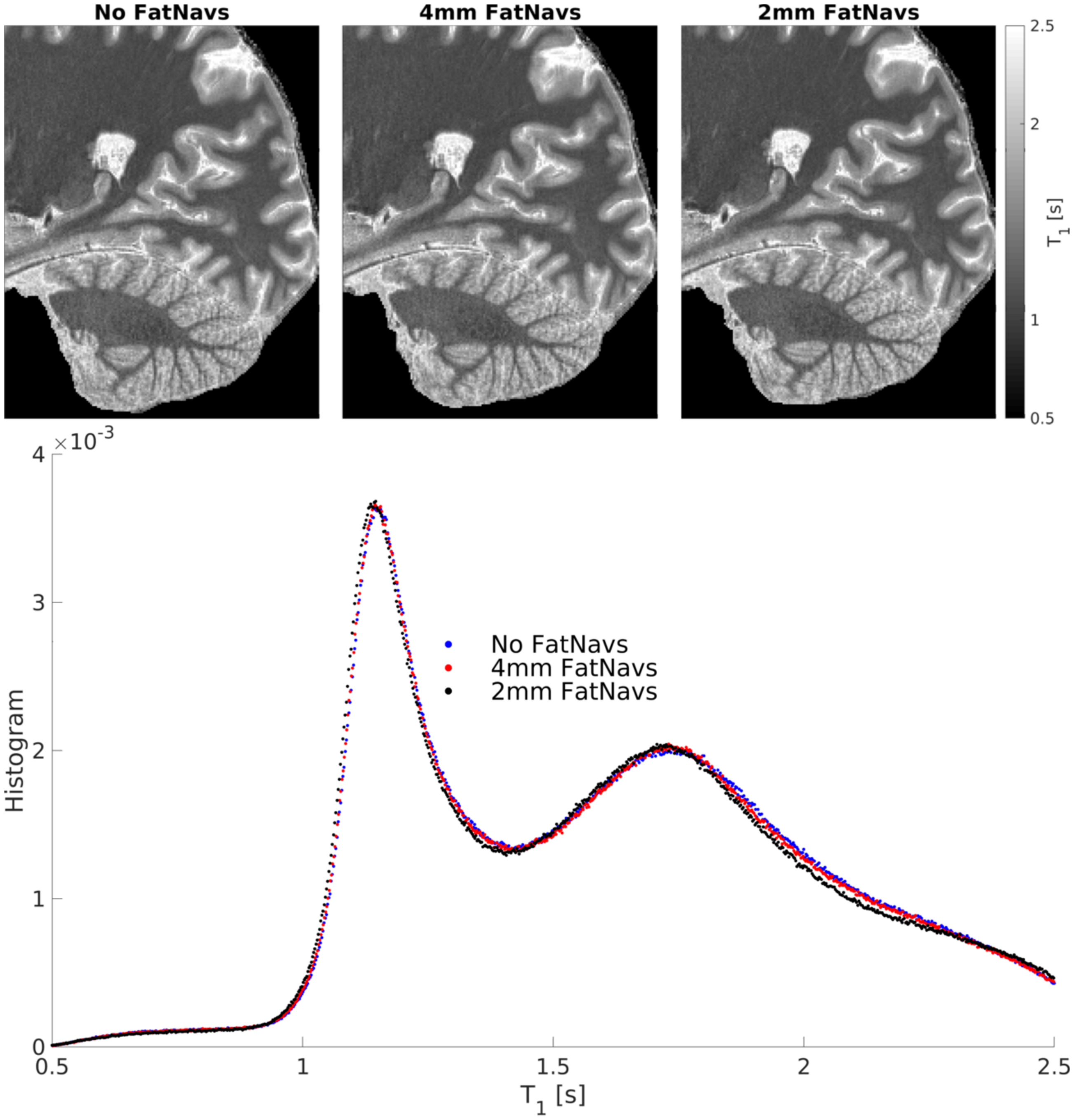

Figure 2.10 – Top: slices of the $T_1$ maps obtained for three high-resolution imaging protocols: without navigators, with 4mm or with 2mm FatNavs. Bottom: the histograms of $T_1$ values obtained after brain masking. The two clear peaks correspond to white-matter and grey-matter voxels.

### 2.1.4 Discussion

**Experiment 1: direct comparison of voluntary motion patterns**

Overall fair agreement was found between tracking modalities, and the reported accuracies confirm that FatNavs as suitable for slow, small scale motion tracking, such as head drifts. Higher resolution navigators (2mm) were closer to MPT estimates than 4mm navigators, as had been expected. An exception to this observation occurred for large continuous motion of the figure eight pattern, where we attribute the superior accuracy of the registration for 4mm FatNavs to their four-times higher temporal resolution.

The reported RMSE values for coughing and swallowing may be slightly biased by the non-continuous nature of these motion patterns, as it is probable that the short rest periods outside of the motion events lower the final metric value.

Clearly, implementing FatNavs for motion correction is subjected to strict constraints by the imaging sequence, so the results presented here are to be understood as indication of FatNavs robustness against such motion patterns rather than FatNavs ability to correct for them, especially because any practical implementation of the FatNavs has a much lower temporal resolution than in this experiment. However, we believe the results obtained confirm them as valid candidates to motion-correct sub-millimeter imaging protocols in cooperative subjects.

**Experiment 2: Comparison of retrospective correction of involuntary motion**

Motion correction based on either modality virtually always improved the quality of the reconstructions. The delineation of high-resolution structures and sharpness obtained were similar across scans and motion tracking modalities. Globally, both methods showed similar performance when correcting for motion retrospectively within the studied cohort of compliant subjects without intentional motion. The presented results confirm that for cooperative subjects that mostly move slowly, FatNavs has a retrospective motion correction ability equivalent to MPT, but requires much less effort experimentally as no custom-made mouth-piece and cameras are required. On the other hand, more agitated subject motion is not fully recoverable by the FatNavs but are by MPT when the mouthpiece is robustly fixated, which represent the vast majority of cases in our experience (ten out of eleven subjects in the present work). Previously reported potential shortcomings of both methods were observed. While conclusive evidence is not available, the results of volunteer 2, which had sub-par MPT performance, can presumably be explained by imperfect marker fixation to the upper jaw as both scans were impaired and similar problems did not occur for any other volunteer. Volunteer 8 demonstrated the limits of the FatNavs approach, as large breathing motion could not be adequately tracked. On the other-hand, MPT was naturally sensitive to these effects and allowed for their correction.

A further effect potentially confounding FatNavs registration is gradient non-linearity. While the individual navigator images are definitely subject to distortions, the motion range is usually limited in practice thanks to head padding, and is low enough for the navigator distortion not to change significantly with motion. This leads to equivalent motion estimates when using un-warped images (data not shown).

The normalized gradient metric analysis corroborates our findings. Small metric variation did not represent a truly perceivable visual image change, but can potentially be due to removal of smaller scale and less coherent artefacts, unlike typical blurring or ringing suppression. Such changes are more difficult to pinpoint on the images. The absolute value of the change is, in our opinion, difficult to interpret, as not only different artifacts levels, but also different artifacts types, such as ringing or blurring, impact the metric in different ways. Still the larger variation definitely correlated to more prominent motion artefacts as expected from the literature. We do not expect a quantitative extrapolation of our findings beyond the studied cohort, however the FatNavs would be expected to underperform in cases where continuous significant motion is present, such as tremor-prone subjects, as they would lack the necessary temporal resolution, unlike MPT.

The $T_1$ histograms showed the expected magnetization transfer impact induced by FatNavs acquisition. However, magnetization transfer is not taken into account in the computation of the MP2RAGE $T_1$ maps by definition, and therefore these maps are susceptible to the specifics of the implementation of the sequence, such as the inversion pulse used (as always for $T_1$ mapping). These small deviations compared to $T_1$ values of a protocol without FatNavs should be kept in mind for any quantitative use of the data, especially if comparing navigated and non-navigated images.

Prospective motion correction, as typically done with MPT, could theoretically reduce the artifacts level further, and especially so for accelerated protocols. Also bypassing the nuFFT based reconstruction theoretically allows for sharper effective resolution because of the absence of local Nyquist criteria violation and interpolation. Nevertheless, the high quality of the MPT reconstruction for volunteer 8, with continuously varying motion during the scans, leaves us confident in the validity of the presented retrospective corrections. We also take the same results to validate our implicit assumption of sufficiently accurate MPT cross-calibration for any residual errors to be neglected.

Implementation of FatNavs into a prospectively motion corrected acquisition might also be useful in some cases. In cases such as the example of volunteer 2 in this work, where we suspect the superiority of the FatNavs correction was due to poor marker attachment, the difference of motion parameters between MPT and FatNavs could be exploited to automatically detect potentially unreliable data from the MPT. Depending on how frequently such irregularities are shown to occur, future work could investigate the utility of additional retrospective FatNav-based correction to account for the offset – as well as whether the MPT marker attachment itself can be made even more reliable.

### 2.1.5 Conclusions

We directly compared the motion estimates of two established brain motion correction techniques, and showed that in a retrospective motion correction framework, both methods are roughly equivalent (up to the studied resolution and motion patterns) within the tested subject cohort. This work confirms the FatNavs as a solid alternative to MPT for compliant subjects. Combining results from both experiments, we recommend to tune the navigator protocol depending not only on the imaging sequence parameters, such as resolution and amount of dead-time available, but also on its purpose, especially so for quantitative studies as the presence of additional RF pulses for the navigator will always have some influence on the main imaging sequence.

### 2.1.6 Acknowledgments

This work was supported in part by the NIH, grant number 1R01-DA021146, the Centre d'Imagerie BioMédicale (CIBM) of the UNIL, UNIGE, HUG, CHUV, EPFL and the Leenaards and Jeantet Foundations, as well as the Swiss National Foundation through Grant 205321_153564.

# Chapter 3

# Block FatNavs for first order $B_0$ fluctuation retrospective correction

This chapter introduces an extension of the standard FatNavs to a dual-echo version, allowing to track and potentially correct for magnetic field fluctuation in addition to motion. Said fluctuation can be of crucial importance at ultra-high field for long echo time GRE protocols, such as SWI or QSM acquisitions. The works is presented as a post-script of a published article.

## 3.1 Post-print

The following is the post-print of the article DOI: 10.1002/mrm.27063. Contributions are as follows:

- Frédéric Gretsch (thesis author): Experiment design, data processing, results analysis, manuscript redaction.
- José P. Marques: Comments on the manuscript.
- Daniel Gallichan: Results discussion and manuscript review.

`Post-print starts here`

### Investigating the accuracy of FatNav-derived estimates of temporal $B_0$ changes and their application to retrospective correction of high-resolution 3D GRE of the human brain at 7T

Frédéric Gretsch,[1] José P. Marques[2], Daniel Gallichan[3,4]

[1] *Laboratory for Functional and Metabolic Imaging, École Polytechnique Fédérale de Lausanne, Lausanne, Switzerland*
[2] *Donders Institute, Radboud University, Nijmegen, the Netherlands*
[3] *Biomedical Imaging Research Center, École Polytechnique Fédérale de Lausanne, Lausanne, Switzerland*
[4] *Cardiff University Brain Research Imaging Centre (CUBRIC), School of Engineering, Cardiff University, Cardiff, UK*

Accepted for publication in *Magnetic Resonance in Medicine* on 6th December 2017

**Purpose:** To investigate the precision of estimates of temporal variations of magnetic field achievable by double-echo fat image navigators (FatNavs), and their potential application to retrospective correction of 3D GRE-based sequences.
**Methods:** Both head motion and temporal changes of $B_0$ were tracked using double-echo highly-accelerated 3D FatNavs as navigators – allowing estimation of the temporal changes in low spatial order field coefficients. The accuracy of the method was determined by direct comparison to controlled offsets in the linear imaging gradients. Double-echo FatNavs were also incorporated into a high-resolution 3D GRE sequence to retrospectively correct for both motion and temporal changes in $B_0$ during natural and deep breathing. The additional scan time was 5 minutes (a 40% increase). Correction was also investigated using only the first echo of the FatNav to explore the trade-off in accuracy vs scan-time.
**Results:** Excellent accuracy (0.27 Hz, 1.57-2.75 Hz/m) was achieved for tracking field changes and no significant bias could be observed. Artefacts in the 3D GRE images induced by temporal field changes, if present, were effectively reduced using either the field estimates from the double-echo or the first-echo-only from the FatNavs.
**Conclusion:** FatNavs were shown to be an excellent candidate for accurate, fast and precise estimation of global field variations for the tested patterns of respiration. Future work will investigate ways to increase the temporal sampling to increase robustness to variations in breathing patterns.

# Introduction

Sequences based on $T_2^*$ contrast have demonstrated great usefulness to brain MRI for identification of various anomalies and conditions such as microbleeds and multiple sclerosis, but also quantitative estimates of physical properties [81–83]. Common sequences for $T_2^*$ contrast, such as susceptibility weighted imaging and quantitative susceptibility mapping, typically require long (>20ms) echo times. While the use of ultra-high field magnets provides a significant boost to the resolution for an equivalent signal-to-noise ratio (SNR), it also unavoidably makes these gradient-echo based sequences more sensitive to uncontrolled phase evolution during the long echo times [84]. These phase variations stem from both static background magnetic field inhomogeneity, but also from dynamic events, such as breathing [85, 86] or system drifts. Several attempts at quantifying and correcting these dynamic changes have been reported, using either navigator techniques [87–89] or external hardware [90–93]. Navigator methods at 7T which incorporate tracking the temporal $B_0$ variation in full 3D have yet to be demonstrated, although some hybrid methods went beyond a single dimension [94], where the sensitivity maps of the RF receive array were used to provide additional 2D in-plane spatial information to a one-dimensional projection. Ultra-high field also allows for high SNR very-high resolution (<0.5mm in plane) 3D acquisitions, but these necessarily imply longer acquisition times, thereby further increasing the probability of the scan being detrimentally affected by subject motion. Using parallel imaging [9, 10] , highly accelerated fat selective navigators (FatNavs) have previously demonstrated the ability to quantitatively track motion and significantly improve image quality using either a retrospective [48] or a prospective [46] correction approach.

In this work we propose an extension of the FatNavs protocol to a double-echo acquisition. This approach allows mapping of the 3D dynamic $B_0$ variation in the fat layer, and to estimate the associated low order field coefficients. Adding the motion information, we also show that both effects can be retrospectively accounted for during image reconstruction, and that applying both of these corrections can result in a pronounced improvement in image quality for cases where these artifacts are strong.

# Methods

All experiments were conducted on a 7T head-only MR scanner (Siemens Healthcare, Germany) using a 32-channel RF coil (Nova Medical Inc.). Two main experiments were conducted: the first aimed at quantifying the accuracy of the $B_0$ field estimates derived from the FatNavs. The second was a high-resolution 3D GRE scan, which will be referred to as the host sequence, into which FatNavs were inserted ($\sim$ 17 minutes). For the second experiment, volunteers were first asked to breathe deeply and slowly, after which a repetition of the scan was acquired, where this time they were asked to breathe in the way that seemed the most natural to them. Asking compliant volunteers to perform heavy deep breathing is expected to simulate the kinds of image artifacts that might arise from $B_0$ variations in less cooperative subjects or within certain patient populations. We now introduce the necessary definitions and notations, and detail the protocols for the different experiments thereafter.

## Retrospective correction of motion and temporal B0 changes

We assume the motion can be well described by a rigid body transformation [73]

$$\mathbf{x}\left(t\right)=R\left(t\right)\mathbf{x_0}+\mathbf{d}(t)$$

where $R$ is a rotation matrix and $\mathbf{d}$ a translation vector. Keeping in mind the implicit time dependence of the various variables, including $\mathbf{k}$, the signal y measured in coil c at $\mathbf{k}-$space position $\mathbf{k}$ is related to the non-moving object $\rho$ by

$$y_c\left(\mathbf{k}\right)=\int s_c\left(x\right)\rho\left(x\right)\exp\left(-i2\pi\left[R\mathbf{k}\cdot\left(\mathbf{x}-\mathbf{d}\right)+\Delta B_0\left(x\right)\left(T_E+\frac{k_{RO}}{G}\right)\right]\right)d^3x \tag{3.1.1}$$

where $s_c$ is the receive coil sensitivity (assumed to be quasi-invariant under motion), $T_E$ is the echo-time, $k_{RO}$ is the readout component of $\mathbf{k}$, and G is the readout gradient amplitude. Neglecting phase accumulation during readout, only temporal variations of $\Delta B_0\left(x\right)$ induce image artifacts. Furthermore, these are generally well represented by low order spherical harmonics [88] . Approximating $\Delta B_0$ to its first order components

$$\Delta B_0\left(x,t\right)=\beta_0\left(t\right)+\boldsymbol{\beta}\left(t\right)\cdot\mathbf{x} \tag{3.1.2}$$

allows for an efficient reconstruction using a nuFFT [23] operator with ten time-dependent parameters: six for motion and four for dynamic field variations. In $\mathbf{k}-$space, $\beta_0$ and $\mathbf{d}$ contribute to a phase correction term, whereas $R$ and $\boldsymbol{\beta}$ respectively amount to local rotations and shifts.

## FatNav protocol and image reconstruction

The navigator protocol was a highly accelerated double-echo 3D GRE with a 1-2-1 binomial fat excitation pulse. It was chosen as a compromise between voxel size, phase evolution time and total acquisition time [77]. Parameters were: 3.94 mm isotropic resolution, $64\times64\times48$ full matrix size, 3/4 partial Fourier undersampling along both phase encode directions, FA = 5° ,$T_{E,1}$ / $T_{E,2}$ / $T_R$ = 1.16 / 4.16 / 5.4 ms, readout bandwidth of 3910 Hz/pixel, and 4x4 GRAPPA acceleration, leading to a volume acquisition time of 583.2 ms. GRAPPA calibration lines were acquired separately as a prescan. An equivalent single echo FatNav would take 260 ms to acquire.

FatNav reconstruction was performed as follows: first, GRAPPA was applied to recover fully sampled k-space, from which square-root sum-of-squares (RSS) volumes of the first echo were co-registered using the *realign* tool in SPM (Statistical Parametric Mapping, version 12, registration parameters: 2 mm resolution interpolation, 3 mm smoothing window) to obtain motion estimates. Then, again from the fully sampled k-space, we directly reconstructed all channels $c$ and echoes $E$ for each volume using a nuFFT with the associated motion parameters. The resulting complex images $I_c(x, E)$ are therefore co-registered with the motion reference volume (the selection of which is explained below) directly in the image reconstruction. The final field map $B_0$ for a given volume was defined by

$$2\pi\left(T_{E,2} - T_{E,1}\right)\Delta B_0(x) = arg\left(\frac{1}{N_c}\sum_{c=1}^{N_c}\frac{I_c^*(x, E_2)\, I_c(x, E_1)}{|I_c(x, E_2)|}\right) \tag{3.1.3}$$

where $N_c$ is the number of receive coils. The temporal variation of the $B_0$-field is readily obtained by a phase difference computation to a reference FatNav. The reference volume, for both motion and $B_0$, was chosen as the one acquired the closest to the host sequence $\mathbf{k}-$space center in experiment 2, and as a fixed number larger than one (necessary for the magnetization to reach a steady state) in experiment 1. At no stage is any partial Fourier filter applied and the Fourier transform is taken after zero-padding. As the phase changes due to breathing are typically smoothly varying, we do not expect the reduction in spatial resolution due to partial Fourier undersampling to affect the fidelity of tracking these phase changes. We validated this assumption by acquiring the same FatNav protocol but without any partial Fourier undersampling on one volunteer. We retrospectively down-sampled it and compared the estimated field change coefficients with and without partial Fourier undersampling.

The fit of the linear coefficients of temporal field variation was restricted to a fat-mask, defined by thresholding the reference volume first-echo RSS image. The threshold value was found by direct visual inspection and was the same for all volunteers.

This reconstruction pipeline gives direct access to the ten parameter time-courses used in the host sequence reconstruction. As expected, the field estimates obtained in this manner are still residually affected by subject motion – which has two main sources. The first is some inaccuracy of the applied method, such as incorrect motion estimation or limitations of the assumption of rigid-body motion. The second is the motion-induced change of the magnetic susceptibility spatial distribution relative to the static superconducting magnet, which in turn produces a change of the net magnetic field [95]. The results presented in this paper lead us to believe that the method is sufficiently accurate for our purposes, and consider the complete quantification of the induced field effect to be outside of the scope of this work.

We also note that the change of phase $\delta\varphi_{ci}$ of a single voxel for a given coil $c$ and echo $i$ can be modeled as

$$\delta\varphi_{ci} = \delta\varphi_c + 2\pi\Delta B_0 T_{E,i} \tag{3.1.4}$$

where $\delta\varphi_c$ is the change of receiver phase due to motion and $\Delta B_0$ is the local temporal variation of field. Therefore, in the case of negligible receive phase change, tracking temporal changes in the field rather than absolute values does not require the use of the second echo. Indeed, letting $I_{c,r}$ be the first echo image of the reference volume for the receive coil $c$, then the field variation map $\Delta B_0$ can be defined as

$$2\pi T_{E,1}\Delta B_0(x) = arg\left(\frac{1}{N_c}\sum_{c=1}^{N_c}\frac{I_c^*(x,E_1)\,I_{c,r}(x)}{|I_c(x,E_1)|}\right). \tag{3.1.5}$$

Additionally, using both FatNav echoes it is also possible to derive a $\delta\varphi_c$ map, allowing for a correction of the host data which incorporates both contributions to the temporal phase changes (changes in receiver phase as well as changes in $B_0$). However, we found that the magnitude of $\delta\varphi_c$ was not large enough to make a noticeable difference in the corrected host data (see Appendix 1 for estimation of expected magnitude for $\delta\varphi_c$). We therefore used (3.1.3) for the dual-echo estimates of $\Delta B_0$ and (3.1.5) for single-echo estimates of $\Delta B_0$– which is sufficient for the purposes of correcting the host data as the 'absolute' value of $B_0$ is not required.

## Experiment 1: Determining the accuracy of field monitoring

In order to estimate the accuracy of the field monitoring, we acquired 72 consecutive FatNavs (after steady state was reached), where every other volume had a predetermined offset of one of the imaging gradients. In order to diminish the motion-related field changes which would reduce the apparent accuracy of the method, visual inspection of the motion parameters ensured that no large motion occurred during these acquisitions. These gradient offsets values were chosen in the (-50,50) Hz/m range. Due to time considerations, not all offsets values for all directions were acquired for each volunteer. However, a 20 Hz/m offset for each direction was always acquired for the four volunteers who completed this experiment to allow direct comparison between subjects. This corresponds approximately to the typical natural breathing range in the z direction at 7T. Using the same value for the x and y directions allows assessment of whether the method might also show some systematic anisotropy.

Two different methods were investigated for estimation of the gradient offset amplitude and the associated error. Let $b_n$, $n = 1,\ldots,2N$ be some field coefficient as defined in (3.1.2), where $N$ is the number of control/offset volumes pairs. We constructed a sequence of field coefficient differences $d_n$ which represents the measured field temporal variation. Two construction methods were investigated: the first method uses the consecutive volume difference (CVD) sequence $d_n = b_{2n} - b_{2n-1}, n = 1,\ldots,N$ . It assumes the field change is exclusively due to the gradient current offset during the measurement time of this pair of volumes. However, residual breathing effects are bound to be captured as well, thereby diminishing the apparent precision of the offset estimate given by the CVD method. The second method, dubbed double linear interpolation difference (DLID), tries to evaluate consecutive FatNavs of the same kind (control or offset) at the same time point than the sandwiched FatNav (offset or control) before doing the difference. Mathematically the sequence studied is

$$d_n = \begin{cases} \frac{1}{2}(b_n + b_{n+2}) - b_{n+1} & \text{if } n \text{ is odd} \\ b_{n+1} - \frac{1}{2}(b_n + b_{n+2}) & \text{if } n \text{ is even} \end{cases} \quad n = 1,\ldots,2N-2 \tag{3.1.6}$$

Given the short volume acquisition time of the FatNavs, this method is assumed to interpolate any residual breathing-related field change, and thus allow a less biased statistical analysis (under the hypothesis of independent uniformly distributed noise realizations).

The precision of the method was defined from the root-mean-square-error (RMSE) of the error sequence given by $d_n - T$, where T is the known input offset (either zero or equal to the chosen linear offset). This RMSE is necessarily larger than the true precision of the method, as the following argument demonstrates. Let $b_i = p_i + T_i + \varepsilon_i$ with $p_i$ the physiological contribution to the field change, $T_i$ the offset (0 or the input offset), and $\varepsilon_i$ the error. Assuming the sums of mixed terms of the form $p_i \varepsilon_j$ to be negligible, which is equivalent to the independence of the physiological field change and the noise realization, the RMSE of the DLID is given by

$$\text{RMSE} = \sqrt{\frac{1}{2N-2} \sum_{i=1}^{2N-2} \left[\frac{1}{2}\left(p_n + p_{n+2}\right) - p_{n+1}\right]^2 + \left[\frac{1}{2}\left(\varepsilon_n + \varepsilon_{n+2}\right) - \varepsilon_{n+1}\right]^2}. \tag{3.1.7}$$

White uncorrelated noise thereby implies RMSE $= \sqrt{\frac{3}{2} < \varepsilon^2 >}$ in the case of perfect physiological contributions suppression. In practice the suppression is certainly not perfect, and the RMSE is larger than the precision of the method itself. We define the field change coefficient precision, noted $\bar{\varepsilon}$, as

$$\bar{\varepsilon} = \sqrt{\frac{2}{3}}\text{RMSE}. \tag{3.1.8}$$

## Experiment 2: High resolution $T_2^*$ scans

The high resolution protocol was a 3D GRE transversal slab, with flow compensation in all directions, nominal resolution: 0.25x0.25x1.2 mm$^3$, full matrix size: $768 \times 672 \times 64$, 3/4 partial Fourier undersampling in both phase encode directions, FA = 9° , TE / TR = 25 / 30 ms, receiver bandwidth = 220 Hz/pixel .

FatNavs were acquired between sequential $\mathbf{k}-$space planes of the host sequence. This way, disruptions to the steady-state water signal are smoothly distributed in $\mathbf{k}-$space along the innermost phase encoding loop direction, inducing only a slight blurring on the final image. Bloch simulations for these experimental parameters for white matter, gray matter and CSF (assumed $T_1 = 1.15/1.9/4.47$ s respectively) showed that the point-spread function of the water image is only marginally changed by the inclusion of the FatNavs. Its zero crossings by any practical measure are identical and the phase changes only outside of the first lobe. The resolution loss compared to the same scan without FatNavs is below 2%. Furthermore, contrast is barely affected: see Figure 3.1. The temporal resolution of the FatNavs was 2 s and the total acquisition time was 17 min 2 s, where the same GRE acquisition could have been performed in 12 min 6 s without the additional time needed for the FatNavs.

Previous studies [96] showed that the average natural breathing period of the studied population lying in the supine position is slightly above 4 seconds. This means that while slow, deep breathing should be accurately sampled by the FatNavs, natural breathing is very close to the limit imposed by the FatNavs temporal resolution. We expect that partial sampling and partial correction can take place in this case (see Discussion for potential solutions to this limitation). The linear field coefficient fits of the FatNav $B_0$ maps were restricted to the host excitation slab, after fat identification by magnitude thresholding (as explained above). Reconstructions using no field, the zeroth ( $\beta_0$ only) and first ( $\beta_0$ and $\boldsymbol{\beta}$) order field corrections were performed separately for data from each receive coil and then combined using RSS. First-order correction based on field coefficients derived from (3.1.5) was also investigated.

Magnitude bias-field correction of the GRE images was performed by a point-wise division of the RSS image with a bias-field map. The bias-field map was found by smoothing a low-resolution version of the image, and interpolating the result back to the 3D GRE high-resolution grid. Quantification of image quality was evaluated using a gradient entropy metric (taking the sum of the image entropy of the finite differences of neighboring pixels in the x, y and z directions), as

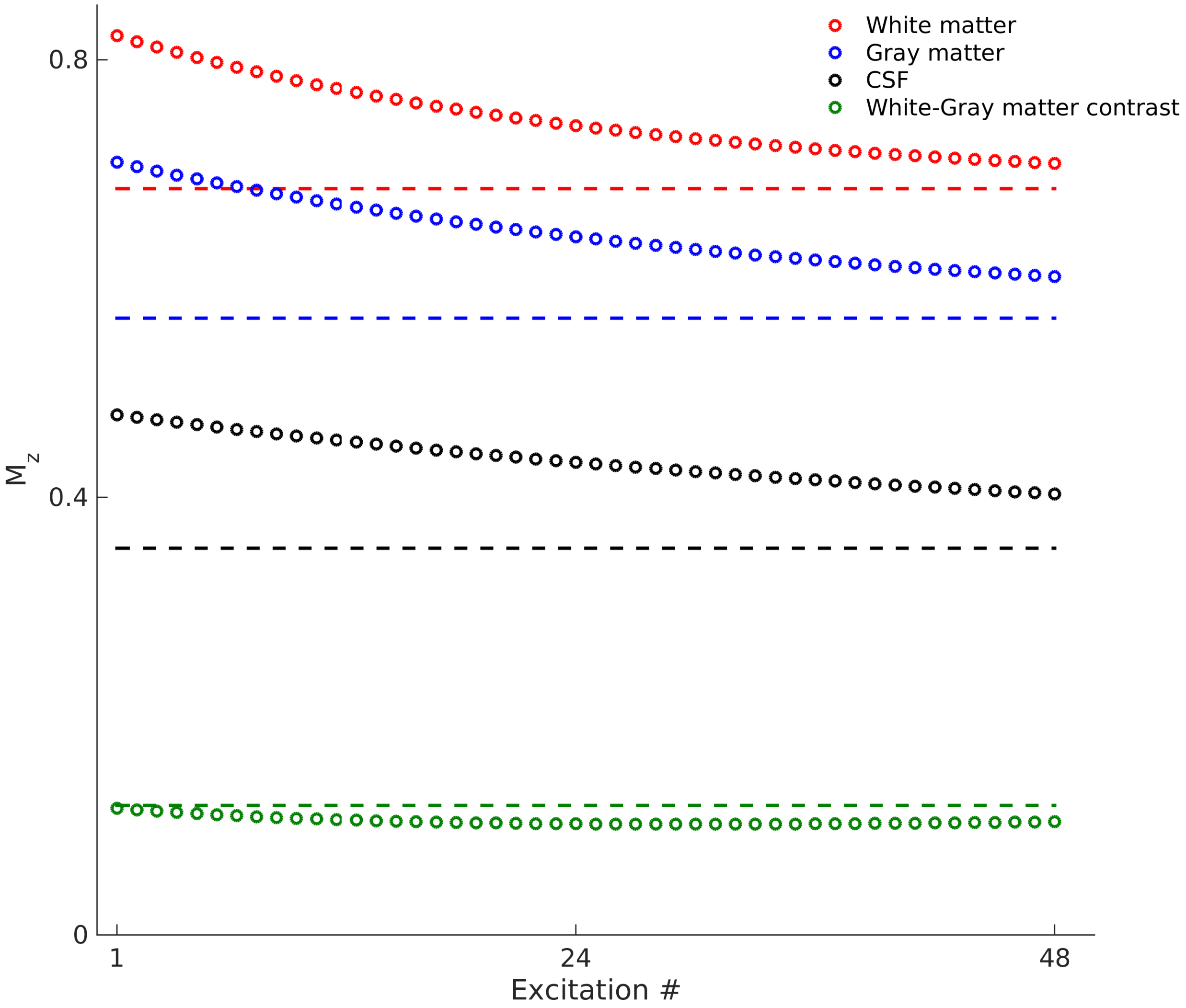

Figure 3.1 – Bloch simulation of the water signal during the high-resolution GRE protocol with FatNav inclusion. Dashed lines represent the steady state in absence of FatNavs. The green line is the white to gray matter contrast. The point-spread functions associated to these signals are found by zero-padding and shifting before taking the Fourier transform to account for the host sequence partial Fourier. They show a resolution loss of less than 2.2%.

previous work [17, 62] showed this metric to be a strong candidate as a surrogate marker for the subjective definition of what a “good” image is.

# Results

## Determining the accuracy of field monitoring

Retrospective partial Fourier down-sampling showed no significant change to the estimates of phase variations, as can be seen in Figure 3.2. The RMSE between with and without retrospective partial Fourier undersampling were 0.1 Hz for the $0^{th}$ order term, and 1.8 / 2.5 / 4 Hz/m for the x / y / z directions. Figure 3.3 illustrates the difference between the CVD and the DLID methods for a field offset of 5 Hz/m in the x direction, thus theoretically leaving only noise and breathing as contribution to the y and z field coefficients variations. Breathing is clearly observed (Figure 3.3 A. and B). The magnitude of the breathing-induced field change is in agreement with previously

published values at 7T. The slight bias in the x direction due to the gradient offset cancels out when taking the mean across breathing peaks and troughs. These were found by extrema identification of the spatial mean $B_0$ value, computed in the fat layer mask using both FatNavs echoes. Because breathing contributes significantly to the error estimates (Figure 3.3 C) for the CVD method, but not for the DLID method, which shows a more homogeneous spectrum (as is expected for random noise), all the following results were obtained using the DLID method. Quantitatively, the mean (maximum in brackets) precision $\bar{\varepsilon}$ across gradient offsets for $\beta_0, \beta_x, \beta_y, \beta_z$ were 0.29 (0.45) Hz, 1.57 (3.14) Hz/m, 2.35 (4.31) Hz/m and 2.75 (5.19) Hz/m respectively. As a current offset in one gradient should not influence the field estimates for the other two directions, these mean and maximum values include the precision of field estimates in these others directions. Measured shift values for all volunteers are shown in Figure 3.4. All estimates matched the target field shift (up to the first standard deviation) for the y and z directions, and one subject falls outside the first standard deviation for the x direction. The precision of the method shows no significant spatial anisotropy, reinforcing the absence of systematical bias in the method (by the choice of phase encoding directions for example).
Similarly, the precision values using only the first echo of the FatNavs for $\beta_0, \beta_x, \beta_y, \beta_z$ were 0.44 (0.91) Hz, 2.63 (5.74) Hz/m, 5.24 (15.79) Hz/m and 4.18 (11.22) Hz/m respectively. These values are approximately double the precision of the dual-echo estimates.

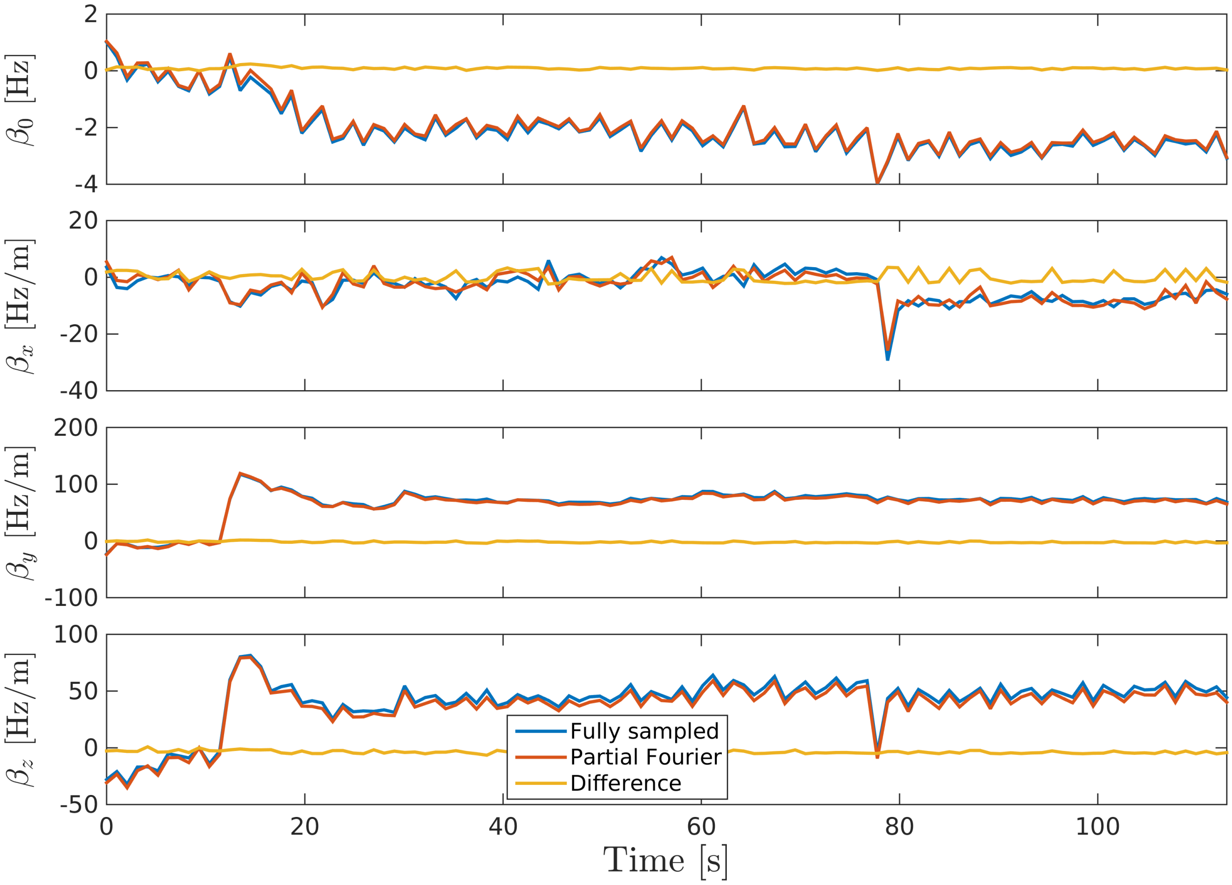

Figure 3.2 – FatNavs without gradient offsets or partial Fourier were acquired. Field change coefficients were estimated using either all the measured data, or after partial Fourier simulation (in x and y). The RMSE between fully-sampled and partial Fourier reconstructions are 0.1 Hz for the 0th order term, and 1.8 / 2.5 / 4 Hz/m for the x / y / z directions. The higher value on z is probably due to breathing during sampling, which is almost twice as long for this protocol than for the one used in the rest of the study (which uses partial Fourier).

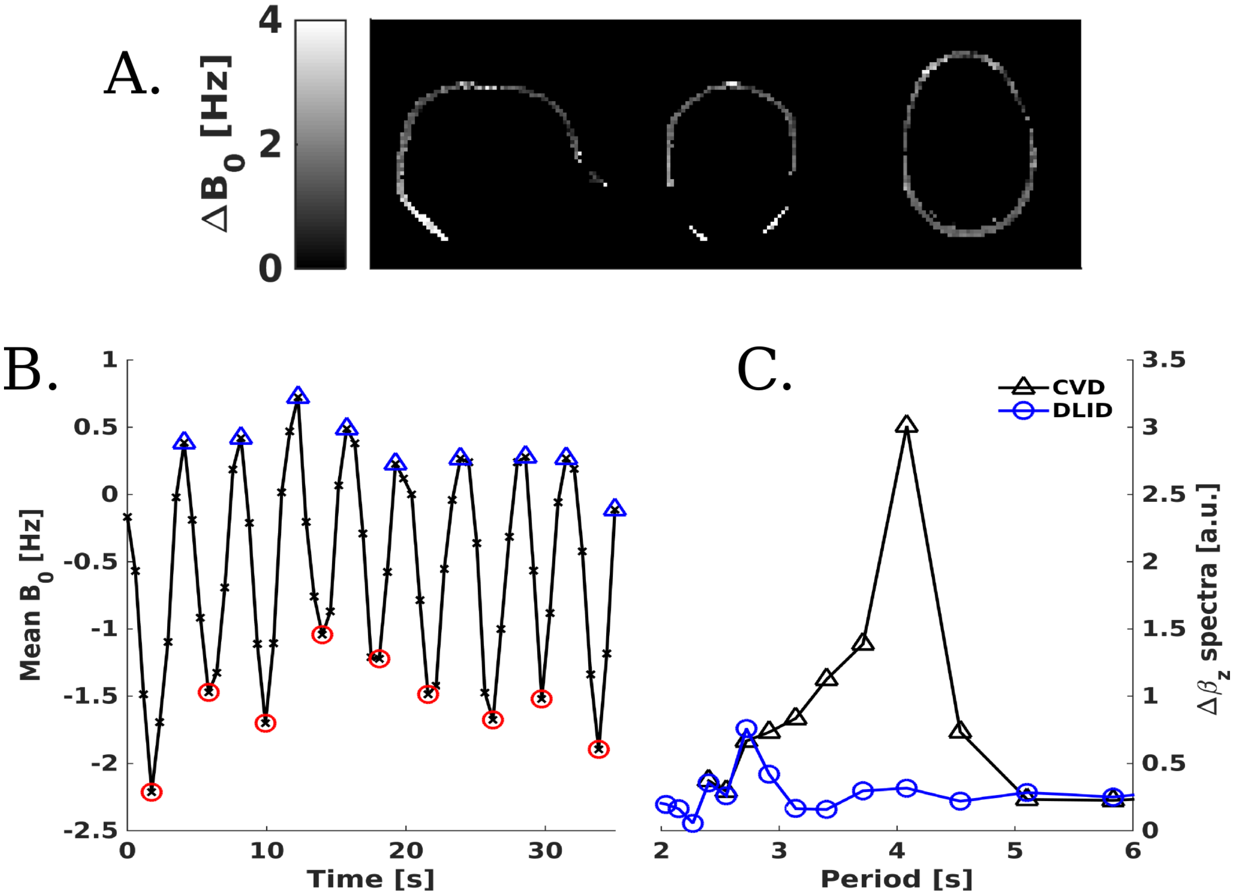

Figure 3.3 – Example data from a single subject with a 5 Hz/m offset in the x direction every other volume. (A) Mean $B_0$ difference between breathing peaks and troughs in the fat layer, after masking for fat signal. (B) Mean $B_0$ field across entire fat signal mask vs time. Markers represent the peaks and troughs of respiration, used to derive the plot (A). (C) Spectra of the time-courses of the estimated linear field change in z derived from both consecutive volume difference (CVD) and double linear interpolation difference (DLID) methods, in arbitrary units [a.u.].

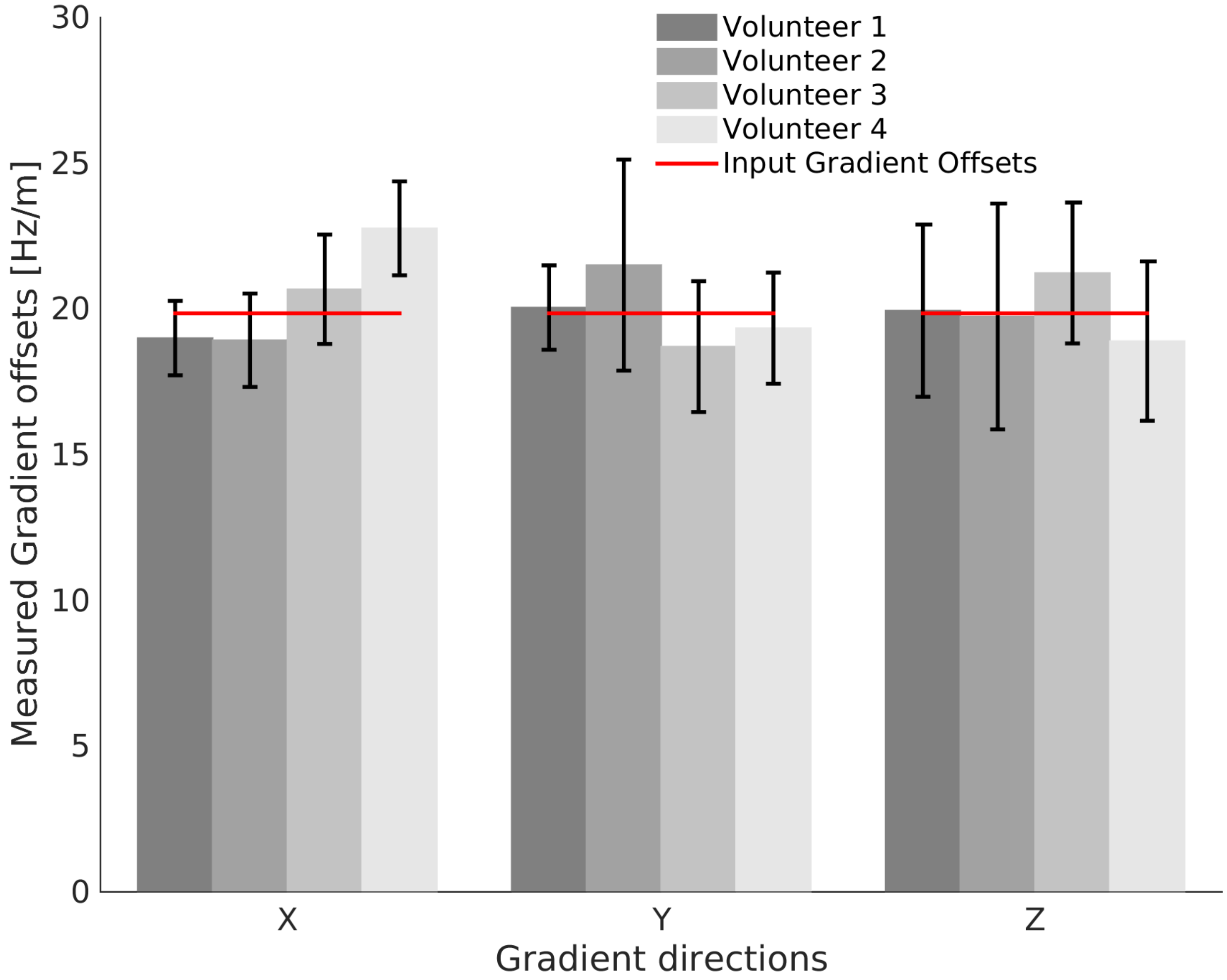

Figure 3.4 – Gradient offsets measured across volunteers. Error bars show +- 1 standard deviation.

## High resolution $T_2^*$ scans

Representative slices of the high-resolution 3D GRE scans while breathing slowly and deeply are shown in Figure 3.5, for all investigated reconstructions. The sharpness of anatomical features is noticeably improved after motion correction. However, the large-scale ghosting and blurring artefacts typically induced by breathing are not suppressed. Incorporating correction of temporal magnetic field variations greatly reduces these artefacts, and first order correction further enhances image quality compared to the zeroth order correction. The six motion and four dual-echo field parameters derived from the FatNavs for these scans are shown in Figure 3.6. The parameters of volunteer 2 deep-breathing scan, where significant field variation induced by breathing also occurs along the y direction, indicating the utility of measuring the field variations using more than one-dimensional projection in such cases.

Similarly, representative results of scans where the subject was asked to breathe naturally are presented in Figure 3.7, and the corresponding motion and field parameters in Figure 3.8. Similar levels of improvement following motion-correction were observed as in the deep-breathing experiment – with the improvement even more striking in Volunteer 1 due to the larger motion during that scan. Notice also that the field coefficients are also affected by motion, even though these are defined in the co-registered FatNav-space. This is most clearly seen when sudden motion takes place in Figure 3.8. While overall it is difficult to identify clear improvements to the image quality when the field variations are corrected for, increasing the number of correction parameters did show increasing image quality for volunteer 1 (this volunteer is also the one who moved the most). These results suggest that for healthy compliant subjects, and under the imaging parameters used in this experiment, breathing artifacts are typically not sufficiently severe for the correction to make a noticeable improvement. It is also plausible that breathing is not well sampled throughout the whole scan, leading to sub-optimal corrections (see Figure 3.7).

Comparison of typical slices in the deep breathing scan for the first-order field correction using dual-echo estimates (from (3.1.3)) or the single-echo estimates (from (3.1.5)) is shown in Figure 3.9. The image quality of both reconstructions is very similar, and areas of subjectively 'better' image quality can be found in either reconstruction. As Figure 3.10 shows, the differences between the first-echo and dual-echo field estimates are largely explained by a simple first-order regression in the motion parameters. This in turn implies that in case of a drift-like motion, the phase terms for image corrections will differ by a drift as well, producing slightly shifted corrected images.

Figure 3.11 shows the reduction of gradient image entropy between the raw reconstruction and the different corrections studied, normalized to the raw reconstruction value. We observe a decreasing gradient entropy (compared to the raw reconstruction) as higher order field terms are taken into accounts. The change is more pronounced for the deep breathing scan, as expected. The differences between first-echo and dual-echo based corrections are inconsistent across scans and volunteers (comparison shown for motion-correction and $B_0$-correction up to $1^{\text{st}}$-order), but the gradient entropies following both these corrections were all lower than from the lower-order corrections.

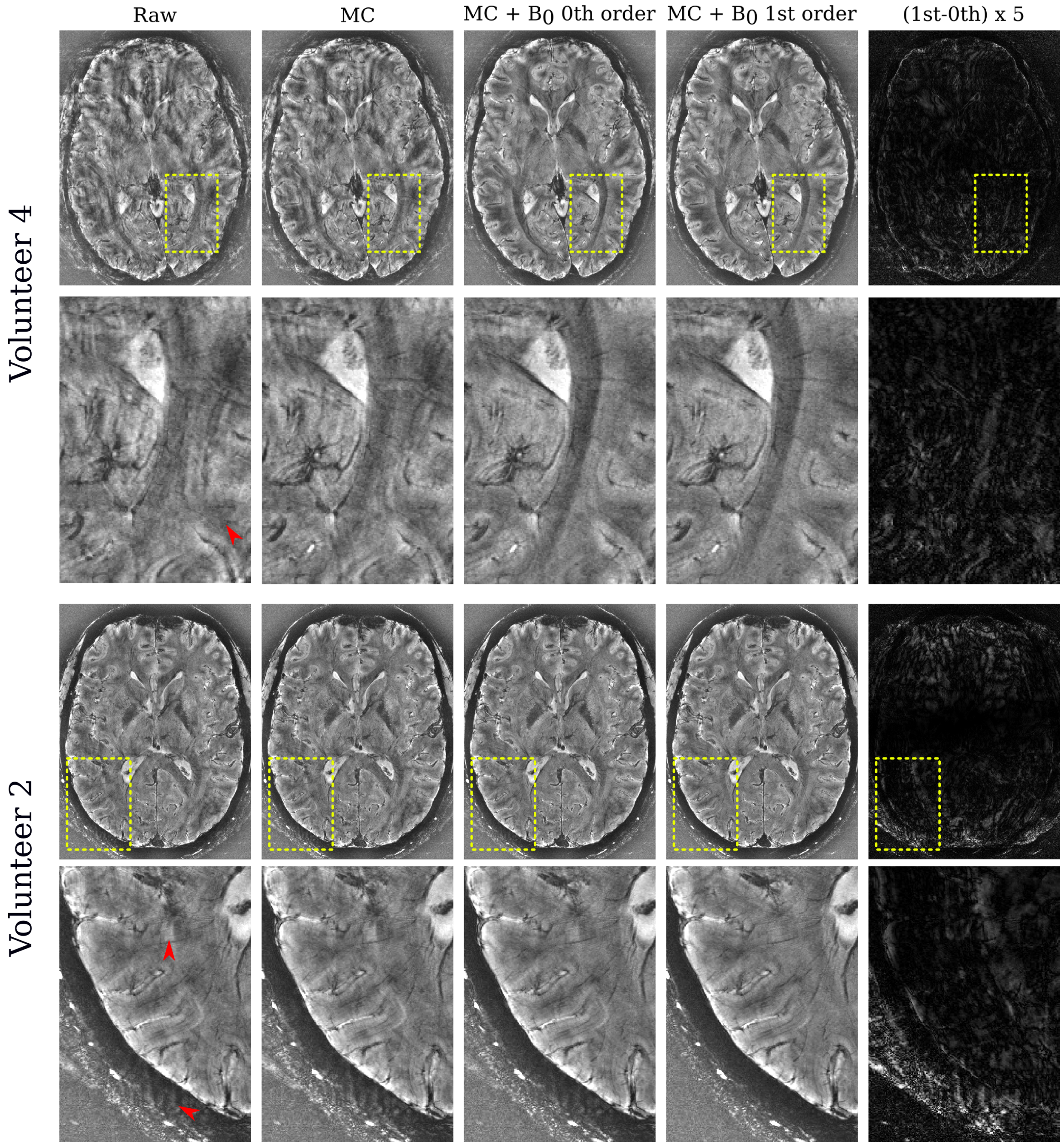
Raw
MC
MC + B0 0th order
MC + B0 1st order
(1st-0th) x 5
Volunteer 4
Volunteer 2

Figure 3.5 – Representative reconstructions example for the high-resolution scan while deep-breathing. Abbreviations stand for: raw reconstruction (Raw), motion correction only (MC), motion and zeroth order $B_0$ corrections, and motion and first order $B_0$ corrections. The bottom right is the absolute difference between both $B_0$ order corrections, multiplied by 5. All images use the same color-map. Red arrows highlight regions where improvements can be most clearly observed with increasing levels of correction.

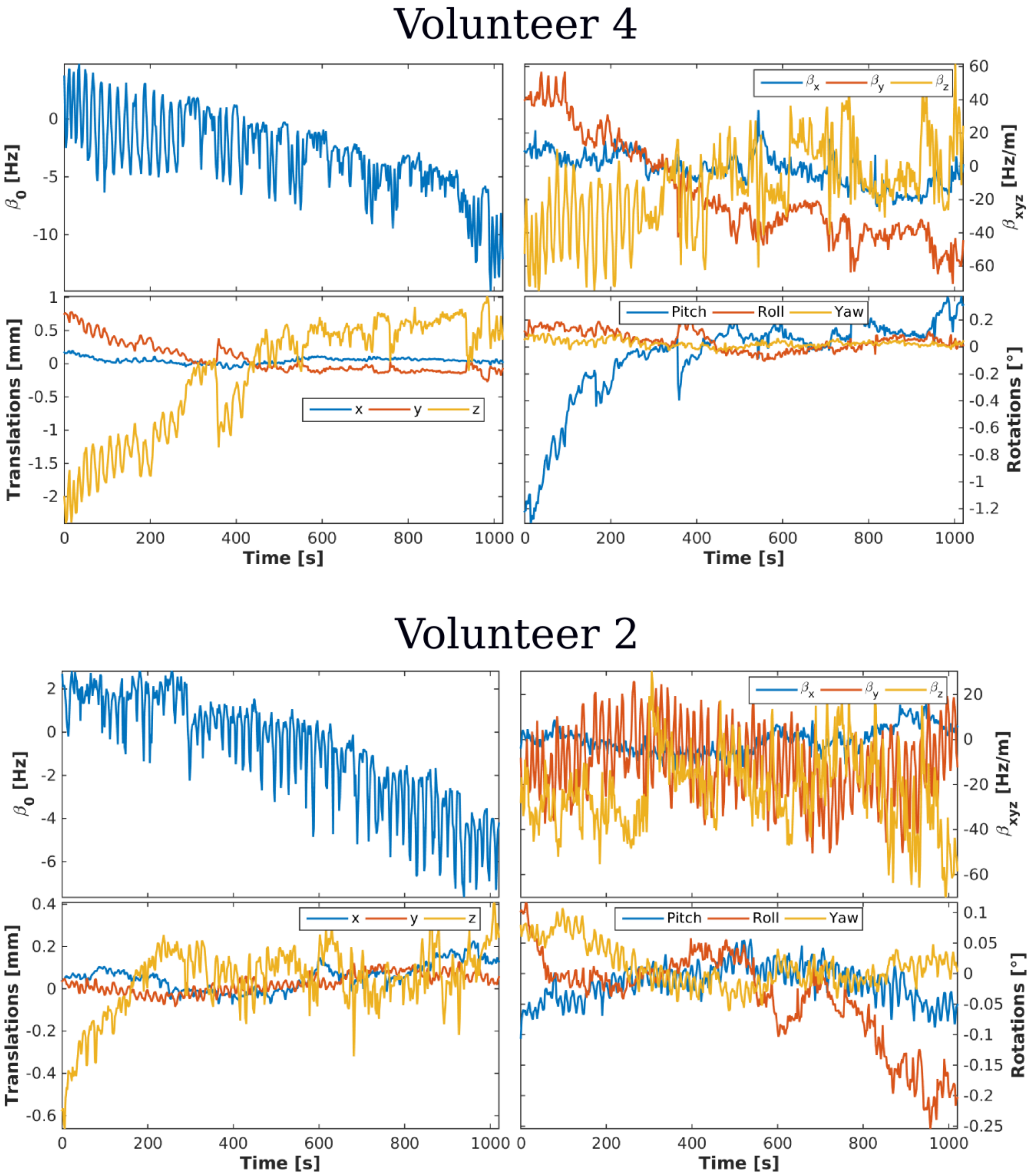

Figure 3.6 – Estimated motion and field parameters for the scans of Figure 3.5 , where the volunteers were asked to breathe deeply.

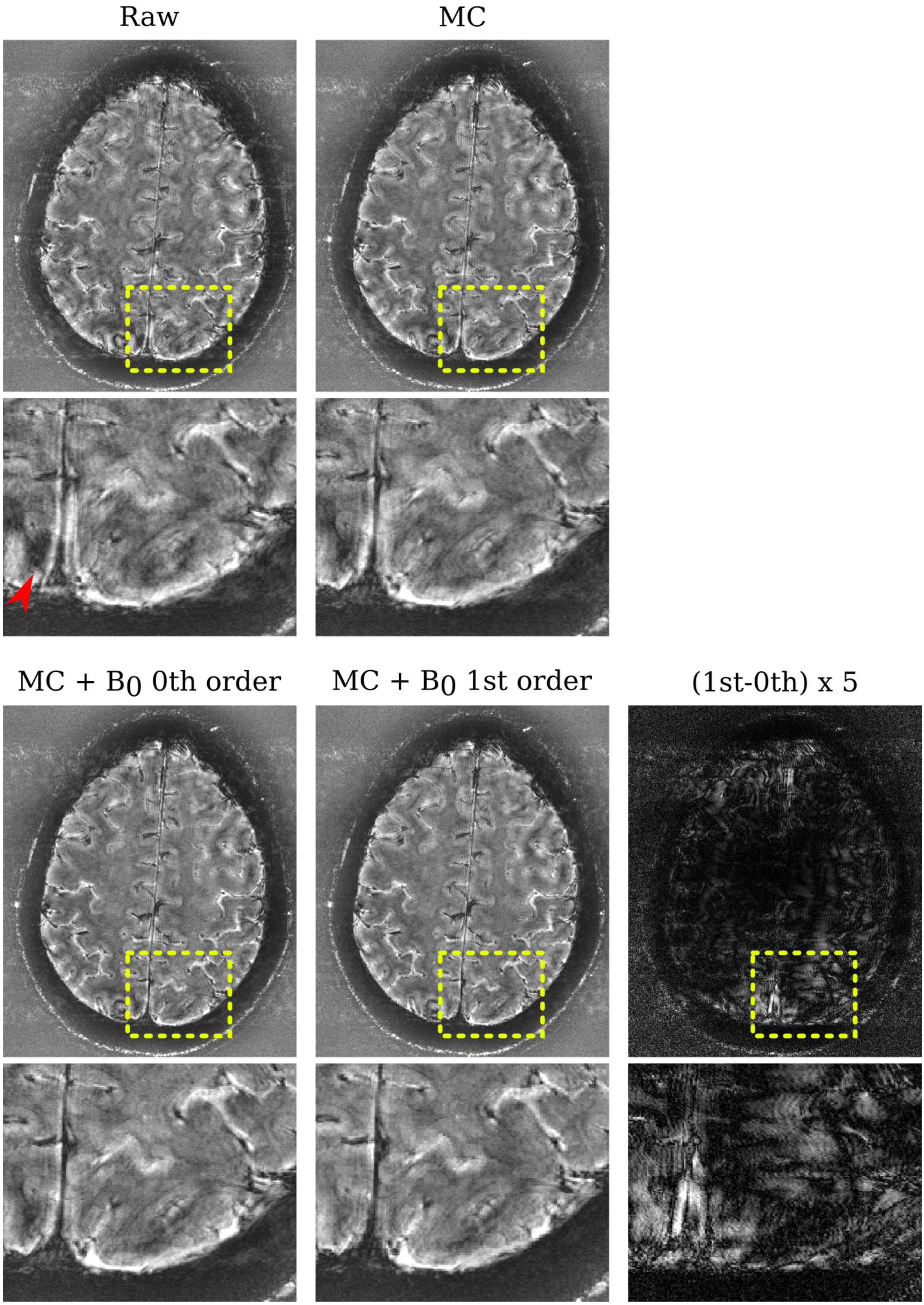
Raw
MC
MC + B0 0th order
MC + B0 1st order
(1st-0th) x 5

Figure 3.7 – Representative reconstructions example for the high-resolution scan while subject breathed naturally. Figure organization is as in Figure 3.5.

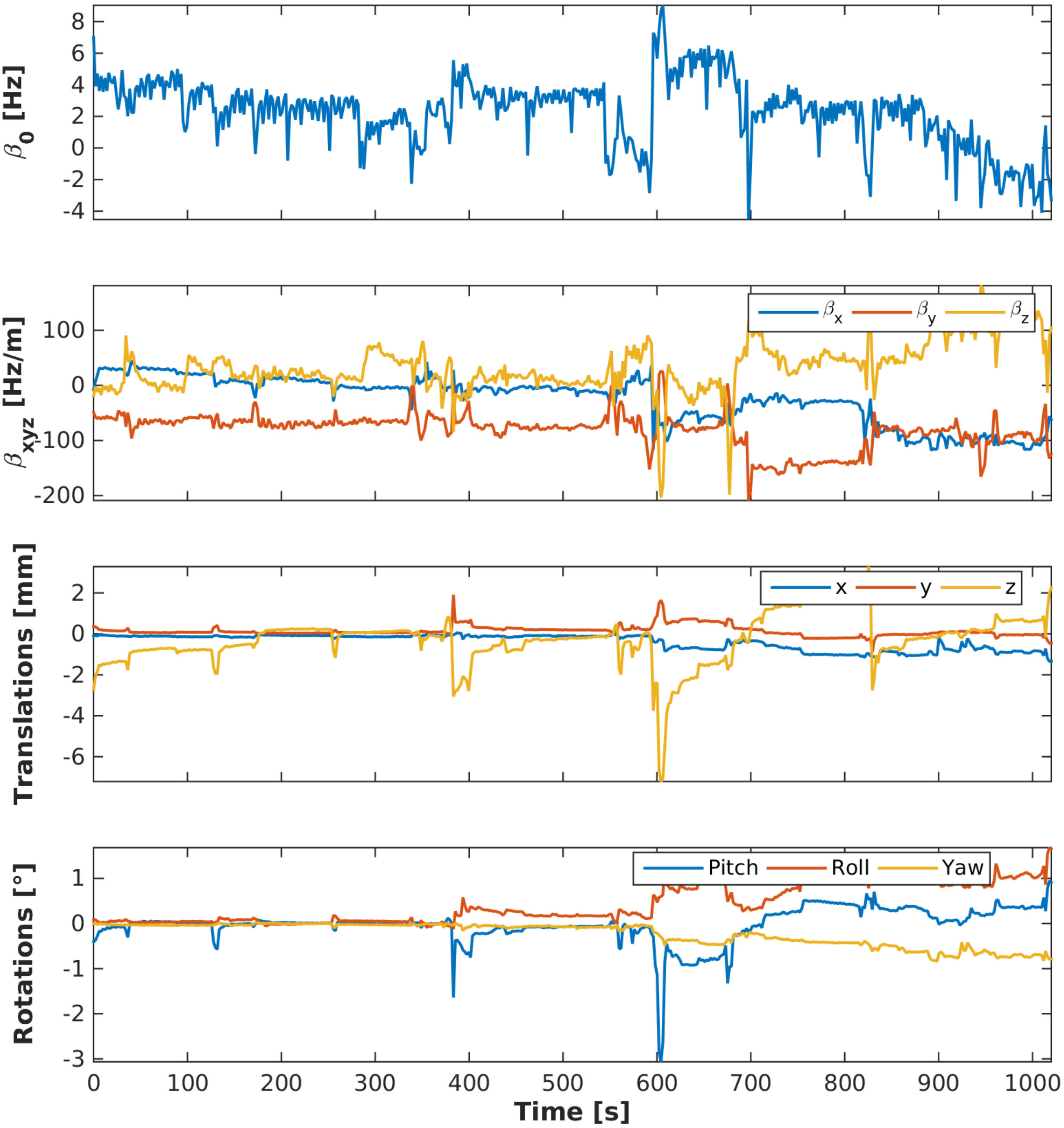

Figure 3.8 – Estimated motion and field parameters for the scan of Figure 3.7 (volunteer 1), where the volunteer was asked to breathe normally.

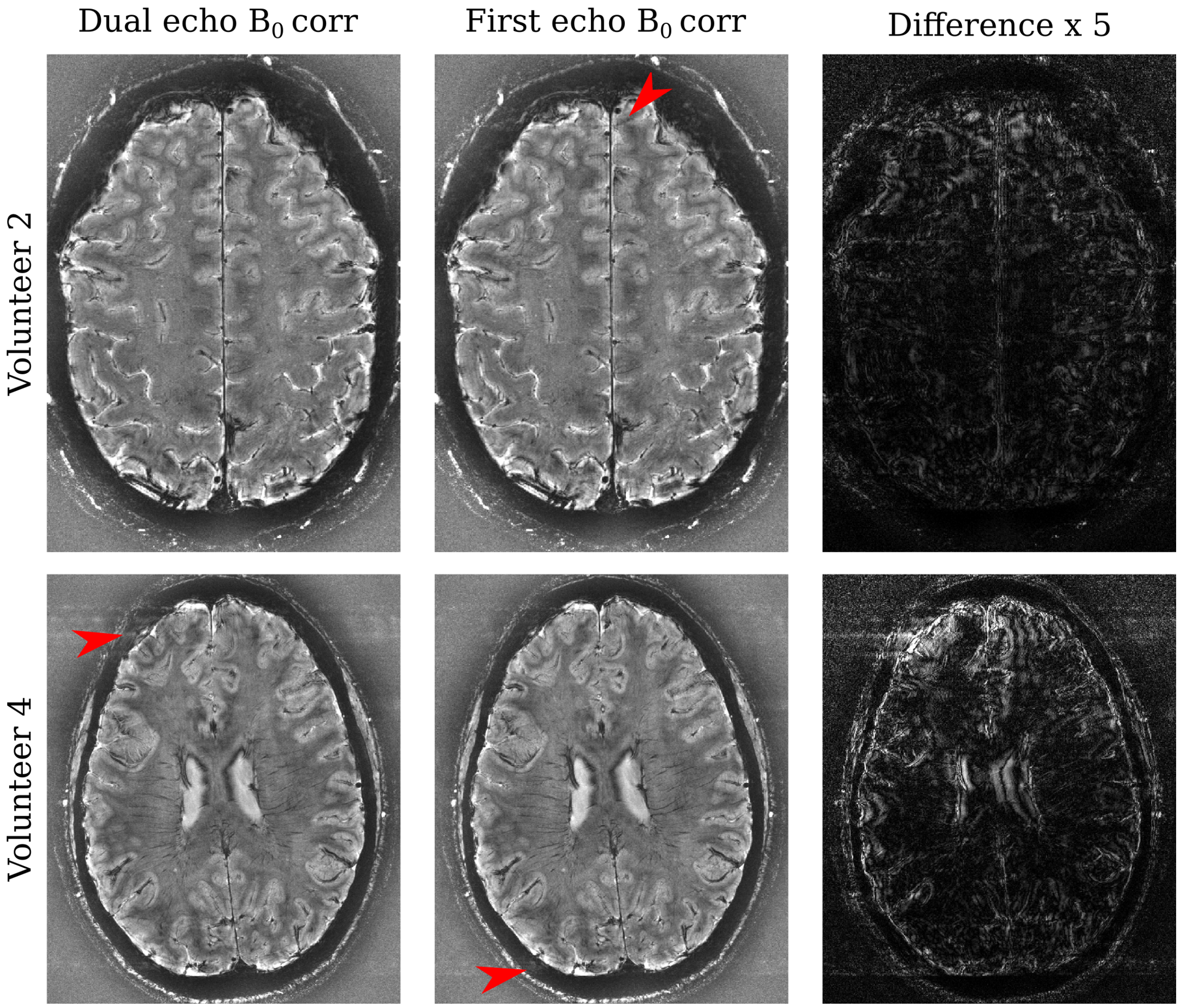
Dual echo B0 corr
First echo B0 corr
Difference x 5
Volunteer 2
Volunteer 4

Figure 3.9 – Representative motion and first-order $B_0$ corrected images in the deep-breathing scan. First column is using both echoes from the FatNavs to estimate the field changes, whereas the second column uses only the first echo. The third column is the absolute difference times 5. Red arrows indicate regions where slight depreciative change of image quality can be found compared to the image without the red arrow.

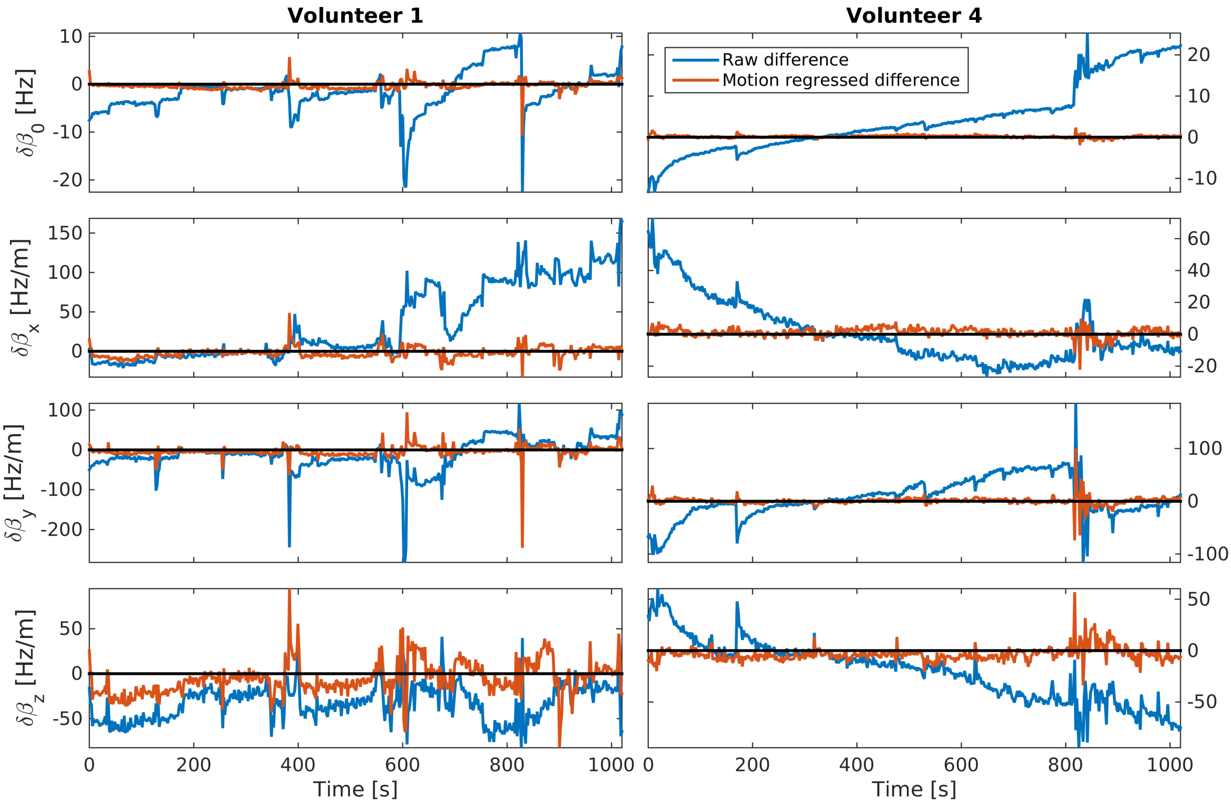

Figure 3.10 – Difference between the dual-echo and first echo field coefficient estimates. The scans shown are those where the volunteers moved the most (both during the natural breathing scan). Both the raw difference and the first-order motion-regressed difference are shown. The horizontal black lines represent the constant zero value.

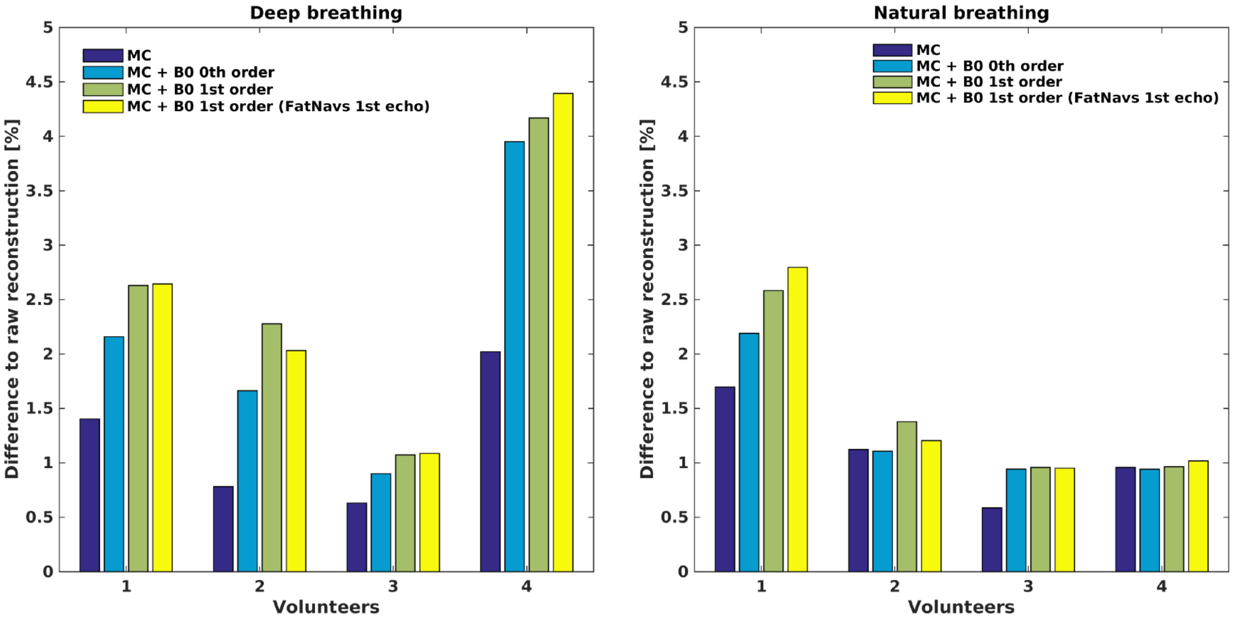

Figure 3.11 – Bar plots showing the relative reduction of image gradient entropy between the raw images and the different corrected images for both deep breathing and natural breathing scans.

# Discussion

## Determining the accuracy of field monitoring

We have developed a new method to study the robustness of estimates of linear field variations. High quality quantification of first-order dynamic field variation was achieved by the dual-echo field estimates. The associated variabilities (RMSE) were significantly lower than the typical range of variation observed due to breathing. The spatial distribution of the field variations due to breathing was also directly observed in the fat layer and agrees well with previous literature with measurements from the brain [85].

In the direct volunteer comparison (Figure 3.4), one of the estimates falls outside one standard deviation of the known value in the x direction. Despite this residual bias, correction using these estimates is expected to be better than no correction at all – and this minor overestimation (in one subject by up to ∼15%) is not expected to appreciably affect the level of correction achievable, especially as this was only observed for a gradient in the x direction where the effect due to breathing is the lowest.

The advantage of alternating reference and offset volumes is that residual motion-induced phase variation is greatly reduced. Indeed, a phase difference of two volume-trains, one of reference volumes and one with field offset volumes, would be strongly influenced by any motion occurring during the acquisition. Only fast and large motion would influence (and artificially diminish) the estimated precision of the DLID method for a given gradient offset. For all volunteers in this study, we could always find a subset of 36 consecutive volume pairs for which no such larger motion took place. Another possibility for estimating the accuracy of the method independently from the physiological phase variations could have been to perform the experiment with breath-holding. However, due to the practical problems of breath-holding, such as good and constant subject cooperation, as well as decreased subject comfort, we think the DLID method, which gave reliable results during free breathing, is a good choice. The remaining limitations of the DLID method imply that the precision estimated in this experiment should be understood as an upper bound for the true precision of the parameter estimation, as DLID is expected to overestimate the true value. This experiment shows that double-echo FatNavs are well suited for accurate, fast low-order dynamic field tracking.

First-echo based field estimates suffer greatly from the associated loss of SNR compared to dual-echo estimates due to the shorter phase evolution period. The accuracy is reduced by a factor of approximately 1.5 to 2. While having a longer echo time would allow for better accuracy, it may be more sensible to acquire several echoes due to the short readout acquisition time.

## High resolution $T_2^*$ scans

In the deep and slow breathing experiments, image quality was always greatly improved by incorporating correction for the temporal variation of the magnetic field. Furthermore, the first order correction demonstrated additional improvement in the reconstruction quality over the zeroth-order correction, demonstrating the utility of accounting for the spatial dependence of temporal field variation at ultra-high field. This dependence is not necessarily restricted to the z direction and hence a true 3D quantification can be necessary. This is achieved by the dual-echo FatNavs but not previous navigator methods at 7T, which typically only focus on the z direction or use approximations to recover some spatial information from projections [94]. These methods also typically neglected motion entirely.

The high quality of the reconstructed images suggests that the motion and field parameters were well captured by the FatNavs. Clear impact of motion on the estimated field coefficients can also

be seen, but the degree to which these are due to a true physical effect, such as magnetic susceptibility distribution change, or due to methodology errors cannot easily be estimated from this data. The consistent observation that the inclusion of each additional set of corrective parameters in Figure 3.5 leads to additional improvements in image quality implies that the observed interdependence of motion and field parameters is likely to have a true physical origin rather than being due to erroneous or incomplete modelling.
In the natural breathing case, the benefits of $B_0$ correction are marginal, and a clear difference between zeroth and first order corrections could only be observed in one subject. While areas of more homogenous contrast in the same tissue after field correction can be found, it is doubtful that these differences would be worth the additional scan-time inherent to the second-echo of the FatNavs. However, previously published results are unclear about the percentage of 3D GRE scans which would show natural breathing artefacts. Breathing itself is very person-specific. Also, the impact of thoracic breathing on the field variation spatial distribution is expected to be different than that of diaphragmatic breathing, due to different air distribution changes [95]. All-in-all, almost all regimes (breathing type, depth and frequency) could certainly be found within the normal range of 'natural breathing' by some individuals. Specific populations can also be more prone to exhibit significant field change, such as Alzheimer's patients [97]. This makes reaching a definitive claim on the usefulness of correcting for breathing-induced field variation very challenging. The method proposed here is shown to make a clear improvement in image quality for a specific sequence and in subjects with a specific breathing profile. Longer echo times would also make the artefact worse for the same breathing pattern. All these considerations necessarily mean that the presented results of double-echo FatNavs inclusion in high-resolution 3D GRE are very much exploratory, but it also shows their usefulness in extreme cases.
It might be expected that the field in the fat layer could be more sensitive to motion than at the center the brain. The fat signal is very close to the large magnetic susceptibility change of the air-tissue boundary and this could lead to local changes in the field in the vicinity of the fat layer that are not reflective of the changes occurring in the center of the brain. This in turn would imply an overestimation of the field change given by the FatNavs compared to the true change in the brain. We observed a good correspondence in this study between the measured field changes and the subsequent improvements in image-quality when these estimates were used for correction, suggesting that over-estimation of motion-induced field changes in the fat layer was not a major problem in this study. We expect that discrepancies between field changes measured at the fat layer and real field changes in the brain could explain some of the residual artifacts present in the corrected images.
The GRE protocol used in this experiment was made ∼40% longer due to the addition of the dual-echo FatNavs. Using only the first echo of the FatNavs for first-order field change correction appears to perform as well as the dual-echo derived correction when assessing the overall final image quality, but would greatly reduce the additional scan-time inherent to the navigators. Each FatNav would be 324 ms shorter, reducing the additional scan-time to ∼18% of the original GRE protocol duration.

The difference between dual-echo and single echo field estimates is strongly correlated to the motion parameters. This likely arises from the fact that the dual-echo estimates remove the phase change under motion of the receive coil sensitivities, whereas the single echo estimates do not (see Appendix 1). This also means that the field change correction terms are *a priori* highly biased by motion because of the short FatNavs echo time, and we are currently investigating the reasons why this bias does not seem to produce additional artifacts in the reconstructions. In this study we found that quantifying image quality was very difficult – and although the reconstructed images corrected using single or dual-echo field estimates are measurably *different*, it is not clear which

image is *better*. Unlike standard point-wise based image difference metrics which would be sensitive to image shifts, gradient image entropy shows the consistent trend that the image quality continues to increase as more correction parameters are used. However, it is insufficient to help us understand which of the dual-echo or first echo based correction is best. Future work will investigate whether a metric can be found that allows a more accurate reflection of the final image quality.
The most direct way to increase the temporal resolution of the FatNavs is to segment the host sequence acquisition and acquire a FatNav between each segment. Single-echo FatNavs in a 2-segment host sequence would be a way to double the FatNavs temporal resolution, while keeping the total scan-time equivalent to the one presented in this study. Previous conclusions suggest that the correction quality would be at least as good as the one presented here. Alternatives which do not add any additional scan-time, such as combination of FID navigators (one per host sequence shot) and FatNavs are also currently being explored, but go beyond the scope of this paper. The field change quantification method presented here can also be directly used for fitting coefficients of higher order than only the first-order terms. The restriction to the first spatial order was chosen solely because it allows for a much more time-efficient retrospective correction, as the linear terms correspond to simple shifts of k-space points. Inclusion of higher-order terms would require the use of more computationally intensive iterative reconstruction techniques [98]. However, it is likely to remain difficult to assess whether the increased computational burden is justified without a reliable corresponding metric for image quality.

# Conclusions

This work shows that extending the previously proposed 3D FatNavs to a double-echo version allows to capture magnetic field temporal variations with excellent precision. Both motion and field variations (up to first order spatially) can be included in a retrospective correction of the full 3D k-space. For strong artifacts caused by heavy breathing this correction can provide substantial enhancement to the final image quality. Single echo estimates based corrections showed comparable results, and hence should allow a significant reduction of the additional scan-time due to the FatNavs second echo. The temporal sampling of the FatNavs in the current implementation is on the limit of critical sampling for normal healthy breathing rates. Future work will investigate approaches to increase the temporal resolution of the FatNavs, without sacrificing spatial resolution and fidelity, to be applicable to more general breathing patterns.

**Acknowledgments**
This work was supported by Centre d'Imagerie BioMédicale (CIBM) of the UNIL, UNIGE, HUG, CHUV, EPFL and the Leenaards and Jeantet Foundations, as well as the Swiss National Foundation through Grant 205321_153564.

# Appendix 1 – Estimation of change in coil phase due to subject motion

We can estimate the local change in coil phase at a particular position within the head, $\delta\varphi_c$, for some moderate motion $\delta x$ as $\delta\varphi_c = \frac{2\pi}{L}\delta x$ where $L$ is the distance over which the phase changes by one full cycle. As a first approximation, we can use the RF wavelength $\lambda$ as an estimate of $L$. The receive phase variation can be considered negligible when the $\Delta B_0$ term in (3.1.4) dominates, which can be formulated as when $2\pi\Delta B_0 T_E \gg \delta\varphi_c$ , which corresponds to the condition $\Delta B_0 T_E \lambda \gg \delta x$.

Assuming a typical value for $\Delta B_0$ (1 Hz) and 20cm for $\lambda$, leads to

$$\delta x\,[mm] \ll 0.2 \times T_E[ms].$$

This shows that, for long echo time, such as the ∼25 ms $T_E$ used in the host sequence, the $\delta\varphi_c$ term is negligible for motion up to around 5 mm (and indeed it was neglected in (3.1.1)).
However, in the case of large motion and short echo-times, the estimates given by (3.1.5) are expected to contain significant bias – which can be exacerbated by the short echo-times used for the FatNav. A single-echo FatNav might therefore falsely attribute a fraction of the measured phase changes to being due to changes in $B_0$ – as it will also be sensitive to $\delta\varphi_c$. This is why in this study we compared the estimated correction terms from the first-echo of the FatNav against those from dual-echo – as well as comparing the effect this has on the corrected images themselves – to test whether a single-echo FatNav would be sufficient for the chosen sequence parameters.

`Post-print ends here`

To summarize, this work showed that FatNavs can track first-order field fluctuation with good precision and allow for the associated retrospective correction, especially so for deep-breathing scans, i.e. when breathing is properly sampled. The application of FatNavs to fluctuation correction in natural breathing cases is explored further in §6.2.1 in conjunction with FID navigators.

# Chapter 4

# EPI-like FatNavs

In order to be efficient, a navigator should have as short as possible duration for a desired motion estimates accuracy. This chapter presents an upgraded version of the 3D FatNavs acquiring several **k**−space lines after each excitation pulse, in the same spirit as EPI acquisitions. It allows for more modularity, such as the possibility to run on lesser performance gradient inserts, at lower field strength than 7T or when included in more restrictive imaging protocols.

As a summary of this chapter, EPI-like FatNavs showed equivalent motion correction capacity than the original FatNavs implementation but with half the acquisition time. Therefore, they can be inserted into a much broader range of imaging protocols and hardware systems, thereby opening the way to more potential FatNavs applications.

## 4.1 Definition, acquisition and corrections

The idea is to acquire several lines of the navigator 3D **k**−space per $T_R$, thereby reducing the loss of time needed by the preparation module, that is by the RF excitation and phase and slice encoding gradients. Figure 4.1 shows this logic with six lines acquired per kernel.

A blip gradient is added on one of the non-readout encoding directions between each readout gradient acquisition. This creates the jump in **k**−space.

This strategy, with $n$ lines acquired by kernel, leads to volume acquisition duration $T$ given by

$$T(n) = \frac{N}{n} * \big(T_p + nT_{RO} + (n-1)T_b + T_s\big) \qquad (4.1.1)$$

where $N$ is the number of kernels needed to acquired an equivalent one readout-per-kernel FatNavs, $T_p$ is excitation and encoding duration, $T_s$ is the rephasing and spoiling duration, $T_{RO}$ the readout duration and $T_b$ the blip duration. Clearly, this implies a strong diminishing return, as the reduction of acquisition time becomes hyperbolically smaller as $n$ increases.

The implementation of this version of the navigator was entirely custom coded into the Siemens IDEA software suite. While monopolar readout gradients were also available, they did not provide clear benefits on the navigator image quality. They also reduced the gained efficiency due as they had to include a rewinder gradient in the readout direction between samplings. Therefore the associated results will not be discussed further.

The chosen encoding order, (i.e. the blip gradient moment) was such that **k**−space was segmented as shown in Figure 4.2. This allows undesired, but systematic, effects to be smoothly distributed, and hence to create less severe artefacts. These effects will now discussed in more details, as well as how to try to correct for them.

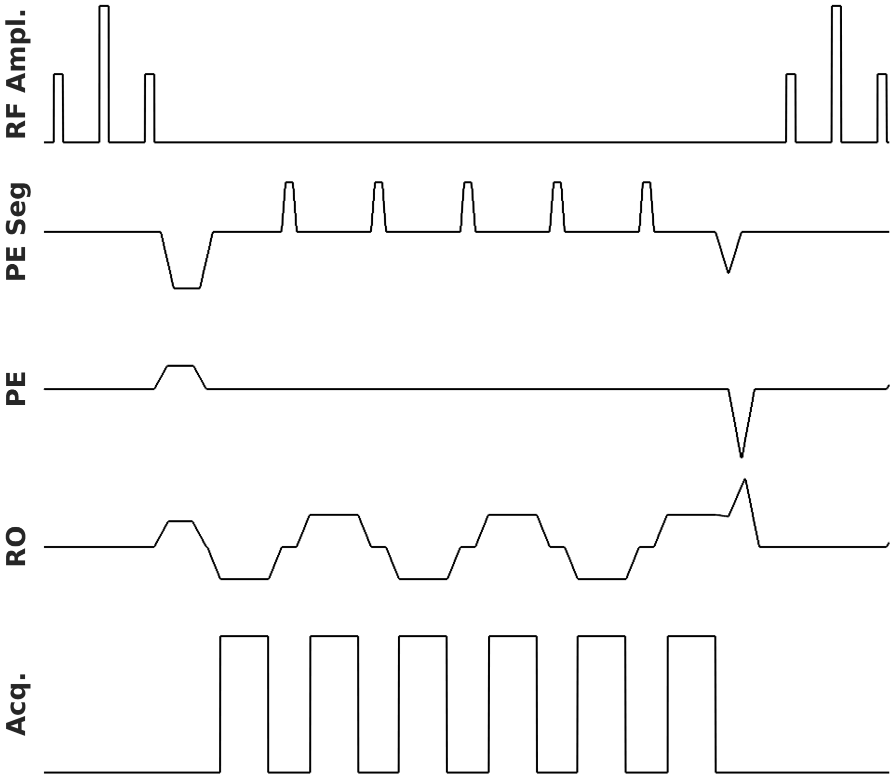
RF Ampl.
PE Seg
PE
RO
Acq.

Figure 4.1 – Kernel for the multiple-readout per $T_R$ FatNavs. This example shows six bipolar readouts.

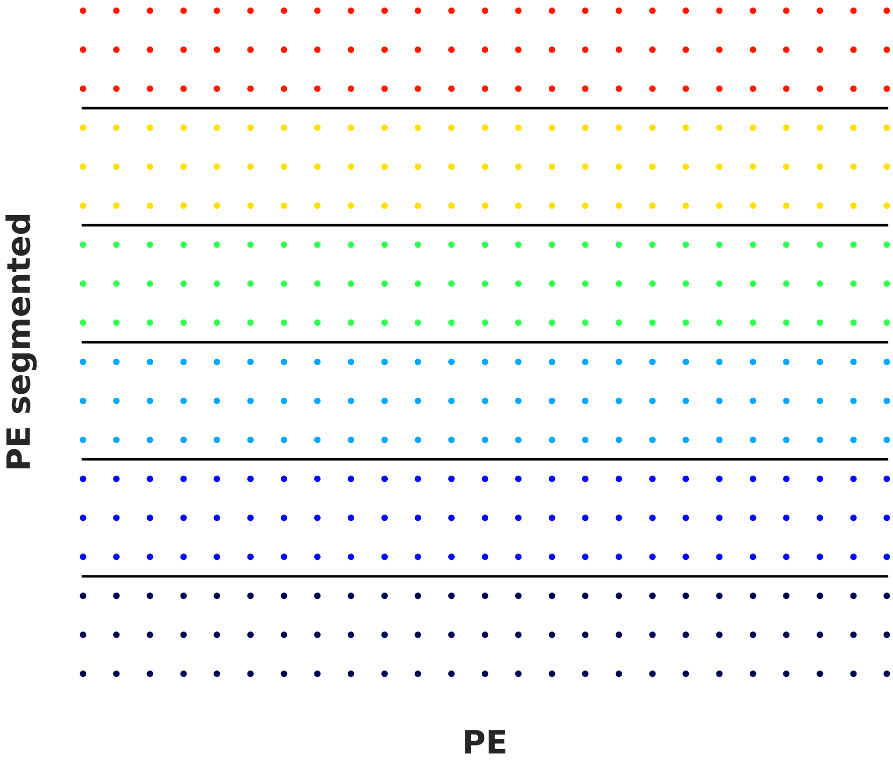
PE segmented
PE

Figure 4.2 – $\mathbf{k}-$space acquisition order for $n = 6$. The blip gradient is played on the segmented direction, and each color is associated to one of the readouts during the kernel.

### 4.1.1 Calibration and correction

Non-identical effects between the successive readouts include $T_2^*$ relaxation, gradient delay and phase drifts due to frequency offset. The chosen ordering allows to cope with signal magnitude decay, as pictured in an exaggerated way in Figure 4.3. This ordering only leads to slight smoothing compared to single-readout acquisition, whereas a consecutive (i.e. classical 3D Cartesian trajectory) would create significant aliasing as shown by the secondary peaks of the point-spread function.

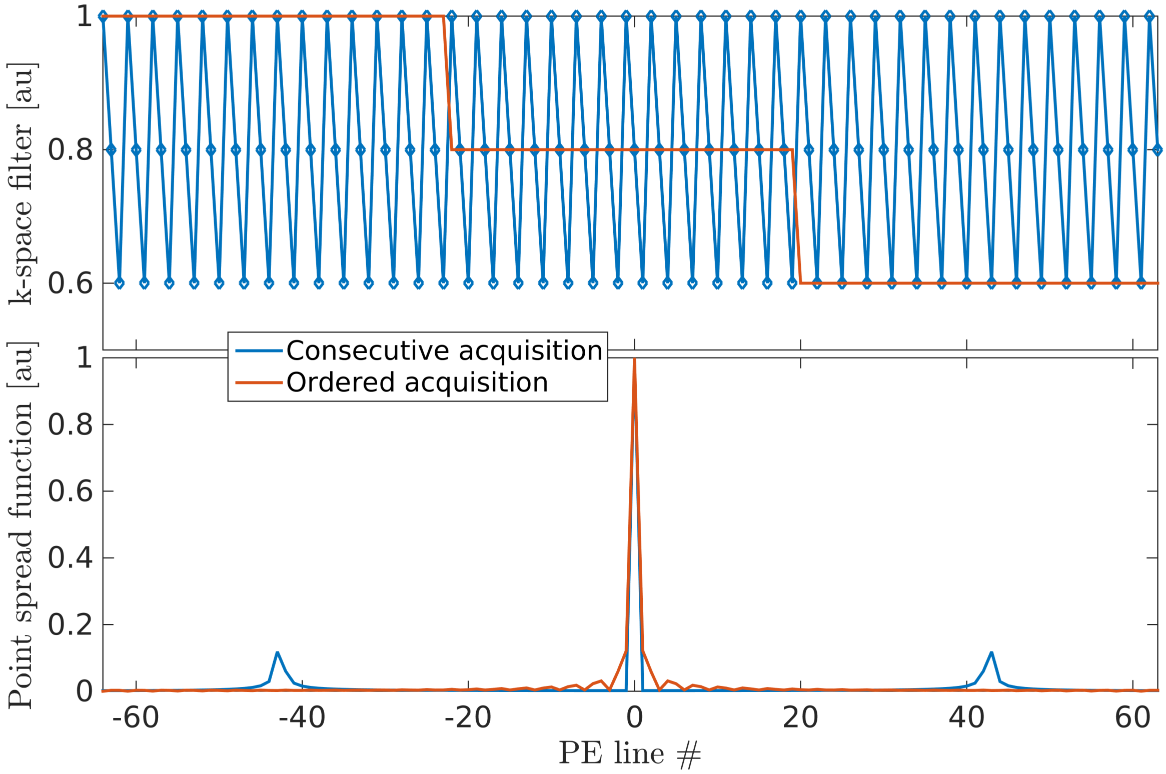

Figure 4.3 – Simulation of the alteration of the point-spread function due to signal relaxation for the standard consecutive ordering and the one used by the EPI-like FatNavs.

While $T_2^*$ decay was not corrected for any further, correcting for the frequency offset and gradient time delays was paramount, as demonstrated in Figure 4.4. This was done by acquiring a so called calibration scan at the beginning of the sequence. This prescan amounts to play the same kernel repetitively, with the phase, slice and blip gradients turned off. Therefore only the central readout $\mathbf{k}-$space line is sampled. The idea is to estimate the erroneous phase factors, caused by a global signal frequency offset compared to signal demodulation frequency, and phase ramps in image space associated to the $\mathbf{k}-$space shifts caused by uncontrolled gradient time delays.
The best corrections were obtained by applying the following procedure to the calibration data.

1. Choose the reference line index ( between 1 and $n$) as the one which will pass by the $\mathbf{k}-$space center during a navigator acquisition. This defines the reference readout signal.

2. Pick the next line and find the phase ramps which minimize the error to the reference signal after Fourier transformation. This phase ramp defines the time delay correction.

3. Apply the time delay correction to the calibration data. Because the readout gradients are the same but of reversed polarity, the gradient delay is systematic across readouts and the

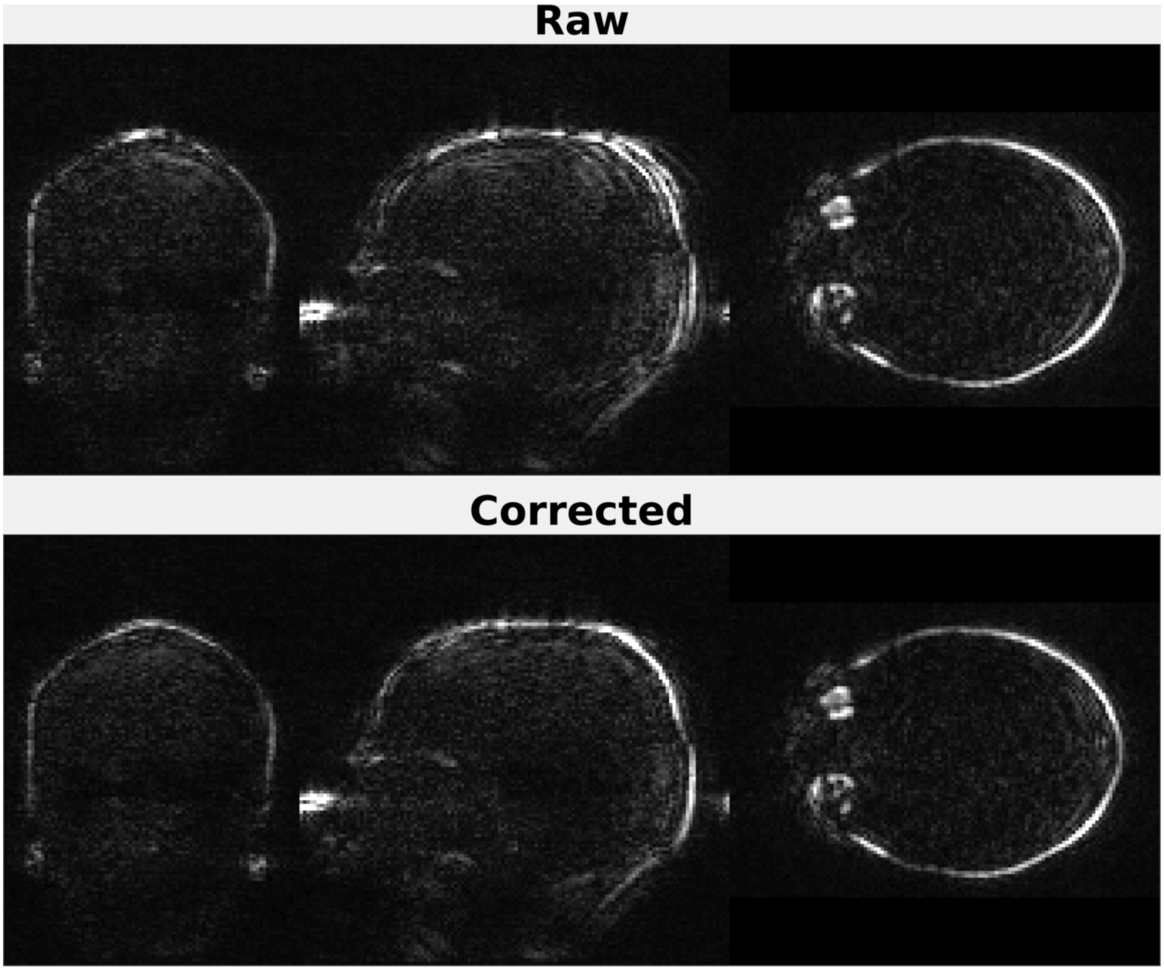

Figure 4.4 – Raw and corrected reconstructions for a five readouts-per-kernel acquisition

associated correction is only applied to readouts of opposite polarities compared to the reference readout.

4. Find the $n-1$ phase factors which minimize the error between the delay corrected calibration data and the delay corrected reference line.

The error metric used was the standard $L_2$ norm for both parameter estimation. The final parameters values were found by direct grid search. The number of calibration kernels should be such to establish steady state and have sufficient SNR to estimate the correction parameters. In practice we found that 200 such kernels were amply sufficient.
Examples of obtained phase values are shown in Figure 4.5a. The correction follows a linear trend, with the same slope for both polarity readout gradients. This is as expected as the phase $\delta_\varphi$ should follow the usual relationship

$$\delta_\varphi(T_E) = fT_E \tag{4.1.2}$$

with $f$ the frequency offset. Estimated delay are shown in Figure 4.5b. The order magnitude matches previously reported values [99]. It is to be noted that in both parameters figures, the low $n$ regime is different than the high $n$ regime. This is certainly due to unequal eddy currents for the first few readouts. This difference occurs because of the initial readout dephasing gradient, which is played only at the beginning of the kernel. Therefore, the higher the value of $n$, the more similar the state of the system for latter acquisitions. This difference, especially in magnitude, for the first two readouts signals was visually directly observed.

Geometrical distortion can be observed despite the proposed correction. This is because of the very large field of view acquired ($\sim 25$ cm in the head-foot direction), making a zeroth order frequency correction insufficient for correcting small spatial $B_0$ inhomogeneity. The distortion gets worse as $n$ increases, which is expected. The use of a 3D $B_0$ map might help to further reduce these distortions, but also introducing such information in an GRAPPA-based reconstruction framework is very challenging. Keeping the diminishing return of large $n$ values in mind, such involved reconstructions were not attempted as they seemed unnecessary.

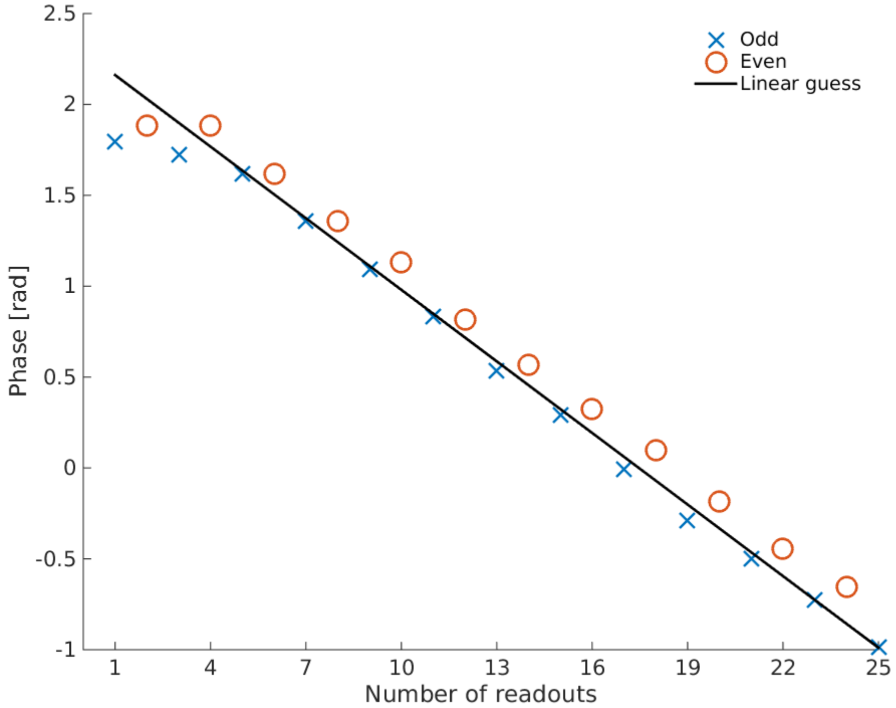

(a) Estimated phase values for frequency offset correction of EPI-like FatNavs, with $n = 25$. The black line represents the linear extrapolation of the last two odd readouts.

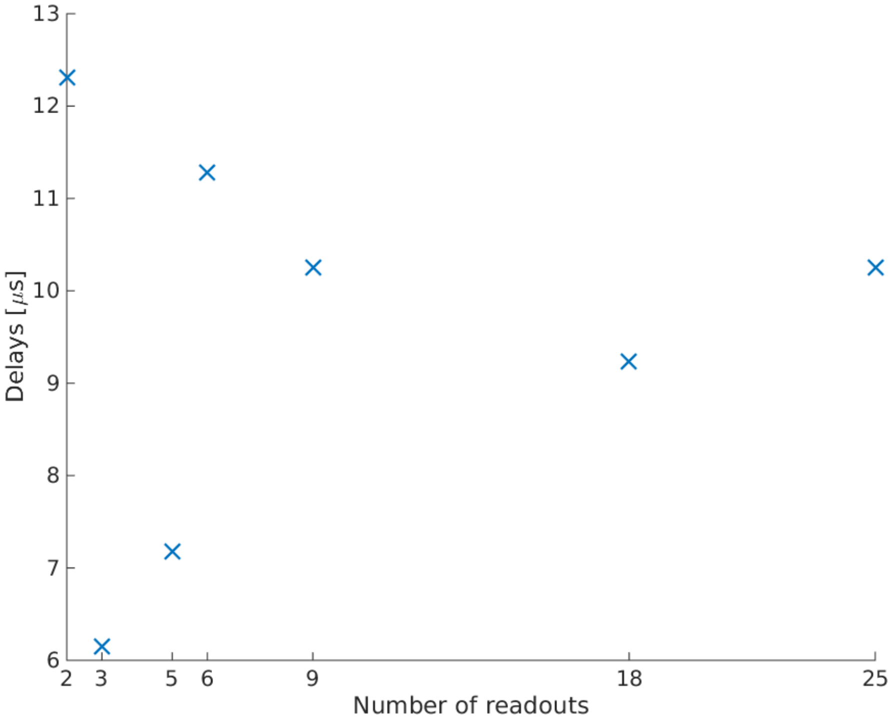

(b) Estimated gradient time delays for EPI-like FatNavs correction.

Figure 4.5 – Examples of the EPI-like FatNavs correction parameters found by the proposed method.

## 4.2 Comparison to standard FatNavs

The motion tracking accuracy of EPI-like FatNavs was estimated on one healthy subject, who was asked to reproduce a deliberate motion pattern for several scans. Each scan was an interleaved acquisition of standard and EPI-like FatNavs, to a total of 70 volumes each. The chosen motion was step-like, i.e. regular pose changes with rest period between changes. Each scan used a different number of readouts (noted $n$) for the EPI-like FatNavs. The FatNav parameters were based on a protocol previously shown to be efficient for motion correction [48]. These were 2mm isotropic resolution with $\frac{3}{4}$ partial Fourier in both phase-encoding directions and $4 \times 4$ undersampling. The flip-angle was 15°. The echo-time of the first readout was always 1.3 ms. The volumes acquisition times are summarized in Table 4.1.

| $n$ | 1 | 2 | 3 | 5 | 6 | 9 | 18 | 25 |
|---|---|---|---|---|---|---|---|---|
| **Volume TR [ms]** | 1382 | 884 | 737 | 611 | 575 | 520 | 454 | 440 |

Table 4.1 – Acquisition times of 2mm EPI-like FatNavs protocols on the 7T CIBM scanner.

The comparsion was done as follows: both types of navigators were separately co-registered. The motion parameters from the standard FatNavs were linearly interpolated to the measurement times of the EPI-like FatNavs before computing the RMSE between the two estimates. This RMSE is interpreted as an indicator of the precision of the EPI-like FatNavs.

Examples of the navigators reconstructions are found in Figure 4.6. Clear lack of fidelity arises above $n \approx 9$. The excitation pulse was centered at -3.3 ppm, making the poor shimming quite noticeable in this experiment, as residual water signal can be observed. Latter experiments and applications of the EPI-like FatNavs use a -7 ppm centered pulse, creating exquisite fat selectivity at the price of lower effective flip-angle for the same RF power. Motion parameters from one scan are graphed in Figure 4.7, where excellent visual agreement is found between both navigator versions. The obtained RMSE for all scans are presented in Figure 4.8.

As expected, the RMSE follows the same trend as the loss of image quality at high $n$ values. However, they are fairly stable up to $n \lesssim 6$. Keeping in mind the diminishing returns in terms of acquisition time, these results motivated EPI-like FatNavs to motion correct an MP2RAGE protocol.

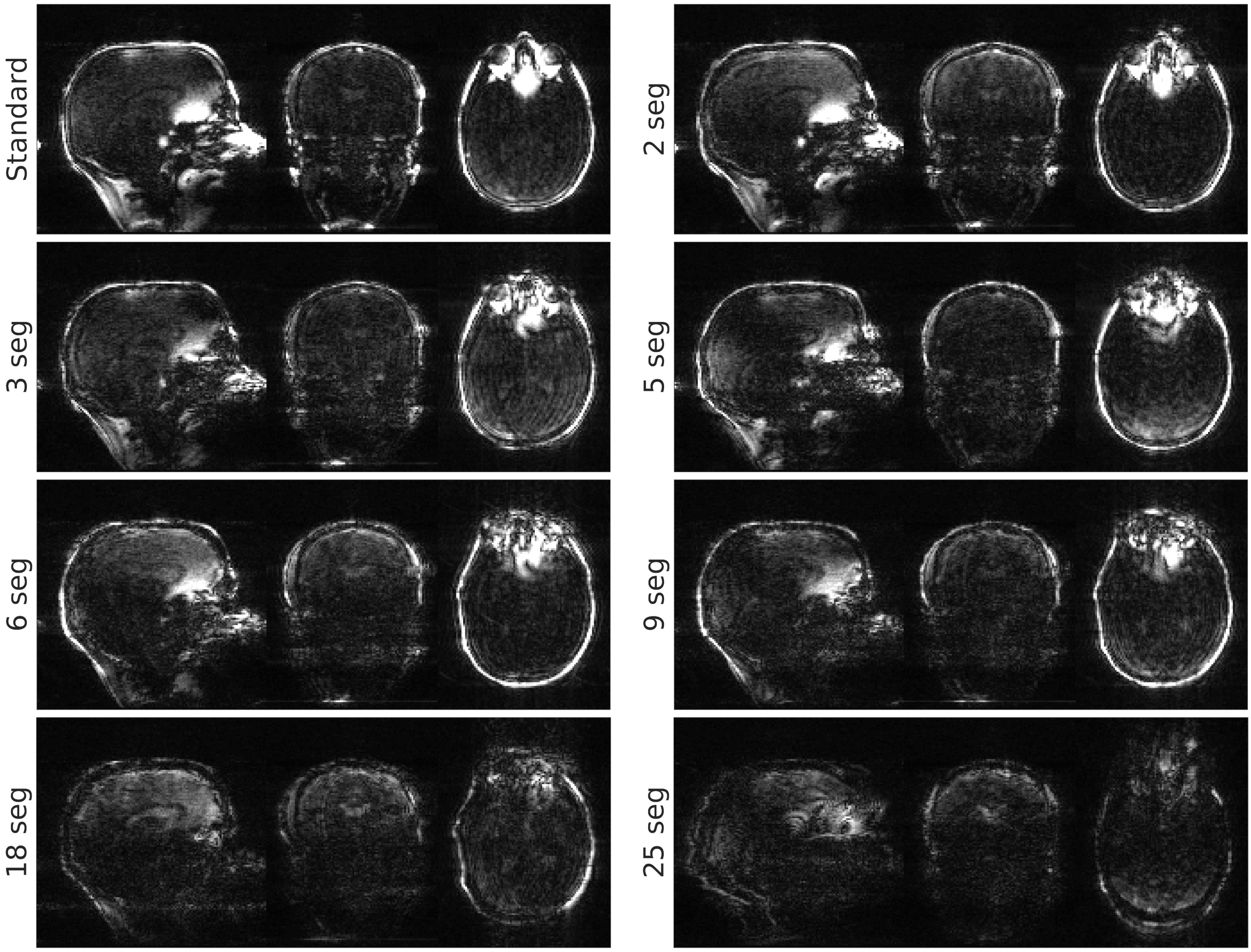
Standard
2 seg
3 seg
5 seg
6 seg
9 seg
18 seg
25 seg

Figure 4.6 – Corrected reconstructions of 2mm EPI-like FatNavs for different numbers of readout-per-kernel.

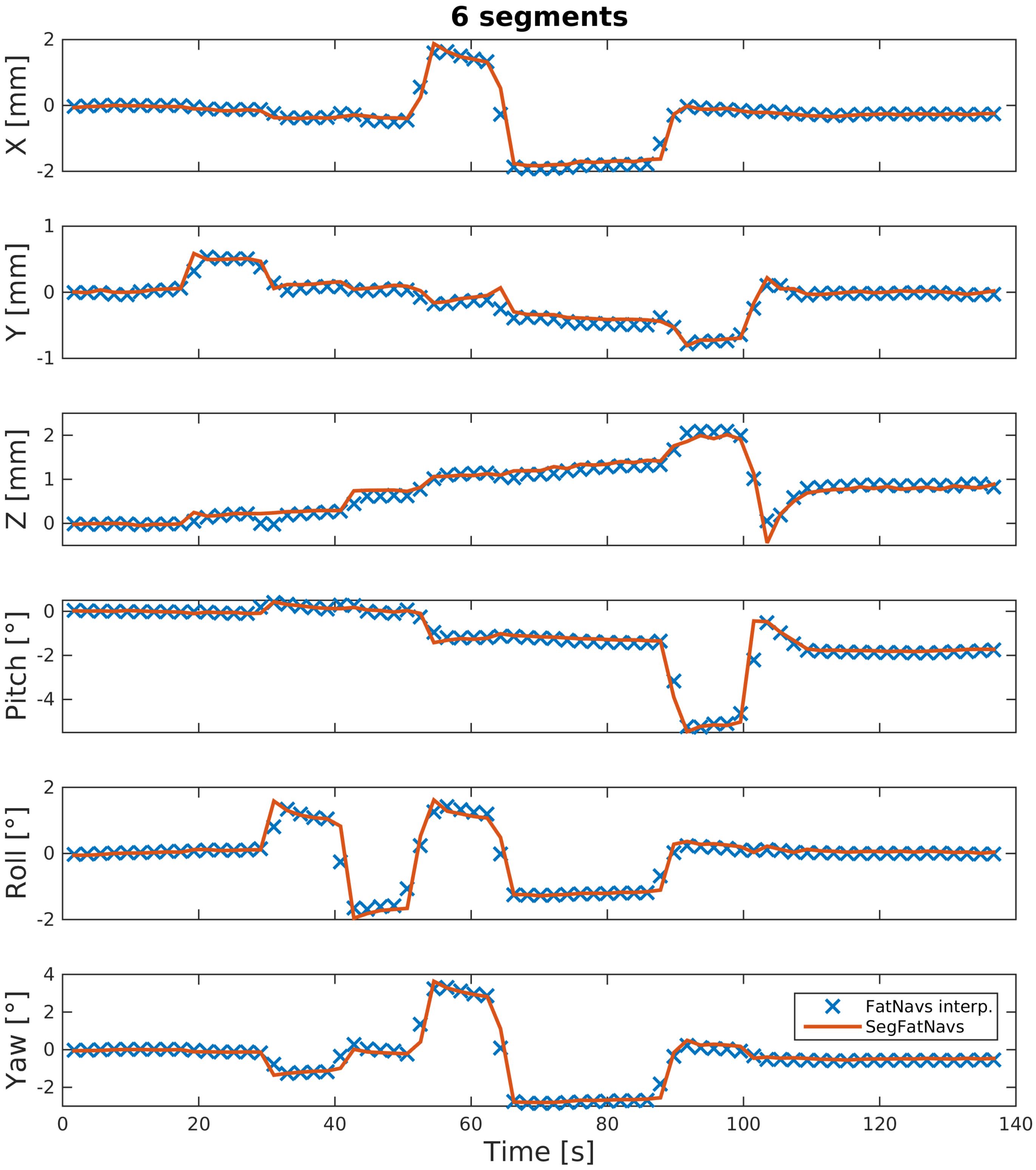

Figure 4.7 – Example of $n = 6$ EPI-like FatNavs motion parameters time-courses comparison to the equivalent standard FatNavs.

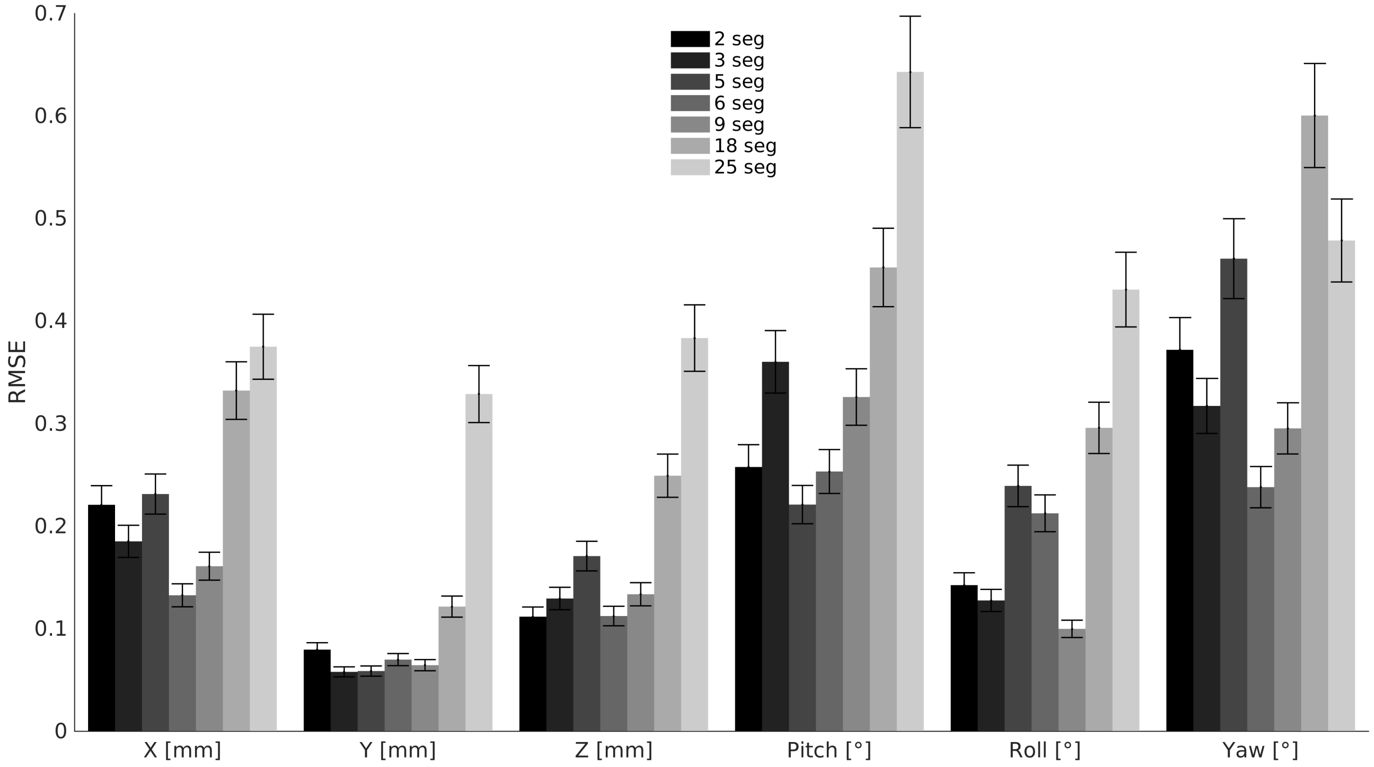

Figure 4.8 – RMSE of the direct comparison experiment of 2mm FatNavs to 2mm EPI-like FatNavs.

## 4.3 Applications and proof of concept

While the flip angle used in the direct comparison experiment was high, it could be much reduced (to 3°) without major impact on the navigator images. The reason why this inclusion is interesting is because it allows more flexibility. For example, it becomes feasible for the hardware to acquire higher-resolution FatNavs without changing the host imaging sequence parameters. Along with the decreased acquisition time, another advantage can be the reduction of induced magnetization transfer induced by the navigator acquisition. More generally, but untested, it also becomes easier to acquire FatNavs on lesser performance gradient inserts, as well as at lower field such as 3T, where a -7 ppm binomial pulse is over 1 ms long.

The direct comparison results have as a natural next step to try and use EPI-like FatNavs to motion correct an MP2RAGE protocol. The imaging resolution was 0.6 mm isotropic. Figure 4.9 is an example of the motion correction achieved by the EPI-like FatNavs (2 mm, $n = 5$). The associated motion parameters are shown in Figure 4.10. Clearly, the brain structures are more sharply delineated in the corrected version, which shows much reduced ringing and blurring artefacts.

Making full use of the shorter navigator duration, 1.5mm EPI-like FatNavs with $n = 4$ were acquired during a 0.6mm isotropic MP2RAGE scan, examples of which can be found in Figure 4.11. In all acquired datasets, retrospective motion-correction using 1.5mm FatNavs was equivalent to the correction based on 2mm downsampled navigators. It is possible that, for that imaging resolution (0.6mm), the accuracy of the 2mm FatNavs is such that the resolution gain of the 1.5mm navigators does not provide significant image enhancement.

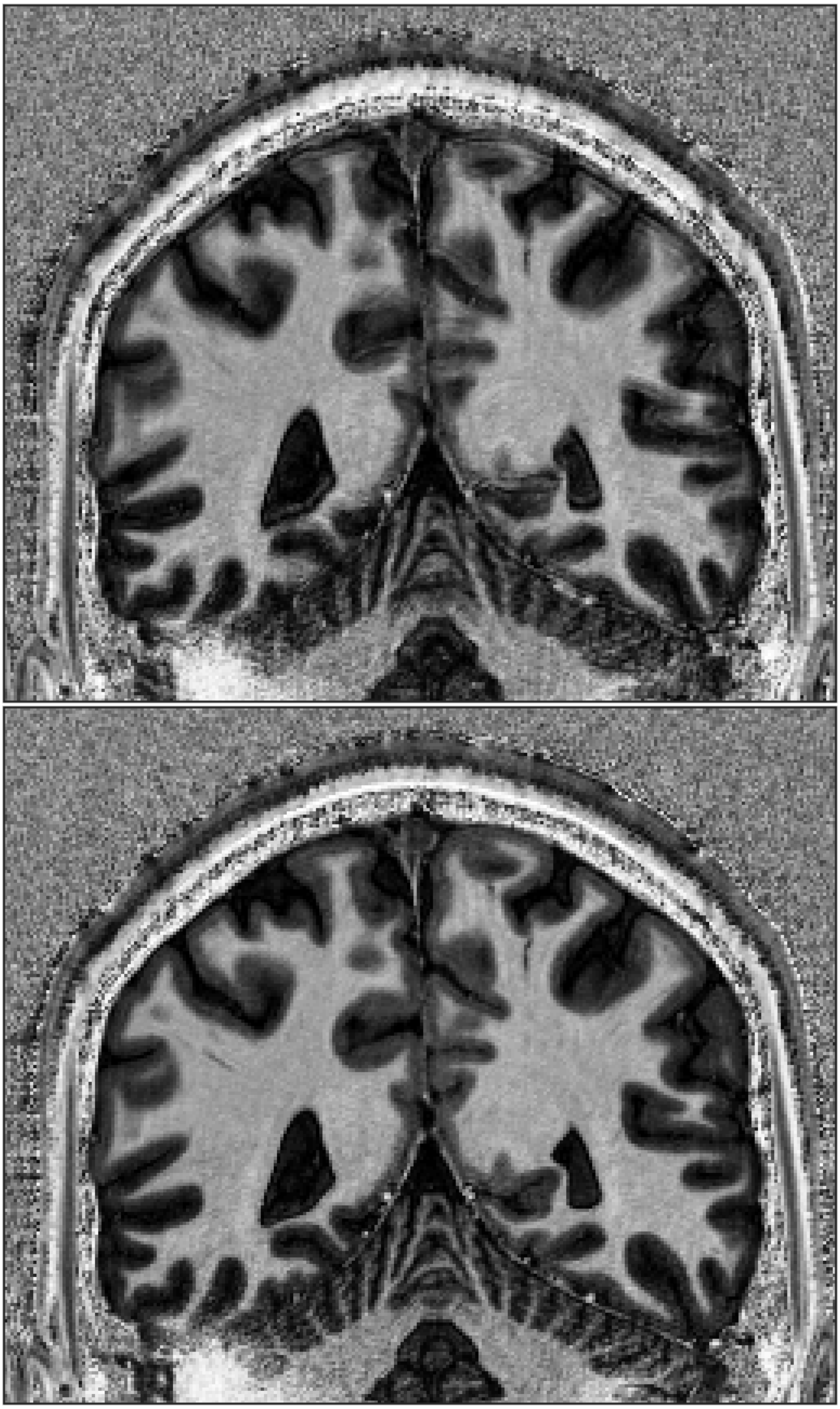

Figure 4.9 – Top: raw reconstruction. Bottom: motion correction using 2 mm EPI-like FatNavs ($n = 5$).

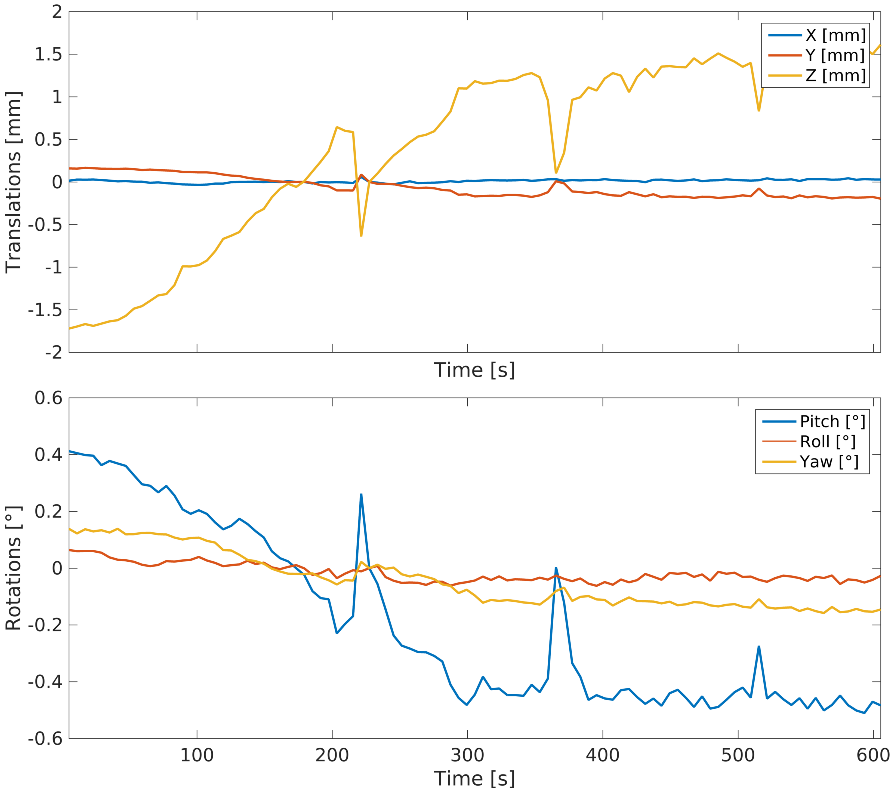

Figure 4.10 – Motion parameters estimated from 2mm EPI-like FatNavs with $n = 5$. Retrospective correction based on these motion parameters is shown in Figure 4.9.

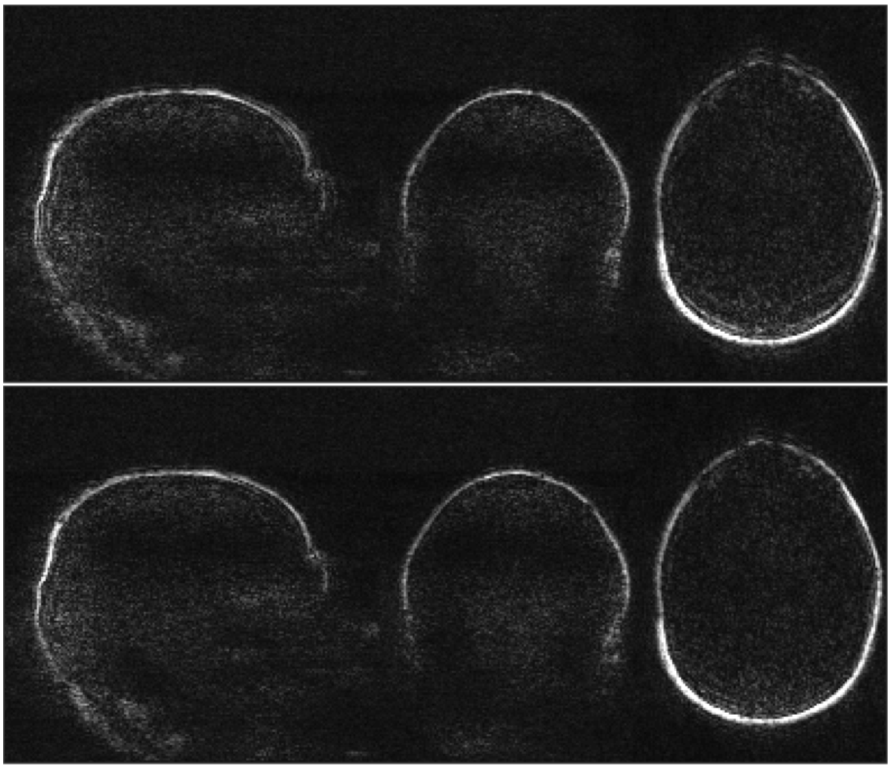

Figure 4.11 – EPI-like 1.5mm FatNavs reconstruction with $n = 4$. Top: uncorrected. Bottom: corrected.

# Chapter 5

# Segmented FatNavs

The idea behind segmented FatNavs (SegFatNavs) is to incorporate FatNavs into imaging sequences which lack dead-time long enough to acquire block FatNavs. The proposed approach focuses on GRE based sequences which represent a considerable proportion of short dead-time imaging sequences. First the general definition of the SegFatNavs, their limitations and processing is introduced. Then, SegFatNavs application to angiography for motion correction is demonstrated. They are shown to correct even for sub-millimeter unintentional motion of high-resolution images. A proof of concept experiment at 3T also proves the validity of the method at clinical field strength. Also the fat-selective excitation pulse MT effects can be exploited to further enhance the vessels-to-tissue contrast.

## 5.1 Segmented FatNavs

### 5.1.1 Definition

The acquisition strategy exploits the relatively short $T_r$ (~3-4 ms) of the FatNav kernels, and inserts said kernel into the available dead-time of the host imaging sequence. Gradient echo (GRE) is the basic block of many important imaging protocols, and finds many applications at ultra-high field, including susceptibility weighted imaging [100], quantitative susceptibility mapping and time-of-flight angiography [75]. The inclusion of segmented Fatnavs into a 3D GRE is depicted in Figure 5.1, where nSegments is the number of navigator readouts acquired after each imaging kernel acquisition.

This approach is by design restricted to low values of nSegments, as otherwise the effective repetition time between the imaging GRE kernels becomes much longer than the value of the navigator-free protocol. The temporal resolution of the FatNavs is defined as the time during which

```
Run FatNavs GRAPPA calibration scan
For iPhaseEncode from 1 to nPhaseEncode
  For iSliceEncode from 1 to nSliceEncode
      Run imaging GRE kernel (iPhaseEncode,iSliceEncode)
      For iSegment from 1 to nSegments
        Run FatNavs kernel
```

Figure 5.1 – Ascending cartesian GRE imaging acquisition scheme with included SegFatNavs. An extra loop over slabs can be easily added above the iPhaseEncode one for multi-slabs imaging protocols.

a full navigator $\mathbf{k}-$space is measured. As discussed previously, the low number of segments imply that the typical temporal resolution is between 2 and 3 seconds for 4 mm, single echo FatNavs. This implementation is thereby limited to capture low temporal resolution motion patterns if one tries to keep the potential additional scan-time to a minimum.

### 5.1.2 Implementation details

Some technical implementation details will be now be detailed. In the case nSegments $> 1$, the FatNavs $\mathbf{k}-$space must be acquired in a reordered fashion, exactly as EPI-like FatNavs described in §4. Indeed, the imaging sequence kernel having a typically longer duration than the FatNavs kernel, the fat magnetization is not equal between readouts if several are acquired in a row. Rather, different steady states are reached for all values of iSegment. This in turn implies an amplitude modulation on the measured navigator signal and hence the $\mathbf{k}-$space acquisition ordering has to be segmented.

In practice, the segmented direction is either the phase or the slice direction of the navigator. After the navigator parameters are fixed, the navigator $\mathbf{k}-$space has effective size $N_p$ and $N_s$ in these directions respectively. These sizes include partial Fourier and under-sampling, so that the number of FatNavs kernel needed to measure one 3D volume is $N_pN_s$. The algorithm to chose the segmented direction is as follows.

- If both directions can be split into nSegments, then the direction which has the largest size is chosen as the segmented one.
- If only one can be split, then it is chosen.
- If neither can be split, then this value of nSegments is considered invalid, and the sequence cannot be run on the scanner.

The last condition can seem restrictive, but in practice is not very relevant. Indeed using a low number of segments (nSegments $\leq 3$) accounts for most FatNav protocols. The navigator parameters, especially the FOV, can also be tuned slightly in order to be “segmentable”. Finally, it could be possible to cope with such parameters by introducing dummy kernels, i.e. without signal acquisition. It was however not worthwhile to be able to account for such cases when coding the sequence, as the gain was minimal for potential practical applications.

Extension of the FatNavs kernel to an EPI-like FatNavs kernel for SegFatNavs can be done, but requires nSegments $= 1$, as otherwise relaxation effects both during the EPI readouts and between the navigator kernel calls would combine and induce non-smooth signal amplitude modulation across $\mathbf{k}-$space. This is certainly more time efficient than separate, single readout kernels, but does not allow dual-echo FatNavs to track $B_0$ fluctuation for example.

### 5.1.3 Acquisition ordering schemes

Now the host imaging sequence $\mathbf{k}-$space sampling scheme shall be discussed. Figure 5.1 assumes an ascending $\mathbf{k}-$space acquisition ordering. Also commonly used are elliptical centric acquisitions (called centric from here on), which measure the region closest to the $\mathbf{k}-$space center in a square spiral trajectory, sampled on the standard Cartesian grid. It was shown to further enhance venous suppression in acquisitions using contrast agents [101]. Furthermore it may potentially reduce the large-scale impact of bulk motion as the center of $\mathbf{k}-$space is more likely to be sampled during identical subject position. When coupled with partial Fourier, the acquisition is split in a square spiral part centered at $k_{\text{Phase}} = k_{\text{Slice}} = 0$ and standard ascending acquisitions to acquire the $\mathbf{k}-$space edges which are left after the center square has been measured. Figure 5.2 shows a graphical representation of both acquisition schemes. The implementation of SegFatNavs is identical in both cases, meaning the navigator kernel(s) is(are) run after the imaging kernel. Of course, in both cases, the slice and phase directions may be exchanged, but we shall keep this convention as it was used for all acquired data.

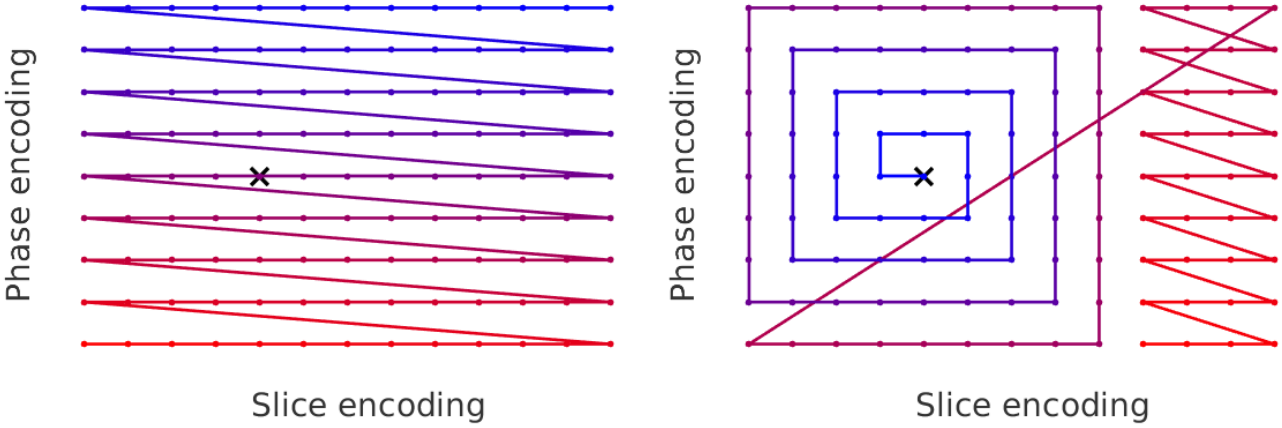

Figure 5.2 – $\mathbf{k}-$space acquisition ordering. Left is ascending and right is centric. The black cross represents the $\mathbf{k}-$space center, and the color line links successive acquisitions.

Focusing on ascending acquisitions, in most cases not all FatNavs volumes are acquired over the same values of iSliceEncode, as this would only be true if

$$N_p N_s/\text{nSegments} = \text{nSliceEncode}. \tag{5.1.1}$$

This is equivalent to say that each FatNav would be acquired during exactly the inner loop of the imaging GRE. However (5.1.1) is rarely satisfied, especially if the goal is to include FatNavs into pre-existing imaging protocols without having to fine-tune them. This is clearly different from the snapshot FatNavs approach, and hence not all FatNavs volumes are a priori expected to look exactly alike, mainly due to different eddy currents states during volume acquisitions. It turns out that these differences can introduce changes in the FatNav images significant enough to induce slight bias in the estimated motion (and $B_0$ fluctuation estimations, as shall be shown in §6.2.1). However they are systematic and predictable, as they fully originate from the sequence acquisition scheme. The next section therefore focuses on how to predict and correct these non-physiological components.

### 5.1.4 Artefacts and correction procedure

The discussion first focuses on ascending acquisitions. Due to the cyclic nature of the acquisition, the artefacts in the motion parameters are found at specific frequencies. After many scans acquired with varying SegFatNavs and inner loop periods, a heuristic rule was found to predict the artefacts fundamental frequency. These scans could easily be performed on a phantom, as the artefacts are independent of the contrast and only depend on the sequence parameters. This is exemplified in Figure 5.3, where the non-central sharp peaks are the artefacts. Indicated in the example spectra are the SegFatNavs period ($N_p N_s/\text{nSegments}$) and the length of the inner loop of imaging sequence (nSliceEncode). These periods are unitless and should be understood as the corresponding number of calls of the imaging sequence kernel. In some cases, the artefacts have not only a fundamental frequency, but also harmonic components at integer multiples of the latter. The predicted artefact period is, as can be expected, the least common multiple of the SegFatNavs period and the inner loop length. While consistent in most of the tested cases, this simple rule sometimes fails as shown in Figure 5.4, where only the fifth harmonic component is amplified. Despite a lot of arithmetic, including the SegFatNavs internal ascending acquisition itself (with inner and outer loop lengths equal to 12 and 9 respectively), no clear reason was found to explain the dominance of the fifth harmonic in this case. For some imaging protocols (i.e, values of (nSliceEncode)), making some SegFatNavs kernels dummy, i.e. without signal sampling, could help reach the divisibility condition and make every SegFatNavs acquisitions equivalent, but it would also come at the price of lower temporal resolution of the motion estimates .

In the case of centric acquisitions, no clear rule was found, but some protocols had similar sharp artefact resonance(s).

Interestingly, in all acquired angiography data, using raw (i.e. with artefacts) or filtered motion parameters never made any obviously detrimental visual difference in the reconstructions. While this is certainly convenient, it makes no sense to use non-physiological correction parameters and hence the filtered version was always used.

In summary, it was found that setting a protocol and measuring its potential artefacts on motion estimates on a phantom was sufficient for all practical purpose. As a consequence, no further research was conducted to establish a more general rule for artefact determination.

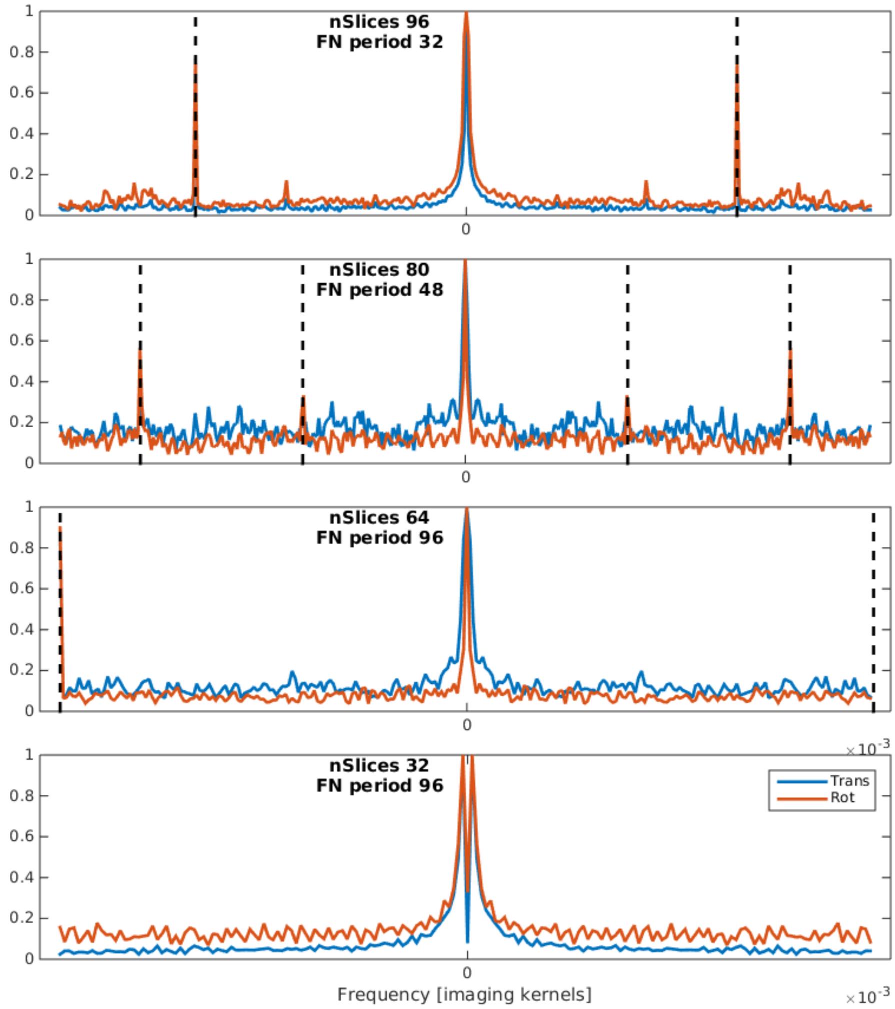

Figure 5.3 – Several examples of the motion parameters spectra for different scanning parameters. Translations and rotations are combined using sum-of squares and scaled for visual convenience. The dashed black lines represent the inverse of the least common multiple of the SegFatNavs period and the inner loop length, as well as multiples thereof.

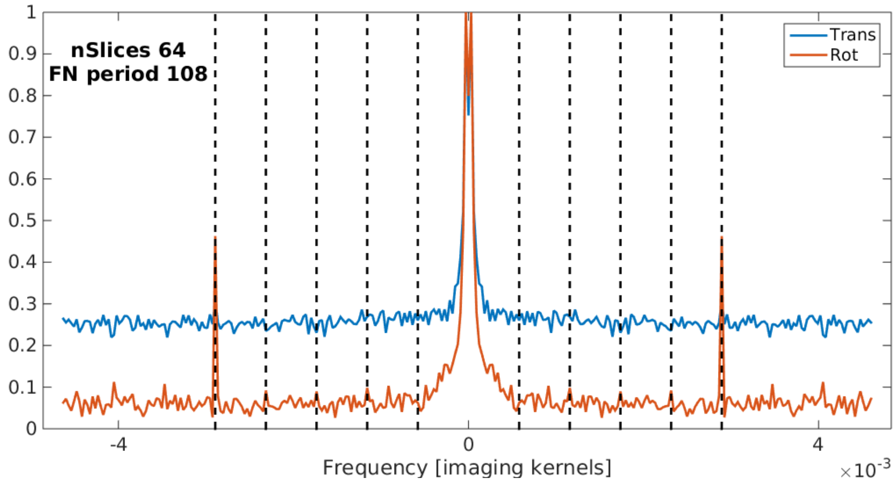

Figure 5.4 – Puzzling example where the artefact appears only at the fifth harmonic of the least common multiple of the SegFatNavs period and inner loop period.

## 5.2 Application: Time-of-Flight

This section will show application of the SegFatnavs for time-of-flight (TOF) angiography. First the homemade TOF sequence implementation will be described, followed by motion correction results of high-resolution protocols at 7T, for both ascending and centric acquisition schemes. The magnetization transfer induced by the SegFatNavs is also studied and discussed. Finally, the transfer of the approach to a clinical 3T scanner will be introduced.

### 5.2.1 Sequence description

The TOF sequence aims at a bright blood signal and a low stationary tissue signal, enabling high vessels-to-brain contrast. The idea is that blood magnetization flowing into the imaged slab will be at thermal equilibrium magnetization, whereas the imaged slab magnetization has seen many previous RF pulses, and hence provides less signal. The rule is therefore for the GRE kernel to have a short echo time, for reduced blood signal decay, and short repetition time, for lower stationary tissues signal. This angiography approach is certainly the most basic but has excellent imaging capabilities [75]. Of course, its simplicity makes it susceptible to many undesired effects. Vessels going out and in again of the imaged slab appear less and less bright along the path of the blood flow. Also, additional modules are needed in order to image arteries only and remove the venous signal. Because the clinical sequence proprietary code was not easily obtainable for the CIBM 7T scanner, a home-made version was coded and shall be described now. The complete sequence kernel, including SegFatNavs, is drawn in Figure 5.5.

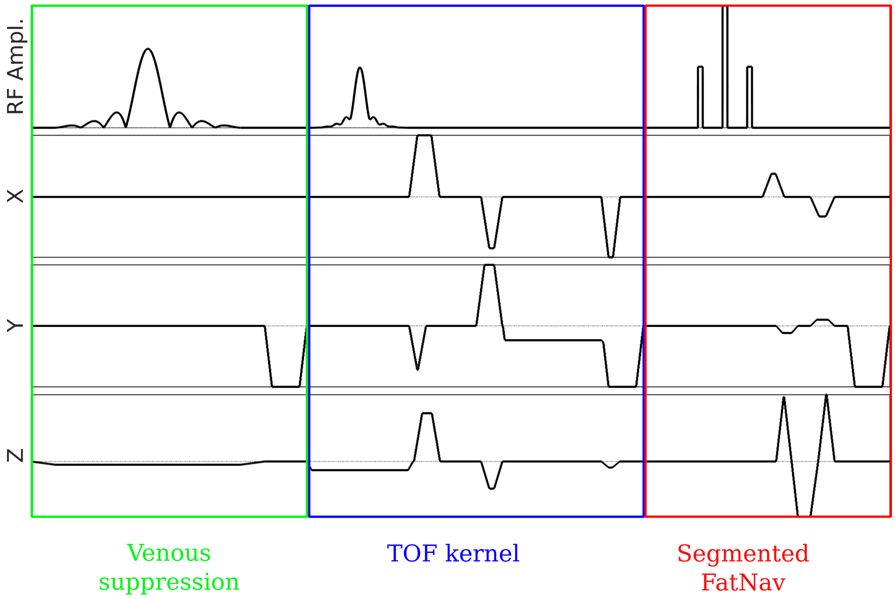

Figure 5.5 – Homemade TOF sequence sequence kernel including venous signal suppression, flow-compensated GRE kernel and SegFatNavs acquisition.

The implemented RF pulse was a TONE pulse, acronym of "tilted optimized nonsaturating excitation" [102]. This pulse is designed to produce a lower flip angle where the blood flow enters the slab, and larger one where the blood exits the slab, thereby mitigating the effects of lower available longitudinal blood magnetization due to RF pulses during the slab traversal. The routinely chosen excitation profile is

$$\tilde{B}_1(\omega) = \begin{cases} B_1(1 + p\frac{\omega}{\omega_m}) & \text{if } |\omega| \leq \omega_m \\ 0 & \text{otherwise} \end{cases} \tag{5.2.1}$$

where $\omega = 0$ is the center frequency of the slab, $p$ is the linear slope of the flip angle profile and $2\omega_m$ is the frequency range of the slab, defined as the slice-selection gradient multiplied by its thickness. Therefore, in the small flip angles regime, the pulse is given by the Fourier transform giving

$$B_1(t) \propto \frac{\sin(w_m t)}{t} + i \frac{p}{\omega_m} \frac{w_m t \cos(w_m t) - \sin(w_m t)}{t^2}. \tag{5.2.2}$$

(5.2.2) is nothing other than the addition of a sinc pulse and $i$ times the time derivative of a sinc pulse. In practice, the pulse is truncated to a chosen duration and hence (5.2.2) is multiplied by a Hann filter to reduce Gibbs ringing.

Flow compensation was implemented in all three directions by adding one extra gradient on all axes allowing to null the gradients first moments (at echo time for the readout direction).

While it is possible to conceive a zero-phase version of the RF pulse, which is basically a time-shifted expression of (5.2.2), it would need to be tailored to account for the slice-selection gradient ramp-down. As such a version of the pulse would not require a refocusing slice gradient by construction, slightly shorter echo-time could have been achieved had such version been implemented, but results obtained without it were judged good enough to leave it as a potential extension. Another extension could be to VERSE the excitation pulse to reduce power deposition [103]. This was not attempted as the proposed sequence proved more than sufficient to test whether SegFatNavs are, in practice, usable as motion correction navigators.

The venous saturation used was a module coded by Siemens, and the saturation band was placed above the imaged slab. In multi-slab acquisitions, it tracks the position of the currently imaged slab.

Direct comparison of the home-made sequence (without navigator) to the the Siemens product sequence was carried out and no apparent differences were observed. This opened the way to investigate the motion correction ability of SegFatNavs for TOF angiography. First the focus will be on protocols using the ascending $\mathbf{k}-$space acquisition ordering, then on those using centric ordering.

### 5.2.2 Motion correction at 7T: ascending ordering

#### Acquisition

The following results were obtained on healthy volunteers who were asked to stay still. Two axial high-resolution isotropic datasets were acquired, with a voxel size of 0.4 mm and 0.25 mm respectively. The imaging slabs were 8.3 cm and 4 cm thick respectively and aimed to image the Circle of Willis. The TONE nominal flip angle was 20° with a slope factor $p$ of 50% in the foot-head direction [104]. The SegFatNavs flip angle was chosen as high as possible while still respecting standard SAR constraints. The acquisitions used nSegments = 1. Venous saturation was set at 45°. The imaging and navigator parameters are summarized in Table 5.1. The GRAPPA reference lines for the SegFatNavs were acquired in a pre-scan (2.3s) for each dataset. The navigator temporal resolution was 2.25s / 2.85s for the 0.4mm / 0.25mm scan, respectively. SegFatNavs were retrospectively co-registered using SPM to obtain the time-courses of the rigid body motion parameters, and retrospective motion correction of the time-of-flight sequence was performed coil-wise using a NUFFT adjoint operator approach. Finally, maximum intensity projections (MIPs) were performed on sum-of-squares images, and brain masks (if used) were always obtained from the motion corrected reconstruction for fairer comparisons.

| | **0.4 mm** | **0.25 mm** | **SegFatNavs** |
|---|---|---|---|
| $T_E$ **[ms]** | 4.6 | 6 | 1.6 |
| **Effective** $T_R$ **[ms]** | 20.8 | 26.4 | - |
| **Undersampling** | - | - | (4 , 4) |
| **Bandwidth [Hz/pix]** | 750 | 510 | 3910 |
| **Matrix size** | 449 × 476 × 208 | 645 × 760 × 160 | 48 × 64 × 64 |
| **Partial Fourier (Phase,Slice)** | (3/4 , 3/4) | (3/4 , 3/4) | (3/4 , 3/4) |
| **Total Acquisition Time** | 18min17s | 25min33s | - |

Table 5.1 – Parameters of the high-resolution TOF protocols and of the included SegFatNavs.

### Results and discussion

Figure 5.6 shows an example of a SegFatNav volume , and the range of the estimated motion for all scans (calculated independently for each motion parameter) is presented on Table 5.2.

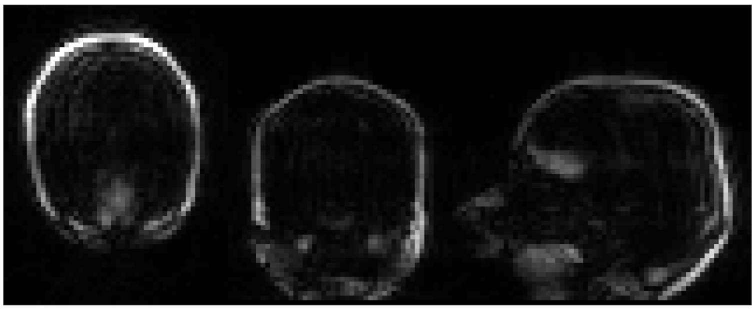

Figure 5.6 – Example of the 4 mm SegFatNavs acquired during the 0.25 mm TOF.

Volunteers 1 and 3 remained very still, whereas volunteer 2 exhibited some mild motion. The uncorrected and corrected images of a 0.4 mm scan are compared on Figure 5.7 (volunteer 2), where the sagittal MIP was performed after brain extraction. The vessel sharpness is greatly increased in the corrected reconstruction.
The 0.25 mm scan of the second volunteer clearly confirms the need of motion correction for high-resolution protocols in even slightly uncooperative subjects. Figure 5.9 is a focus on the circle of Willis of this scan, where significant vessels sharpness increase is obtained by motion correction. The associated motion parameters can be found in Figure 5.9.
Figure 5.11 shows the 0.25mm scans results : the top image (volunteer 1) demonstrates excellent venous and fat suppressions, while the bottom zoom (volunteer 3) resulted in slightly higher vessel signal and better contrast after correction, leading to enhanced vessels visualization in this small motion case (translations $< 0.53$ mm, rotations $< 0.63°$). The SegFatNavs motion of these scans are shown in Figure 5.12.

| | Translation range [mm] | | | Rotation range [°] | | |
|---|---|---|---|---|---|---|
| | X | Y | Z | Pitch | Roll | Yaw |
| **Volunteer 1** | | | | | | |
| 0.4 mm scan | 0.54 | 0.27 | 1.12 | 0.54 | 0.69 | 0.56 |
| 0.25 mm scan | 0.39 | 0.38 | 0.62 | 0.29 | 0.44 | 0.21 |
| **Volunteer 2** | | | | | | |
| 0.4 mm scan | 0.67 | 0.65 | 2.78 | 1.06 | 1.16 | 0.43 |
| 0.25 mm scan | 0.62 | 0.99 | 2.97 | 1.74 | 0.62 | 0.49 |
| **Volunteer 3** | | | | | | |
| 0.4 mm scan | 0.69 | 0.24 | 0.76 | 0.51 | 0.7 | 0.32 |
| 0.25 mm scan | 0.52 | 0.19 | 0.43 | 0.33 | 0.62 | 0.27 |

Table 5.2 – Motion range, defined as the difference between the maximum and the minimum value, for all presented 0.4 mm and 0.25 mm scans.

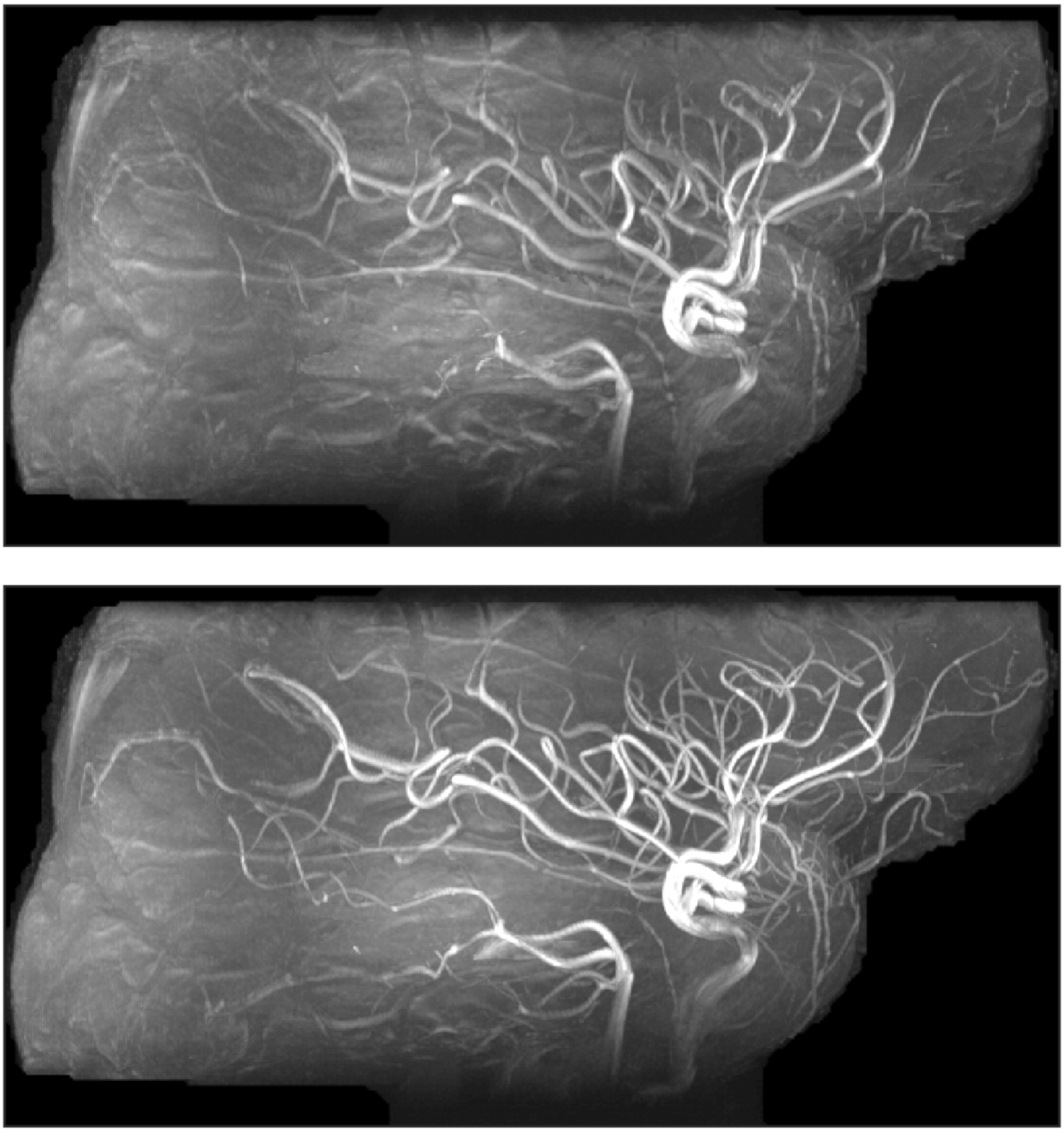

Figure 5.7 – Brain masked sagittal MIP of raw (top) and motion corrected (bottom) reconstructions for the 0.4 mm TOF. Associated motion parameters can be found in Figure 5.8.

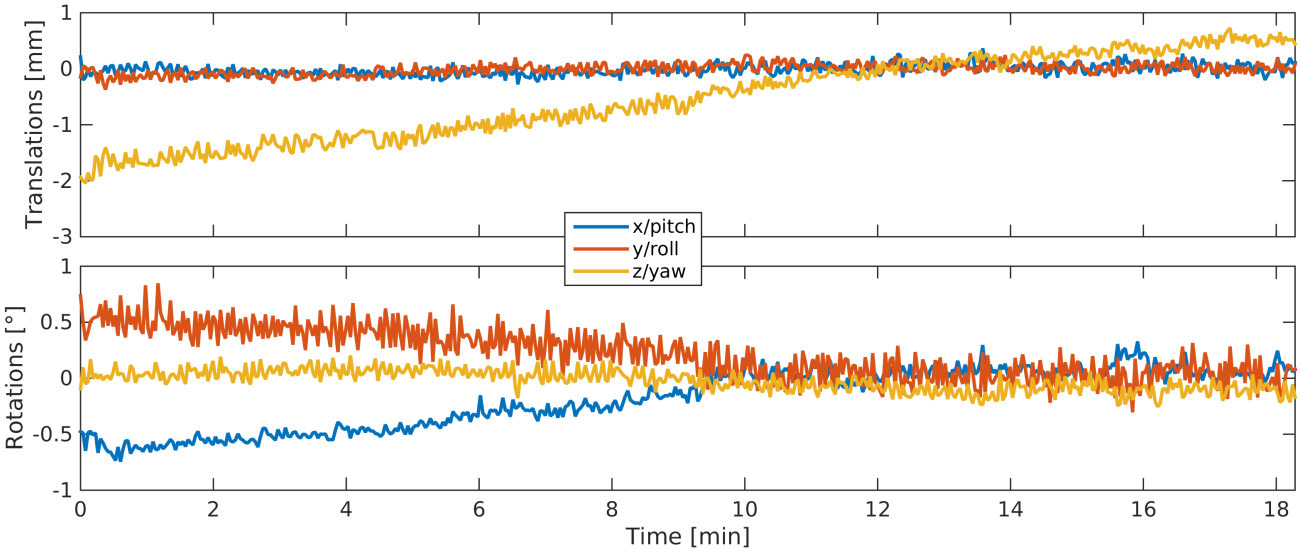

Figure 5.8 – Motion parameters of the 0.4 mm scan presented in Figure 5.7.

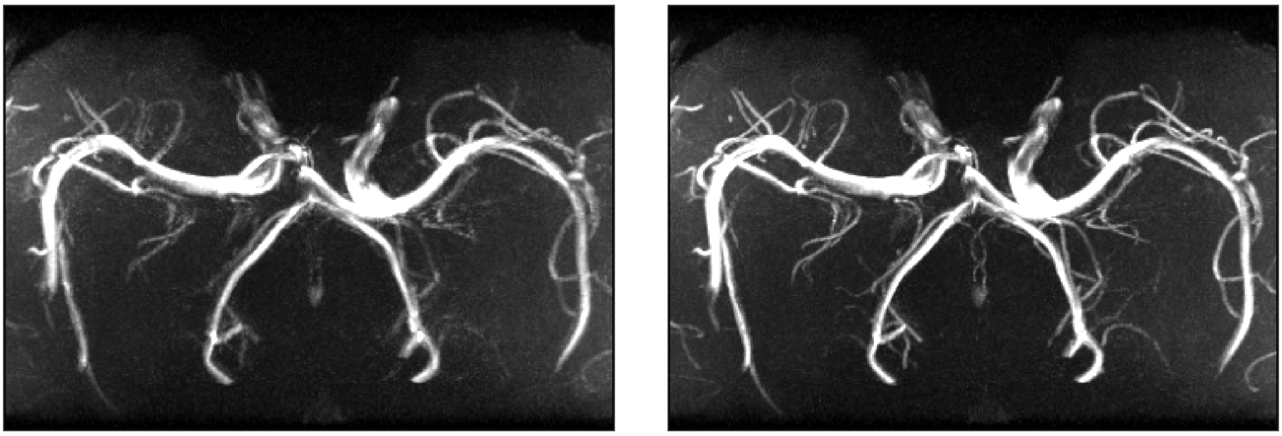

Figure 5.9 – Focus on the Circle of Willis for a 0.25 mm scan (volunteer 2). Raw (left) and motion corrected (right) reconstructions. Figure 5.10 shows the estimated motion parameters for this scan.

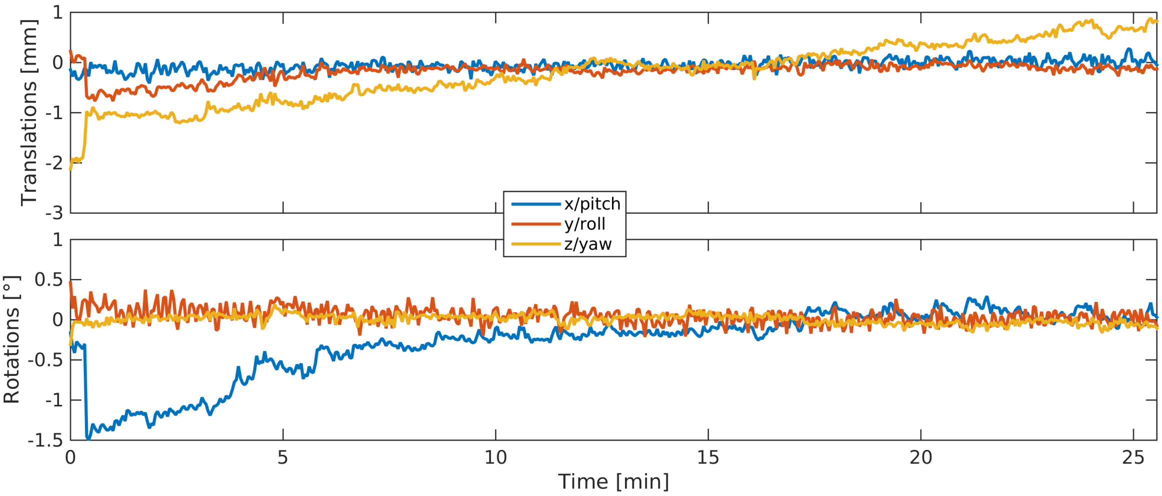

Figure 5.10 – Motion parameters of the 0.25 mm scan presented in Figure 5.9.

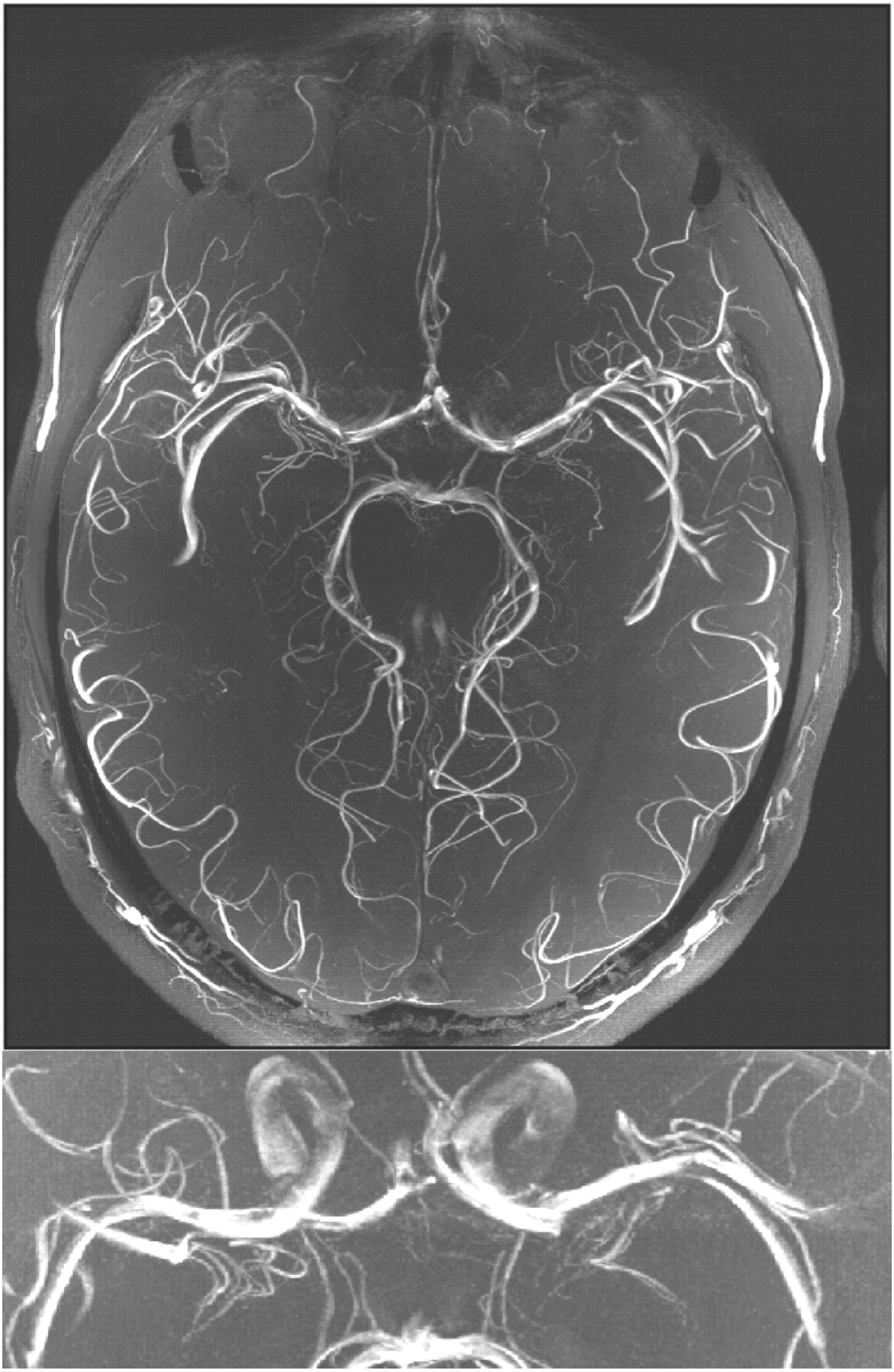

Figure 5.11 – Small motion 0.25 mm scan MIPs. Top: volunteer 1, bottom: volunteer 2.

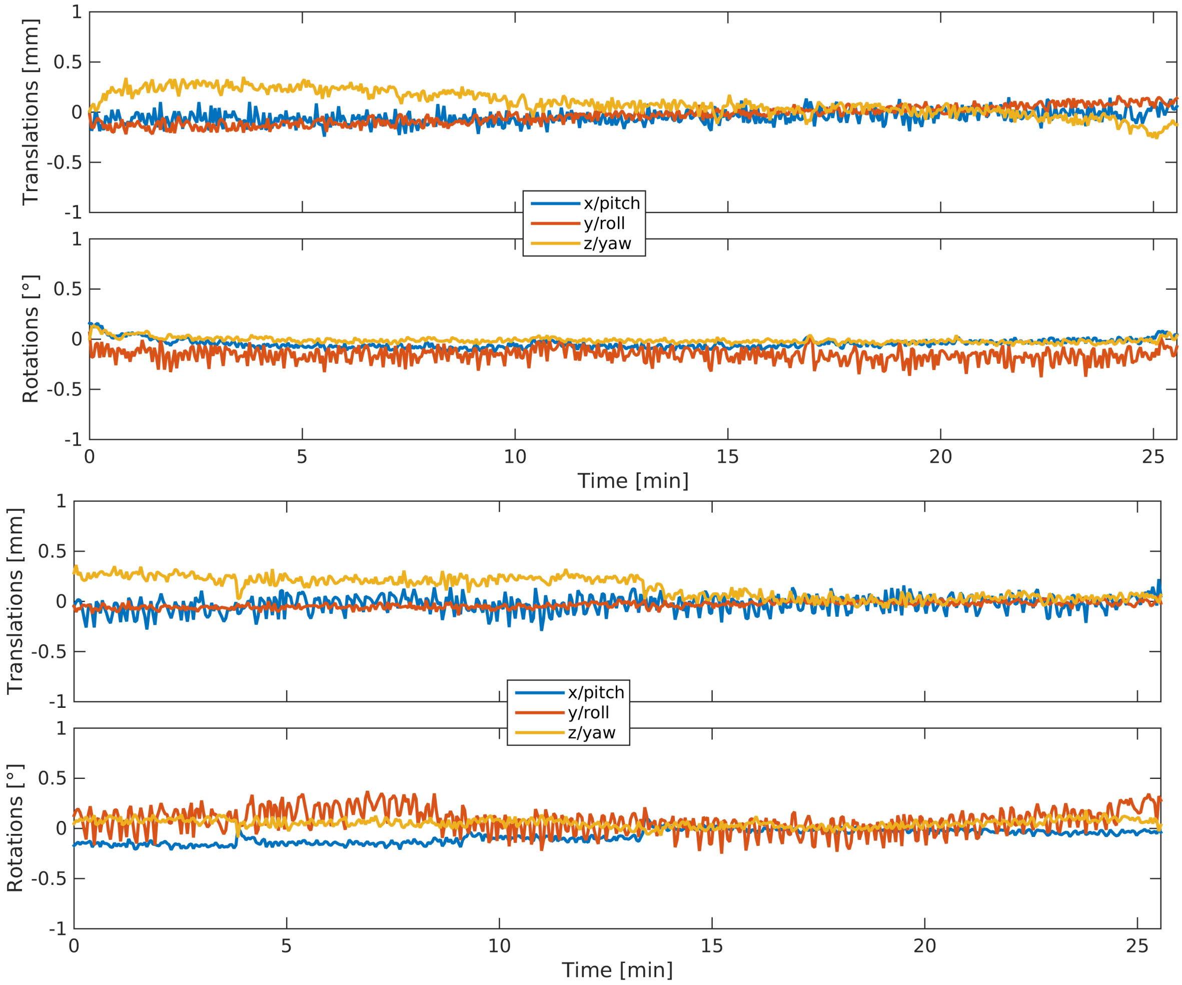

Figure 5.12 – Motion parameters of the 0.25mm scans presented in Figure 5.11. Top: volunteer 1, bottom: volunteer 2.

### 5.2.3 Motion correction of centric acquisitions

As it is common in the clinical setting to use centric acquisitions, this part of the thesis is to check the applicability of SegFatNavs to such protocols.

#### Acquired protocols

The acquired protocols were 0.5 mm isotropic axial scans, with 3/4 partial Fourier in phase and slice directions. The imaged slab was 6.4 cm thick and the echo time was 5 ms, with an effective repetition time of 20.7 ms. TONE and venous saturation parameters were as in §5.2.2. Two slightly different protocols were acquired, both with nSliceEncode = 108, accounting for partial Fourier. One scan had equal SegFatNavs period (108), and the other a slightly different value (96). These scans shall be called cycle-matched and cycle-unmatched respectively. Of course the notion of cycle length only makes sense for the outer edges of $\mathbf{k}-$space acquisition, as depicted in Figure 5.2. In both cases, SegFatNavs were 4x4 undersampled 4mm SegFatNavs, with nSegments = 1, but with slightly different FOV in the left-right direction. Scan durations were 11 minutes. The reference pose is defined as the last fully sampled SegFatNav, as the acquired trajectory passed by the $\mathbf{k}-$space center last.
Volunteers were always asked to stay still. A few representative scans of the total acquired data shall be presented, as results are similar to the ones from the ascending acquisitions.

#### Results

Figure 5.13 shows an example of achievable motion correction by SegFatNavs for the cycle-matched centric acquisition described above, with the detected motion shown in Figure 5.14. All vessels a noticeably sharper after correction. Smaller vessels emerge after correction, while in the raw reconstruction they were undetectable. No filtering of the motion parameters was necessary in this case.
As for cycle-unmatched acquisitions, an example of small motion detection and correction is shown in Figure 5.15. The motion parameters are shown in Figure 5.16 and were filtered. However, correction based on the unfiltered parameters were visually indistinguishable from the filtered based reconstruction. While the difference between filtered and unfiltered corrections was not distinguishable at this imaging resolution, non-physiological components would have the same amplitude for arbitrarily higher in-plane resolution, reinforcing the idea that using the filtered version is the best practice in the general case.

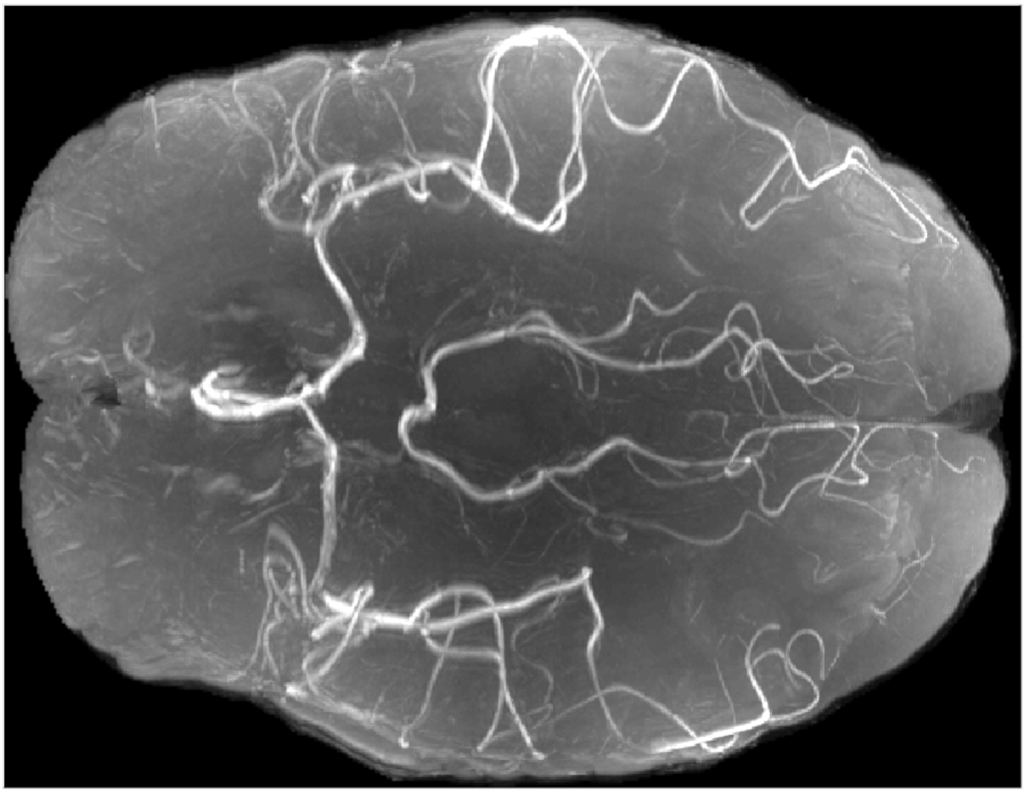

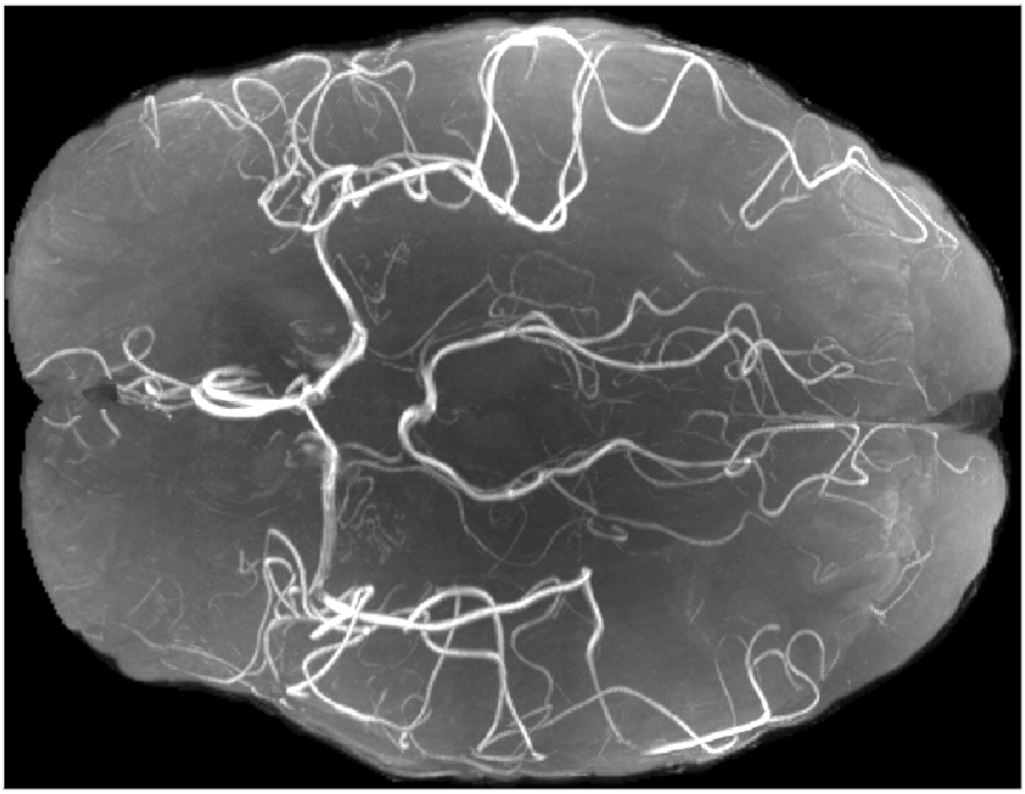

Figure 5.13 – Raw (top) and motion corrected (bottom) 0.5 mm centric cycle-matched acquisition. Motion parameters are plotted on Figure 5.14.

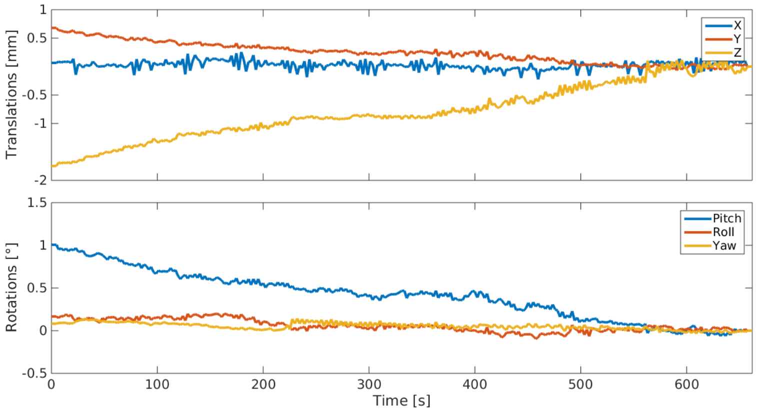

Figure 5.14 – Estimated motion during the 0.5 mm centric cycle-matched scan shown in Figure 5.13.

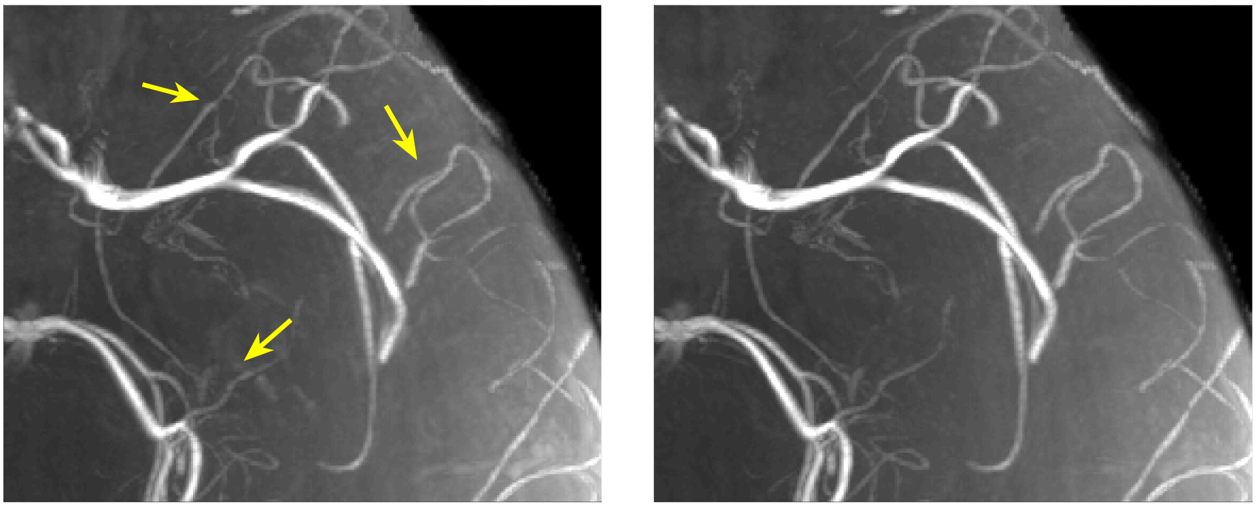

Figure 5.15 – Zooms on raw (left) and motion corrected (right) reconstruction of a 0.5 mm centric cycle-unmatched acquisition. Yellow arrows indicate regions of signal enhancement and blurring reduction. Associated motion parameters are presented in Figure 5.16.

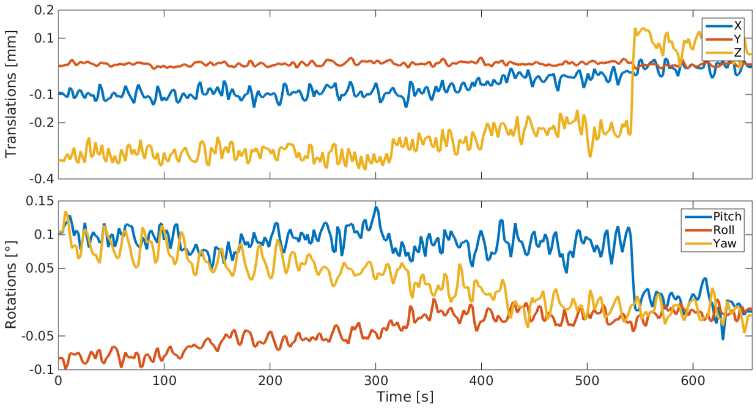

Figure 5.16 – Filtered motion parameters associated to Figure 5.15. Notice the very small range of motion.

### 5.2.4 SegFatNavs for inducing magnetization transfer

Historically, the $1 - \bar{2} - 1$ binomial pulse, with no phase-evolution time, was one of the first proposed magnetization transfer (MT) inducing strategy for TOF angiography [105] where the additional MT effect can further suppress the signal of static tissues, enhancing the vessel contrast. This short section explores the MT effect obtainable by SegFatNavs and then compares it to the vendor supplied, default MT weighted acquisition.

**SegFatNavs flip angle impact**

In this first test, two 1mm isotropic TOF acquisitions, using low and high SegFatNavs flip angle respectively, were directly compared. Example slices are shown in Figure 5.17. The static tissue signal is lower in the high flip angle image, as expected. Retrospectively, this motivates why the SegFatNavs flip angle was chosen as high as possible in §5.2.2.

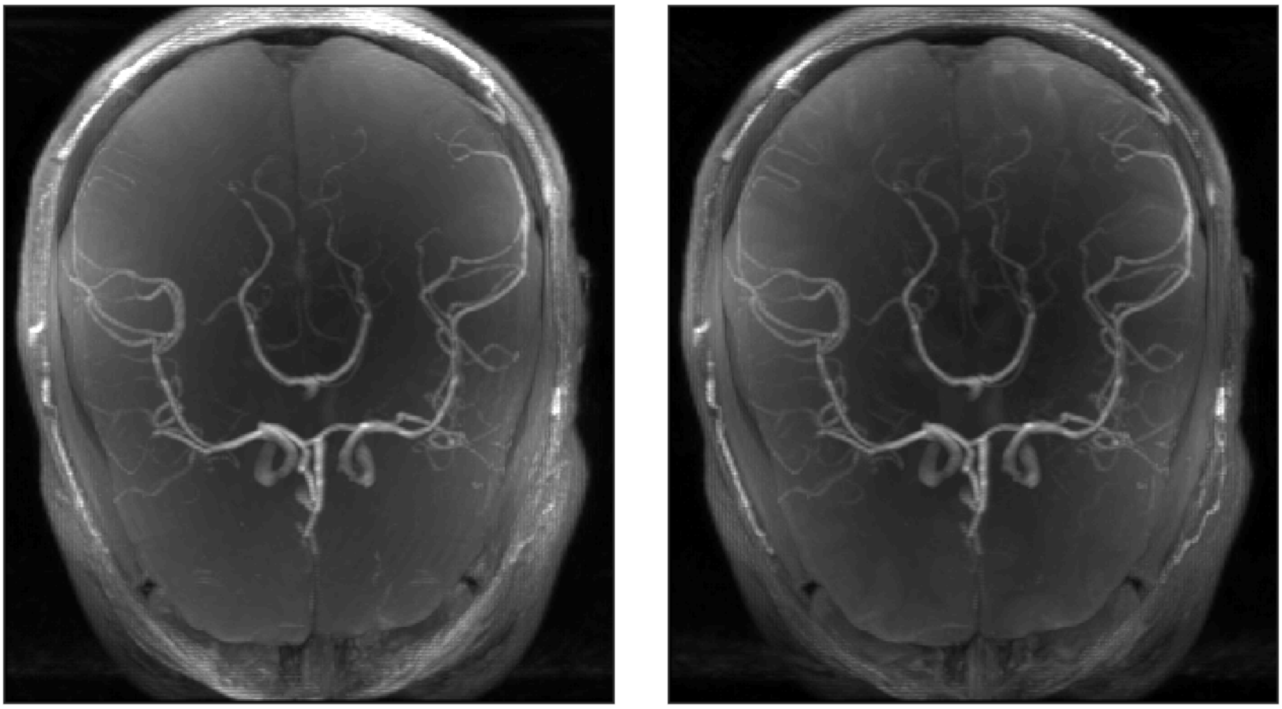

Figure 5.17 – 1mm isotropic images with low (left) and high (right) SegFatNavs flip angle. The images are displayed on the same windowing scale. The higher SegFatNavs flip angle induces lower brain tissues (and fat) signals in the TOF image.

**Comparison to default MT pulse**

The second test compared using the Siemens built MT module, which is a Gaussian pulse with a 1200 Hz frequency offset, 10ms duration and 500° flip-angle navigator free acquisition, to a 90° SegFatNavs acquisition. Because of the SAR constraint of the Siemens MT pulse, an effective repetition time of 60 ms was used in both scans. Figure 5.18 shows a combination of both acquisitions, and no clear contrast differences are observable. Figure 5.19 shows the signal ratio of both acquisitions after 2mm 3D tukey filtering. The ratio being very close to 1 in the brain shows the equivalence of the MT induced by both methods.

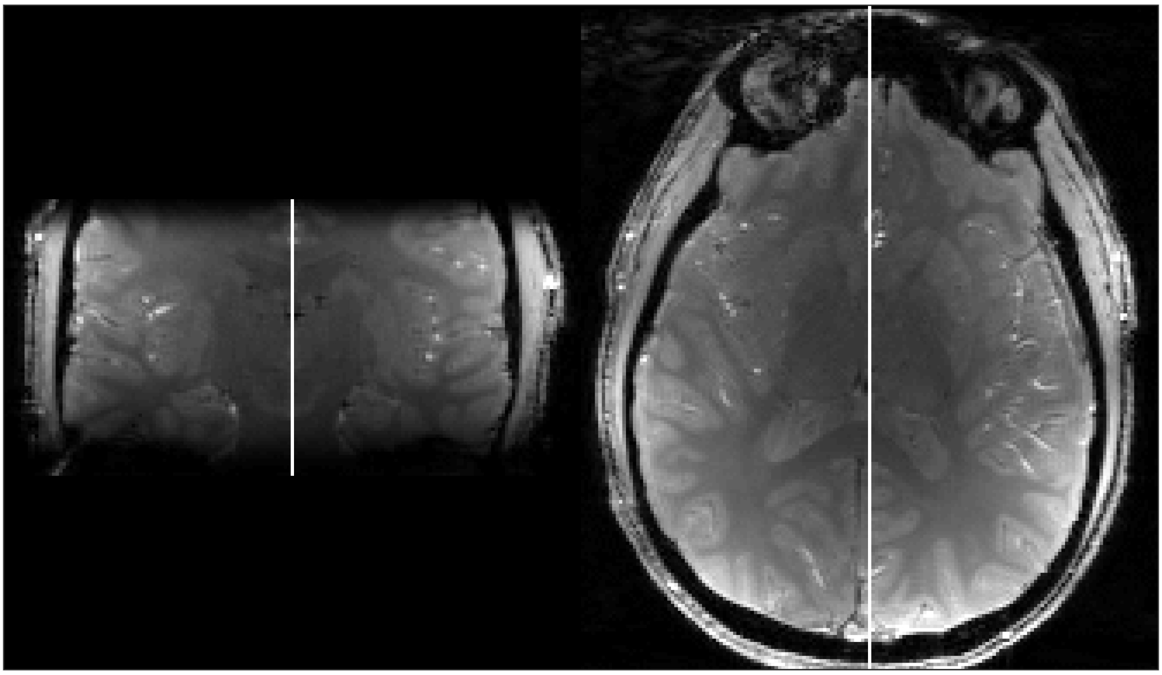

Figure 5.18 – 1mm isotropic acquisitions for comparing standard MT module to MT induced by SegFatNavs. The left side of the vertical white line is using the Siemens MT module, and the right side high flip angle SegFatNavs. White / gray matter contrast is visibly identical in both acquisitions.

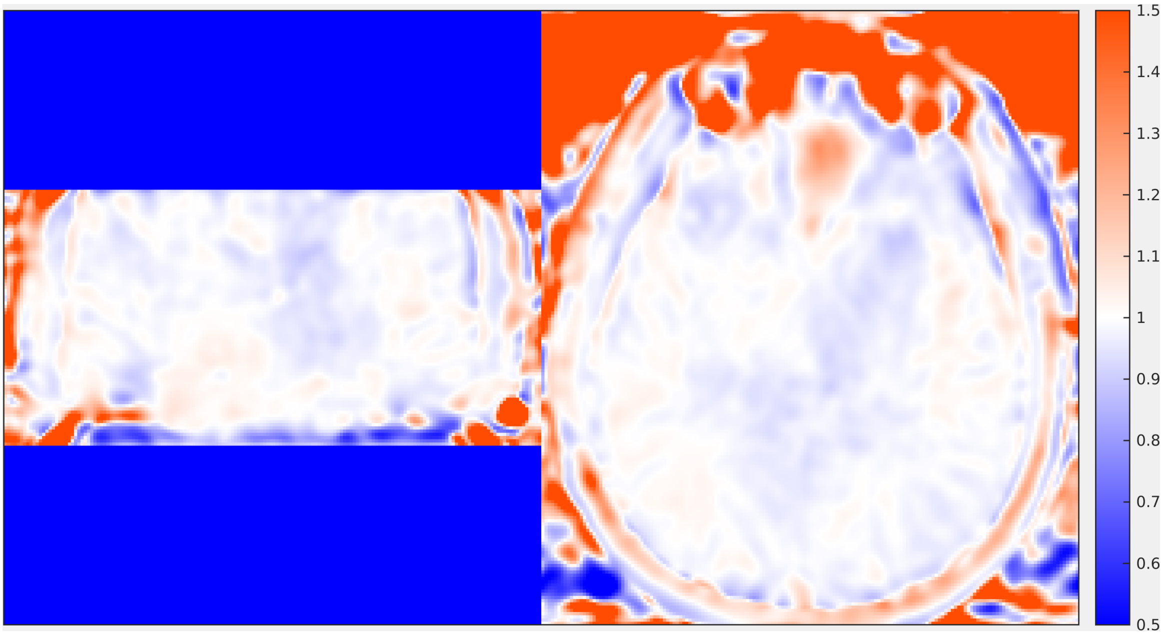

Figure 5.19 – Siemens MT module image divided by high SegFatNavs flip angle image after 2mm 3D tukey filtering. The ratio being very close to one indicates equivalent MT effects in both acquisitions.

**Discussion and concluding remarks**

In practice, a compromise has to be found between venous suppression, SegFatNavs flip angle and power deposition limits (SAR). For a typical repetition time of around 20 ms, as is common for TOF protocols, acquired data suggest that 45° venous suppression is sufficient, and while SegFatNavs flip angle can often reach 60° in such conditions, the added advantages to the final maximal intensity projection images were not actually clear-cut. Therefore, as long a sufficient venous suppression takes place, equivalent final image quality can be reached for lower SegFatNavs flip angle. This led to try to aim at sharper slab excitation, which is equivalent to adding zero crossings to the TONE RF pulse. Results of these tests found that the previously used number of 5 proved to be sufficient in all tested conditions, leading to the results presented previously in §5.2.2, §5.2.3.

### 5.2.5 Transfer to clinical field strength

The implementation of SegFatNavs was also tested at the Lausanne Hospital (CHUV). For this 3T implementation, the proprietary code from Siemens clinical sequence was available, and hence the sequence differed slightly to the home-made 7T version. The main difference was that the TONE excitation is a zero-phase version, allowing for slightly shorter echo time. Unlike at 7T, the venous saturation flip angle can be put at 90° while staying within the safety power deposition limits. Also, the Siemens sequence acquires the $\mathbf{k}-$space center first (center-out acquisition scheme), opposite to the 7T implementation.

On the other hand the CHUV scanner is a PRISMA model, and has lower gradients slew-rates. Overall this meant the repetition time of the sequence had to be lengthened to insert the SegFatNavs acquisition, eventhough all SegFatNavs were centered at -7 ppm from water in order to shorten the fat excitation duration.

As a proof of principle, a centric 0.5×0.5×1 mm axial scan was acquired, during which the subject deliberately performed a nodding motion, similar to repositioning his head in search of better comfort. Figure 5.20 shows the gain in vessel delineation as expected. The detected motion can be found in Figure 5.21.

SegFatNavs were also added to a routine TOF clinical protocol. This routine protocol is a 0.5 mm isotropic whole brain acquisition, divided in six slabs. The effective repetition time had to be increased from 21 ms to 25 ms in order to include SegFatNavs. This protocol showing similar image quality than the non-navigated one, it replaces it when a TOF contrast acquisition is requested for a patient. An example of the 4mm navigators is shown in Figure 5.22. Clearly the imaged slab and the venous saturation slab also impact the fat signal, as the two darker horizontal bands in the coronal and sagittal planes illustrate. The slabs are acquired sequentially, and hence all processing steps are slab specific in order to cope with these interactions. All navigator volumes acquired during a slab are registered to the reference one (for this slab), and the slab data is motion corrected in the same manner as previously. The slabs are combined after individual correction. However, up to now, no data showed any significant motion artefacts in the MIPs, and the obtained corrections are for all relevant purposes identical to the uncorrected version.

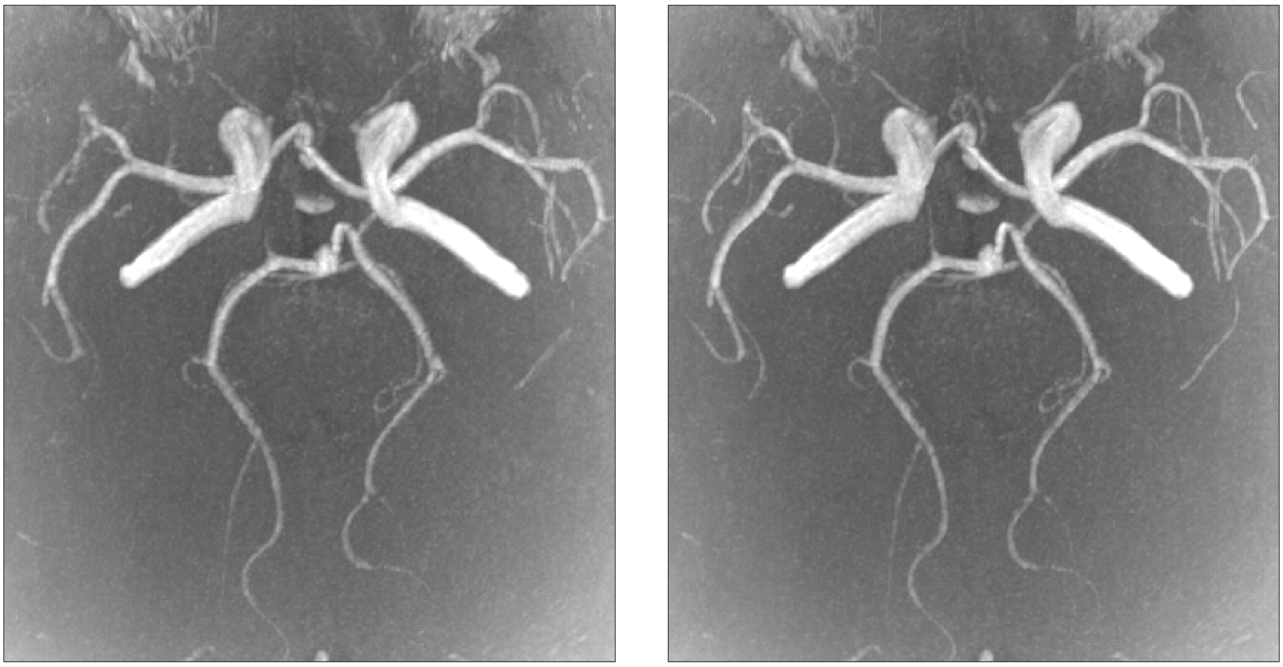

Figure 5.20 – Raw (left) and motion corrected (right) 3T TOF 0.5×0.5×1 mm protocol, with a deliberate nodding motion during the scan.

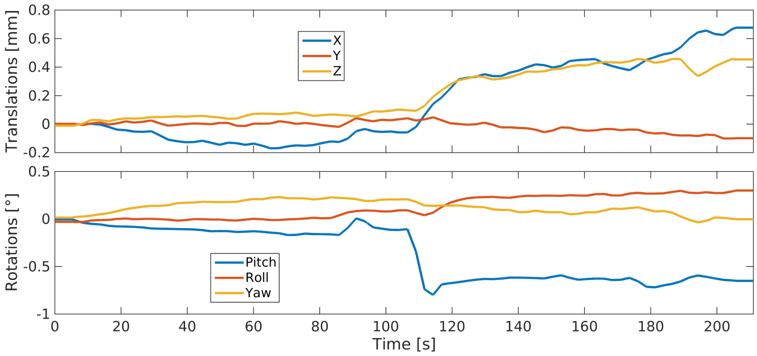

Figure 5.21 – SegFatNavs during a 3T TOF 0.5×0.5×1 mm protocol, with a deliberate nodding motion during the scan.

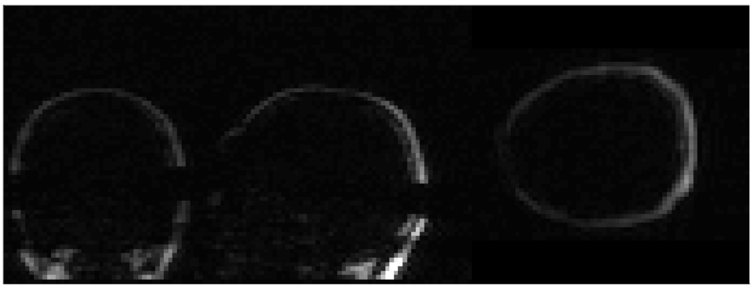

Figure 5.22 – Example of 4mm SegFatNavs incorporated in the clinical TOF protocol at 3T.

## 5.3 Summary and outlook

In this chapter, it was demonstrated how SegFatNavs can visibly help to restore high image quality of high resolution angiography protocols. Consideration of the imaging sequence $\mathbf{k}-$space ordering and overall parameters should be kept in mind during the processing to prevent non-physiological artefacts in the estimated motion. MT effects can be tuned to further enhance TOF imaging if needed, and implementation at 3T proved successful for high-resolution acquisitions with moderate motion.

While only the application to TOF angiography was presented, the modularity and versatility of the SegFatNavs approach opens the way to many other imaging sequence motion navigation. Chapter §6 will study an extension of the SegFatNavs to $B_0$ fluctuation monitoring, and jointly with FID navigators their application to retrospective field and motion correction in a long echo time GRE sequence.

# Chapter 6

# Combining segmented FatNavs and FID navigators

While the SegFatNavs approach allows for varied implementations, it suffers from relatively low temporal resolution, typically $\sim 2$ s for a 4 mm navigator resolution. This might often be unsatisfactory if one aims to sample breathing. This chapter will introduce the FID navigators (FIDNavs), and how to implement both navigators into GRE-like sequences to obtain higher temporal resolution motion information. As example applications, combination with dual-echo SegFatNavs to correct for field fluctuation will be presented, as well as a sudden intentional nodding experiment.

## 6.1 FID Navigators

### 6.1.1 Description and relation to motion

The free induction decay (FID) signal is, by its standard definition, the acquisition of the center of $\mathbf{k}-$space. Spatial information does exist in the signal $y$, as for each receive channel $c$ it is weighted by the associated sensitivity map $s_c$:

$$y_c(t) = \int s_c(x) m_\perp(x,t) \mathrm{d}V \tag{6.1.1}$$

where $m_\perp$ is the total transverse magnetization. Neglecting relaxation during signal acquisition and under motion modeled by $x(t) = R(t)x_0 + d(t)$, the FID signal becomes

$$y_c(t) = \int s_c(R^{-1}(x-d)) m_\perp(x_0) \mathrm{d}V. \tag{6.1.2}$$

FID navigators are easily introduced into almost any imaging sequence, because the duration of the navigator acquisition is very short, under 1 ms. The signal variation has been used to detect motion [54], and possibly trigger image navigators for prospective correction in MPRAGE sequence [55]. As can be seen from (6.1.2), there is no direct way to estimate motion from the FID signal without prior knowledge. Labeling the six motion parameters by $\mathbf{p}$ and the signal from all receive coils by $\mathbf{y}$, the goal is to find a mapping model $F$ such that

$$\mathbf{p}(t) = F(\mathbf{y}(t)). \tag{6.1.3}$$

The most natural expansion is the first order Taylor development of (6.1.2), giving a simple linear model

$$\mathbf{y}(t) = \mathbf{y}(0) + \sum_i p_i(t) \int \left[ \frac{\partial}{\partial p_i} s_c(R^{-1}(x-d)) \right]_{\mathbf{p}=0} m_\perp(x_0) \mathrm{d}V + O(p^2). \tag{6.1.4}$$

In practice, (6.1.4) has to be inversed during a calibration process. A standard pseudo-inverse approach is thereby used to solve the associated model parameters $A$ and $C$ where

$$\mathbf{p}(t) = \mathbf{C} + A\mathbf{y}(t). \tag{6.1.5}$$

While according to (6.1.4), the constant term $\mathbf{C}$ should be linked to $A$ and the FID signal at the time of reference, it was found that fitting for it provides better performance, especially if the FID navigators have a higher temporal resolution than the calibration data providing $\mathbf{p}$, as will be the case for the presented applications to segmented FatNavs (SegFatNavs from §5) in the next section. Using external optical tracking to provide the calibration data, several linear models were tested [106]. The best accuracy was obtained from considering both the real and imaginary parts of the FID signal, which fits the natural expectation from (6.1.2).

While it is assumed that the range of motion is such that the sensitivity map can be well approximated as static, the change of subject pose induces a load variation to the coil, and slightly changes the sensitivity profiles of the receive channels (at a fixed location). However, as long as these variations are smooth and sufficiently slow, they are included in low order expansion models.

Finally, it has been proposed to use two pre-scans where the subject is still, one acquired with the body coil and one with the surface coil array to estimate the sensitivity [107]. If the pre-scans have the same contrast than the FID navigator will have in the imaging sequence, the FID signal for a given motion state can be simulated from the pre-scans to train the model. In that study the second order expansion increased the motion estimates accuracy for motion above 4 mm or °, but the proposed model only used the magnitude of the FID signal.

In summary, the FID navigators have excellent temporal resolution, but very poor spatial information, and therefore require some model based on prior knowledge of the motion estimates. This motivated the combined use of FIDNavs and SegFatNavs to try and combine the advantages of both methods: the accuracy of motion estimates from the SegFatNavs and the high temporal resolution from the FIDNavs.

### 6.1.2 Implementation

There are two ways to acquire FIDNavs without introducing additional RF pulses: either in the imaging sequence or in the SegFatNavs. Both offer the same temporal resolution, with the advantage of higher SNR in the SegFatNavs case if more than one navigator is acquired after each imaging kernel call.

Due to the imaging sequence using a slab selective excitation in most protocols, a dilemma arises. In order to acquire a true FID signal, a slice-selection gradient rewinder is required as the $\mathbf{k}-$space position has non-zero component in the slice direction (in the routine case where zero-phase excitation pulses are not used). While completely doable in theory, in practice the slice gradient rewinder and encoding are combined in a single effective gradient. In the Siemens GRE proprietary code, the implementation of a true FID navigator is therefore not a trivial alteration due to all subsequent timing computations, such as flow compensation in the slice direction. On the other hand, this code is very versatile and allows the acquisition of many different protocols. The compromise chosen by Maryna Waszak of the Siemens team was to acquire the navigator between the excitation and the slice encoding. Therefore, the signal is not at $\mathbf{k}-$space center. However, in a very practical mindset, the reasoning of modeling the navigator signal variations as linear functions of the motion parameters is still expected to hold. With this in mind such navigator will still be called FIDNavs, even if they do not correspond to the strict definition. Conversely, FIDNavs included in SegFatNavs can be acquired directly after the binomial excitation and are the **k**−space center signal, because the excitation is not spatially selective.

A priori, including the FID into the SegFatNavs would be advantageous because of the fat spatial distribution. Indeed it can be expected that the receive channels FID signals are more different from one another due to the larger difference in the associated coil sensitivity profiles. However it was found that the large number of channels ($\geq 32$) usually available for head imaging reduces this advantages, as enough channels have significantly different profiles on the water signal domain to robustly fit the six motion parameters..

The FIDNav signal is defined as the mean of all the samples during one FIDNav acquisition, leaving $n_c$ complex values per FIDNav, where $n_c$ is the number of receive channels. In practice, roughly the first half of the acquisition has to be discarded. This is because the navigator is acquired as soon as possible after the end of the excitation (RF pulse and potential slice-selective gradient) and hence residual signal modulation effects are still observable at the beginning of the FID acquisition, see Figure 6.1. The intial fluctuation are not explainable by motion, and hence are discarded.

Finally, a yet undiscussed effect can take place in spatially selective imaging. Through slab motion induces spin history effects which is expected to affect the FID signal as magnetization closer to thermal equilibrium enters the slab while steady state magnetization leaves it. This means an overshoot is expected under such motion, which may become significant for thin slabs. In such cases, it is doubtful the FID approach can faithfully predict motion before the slab magnetization reaches equilibrium again. More generally, this effect becomes only large if the motion scale is of the order of the slice excitation profile side-lobes. This would simultaneously contradict the retrospective motion correction approach due to the imaged anatomy changing significantly during the image acquisition.

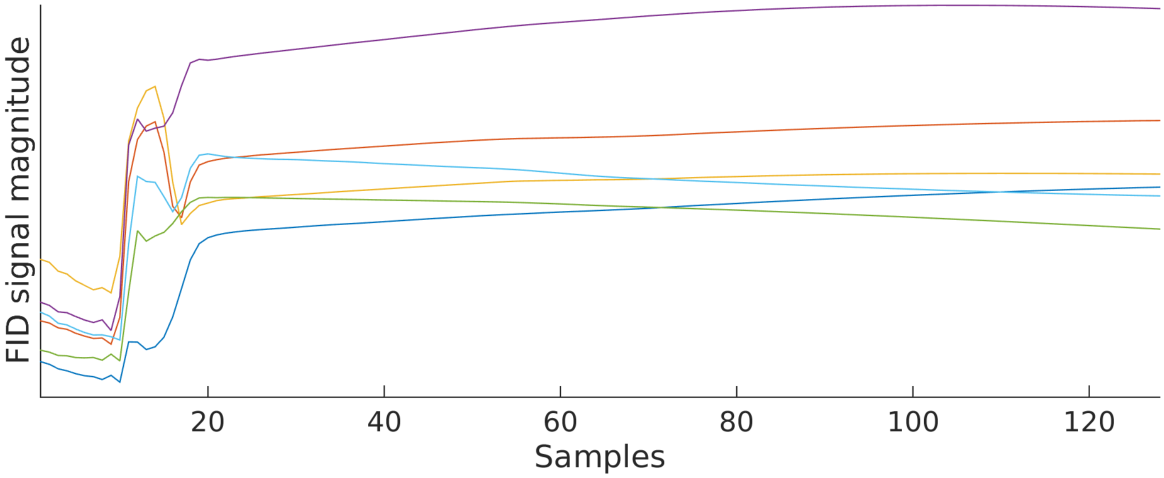

Figure 6.1 – Magnitude of the mean FID signal across all acquisitions. Six receive channels are displayed. The initial fluctuations are discarded.

### 6.1.3 Artefacts

Similarly to the SegFatNavs artefacts, the FID signal being acquired every $T_R$, it is sensitive to variations in eddy currents. Tests were made on a phantom in acquisitions without SegFatNavs, where the imaging sequence slice resolution and $T_R$ was varied. The default ascending **k**−space ordering as well as a smoother scheme, presented in Figure 6.2, were also compared.

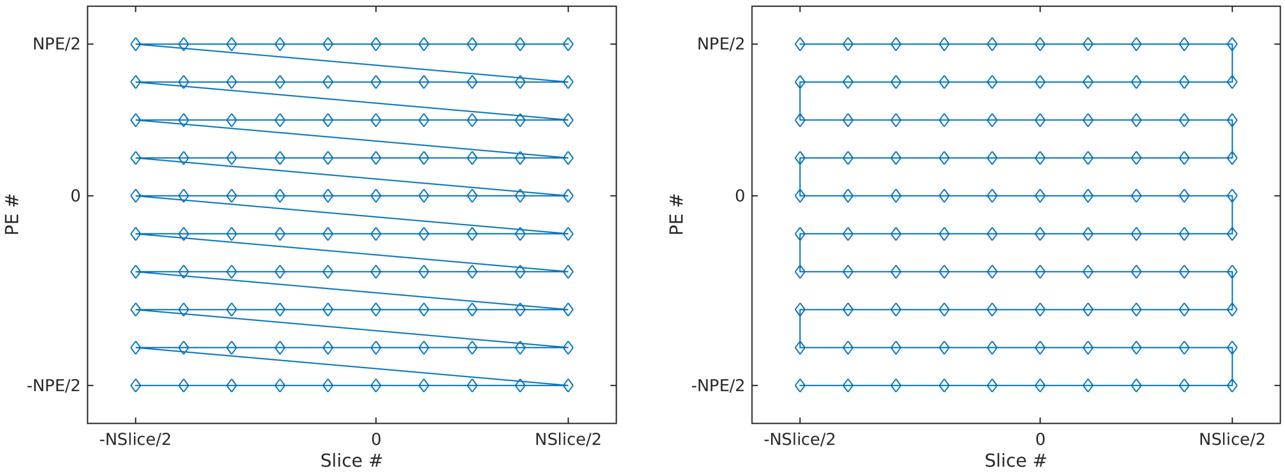

Figure 6.2 – Default ascending $\mathbf{k}-$space acquisition order (left) and modified smoother version (right).

The FIDNavs signal for both trajectories is shown in Figure 6.3. The peaks in the default Siemens trajectory happens when the inner loop of the 3D GRE starts over. This physically corresponds to the electric current in the gradient coil having the maximum positive value at the end of loop and having the largest negative value at the beginning of the loop. Roughly speaking, this reverses the eddy currents and hence induces a transient state (the peak). Afterwards, the system goes back to a constant change between kernel calls as visible by the low positive slope before the next loop iteration. In the smoother trajectory, the electric current variation is as small as possible, and hence no large peaks occur, but the slope changes polarity every other cycle. This corresponds to one polarity for progressing in the right direction in Figure 6.2, and the other for progressing left. Increasing the repetition time and hence the dead time before excitation, the artefacts magnitude decreases as expected. However even a 10 ms increase does not suffice to produce artefacts free navigators, see Figure 6.4. Also, decreasing the slice resolution and hence the maximum electric current has the same effect. Even at low resolution (2mm) and long repetition time, the artefact are significant and should be removed in order for the navigator signal change to be of physiological origin.

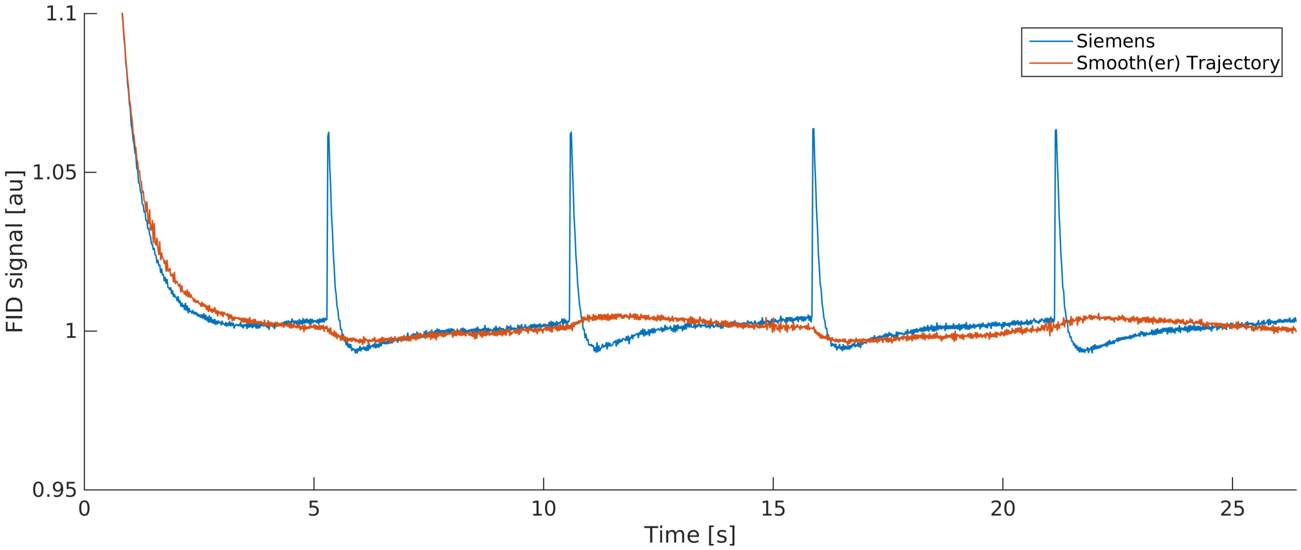

Figure 6.3 – FIDNavs signal for both trajectories of Figure 6.2 without SegFatNavs.

Figure 6.5 shows the impact of SegFatNavs inclusion. As is naturally expected, an additional

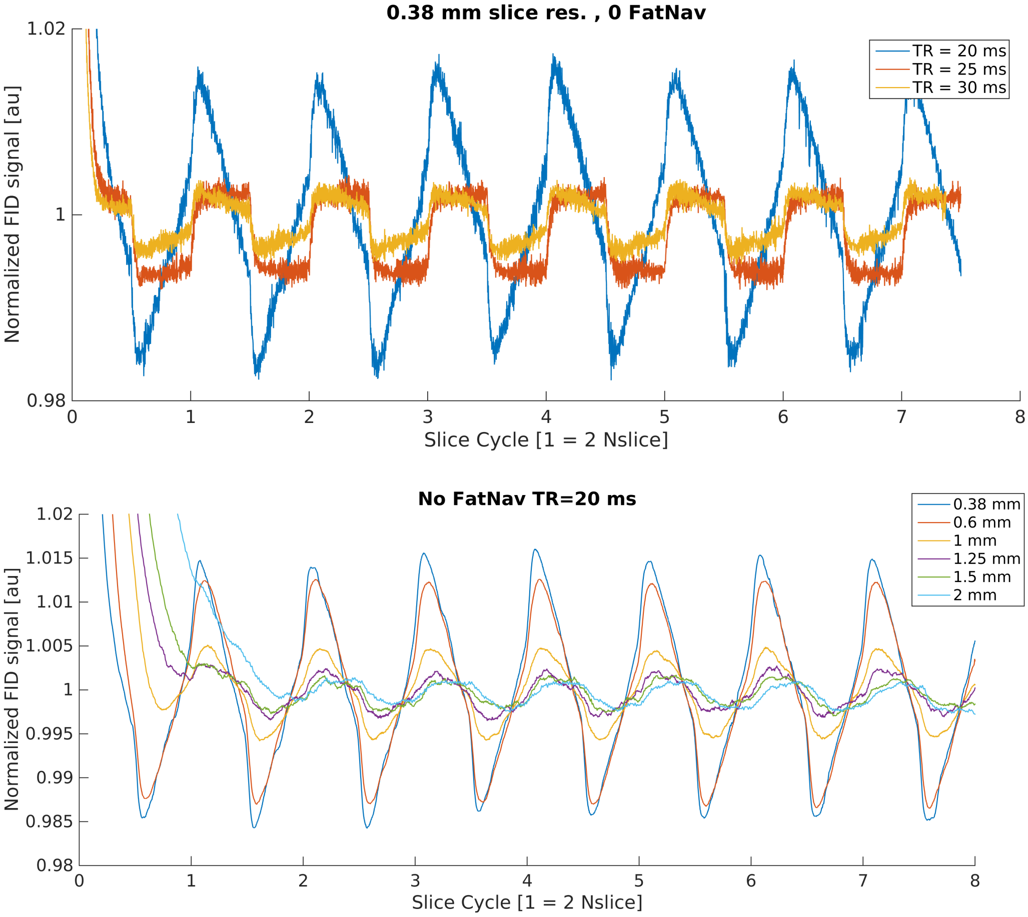

Figure 6.4 – FIDNavs signal of the smoother trajectory when changing the repetition time (top) or the slice resolution (bottom). The signal is smoothed in the resolution comparison for visual convenience.

repetitive fluctuation cycle linked to the SegFatNavs can be observed. It turns out that frequency analysis of the FIDNavs signal shows two fundamental frequencies associated with the SegFatNavs. The first is the inverse of the temporal resolution of the SegFatNavs. The second corresponds to the length of the inner loop of the SegFatNavs. For example, if the segmented direction has 12 steps and nSegments = 3, then the associated FID signal artefact will happen every 4 navigators. Despite the major artefact reduction of the smoother trajectory, it presents drawbacks. Due to its definition, it is highly similar every other phase encode steps in **k**−space (see Figure 6.2), so that eddy currents are exactly the same for every odd (or even) phase encode lines, but not between even and odd. This implies a slight FOV/2 ghosting in the phase encode direction in the final image. This was only noticeable in high-resolution phantom scans and not really significant in vivo. Also, as the FIDNavs cyclic artefacts are not removed but only diminished, they still need to be dealt with. The frequency of the smoother trajectory is half of the Siemens standard fully ascending trajectory, which implies that twice more harmonics need to be removed. Therefore, after careful considerations, the chosen implementation of the FIDNavs uses the Siemens trajectory and filters out the artefact frequencies before using the FIDNavs in conjunction with motion information.

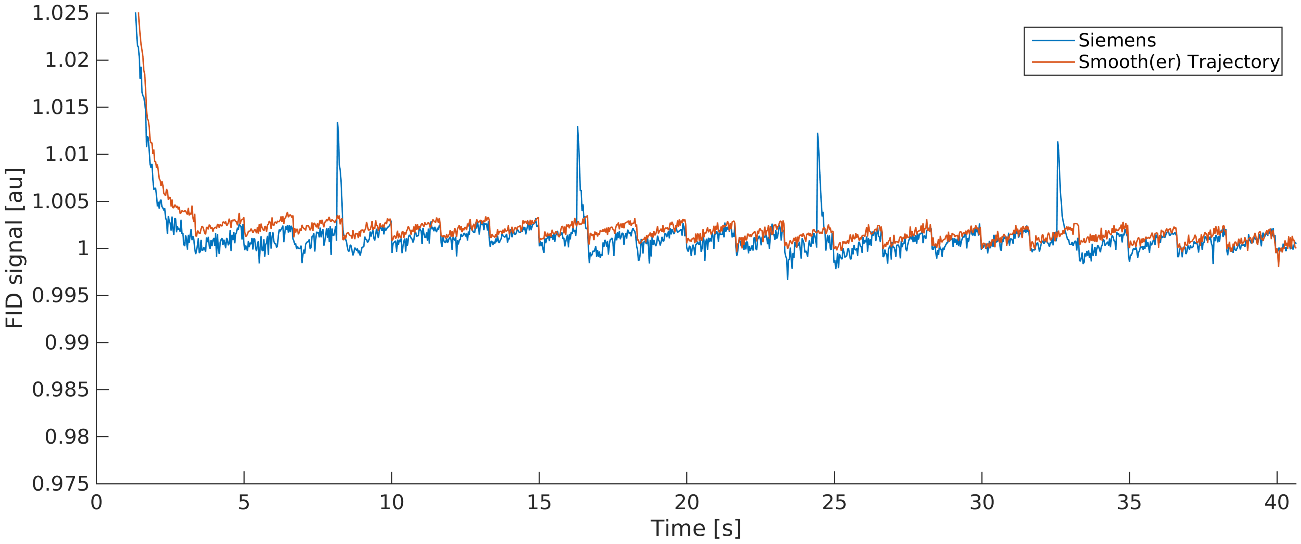

Figure 6.5 – FIDNavs signal for both trajectories of Figure 6.2 with SegFatNavs (nSegments $= 2$).

### 6.1.4 SegFatNavs as prior knowledge to the FID motion model

Here the procedure to use the motion information derived from the SegFatNavs as the training data to FIDNavs will be described.

1. The FIDNavs signal and motion parameters are filtered in the frequency domain to remove the sharp artefacts peaks (also see §5.1.4). The following filtering rule produced satisfactory results. As each fundamental frequency peak is of the form $1/M$, where $M$ is the number of imaging kernel calls needed for a cycle to repeat, the filter is defined as zeroing the spectra around all harmonics within a window of width $\frac{4}{M^2}$. The square comes from the approximation of the difference to a cycle of length $M+1$, i.e.

   $$\frac{1}{M} - \frac{1}{M+1} \approx \frac{1}{M^2}$$

   for large M.

2. Due to the vast difference in temporal resolution between both navigator types, ones needs to define a representative FID signal to associate with each SegFatNavs motion estimate. Let $t_f$ be the times of measurement of the FIDNavs and $\mathbf{y}_f$ the associated signals. $\mathbf{y}_f$ is a $2n_c$ dimensional vector at each time-points, where the factor 2 is because the real and imaginary part are concatenated.

   Let the SegFatNavs measurement times (of $\mathbf{k}-$space center) be called $t_s$ and the associated motion parameters $\mathbf{p}_s$. One must define a mapping function $T$ such that

   $$T(\mathbf{y}_f) \to \{\mathbf{y}_f\}_s \tag{6.1.6}$$

   where $\{\mathbf{y}_f\}_s$ is the representative FIDNav signal for the SegFatNav $s$ and its motion estimates.

   The natural candidate for $T$ is a combination of the FIDNavs acquired at times closest to $t_s$. In practice the mean of the $N_{\text{calib}}$ closest FIDNavs was chosen.

3. We can now turn to find the mapping functions between the representative FID signal and the motion parameters. In the spirit of [106], this was done by solving the linear model

$$\mathbf{p}_s = A\{\mathbf{y}_f\}_s + \mathbf{C} \tag{6.1.7}$$

for $A$ and $C$. In practice, the efficient and numerically stable way of solving such equation is to rescale the $2n_c$ FID signals to a value close to 1, and add a dummy constant FID signal equals to 1, leading to the usual pseudo-inverse inversion problem.

4. With the mapping in hand, it is applied back to the original FIDNavs to produce high temporal resolution motion estimates $\mathbf{p}_f$

$$\mathbf{p}_f = A\mathbf{y}_f + \mathbf{C}. \tag{6.1.8}$$

Due to the very short repetition time, of less than 50 ms in almost all cases, the subject pose is not expected to range significantly over few FIDNavs, therefore in practice $\mathbf{p}_f$ is temporally smoothed. Due to the linearity of the mapping, it is equivalent to apply the mapping to smoother FID signal. Roughly speaking, it amounts to trade some (unnecessary) temporal resolution for higher SNR of the motion estimates. The filter used in this work is the Tukey filter, which is defined as

$$f(\nu) = \begin{cases} 1 & \text{if } |\nu| < C \\ \cos^2\left(\dfrac{(|\nu| - C)}{P - C}\dfrac{\pi}{2}\right) & \text{if } C < |\nu| < P \\ 0 & \text{if } |\nu| > P \end{cases} \tag{6.1.9}$$

for passband $P$ and constant window $C$. It allows a reduction of Gibbs ringing while suppressing the high-frequency components and keeping the low frequencies ones unaltered.

The validity of the linear model was confirmed in practice in two ways. First, it can be thought a priori that, in order to capture non-linear effects, steps 3 and 4 can be applied repeatedly in a sliding window approach, allowing the combination of multiple local (in time) linear expansions. However, this approach did not produce any significantly different final motion estimates or associated corrections. Second, in datasets with many SegFatNavs volumes, a second order of the FID signal can be incorporated into the mapping and still stay a well posed inversion problem. The difference of the estimated motion to the linear model results were insignificant for compliant subjects. Of course while these observations are subject (or more precisely motion) specific, their redundancy, repeatability and concordance with [106] suggest the linear model as a reasonable assumption. One exception where the quadratic model proved superior will be presented in §6.2.3. Finally, if the SegFatNavs are dual echo, estimates of the $B_0$ temporal variations can be computed as in §3. Then, the exact same calibration and temporal resolution enhancement can be applied to the field fluctuation parameters.

The value of $N_{\text{calib}}$ should a priori be very important. A trade-off between staying close to the model and insure the motion state is close to SegFatNav estimate (small $N_{\text{calib}}$ values) and larger SNR (large $N_{\text{calib}}$ values) would be expected. In practice resulting motion parameters are very close for $N_{\text{calib}} = 5$ and $N_{\text{calib}} = 36$ for example, and associated motion corrected reconstructions only showed a few percent change in the voxels values, making them effectively the same image. Also, because the mapping does not mix the motion parameters, different values of $N_{\text{calib}}$ give the lowest residual error during the calibrations. However the differences of said errors were so small they did not justify further optimization.

## 6.2 Example applications

First, §6.2.1 presents application of FIDNavs and dual-echo SegFatNavs acquired on elderly subjects. Then in §6.2.2, direct link of the FIDNavs-based motion estimates to breathing and cardiac physiological trace will be demonstrated, as well as comparison of field fluctuation correction from FIDNavs and SegFatNavs when the latter sample breathing adequately. Finally, an intentional motion experiment will explore the limits of the method in the case of large motion.

### 6.2.1 $B_0$ fluctuation correction

#### Methods

Twelve healthy elderly subjects were scanned as part of a larger study. Scans were conducted by Dr. João Jorge on the 7T CIBM scanner. One of the acquired protocols was a 3D flow-compensated 3D-GRE axial scan, with a 0.375 × 0.375 × 1 mm resolution. Echo time was 20 ms and a 12° flip angle was used, along with a 120 Hz/pixel readout bandwidth. Two-fold undersampling with 64 reference lines, as well as 3/4 partial Fourier were used in the phase-encoding (left-right) direction to reduce the total scan duration.
The effective repetition time was 41 ms. Total scan duration was 11 minutes. The SegFatNavs module use the dual-echo protocol from §3 with nSegments = 2, leading a 2.2 s temporal resolution. The FIDNavs was acquired after the imaging sequence excitation pulse, had a 200 $\mu s$ duration and consisted of 64 samples the first half of which was discarded as discussed in §6.1.2. A sequence kernel schematic can be found in Figure 6.6.

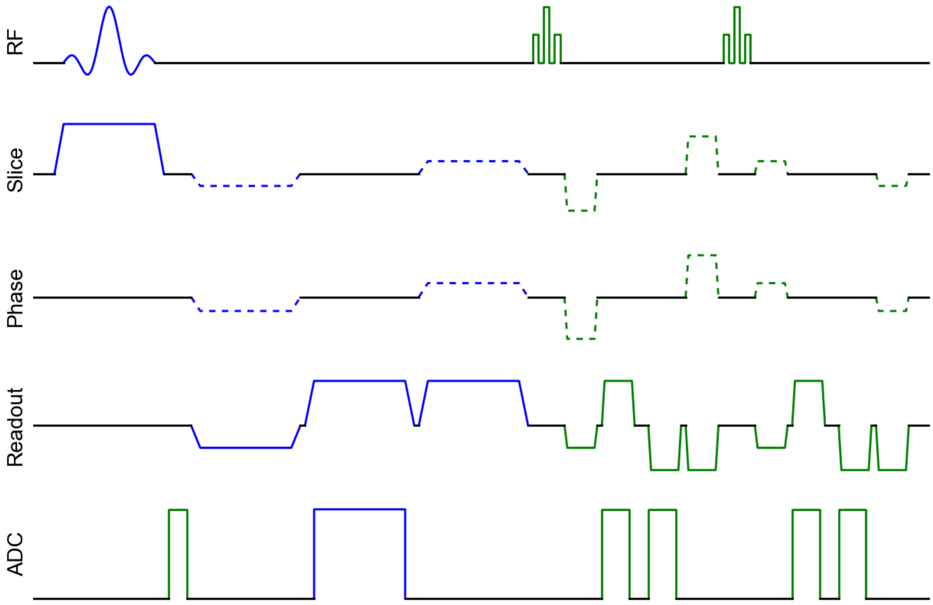

Figure 6.6 – Schematic of the sequence. Host imaging sequence is drawn blue and navigators green. Flow compensation gradients are omitted for simplicity. While the spoiling direction is consistent between host and SegFatNavs, the physical ($xyz$) axis represented by readout, phase and slice are different in practice, but are drawn on the same line here.

The six motion and four $B_0$ fluctuation parameters were estimated by the SegFatNavs and served as calibration to the FIDNavs as described in §6.1.4, with $N_{\text{calib}} = 54$. The resulting estimates were smoothed in time by a Tukey filter with a 1 Hz passing window and a 0.5 Hz constant window. Motion correction was applied both with and without field fluctuation.
All reconstructions were quantitatively compared to the raw reconstruction by computing the relative change of the normalized gradient squared metric, as for the MPT comparison work presented in §2.

### Results and discussion

Motion correction always improved the tissues boundaries sharpness, but visually no clear differences between the FIDNavs and SegFatNavs based reconstructions could be discerned. In most cases, significant field fluctuation artefacts remained and justified the inclusion of the dual-echo SegFatnavs. Overall, the FID based corrections showed significant improvements over the SegFatNavs based corrections, with better tissues homogeneity and reduced field fluctuation induced darkening, as is exemplified in Figure 6.7.

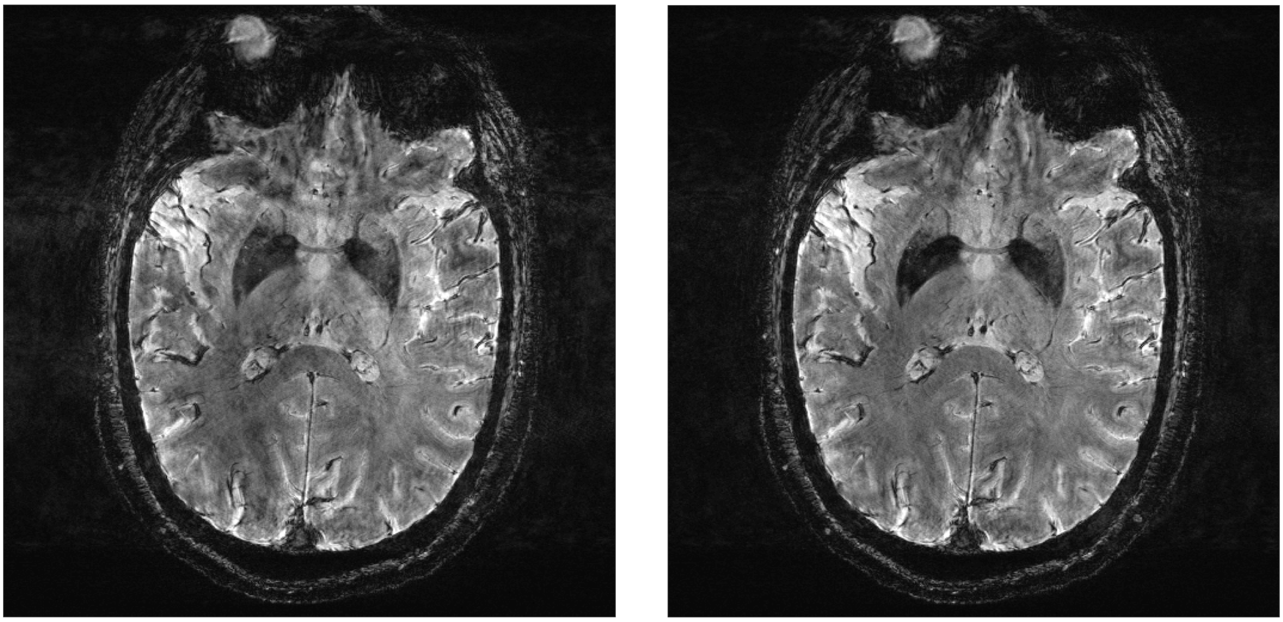

Figure 6.7 – Example of superior image quality obtained by the FID based correction (right) compared to the SegFatNavs based correction (left) (volunteer 1). The difference stems from the field fluctuation correction, see Figure 6.8.

The associated field fluctuation parameters are shown in Figure 6.8, where cyclic variations are recovered in the FID based estimates but missed in the SegFatNavs. While no physiological information was monitored during the scan, it is plausible that these cyclic variations are the expected breathing induced field change, as the most varying first spatial order component is in the head-foot direction. This is the demonstration of the FIDNavs allowing to retrospectively enhance the temporal resolution of correction parameters, which is the goal of the SegFatNavs and FIDNavs combination. This also proves to be a valid alternative to the snapshot FatNavs approach presented in §3, which highly suffered from low temporal resolution.
The artefacts filtering step applied to FIDNavs and SegFatNavs parameters consistently showed superior performances compared to unfiltered parameters based corrections. Jointly, excellent image quality of the uncorrected reconstruction for a very still subject suggests no major

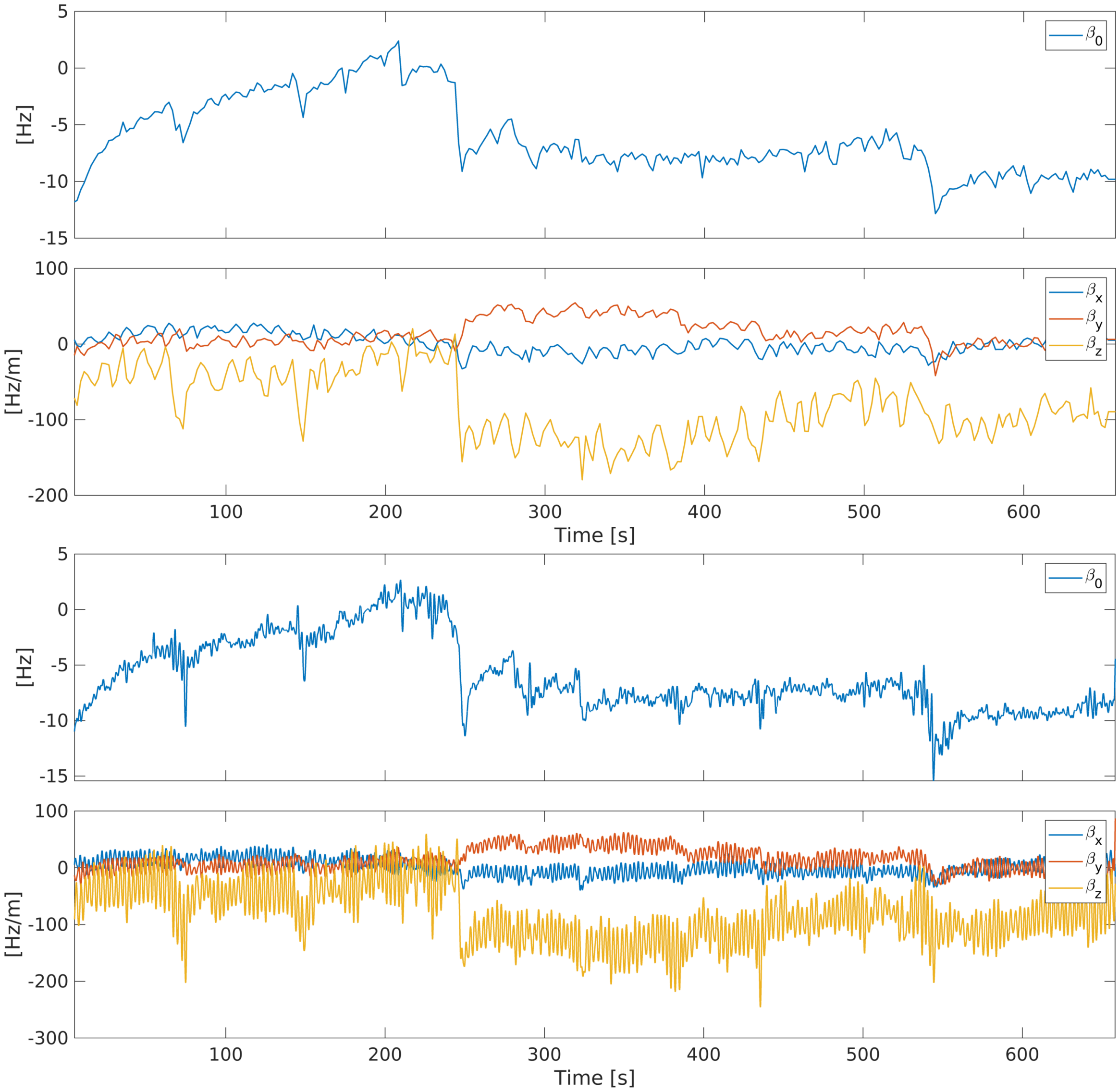

Figure 6.8 – Field fluctuation parameters (top: SegFatNavs, bottom: FIDs) associated to the reconstructions of Figure 6.7.

interferences between the imaging sequence and the SegFatNavs, see Figure 6.9 and Figure 6.10. The corrected reconstructions showed only subtle differences for this subject. Considered together, these observations strongly indicate that the source of cyclic artefacts found in the FIDs has no visible impact in the images but only on the navigators.

Figure 6.11 shows the metric change for all investigated corrections. Every previous visual observations are consistent with the quantitative results. Changes under 2% often do not represent clearly visually different images. As expected from the images, the field fluctuation correction greatly increases the metric further than motion correction only. The FIDNavs based reconstructions always out-performed the SegFatNavs based reconstructions, except for the motion only reconstruction of volunteers one and three, where the difference values are so low that they represent absolutely no visible change of the images themselves. This better performance of the FIDNavs based correction supports a posteriori the soundness of the implementation and the modeling choices.

Taking a step back, using dual-echo segmented FatNavs can be thought as audacious, as the

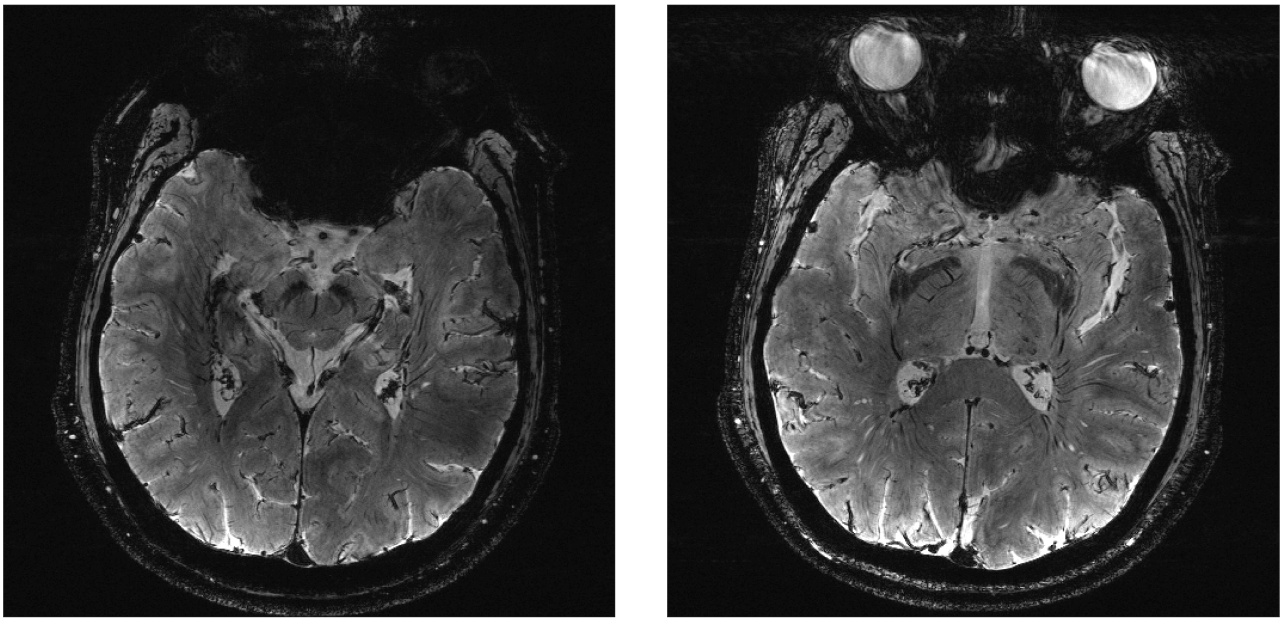

Figure 6.9 – Slices of the raw reconstruction of very compliant subject (volunteer 2).

navigator acquisition is spread over 2 seconds. This period is much longer than the period during which the field is in good approximation constant for natural breathing. The reason why retrospective correction is nevertheless achievable is the following. The fluctuating component of the field has a large spatial scale compared to the navigator resolution, as was discussed in §3. This means that only the center of the navigator $\mathbf{k}-$space really impacts the final estimates, and the region around said center is acquired in a shorter time-span. For example the 1 cm effective resolution $\mathbf{k}-$space is acquired in 0.67 s.

Finally, let us notice that the corrected results still show some signal artefacts outside of the brain, which indicates that the correction (most probably the field correction) is incomplete. The RMS value of the calibration residuals (during step 3, page 130), for all volunteers, is shown in Figure 6.12. While the linear model provides excellent values for motion, the field coefficient are close to the breathing range. This suggests the linear model is not a fully adequate model for FIDNavs based field fluctuation correction. While the FIDNavs allow partial correction and breathing recovery, the comparison to a SegFatNavs with sufficient temporal resolution to sample breathing was not attainable in this data. Therefore a dedicated experiment was performed and is the subject of the next section, where the link between physiological data and FIDNavs estimates will also be directly observable.

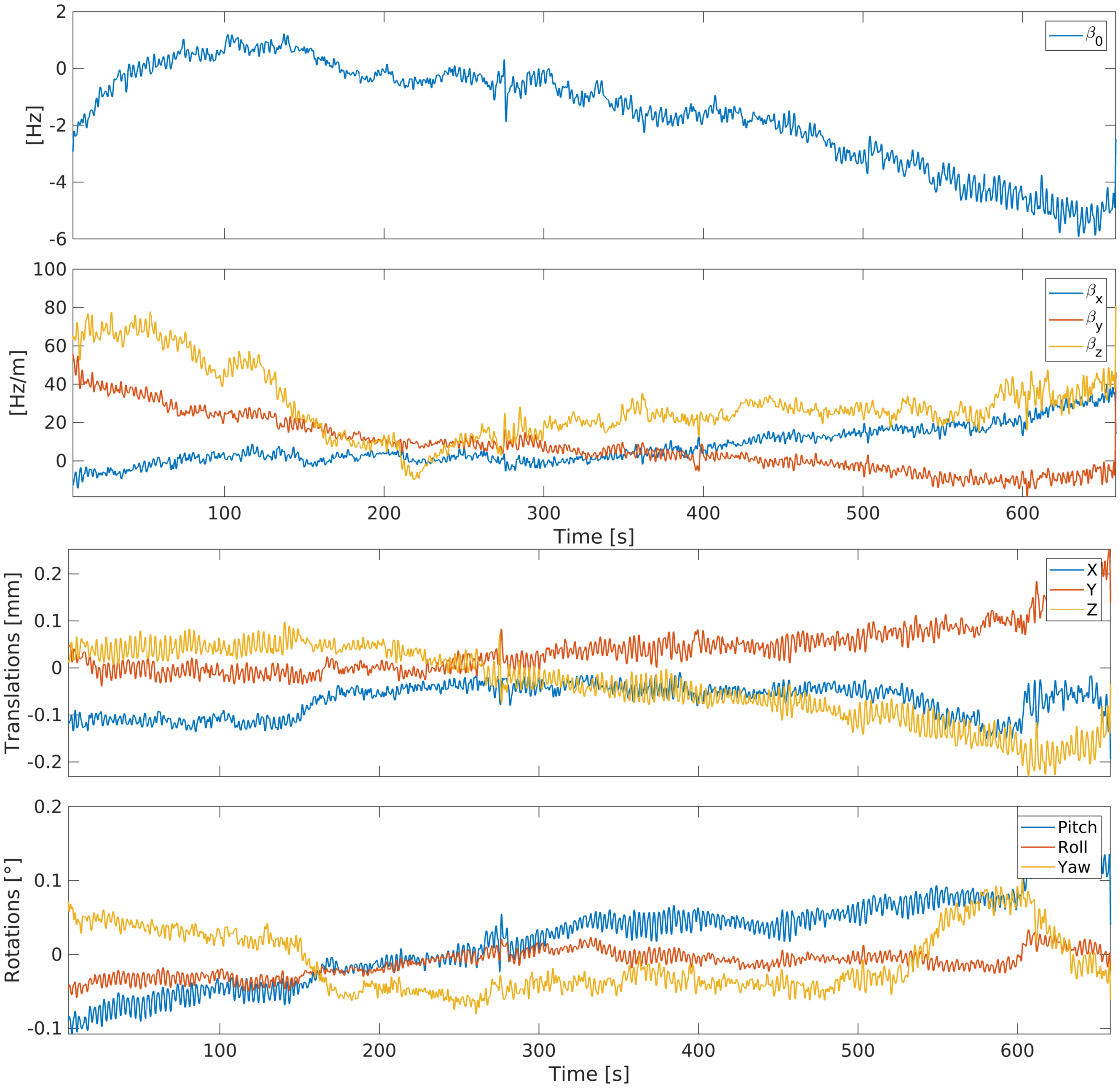

Figure 6.10 – Field and motion parameters of volunteer 2, as estimated by the FIDs.

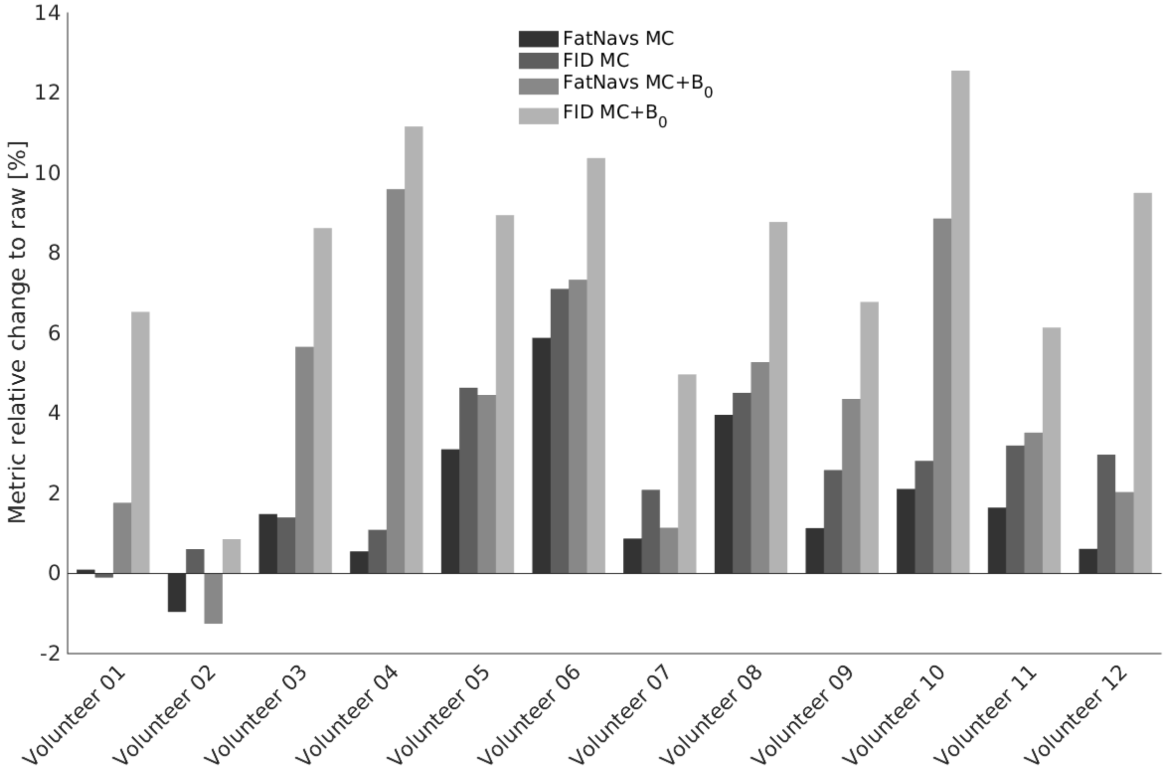

Figure 6.11 – Relative change of the gradient squared metric to the raw reconstruction for all corrections (MC = Motion correction).

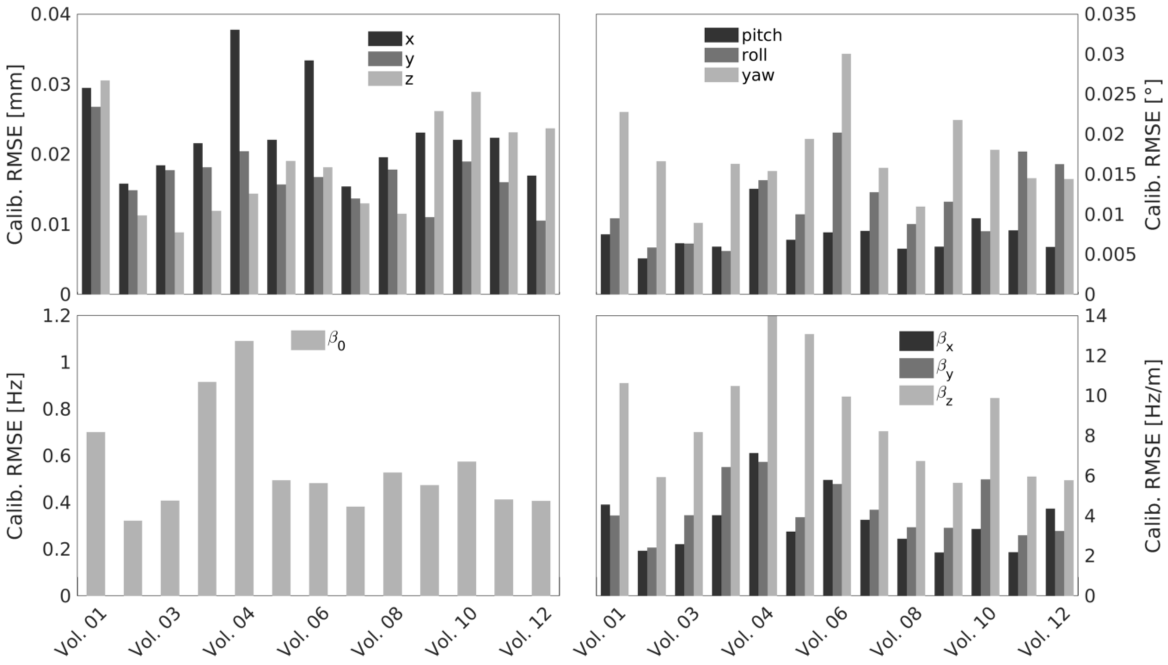

Figure 6.12 – RMS of the residual errors of the FIDNavs to SegFatNavs parameters calibration.

### 6.2.2 Link to physiological processes

**Methods**

A compliant healthy volunteer was asked to breath deeply and slowly during a high-resolution 3D GRE axial scan. The protocol parameters were 0.25 mm in-plane resolution and 1mm in the slab direction, 3/4 partial Fourier in phase and slice direction, and a readout bandwidth of 40 Hz/pix with $T_E/T_R$ 24/56 ms. No further undersampling lead to a 32 min 25 sec long acquisition. SegFatNavs parameters were the same as in §6.2.1 (4mm dual-echo), but with nSegments = 3 giving a temporal resolution of 2 seconds.
Physiological data was acquired by a respiration belt and a pulse oximeter placed on the right hand index finger. An optical trigger sent every FIDNavs allows synchronization between the physiological data and the MR data.
It should be recalled that this protocol was tailored to sample breathing with the SegFatNavs, and is not optimized in any other way. Due to the long repetition time of the dual-echo SegFatNavs, it is unlikely such high values of nSegments would ever find their place in established protocols.
All reconstruction and quantification processing was done as presented in §6.2.1. Results were compared to those of the elderly subjects study of §6.2.1 in order to compare the $B_0$ fluctuation correction of SegFatNavs to that of FIDNavs.
Additionally, every FIDNavs based parameter estimates (un-smoothed) was mapped to the closest cardiac event, and the time to the cardiac peak was stored as well. This was done after local (in-time) demeaning to remove slow drifts. The resulting data was binned to extract the mean motion during the cardiac cycle. A time-delay (0.17 s) was determined empirically to account for the travel distance differences between the brain and the index finger where the cardiac trace was measured.

**Results**

No visible differences between SegFatNavs and FIDNavs based reconstructions were found for motion only corrections. However, the SegFatNavs-based field fluctuation correction was visibly of higher image quality, with reduce blurring compared to the FIDNavs-based one, as is visible in Figure 6.13 (the residual signal outside the brain is good indicator of incomplete artefact removal). These observations are confirmed by the larger difference in the metric increase after correction, summarized in Table 6.1. In this case the SegFatNavs corrections always quantitatively outperformed the FIDNavs based corrections. When field fluctuation correction is applied, the SegFatNavs correction had an additional 2% increase compared to the FIDNavs correction. This in clear contrast to the results of the previous section §6.2.1, where the FIDNavs corrections had consistently higher metric compared to the SegFatNavs.

| **Reconstruction** | **Motion Corr.** | **Motion Corr.+ $B_0$** |
|---|---|---|
| SegFatNavs | 4.3 | 12.2 |
| FIDNavs | 4.0 | 9.8 |

Table 6.1 – Gradient squared metric percentage increase compared to the raw reconstruction.

The calibration residual RMS values of the FIDNavs mapping are shown in Table 6.2. These values are in the medium range of the previous experiment in §6.2.1. The ranges of $B_0$ parameters oscillations were also comparable.

| **x [mm]** | **y[mm]** | **z[mm]** | **Pitch [°]** | **Roll [°]** | **Yaw [°]** |
|---|---|---|---|---|---|
| 0.02 | 0.01 | 0.01 | 0.009 | 0.009 | 0.02 |

| $\beta_0$ **[Hz]** | $\beta_x$ **[Hz/m]** | $\beta_y$ **[Hz/m]** | $\beta_z$ **[Hz/m]** |
|---|---|---|---|
| 0.48 | 3.7 | 5.8 | 8.6 |

Table 6.2 – RMS of the residual errors of the FIDNavs to SegFatNavs calibration.

After Tukey filtering with a 0.5 Hz constant windows and a 1 Hz passband, the motion parameters time-courses were compared to the physiological data. The head-foot translation is shown in Figure 6.14. The respiration trace is nicely visible in the estimated motion, and the cardiac cycle can also be distinguished. However, for the cardiac motion, the superposition of all motion sources makes the observation more suggestive.

The motion parameters histograms around the cardiac trace peaks are presented in Figure 6.15. These results are very similar in amplitude to those found by MPT in [21]. The oscillatory cardiac pattern is nicely observed in the $y$ and $z$ translations and in the pitch rotation, as could be expected from the nod-like motion linked to blood flow direction.

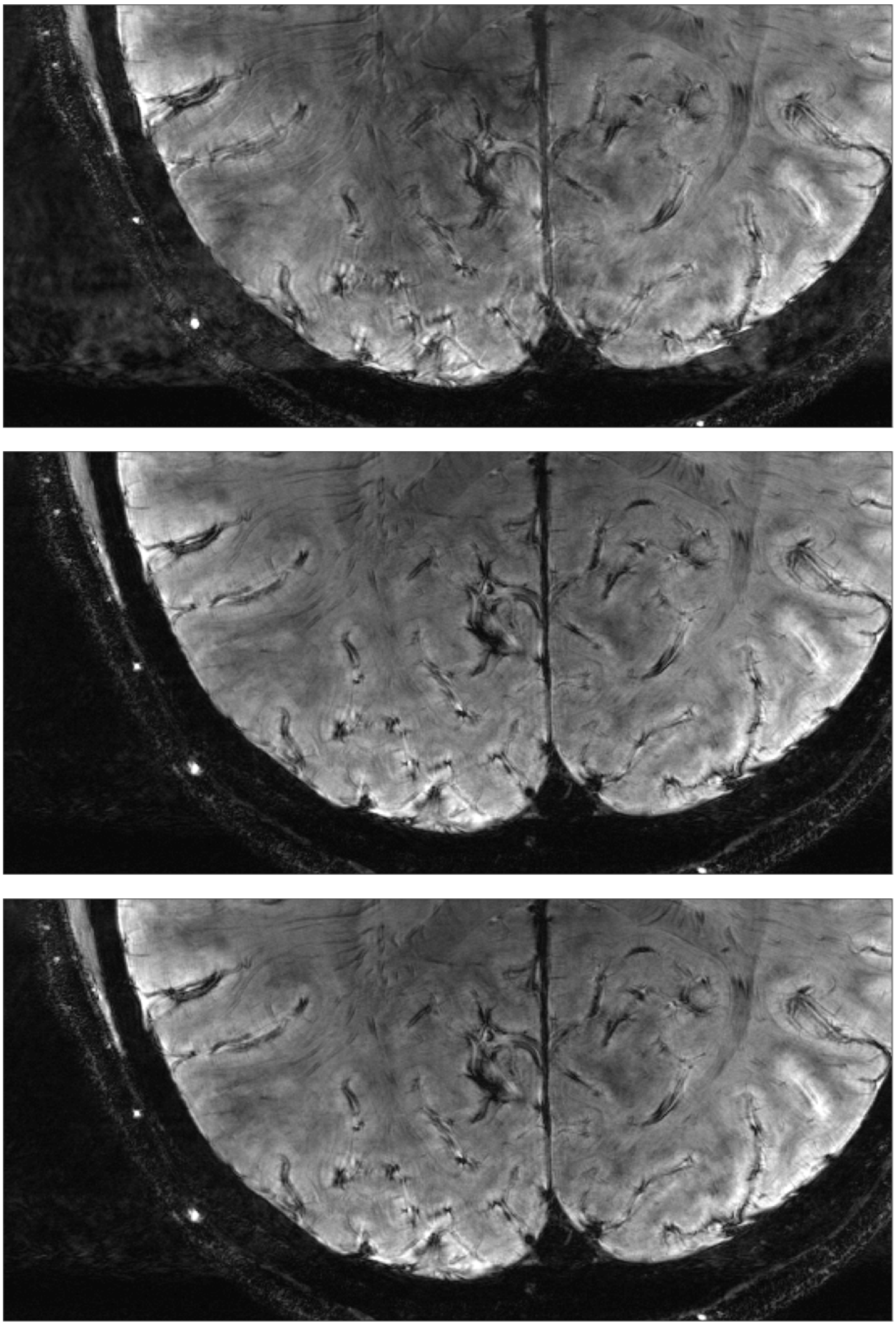

Figure 6.13 – Reconstructions where SegFatNavs sample deep breathing adequately. From top to bottom: raw, SegFatNavs-based correction, FIDNavs-based correction. All corrections include motion and first order $B_0$ compensation.

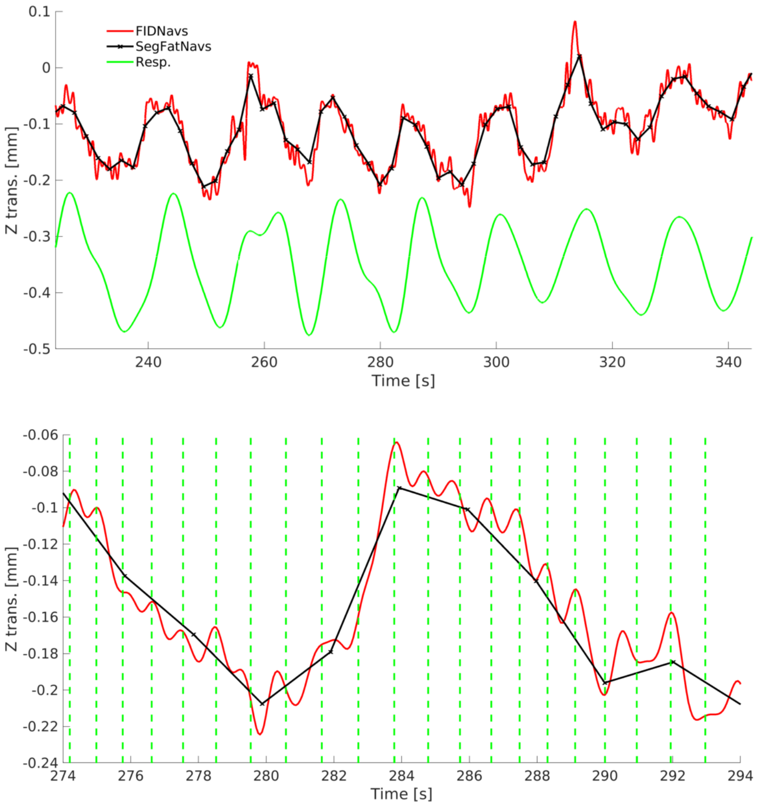

Figure 6.14 – $Z$ translation as estimated by the FIDNavs, after Tukey filtering (1 Hz constant window and 2 Hz passband). In green is the physiological data: breathing (top) and cardiac trace peaks (bottom).

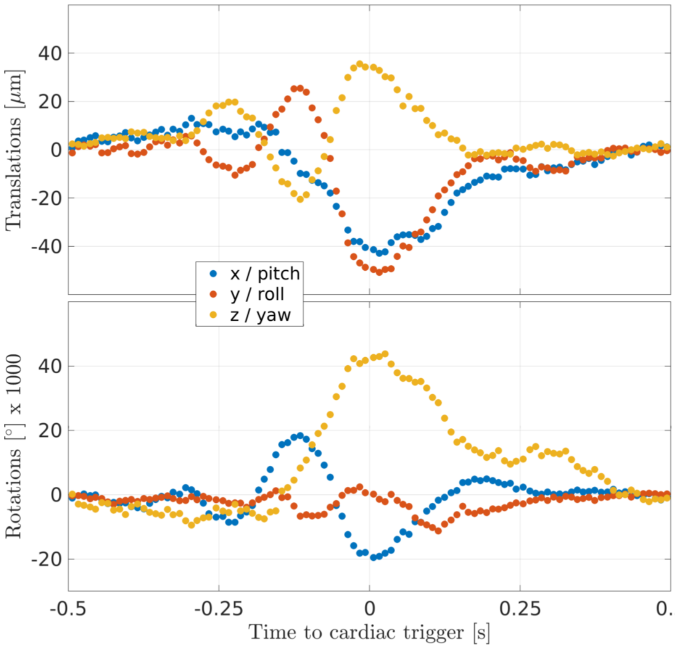

Figure 6.15 – Histogram of the FIDNavs motion parameters during the cardiac cycle.

### Discussion

While undeniable gain of image quality was achieved by the FIDNavs, the SegFatNavs proved superior for field fluctuation correction. The calibration errors and the field fluctuation amplitude were comparable to the previously presented data, making the temporal resolution the most significant difference.

The logical conclusion to all the results obtained by the FIDNavs is that while they allow to enhance temporal resolution, their estimates of field fluctuation parameters is inferior to that of SegFatNavs. As by definition of the method it is always possible to reconstruct corrected images based on either navigator types, the inclusion of FIDNavs is always advantageous. A quick look at the correction parameters from both modalities (such as Figure 6.8 and Figure 6.14) immediately hints at which reconstruction is likely to be the most adequate. In any case both corrected images can also be compared directly.

The motion during the cardiac cycle could be identified, and is close to previously reported data from MPT tracking. Clearly, compared to the presented mean motion during the scan, there is a lot of variability in the motion trace during each cardiac events. This variability stems from the superposition of different motion patterns (cardiac, breathing, drifts, etc ....) on one side, and from the inherent precision of the FIDNavs motion estimates. The latter is impossible to estimate in vivo without external tracking, as it would require a perfectly still subject, without breathing or cardiac activity.

However, practically speaking, the usefulness of including motion frequency components higher than 1 Hz is questionable, as the associated motion is, at most, around 0.1 mm. The range of pulsatile motion which isn't properly described by non-rigid motion is of the same order [20], so it is more than likely that investing large efforts to correct for the rigid-body component is not worthwhile.

### 6.2.3 Sudden intentional motion as a limitations demonstration

#### Methods

The acquired protocol was a single slab of a 3D home-made TOF sequence, as presented in §5.2. The nominal resolution was 0.5 mm isotropic with a 128 size in the slab direction. Undersampling was performed via a partial Fourier factor of $^3/_4$ in phase and slice directions, as well as two-fold acceleration in the phase encoding direction (left-right) with 32 calibration lines. The $\mathbf{k}-$space trajectory was the standard Cartesian ascending scheme. The SegFatNavs was the 4mm protocol as presented before with nSegments = 1, and the FIDNavs were included in the SegFatNavs. The venous saturation flip-angle was 45°and the readout bandwidth 330 Hz/pixel. The effective repetition time and the SegFatNavs temporal resolution were 21 ms and 2 s respectively. The acquisition time was 4 min 59 s.

Five different scans were acquired. One with no intentional motion (rest), and four with an intentional nod-like motion. The motion was induced by a direct visual instruction, visualized via a mirror attached to the RF coil array. The display viewed by the participant read *Do no move* as a static screen, and a blinking red *MOVE* text when at a particular completion of the $\mathbf{k}-$space acquisition. Three intentional motion scans had a single nod, at the $\mathbf{k}-$space center, edge and intermediate positions respectively. The last intentional motion scan had a nod instruction every 21 s. These different patterns are summarized in Figure 6.16.

Raw, SegFatNavs and FIDNavs based reconstructions were compared. The motion parameters estimated from the FIDNavs were smoothed with a 1Hz constant band and and 2 Hz passband Tukey filter before correction. Three FIDNavs based reconstructions will be presented: one with $N_{\text{calib}} = 96$ (equivalent one whole SegFatNavs volume), one with $N_{\text{calib}} = 5$ and the last with $N_{\text{calib}} = 5$ and a quadratic model mapping the FIDNavs signal to the motion parameters. The reasoning behind these variations are that the motion being intentional larger motion range may occur than otherwise for a compliant subject. Also, as the motion is sudden, the impact of varying $N_{\text{calib}}$ may be more significant.

For each scan, the motion range (derived from SegFatnavs) was defined as the difference between the maximum and the minimum motion parameters values. Additionally to the normalized gradient squared norm computed on the 3D reconstructions, the average edge strength (AES) was computed on the axial maximum intensity projection (MIP). It is defined as (see [108])

$$\text{AES} = \frac{\sqrt{(E\mathbf{m})^2}}{\sum_i E_i} \tag{6.2.1}$$

where $\mathbf{m}$ is the 2D image vector and $E$ is the edge mask. For angiography images, it was found to make little difference to compute the metric on the full image, as it is in good approximation its own edge mask. Results from a healthy volunteer will be discussed.

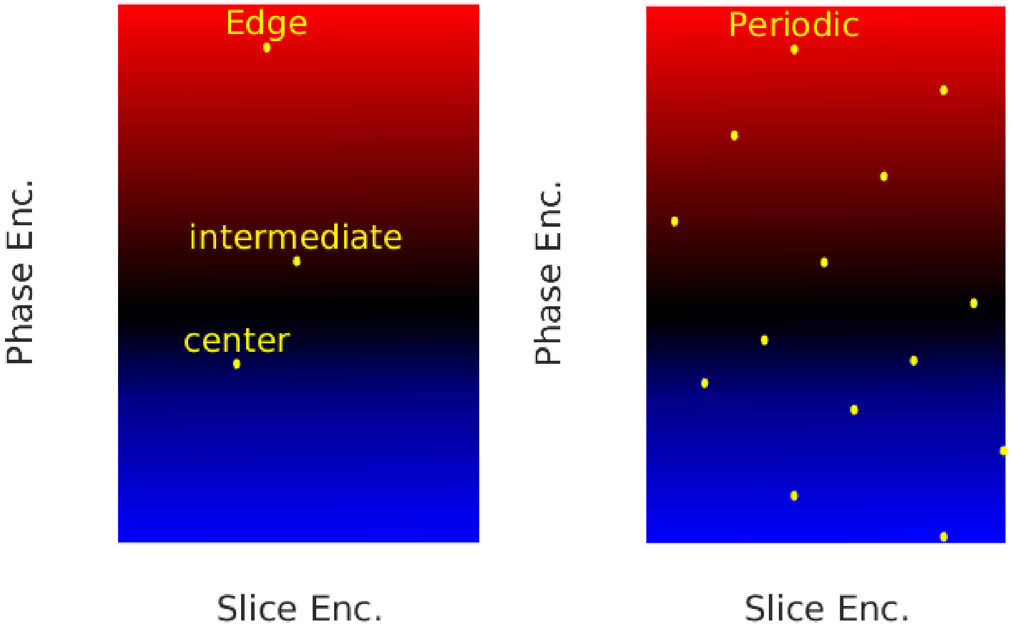

Figure 6.16 – Color-coded **k**−space trajectory (from red to black to blue), with yellow markers representing when the nodding instruction was presented to the subject. Single nod scans are on the left and the periodic instruction scan on the right.

### Results

Table 6.3 shows the motion ranges for each scans. The volunteer was compliant as can be seen from the rest scan. For all intentional motion scans, the pitch rotation angle and the $y$ shift are the most varying parameters, as expected from a nod. The periodic scan had a significantly larger range ($\geq 7°$) than the other intentional motion scans ($\leq 3°$). For this and for its periodicity, the associated results shall be discussed last.

First, let us present the direct observations of the different FIDNavs based reconstructions. Comparison of the 3D datasets showed the quadratic model allowed to reduce ringing for the center scan, but was otherwise indistinguishable to the linear model for the rest, edge and intermediate scans. Changing the value of $N_{\text{calib}}$ showed no clear differences, except for the center scan where blurring was slightly reduced in the $N_{\text{calib}} = 5$ reconstruction. For these reasons, all FIDNavs images presented here are using $N_{\text{calib}} = 5$ and the quadratic model.

For the rest and single nod scans, the SegFatNavs and FIDNavs reconstructions did not present significant visual differences, and did improve image quality. All FIDNavs reconstructions of these scans are shown in Figure 6.17. The closer to the **k**−space center the motion takes place, the more

| | **x** | **y** | **z** | **Pitch** | **Roll** | **Yaw** |
|---|---|---|---|---|---|---|
| **Rest** | 0.29 | 0.30 | 0.45 | 0.32 | 0.14 | 0.16 |
| **Edge** | 0.48 | 2.97 | 0.74 | 2.13 | 0.20 | 0.12 |
| **Intermediate** | 0.64 | 3.35 | 1.25 | 2.34 | 0.42 | 0.22 |
| **Center** | 0.50 | 4.50 | 1.56 | 2.85 | 0.28 | 0.24 |
| **Periodic** | 1.88 | 14.06 | 4.90 | 7.21 | 1.05 | 0.76 |

Table 6.3 – Motion range for all scans as estimated from the SegFatNavs.

incomplete the motion correction, as can be seen from the increasing blurring signal outside of the brain and the decreasing vessels SNR.

Figure 6.18 shows the SegFatNavs and FIDNavs reconstructions of the periodic nods scan. While improvement compared to the raw reconstruction was visible, the motion corrected reconstructions remained very far from diagnostic quality (see the rest scan in Figure 6.17 for comparison). While the SegFatNavs scans shows slightly sharper vessels delineation, the significant large scale artefacts present in both reconstructions make a clear-cut comparison difficult.

The metrics percentage increases compared to the raw reconstruction are shown in Figure 6.19. For single nod scans, both metrics reflected the qualitative observations. The quadratic FIDNavs reconstruction was the better performing of the three FIDNavs reconstruction. For the rest and single nod scans, the AES metric follows the observations made on MIPs and the normalized gradient squared metric the ones on the 3D data. AES tends to be less sensitive to ringing as such artefacts have lower visibility in maximum intensity projection, arguably explaining the discrepancy between AES and the gradient squared results for the non quadratic FIDNavs reconstructions of the center scan. For the periodic scan, the gradient squared metric was always decreasing, unlike image quality, and the AES showed improvement for the SegFatNavs reconstruction but not for the FIDNavs one, again unlike qualitative observations.

Finally, out of completeness, the reference SegFatNavs volume for registration was changed to the third one in the center scan to check if this could be another source of error, as the reference volume is standardly picked as the one closest to the $\mathbf{k}-$space center. The comparison between both motion traces showed the differences were negligible.

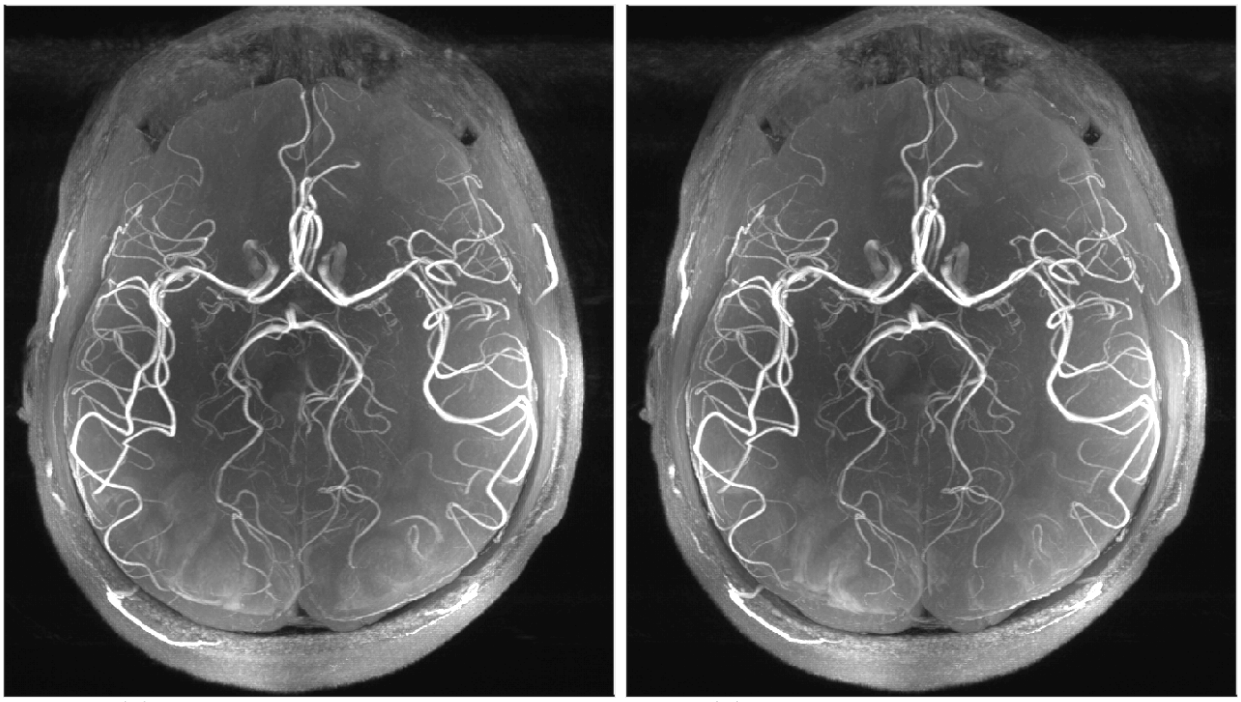

(a) No intentional motion scan.

(b) Motion trigger at $\mathbf{k}-$space edge.

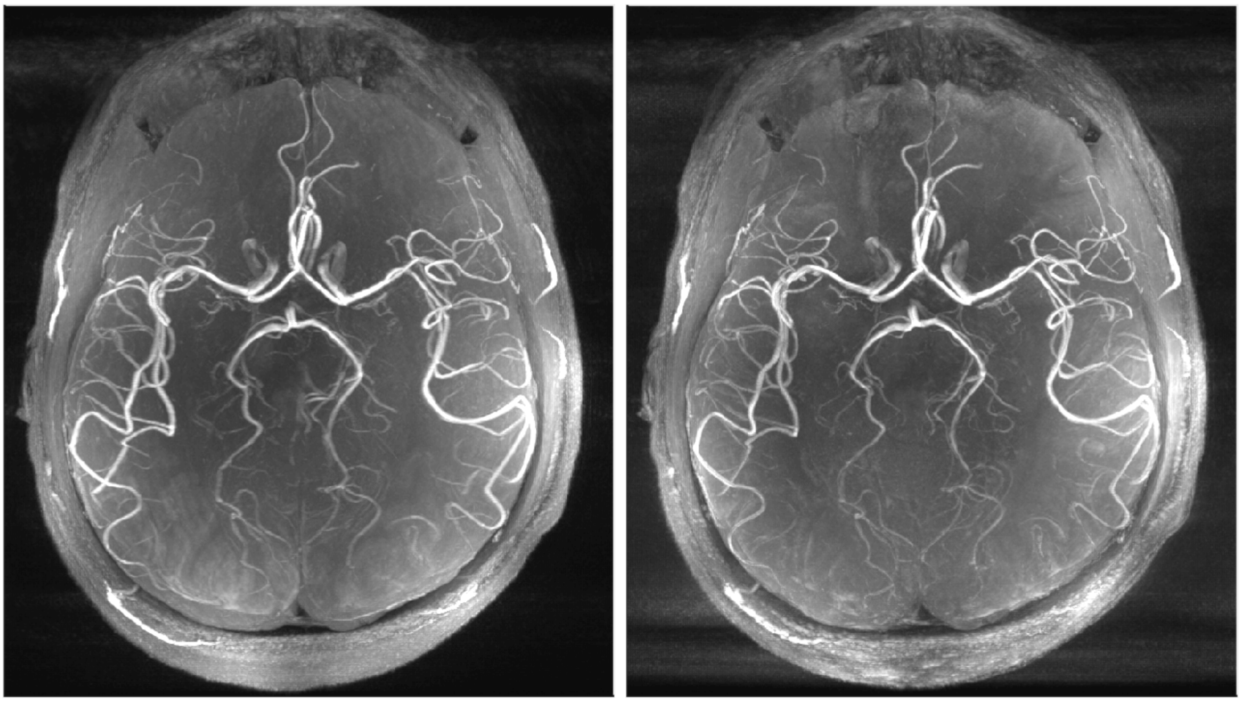

(c) Motion trigger at intermediate $\mathbf{k}-$space position.

(d) Motion trigger at $\mathbf{k}-$space center.

Figure 6.17 – Axial MIP of the FIDNavs based motion corrected reconstructions for the rest and single-nod scans.

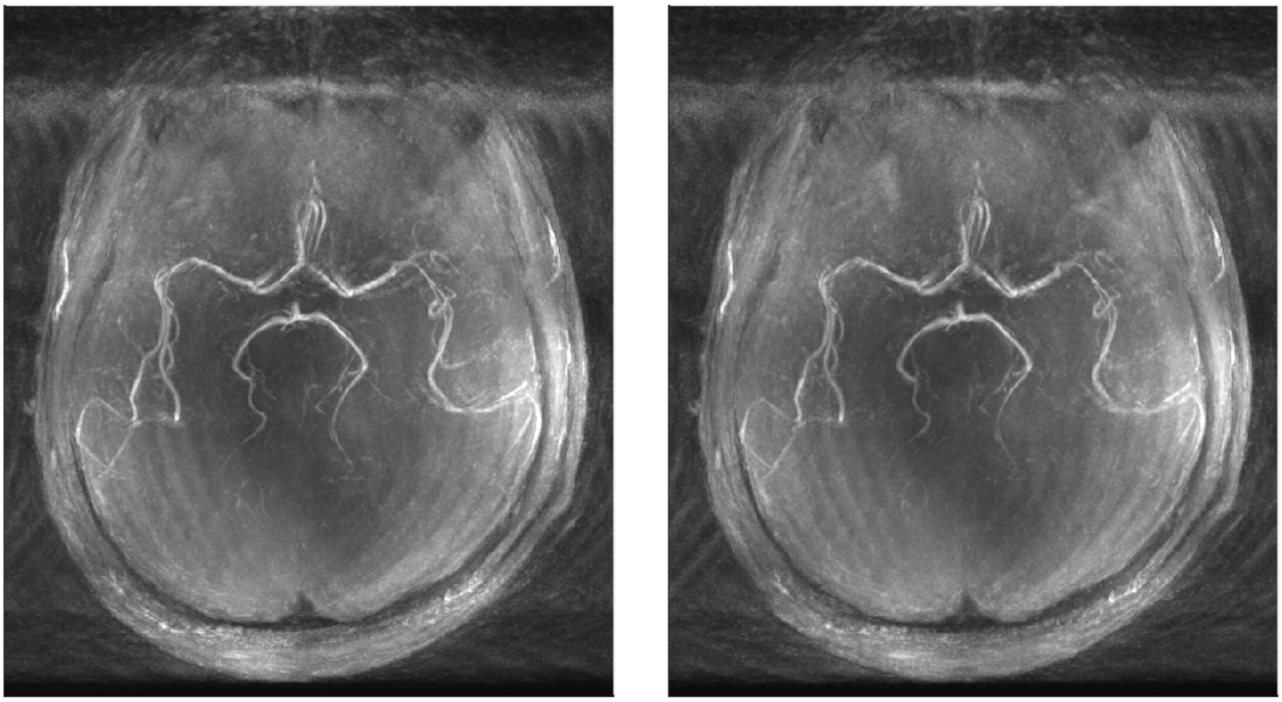

Figure 6.18 – Axial MIP of the SegFatNavs (left) and FIDNavs based motion corrected reconstructions for the periodic nod scan.

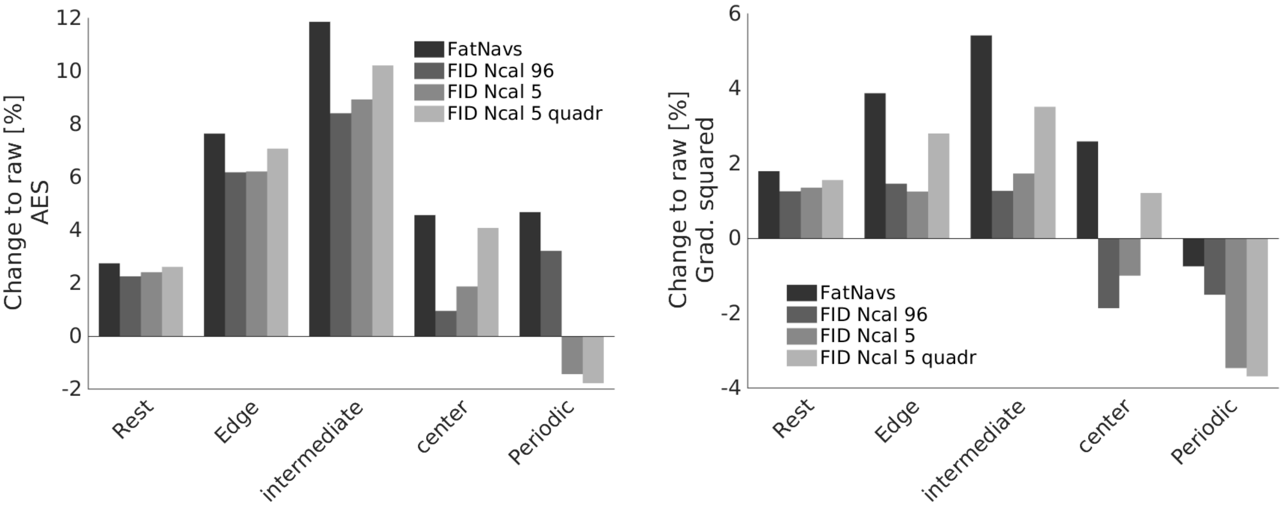

Figure 6.19 – Relative metrics change to the raw reconstruction: AES (left) and gradient squared (right).

### Discussion

While definite gain of image quality was obtained by the motion corrections, only the edge intentional motion scan was on par with the rest scan. The intermediate and center scans were noticeably of lesser quality, with added blurring and slightly lower vessel sharpness associated to lower signal. The periodic scan reconstructions would be unusable for diagnostics. This can arguably be due to the larger motion range during the scans and the more frequent nodding, as it can be thought as adding together the artefacts of single-nod scans. SegFatNavs and FIDNavs reconstructions were on par in all scans except the periodic one.

The metrics results were corroborating visual observations for the rest and single nod scans. The FIDNavs correction using a quadratic model was visually superior to a linear one for the center scan but equivalent otherwise. The metrics however always deemed it superior.

The periodic scan results have to be taken with a grain of salt. While image improvement was visible, it remained largely insufficient. Furthermore, the AES should presumably not be computed without an edge mask in this case due to the large blurring artefacts. Given the large incompleteness of the correction, no further attempts to quantify its efficacy were investigated.

In a broader perspective and comparing to all previous results obtained by SegFatNavs and FIDNavs, large and through plane motion is certainly a main source of the poorer performance of the retrospective motion correction in this experiment, despite the relatively large (6 cm) slab thickness. Also, the large range of motion of this experiment certainly explains the superiority of the quadratic model for the FIDNavs correction, whereas such model had not presented any advantage for the previous applications.

Further work could look to repeat this experiment for in-plane motion or non-slab selective protocols. While a definite study of the most likely motion during a scan is still lacking, it is reasonable to think that nodding is among the predominant types, while a left-right motion isn't. Most slab-selective scans are however axial, hence the choices made for this experiment. While high-resolution non-slab selective scans would certainly induce excessively long scan session duration, larger slabs may be a worthy compromise to reduce uncorrectable spin-history effects and better define the applicability boundaries of retrospective motion correction.

## 6.3 Summary and outlook

This chapter demonstrated that FIDNavs can be used to retrospectively up-sample the temporal resolution of correction parameters obtained from SegFatNavs. While the impact on motion correction was not significant, tremendous gain of final image quality was obtained for field fluctuation correction in cases where SegFatNavs under-sampled breathing. However, in cases where the breathing is properly sampled by the fat navigators, the SegFatNavs correction is slightly superior to the FIDNavs one, a potential sign of the limits of the quality of obtainable information from the FID signal fluctuations.

As an extension, combination of the navigators methods presented here with auto-focusing methods for both motion [62] and $B_0$ fluctuation [109, 110] is certainly worthy of study. It would allow either to constrain the auto-focusing methods by using the navigators information as prior knowledge or initial parameters value input, or to potentially bypass some of navigators modeling errors by giving more freedom to the self-driven methods.

Finally, the intentional nodding experiment demonstrated that FIDNavs provide similar motion correction performance to SegFatNavs if using a quadratic model in the case of nodding. However, they also hit the inherent limitations of the retrospective correction approach by proving incapable of fully compensating motion when it is large and close to $\mathbf{k}-$space center, as well as providing non-diagnostic final image quality for large periodic motion.

# Chapter 7

# Thesis summary and outlook

In this conclusion chapter the main results of the thesis are summarized and outlooks for future works are discussed.

## 7.1 Summary of the results

Refinements of the original FatNavs implementation was proposed. Tailoring the excitation pulse allowed to further reduce off-resonance water excitation during fat selection. Also, MT effects were diminished when included in MP2RAGE by lowering the navigator flip-angle and maximizing dead-time before the inversion pulse. However, in the case of very-high resolution protocols some slight difference compared to navigator-free acquisitions can still be observed. Finally, EPI-like FatNavs showed similar motion tracking and correction performance, while reducing the acquisition time by half, making a 2 mm volume obtainable in around 600 ms. This opens the way to wider applications of FatNavs.
Direction comparison to Moiré Phase Tracking confirmed the expected benefits and downsides of FatNavs of different resolution and temporal resolution for tracking specific motion patterns. For a still subject, both tracking methods agreed up to an accuracy $\lesssim 0.1$ mm (°) for 2 mm FatNavs, and $\lesssim 0.2$ mm (°) for 4 mm FatNavs. The corrected 0.5 mm MP2RAGE images based on either MPT or FatNavs were indistinguishable for a vast majority of the compliant subjects (7/9, two scans each), superior to MPT in one case and inferior in the last one. This study establishes FatNavs as a valid alternative to MPT in neuro-imaging research of cooperative subjects.
In order to be implemented into a much wider class of imaging sequences, segmented FatNavs were proposed. While they retain some inherent limitations of the original FatNavs, such as low temporal resolution, and require additional processing, they showed great potential for time-of-flight angiography, where for example ultra-high resolution 0.25 mm scans clearly benefited from the added motion correction. Also, the MT induced by the SegFatNavs was shown to be equivalent to the vendor-provided MT pulse.
Combination of SegFatFavs with FIDNavs allowed to enhance the temporal resolution of the motion estimates, and direct link to physiological events, notably breathing and cardiac functions, was established. Still, the approach was unable to correct for large motion which took place close to the $\mathbf{k}-$space center or repeatedly during the scan.
Finally, extension of FatNavs to a dual-echo version allowed to quantify and correct for up to first order magnetic field fluctuations. The estimated accuracy of the method was 0.3 Hz for the zeroth order and 2.8 Hz/m for the first order components respectively. While combination with FIDNavs made this approach more effective for subjects breathing naturally, the FIDNavs based corrections were slightly inferior in cases where the SegFatNavs temporal resolution was sufficient to sample

breathing. Still, very significant image quality improvements were consistently observed in elderly subjects.

## 7.2 Outlook

Given the results of this work, it seems clear that some FatNavs implementations are ready to be tested in some clinical protocols. As the original FatNavs aim mainly to capture drifts and periods of constant pose, they are expected to work best for cooperative subjects cohort. More generally, the implementation of some robust motion correction strategy may initiate a trend to acquire higher-resolution images in hospitals, which in turn could help refine diagnosis in a reliable manner compared to current protocols.

The question of the performance attained by (Seg)FatNavs in a clinical setting for a patient cohort, potentially along FIDNavs, remains only partially explored, and is certainly of interest for further studies as many clinical imaging protocols can afford some FatNav implementation with little impact on the water signal and scan duration.

Applications of the SegFatNavs/FIDNavs combination to ultra-high field, phase based imaging such as SWI or QSM may allow to reduce method-induced variability between subjects/scans, which would be a valuable addition in neuroscience research. Furthermore, it may also prove beneficial for MR spectroscopy, where the field change associated to motion and the long acquisition time can often lead to unusable datasets. The impact of the navigator inclusion on the metabolites quantification would need to be carefully studied in such implementations.

Additional contrasts not explored in this work could benefit from FatNavs, such as arterial spin labeling or phase contrast angiography. However, not all sequences would be fit for FatNavs. For example, introduction of FatNavs into a bSSFP type sequence should lead to significant impact on the imaging contrast, and hence other motion correction would a priori be preferable.

Deep learning has been the source of significant interest in recent years, including applications to medical imaging. While current deep learning based motion correction works tend to produce over-smoothed images, implementation of deep learning steps into others motion correction methods are without a doubt worthy of study. For example it seems a priori possible, given enough training data, to bypass navigators reconstructions entirely and go directly from $\mathbf{k}-$space data to motion parameters. Combining navigator based motion corrected reconstructions with additional specific deep learning tools should also help reduce residual artefacts, sourcing from either motion or other phenomena, such as pulsatility artefacts.

In the same line of thinking, incorporating navigator information into auto-focusing algorithm may help convergence to more accurate motion parameters estimates. Conversely, the auto-focusing part could help augment the temporal resolution of navigator information and reduce the impact of insufficiently accurate motion estimates.

# References

## References

[1] I. I. Rabi, J. R. Zacharias, S. Millman, and P. Kusch, “A New Method of Measuring Nuclear Magnetic Moment”, *Physical Review*, vol. 53, no. 4, pp. 318–318, 1938, ISSN: 0031-899X. DOI: `10.1103/PhysRev.53.318`. [Online]. Available: `https://link.aps.org/doi/10.1103/PhysRev.53.318`.

[2] F. Bloch and I. I. Rabi, “Atoms in variable magnetic fields”, *Reviews of Modern Physics*, vol. 17, no. 2-3, pp. 237–244, 1945, ISSN: 00346861. DOI: `10.1103/RevModPhys.17.237`.

[3] N Bloembergen, E. Purcell, and R. Pound, “Relaxation effects in nuclear magnetic resonance absorption”, *Physical Review*, vol. 73, no. 7, pp. 679–715, 1948, ISSN: 0031-899X. DOI: `10.1103/PhysRev.73.679`. [Online]. Available: `http://prola.aps.org/abstract/PR/v73/i7/p679{\_}1`.

[4] I. R. Kleckner and M. P. Foster, “An introduction to NMR-based approaches for measuring protein dynamics”, *Biochimica et Biophysica Acta (BBA) - Proteins and Proteomics*, vol. 1814, no. 8, pp. 942–968, 2011, ISSN: 15709639. DOI: `10.1016/j.bbapap.2010.10.012`. [Online]. Available: `https://linkinghub.elsevier.com/retrieve/pii/S1570963910002864`.

[5] P Mansfield and A. A. Maudsley, “Medical imaging by NMR.”, *The British journal of radiology*, vol. 50, no. 591, pp. 188–94, 1977, ISSN: 0007-1285. DOI: `10.1259/0007-1285-50-591-188`. [Online]. Available: `http://www.ncbi.nlm.nih.gov/pubmed/849520`.

[6] P. C. LAUTERBUR, “Image Formation by Induced Local Interactions: Examples Employing Nuclear Magnetic Resonance”, *Nature*, vol. 242, no. 5394, pp. 190–191, 1973, ISSN: 0028-0836. DOI: `10.1038/242190a0`. [Online]. Available: `isi:A1973P031700041{\%}5CnnotlistedinPubMed{\%}5Cnfile:///P:/DownloadPaper/Nature/Nature{\_}242{\_}190.pdfhttp://www.nature.com/articles/242190a0`.

[7] R Damadian, “Field Focusing n.m.r. (FONAR) and the Formation of Chemical Images in Man”, *Philosophical Transactions of the Royal Society of London. Series B, Biological Sciences*, vol. 289, no. 1037, pp. 489–500, 1980, ISSN: 00804622. [Online]. Available: `http://www.jstor.org/stable/2395533`.

[8] S. Ogawa, T.-M. Lee, A. S. Nayak, and P. Glynn, “Oxygenation-sensitive contrast in magnetic resonance image of rodent brain at high magnetic fields”, *Magnetic Resonance in Medicine*, vol. 14, no. 1, pp. 68–78, 1990, ISSN: 07403194. DOI: `10.1002/mrm.1910140108`. [Online]. Available: `http://doi.wiley.com/10.1002/mrm.1910140108`.

[9] K. P. Pruessmann, M. Weiger, M. B. Scheidegger, and P. Boesiger, "SENSE: Sensitivity encoding for fast MRI", *Magnetic Resonance in Medicine*, vol. 42, no. 5, pp. 952–962, 1999, ISSN: 07403194. DOI: `10.1002/(SICI)1522-2594(199911)42:5<952::AID-MRM16>3.0.CO;2-S`.

[10] M. A. Griswold, P. M. Jakob, R. M. Heidemann, M. Nittka, V. Jellus, J. Wang, B. Kiefer, and A. Haase, "Generalized Autocalibrating Partially Parallel Acquisitions (GRAPPA)", *Magnetic Resonance in Medicine*, vol. 47, no. 6, pp. 1202–1210, 2002, ISSN: 07403194. DOI: `10.1002/mrm.10171`.

[11] J. P. Marques, T. Kober, G. Krueger, W. van der Zwaag, P.-F. Van de Moortele, and R. Gruetter, "MP2RAGE, a self bias-field corrected sequence for improved segmentation and T1-mapping at high field", *NeuroImage*, vol. 49, no. 2, pp. 1271–1281, 2010, ISSN: 10538119. DOI: `10.1016/j.neuroimage.2009.10.002`. arXiv: `9605103 [cs]`. [Online]. Available: `http://dx.doi.org/10.1016/j.neuroimage.2009.10.002http://linkinghub.elsevier.com/retrieve/pii/S1053811909010738`.

[12] J. B. Andre, B. W. Bresnahan, M. Mossa-Basha, M. N. Hoff, C. Patrick Smith, Y. Anzai, and W. A. Cohen, "Toward quantifying the prevalence, severity, and cost associated with patient motion during clinical MR examinations", *Journal of the American College of Radiology*, vol. 12, no. 7, pp. 689–695, 2015, ISSN: 1558349X. DOI: `10.1016/j.jacr.2015.03.007`.

[13] A Abragam, *The principles of nuclear magnetism.* English. Oxford: Clarendon Press, 1961.

[14] M. Levitt, *Spin Dynamics: Basics of Nuclear Magnetic Resonance.* 2000, p. 679, ISBN: 9780470511183.

[15] R. M. Henkelman, G. J. Stanisz, and S. J. Graham, "Magnetization transfer in MRI: A review", *NMR in Biomedicine*, vol. 14, no. 2, pp. 57–64, 2001, ISSN: 09523480. DOI: `10.1002/nbm.683`.

[16] E. M. Haacke, R. W. Brown, M. R. Thompson, R. Venkatesan, and Others, *Magnetic Resonance Imaging*, R. W. Brown, Y.-C. N. Cheng, E. M. Haacke, M. R. Thompson, and R. Venkatesan, Eds. Chichester, UK: John Wiley & Sons Ltd, 2014, vol. 82, ISBN: 9781118633953. DOI: `10.1002/9781118633953`. [Online]. Available: `http://doi.wiley.com/10.1002/9781118633953`.

[17] K. P. McGee, A. Manduca, J. P. Felmlee, S. J. Riederer, and R. L. Ehman, "Image metric-based correction (Autocorrection) of motion effects: Analysis of image metrics", *Journal of Magnetic Resonance Imaging*, vol. 11, no. 2, pp. 174–181, 2000, ISSN: 10531807. DOI: `10.1002/(SICI)1522-2586(200002)11:2<174::AID-JMRI15>3.0.CO;2-3`.

[18] E. Haacke and G. Lenz, "Improving MR image quality in the presence of motion by using rephasing gradients", *American Journal of Roentgenology*, vol. 148, no. 6, pp. 1251–1258, 1987, ISSN: 0361-803X. DOI: `10.2214/ajr.148.6.1251`. [Online]. Available: `http://www.ajronline.org/doi/10.2214/ajr.148.6.1251`.

[19] L. Minati and W. P. Węglarz, "Physical foundations, models, and methods of diffusion magnetic resonance imaging of the brain: A review", *Concepts in Magnetic Resonance Part A*, vol. 30A, no. 5, pp. 278–307, 2007, ISSN: 15466086. DOI: `10.1002/cmr.a.20094`. [Online]. Available: `http://doi.wiley.com/10.1002/cmr.a.20094`.

[20] M. Soellinger, A. K. Rutz, S. Kozerke, and P. Boesiger, "3D cine displacement-encoded MRI of pulsatile brain motion", *Magnetic Resonance in Medicine*, vol. 61, no. 1, pp. 153–162, 2009, ISSN: 07403194. DOI: `10.1002/mrm.21802`.

[21] J. Maclaren, B. S. R. Armstrong, R. T. Barrows, K. A. Danishad, T. Ernst, C. L. Foster, K. Gumus, M. Herbst, I. Y. Kadashevich, T. P. Kusik, Q. Li, C. Lovell-Smith, T. Prieto, P. Schulze, O. Speck, D. Stucht, and M. Zaitsev, "Measurement and Correction of Microscopic Head Motion during Magnetic Resonance Imaging of the Brain", *PLoS ONE*, vol. 7, no. 11, pp. 3–11, 2012, ISSN: 19326203. DOI: `10.1371/journal.pone.0048088`.

[22] E. L. Gedamu and A. Gedamu, "Subject movement during multislice interleaved MR acquisitions: Prevalence and potential effect on MRI-derived brain pathology measurements and multicenter clinical trials of therapeutics for multiple sclerosis", *Journal of Magnetic Resonance Imaging*, vol. 36, no. 2, pp. 332–343, 2012, ISSN: 10531807. DOI: `10.1002/jmri.23666`.

[23] J. Fessler and B. Sutton, "Nonuniform fast fourier transforms using min-max interpolation", *IEEE Transactions on Signal Processing*, vol. 51, no. 2, pp. 560–574, 2003, ISSN: 1053-587X. DOI: `10.1109/TSP.2002.807005`. [Online]. Available: `http://ieeexplore.ieee.org/document/1166689/`.

[24] B. Zahneisen, B. Keating, A. Singh, M. Herbst, and T. Ernst, "Reverse retrospective motion correction", *Magnetic Resonance in Medicine*, vol. 2349, pp. 2341–2349, 2015, ISSN: 15222594. DOI: `10.1002/mrm.25830`.

[25] C. Forman, M. Aksoy, J. Hornegger, and R. Bammer, "Self-encoded marker for optical prospective head motion correction in MRI.", *Medical image analysis*, vol. 15, no. 5, pp. 708–19, 2011, ISSN: 1361-8423. DOI: `10.1016/j.media.2011.05.018`. [Online]. Available: `http://dx.doi.org/10.1016/j.media.2011.05.018http://www.ncbi.nlm.nih.gov/pubmed/21708477http://www.pubmedcentral.nih.gov/articlerender.fcgi?artid=PMC3164440`.

[26] M. Erikshøj, O. V. Olesen, K. Conradsen, L. Højgaard, and R. Larsen, "Structured light-based motion tracking in the limited view of an MR head coil", *Nuclear Instruments and Methods in Physics Research, Section A: Accelerators, Spectrometers, Detectors and Associated Equipment*, vol. 702, pp. 117–120, 2013, ISSN: 01689002. DOI: `10.1016/j.nima.2012.08.071`. [Online]. Available: `http://dx.doi.org/10.1016/j.nima.2012.08.071`.

[27] D. Stucht, K. A. Danishad, P. Schulze, F. Godenschweger, M. Zaitsev, and O. Speck, "Highest Resolution In Vivo Human Brain MRI Using Prospective Motion Correction.", *PloS one*, vol. 10, no. 7, e0133921, 2015, ISSN: 1932-6203. DOI: `10.1371/journal.pone.0133921`. [Online]. Available: `http://www.ncbi.nlm.nih.gov/pubmed/26226146http://www.pubmedcentral.nih.gov/articlerender.fcgi?artid=PMC4520483`.

[28] N. Todd, O. Josephs, M. F. Callaghan, A. Lutti, and N. Weiskopf, "Prospective motion correction of 3D echo-planar imaging data for functional MRI using optical tracking", *NeuroImage*, vol. 113, pp. 1–12, 2015, ISSN: 10959572. DOI: `10.1016/j.neuroimage.2015.03.013`. [Online]. Available: `http://dx.doi.org/10.1016/j.neuroimage.2015.03.013`.

[29] M. F. Callaghan, O. Josephs, M. Herbst, M. Zaitsev, N. Todd, and N. Weiskopf, "An evaluation of prospective motion correction (PMC) for high resolution quantitative MRI", *Frontiers in Neuroscience*, vol. 9, no. MAR, pp. 1–9, 2015, ISSN: 1662453X. DOI: `10.3389/fnins.2015.00097`.

[30] B. Zahneisen, B. Keating, and T. Ernst, "Propagation of calibration errors in prospective motion correction using external tracking", *Magnetic Resonance in Medicine*, vol. 72, no. 2, pp. 381–388, 2014, ISSN: 15222594. DOI: `10.1002/mrm.24943`.

[31] A Van Niekerk, A Van Der Kouwe, and E Meintjes, "A Method for Measuring Orientation Within a Magnetic Resonance Imaging Scanner Using Gravity and the Static Magnetic Field (VectOrient)", *IEEE Transactions on Medical Imaging*, vol. 36, no. 5, pp. 1129–1139, 2017. DOI: `10.1109/TMI.2017.2652502`. [Online]. Available: `https://www.scopus.com/inward/record.uri?eid=2-s2.0-85019235165{\&}doi=10.1109{\%}2FTMI.2017.2652502{\&}partnerID=40{\&}md5=c46656c0931db3027355ae5238798955`.

[32] M. B. Ooi, S. Krueger, W. J. Thomas, S. V. Swaminathan, and T. R. Brown, "Prospective real-time correction for arbitrary head motion using active markers", *Magnetic Resonance in Medicine*, vol. 62, no. 4, pp. 943–954, 2009, ISSN: 07403194. DOI: `10.1002/mrm.22082`. arXiv: `NIHMS150003`.

[33] L. Qin, E. J. Schmidt, Z. T. H. Tse, J. Santos, W. S. Hoge, C. Tempany-Afdhal, K. Butts-Pauly, and C. L. Dumoulin, "Prospective motion correction using tracking coils", *Magnetic Resonance in Medicine*, vol. 69, no. 3, pp. 749–759, 2013, ISSN: 07403194. DOI: `10.1002/mrm.24310`. arXiv: `NIHMS150003`.

[34] M. B. Ooi, M. Aksoy, J. MacLaren, R. D. Watkins, and R. Bammer, "Prospective motion correction using inductively coupled wireless RF coils", *Magnetic Resonance in Medicine*, vol. 70, no. 3, pp. 639–647, 2013, ISSN: 07403194. DOI: `10.1002/mrm.24845`.

[35] Y. Shu, A. M. Elliott, S. J. Riederer, and M. A. Bernstein, "Motion correction properties of the shells k-space trajectory", *Magnetic Resonance Imaging*, vol. 24, no. 6, pp. 739–749, 2006, ISSN: 0730725X. DOI: `10.1016/j.mri.2005.10.038`.

[36] M. Haeberlin, L. Kasper, C. Barmet, D. O. Brunner, B. E. Dietrich, S. Gross, B. J. Wilm, S. Kozerke, and K. P. Pruessmann, "Real-time motion correction using gradient tones and head-mounted NMR field probes", *Magnetic Resonance in Medicine*, vol. 74, no. 3, pp. 647–660, 2015, ISSN: 15222594. DOI: `10.1002/mrm.25432`.

[37] A. Aranovitch, M. Haeberlin, S. Gross, B. E. Dietrich, B. J. Wilm, D. O. Brunner, T. Schmid, R. Luechinger, and K. P. Pruessmann, "Prospective motion correction with NMR markers using only native sequence elements", *Magnetic Resonance in Medicine*, vol. 00, pp. 1–11, 2017, ISSN: 07403194. DOI: `10.1002/mrm.26877`. [Online]. Available: `http://doi.wiley.com/10.1002/mrm.26877http://www.ncbi.nlm.nih.gov/pubmed/28840611`.

[38] A. J. W. Van Der Kouwe, T. Benner, and A. M. Dale, "Real-time rigid body motion correction and shimming using cloverleaf navigators", *Magnetic Resonance in Medicine*, vol. 56, no. 5, pp. 1019–1032, 2006, ISSN: 07403194. DOI: `10.1002/mrm.21038`.

[39] E. B. Welch, A. Manduca, R. C. Grimm, H. A. Ward, and C. R. Jack, "Spherical navigator echoes for full 3D rigid body motion measurement in MRI", *Magnetic Resonance in Medicine*, vol. 47, no. 1, pp. 32–41, 2002, ISSN: 07403194. DOI: `10.1002/mrm.10012`.

[40] P. M. Johnson, J. Liu, T. Wade, M. A. Tavallaei, and M. Drangova, "Retrospective 3D motion correction using spherical navigator echoes", *Magnetic Resonance Imaging*, vol. 34, no. 9, pp. 1274–1282, 2016, ISSN: 18735894. DOI: `10.1016/j.mri.2016.06.006`. [Online]. Available: `http://dx.doi.org/10.1016/j.mri.2016.06.006`.

[41] M. D. Tisdall, A. T. Hess, M. Reuter, E. M. Meintjes, B. Fischl, and A. J. W. Van Der Kouwe, "Volumetric navigators for prospective motion correction and selective reacquisition in neuroanatomical MRI", *Magnetic Resonance in Medicine*, vol. 68, no. 2, pp. 389–399, 2012, ISSN: 07403194. DOI: `10.1002/mrm.23228`. arXiv: `NIHMS150003`.

[42] A. T. Hess, O. C. Andronesi, M. Dylan Tisdall, A. Gregory Sorensen, A. J. W. van der Kouwe, and E. M. Meintjes, "Real-time motion and B 0 correction for localized adiabatic selective refocusing (LASER) MRSI using echo planar imaging volumetric navigators", *NMR in Biomedicine*, vol. 25, no. 2, pp. 347–358, 2012, ISSN: 09523480. DOI: `10.1002/nbm.1756`.

[43] M. D. Tisdall, M. Reuter, A. Qureshi, R. L. Buckner, B. Fischl, and A. J. W. van der Kouwe, "Prospective motion correction with volumetric navigators (vNavs) reduces the bias and variance in brain morphometry induced by subject motion", *NeuroImage*, vol. 127, pp. 11–22, 2016, ISSN: 10959572. DOI: `10.1016/j.neuroimage.2015.11.054`. [Online]. Available: `http://dx.doi.org/10.1016/j.neuroimage.2015.11.054`.

[44] M. D. Tisdall, J. R. Polimeni, and A. J. van der Kouwe, "Motion-Corrected 350 $\mu$m Isotropic MPRAGE at 3 T Using Volumetric Navigators (VNavs)", in *Proc. Intl. Soc. Mag. Reson. Med. 21*, 2013, p. 0268.

[45] N. White, C. Roddey, A. Shankaranarayanan, E. Han, D. Rettmann, J. Santos, J. Kuperman, and A. Dale, "PROMO: Real-time prospective motion correction in MRI using image-based tracking", *Magnetic Resonance in Medicine*, vol. 63, no. 1, pp. 91–105, 2010, ISSN: 07403194. DOI: `10.1002/mrm.22176`.

[46] S. Skare, A. Hartwig, M. Mårtensson, E. Avventi, and M. Engström, "Properties of a 2D fat navigator for prospective image domain correction of nodding motion in brain MRI.", *Magnetic resonance in medicine*, vol. 73, no. 3, pp. 1110–9, 2015, ISSN: 1522-2594. DOI: `10.1002/mrm.25234`. [Online]. Available: `http://doi.wiley.com/10.1002/mrm.25234http://www.ncbi.nlm.nih.gov/pubmed/24733744`.

[47] M. Engström, M. Mårtensson, E. Avventi, O. Norbeck, and S. Skare, "Collapsed fat navigators for brain 3D rigid body motion", *Magnetic Resonance Imaging*, vol. 33, no. 8, pp. 984–991, 2015, ISSN: 0730725X. DOI: `10.1016/j.mri.2015.06.014`. [Online]. Available: `http://dx.doi.org/10.1016/j.mri.2015.06.014http://linkinghub.elsevier.com/retrieve/pii/S0730725X15001599`.

[48] D. Gallichan, J. P. Marques, and R. Gruetter, "Retrospective correction of involuntary microscopic head movement using highly accelerated fat image navigators (3D FatNavs) at 7T", *Magnetic Resonance in Medicine*, vol. 00, pp. 1–10, 2015, ISSN: 15222594. DOI: `10.1002/mrm.25670`.

[49] J. G. Pipe, "Motion correction with PROPELLER MRI: Application to head motion and free-breathing cardiac imaging", *Magnetic Resonance in Medicine*, vol. 42, no. 5, pp. 963–969, 1999, ISSN: 07403194. DOI: `10.1002/(SICI)1522-2594(199911)42:5<963::AID-MRM17>3.0.CO;2-L`.

[50] E. B. Welch, P. J. Rossman, J. P. Felmlee, and A. Manduca, "Self-navigated motion correction using moments of spatial projections in radial MRI", *Magnetic Resonance in Medicine*, vol. 52, no. 2, pp. 337–345, 2004, ISSN: 07403194. DOI: `10.1002/mrm.20151`.

[51] G. Vaillant, C. Prieto, C. Kolbitsch, G. Penney, and T. Schaeffter, "Retrospective rigid motion correction in k-space for segmented radial MRI", *IEEE Transactions on Medical Imaging*, vol. 33, no. 1, pp. 1–10, 2014, ISSN: 02780062. DOI: `10.1109/TMI.2013.2268898`.

[52] A. G. Anderson, J. Velikina, W. Block, O. Wieben, and A. Samsonov, “Adaptive retrospective correction of motion artifacts in cranial MRI with multicoil three-dimensional radial acquisitions”, *Magnetic Resonance in Medicine*, vol. 69, no. 4, pp. 1094–1103, 2013, ISSN: 07403194. DOI: `10.1002/mrm.24348`.

[53] W. Lin, F. Huang, G. R. Duensing, and A. Reykowski, “High temporal resolution retrospective motion correction with radial parallel imaging”, *Magnetic Resonance in Medicine*, vol. 67, no. 4, pp. 1097–1105, 2012, ISSN: 07403194. DOI: `10.1002/mrm.23092`.

[54] T. Kober, J. P. Marques, R. Gruetter, and G. Krueger, “Head motion detection using FID navigators”, *Magnetic Resonance in Medicine*, vol. 66, no. 1, pp. 135–143, 2011, ISSN: 07403194. DOI: `10.1002/mrm.22797`.

[55] M. Waszak, P. Falkovskiy, T. Hilbert, G. Bonnier, B. Maréchal, R. Meuli, R. Gruetter, T. Kober, and G. Krueger, “Prospective head motion correction using FID-guided on-demand image navigators”, *Magnetic Resonance in Medicine*, vol. 00, no. June, 2016, ISSN: 15222594. DOI: `10.1002/mrm.26364`.

[56] M. Bydder, D. Atkinson, D. J. Larkman, D. L. Hill, and J. V. Hajnal, “Smash navigators”, *Magnetic Resonance in Medicine*, vol. 49, no. 3, pp. 493–500, 2003, ISSN: 07403194. DOI: `10.1002/mrm.10388`.

[57] J. Mendes, E. Kholmovski, and D. L. Parker, “Rigid-body motion correction with self-navigation MRI”, *Magnetic Resonance in Medicine*, vol. 61, no. 3, pp. 739–747, 2009, ISSN: 07403194. DOI: `10.1002/mrm.21883`.

[58] J. Mendes and D. L. Parker, “Intrinsic detection of motion in segmented sequences.”, *Magnetic resonance in medicine : official journal of the Society of Magnetic Resonance in Medicine / Society of Magnetic Resonance in Medicine*, vol. 65, no. 4, pp. 1084–1089, 2011, ISSN: 15222594. DOI: `10.1002/mrm.22681`.

[59] A. A. Samsonov, J. Velikina, Y. Jung, E. G. Kholmovski, C. R. Johnson, and W. F. Block, “Pocs-enhanced correction of motion artifacts in parallel MRI”, *Magnetic Resonance in Medicine*, vol. 63, no. 4, pp. 1104–1110, 2010, ISSN: 07403194. DOI: `10.1002/mrm.22254`.

[60] K. Gumus, B. Keating, N. White, B. Andrews-Shigaki, B. Armstrong, J. Maclaren, M. Zaitsev, A. Dale, and T. Ernst, “Comparison of optical and MR-based tracking”, *Magnetic Resonance in Medicine*, vol. 74, no. 3, pp. 894–902, 2015, ISSN: 15222594. DOI: `10.1002/mrm.25472`.

[61] D. Atkinson, D. L. G. Hill, P. N. R. Stoyle, P. E. Summers, S. Clare, R. Bowtell, and S. F. Keevil, “Automatic compensation of motion artifacts in MRI”, *Magnetic Resonance in Medicine*, vol. 41, no. 1, pp. 163–170, 1999, ISSN: 07403194. DOI: `10.1002/(SICI)1522-2594(199901)41:1<163::AID-MRM23>3.0.CO;2-9`.

[62] A. Loktyushin, H. Nickisch, R. Pohmann, and B. Schölkopf, “Blind retrospective motion correction of MR images”, *Magnetic Resonance in Medicine*, vol. 70, no. 6, pp. 1608–1618, 2013, ISSN: 07403194. DOI: `10.1002/mrm.24615`. [Online]. Available: `http://doi.wiley.com/10.1002/mrm.24615`.

[63] L. Cordero-Grande, E. J. Hughes, J. Hutter, A. N. Price, and J. V. Hajnal, “Three-dimensional motion corrected sensitivity encoding reconstruction for multi-shot multi-slice MRI: Application to neonatal brain imaging.”, *Magnetic resonance in medicine*, vol. 79, no. 3, pp. 1365–1376, 2018, ISSN: 1522-2594. DOI: `10.1002/mrm.26796`. [Online]. Available: `http://www.ncbi.nlm.nih.gov/pubmed/28626962`.

[64] L. Cordero-Grande, G. Ferrazzi, R. P. A. Teixeira, H. Shahzad, A. N. Price, and J. V. Hajnal, "Motion correction in volumetric brain imaging based on DISORDER: Distributed and Incoherent Sample Orders for Reconstruction Disentanglement using Encoding Redundancy", in *Proc. Intl. Soc. Mag. Reson. Med. 25*, 2017, p. 0301.

[65] J. Ren, I. Dimitrov, A. D. Sherry, and C. R. Malloy, "Composition of adipose tissue and marrow fat in humans by 1H NMR at 7 Tesla.", *Journal of lipid research*, vol. 49, no. 9, pp. 2055–62, 2008, ISSN: 0022-2275. DOI: `10.1194/jlr.D800010-JLR200`. [Online]. Available: `http://www.jlr.org/lookup/doi/10.1194/jlr.D800010-JLR200http://www.ncbi.nlm.nih.gov/pubmed/18509197http://www.pubmedcentral.nih.gov/articlerender.fcgi?artid=PMC2515528`.

[66] A van der Kouwe, T Benner, and L Wald, "Decoupling motion navigation from imaging using spatial-spectral RF pulses", *Proceedings 16th Scientific Meeting, International Society for Magnetic Resonance in Medicine*, vol. Toronto, p. 1465, 2008. [Online]. Available: `/MyPathway2008/1465`.

[67] F. A. Breuer, M. Blaimer, M. F. Mueller, N. Seiberlich, R. M. Heidemann, M. A. Griswold, and P. M. Jakob, "Controlled aliasing in volumetric parallel imaging (2D CAIPIRINHA)", *Magnetic Resonance in Medicine*, vol. 55, no. 3, pp. 549–556, 2006, ISSN: 07403194. DOI: `10.1002/mrm.20787`.

[68] M. Lustig, D. Donoho, and J. M. Pauly, "Sparse MRI: The application of compressed sensing for rapid MR imaging", *Magnetic Resonance in Medicine*, vol. 58, no. 6, pp. 1182–1195, 2007, ISSN: 07403194. DOI: `10.1002/mrm.21391`.

[69] K. Okamoto, J. Ito, K. Ishikawa, K. Sakai, and S. Tokiguchi, "Change in signal intensity on MRI of fat in the head of markedly emaciated patients", *Neuroradiology*, vol. 43, no. 2, pp. 134–138, 2001, ISSN: 00283940. DOI: `10.1007/s002340000453`.

[70] J. G. Sled, G. B. Pike, and G. Bruce Pike, "Quantitative imaging of magnetization transfer exchange and relaxation properties in vivo using MRI", *Magnetic resonance in medicine : official journal of the Society of Magnetic Resonance in Medicine / Society of Magnetic Resonance in Medicine*, vol. 46, pp. 923–931, 2001, ISSN: 0740-3194. DOI: `10.1002/mrm.1278`.

[71] J. B. Andre, B. W. Bresnahan, M. Mossa-Basha, M. N. Hoff, C. Patrick Smith, Y. Anzai, and W. A. Cohen, "Toward quantifying the prevalence, severity, and cost associated with patient motion during clinical MR examinations", *Journal of the American College of Radiology*, vol. 12, no. 7, pp. 689–695, 2015, ISSN: 1558349X. DOI: `10.1016/j.jacr.2015.03.007`. [Online]. Available: `http://dx.doi.org/10.1016/j.jacr.2015.03.007`.

[72] M. Herbst, J. MacLaren, C. Lovell-Smith, R. Sostheim, K. Egger, A. Harloff, J. Korvink, J. Hennig, and M. Zaitsev, "Reproduction of motion artifacts for performance analysis of prospective motion correction in MRI", *Magnetic Resonance in Medicine*, vol. 71, no. 1, pp. 182–190, 2014, ISSN: 07403194. DOI: `10.1002/mrm.24645`.

[73] M. Zaitsev, J. Maclaren, and M. Herbst, "Motion artifacts in MRI: A complex problem with many partial solutions", *Journal of Magnetic Resonance Imaging*, vol. 42, no. 4, pp. 887–901, 2015, ISSN: 15222586. DOI: `10.1002/jmri.24850`.

[74] F. Lüsebrink, A. Sciarra, H. Mattern, R. Yakupov, and O. Speck, "T1-weighted in vivo human whole brain MRI dataset with an ultrahigh isotropic resolution of 250 $\mu$m", *Scientific Data*, vol. 4, p. 170 032, 2017, ISSN: 2052-4463. DOI: `10.1038/sdata.2017.32`. [Online]. Available: `http://www.nature.com/articles/sdata201732{\%}0Ahttp://www.ncbi.nlm.nih.gov/pubmed/28291265{\%}0Ahttp://www.pubmedcentral.nih.gov/articlerender.fcgi?artid=PMC5349250`.

[75] H. Mattern, A. Sciarra, F. Godenschweger, D. Stucht, F. Lüsebrink, G. Rose, and O. Speck, "Prospective motion correction enables highest resolution time-of-flight angiography at 7T", *Magnetic Resonance in Medicine*, vol. 00, pp. 1–11, 2017, ISSN: 07403194. DOI: `10.1002/mrm.27033`. [Online]. Available: `http://doi.wiley.com/10.1002/mrm.27033`.

[76] M. Eschelbach, A. Aghaeifar, J. Bause, J. Handwerker, J. Anders, E.-M. Engel, A. Thielscher, and K. Scheffler, "Comparison of Prospective Head Motion Correction with NMR Field Probes and an Optical Tracking System", *Magnetic Resonance in Medicine*, no. October 2017, pp. 1–11, 2018, ISSN: 07403194. DOI: `10.1002/mrm.27343`.

[77] D. Gallichan and J. P. Marques, "Optimizing the acceleration and resolution of three-dimensional fat image navigators for high-resolution motion correction at 7T", *Magnetic Resonance in Medicine*, vol. 77, no. 2, pp. 547–558, 2017, ISSN: 07403194. DOI: `10.1002/mrm.26127`. [Online]. Available: `http://doi.wiley.com/10.1002/mrm.26127`.

[78] F. Gretsch, J. P. Marques, and D. Gallichan, "Investigating the accuracy of FatNav-derived estimates of temporal B0 changes and their application to retrospective correction of high-resolution 3D GRE of the human brain at 7T", *Magnetic Resonance in Medicine*, vol. 80, no. 2, pp. 585–597, 2018, ISSN: 07403194. DOI: `10.1002/mrm.27063`. [Online]. Available: `http://doi.wiley.com/10.1002/mrm.27063`.

[79] J. P. Marques and R. Gruetter, "New Developments and Applications of the MP2RAGE Sequence - Focusing the Contrast and High Spatial Resolution R1Mapping", *PLoS ONE*, vol. 8, no. 7, 2013, ISSN: 19326203. DOI: `10.1371/journal.pone.0069294`.

[80] D. Gallichan, *retroMoCoBox: https://github.com/dgallichan/retroMoCoBox*. [Online]. Available: `https://github.com/dgallichan/retroMoCoBox`.

[81] E. M. Haacke, S. Liu, S. Buch, W. Zheng, D. Wu, and Y. Ye, "Quantitative susceptibility mapping: Current status and future directions", *Magnetic Resonance Imaging*, vol. 33, no. 1, pp. 1–25, 2015, ISSN: 18735894. DOI: `10.1016/j.mri.2014.09.004`. [Online]. Available: `http://dx.doi.org/10.1016/j.mri.2014.09.004`.

[82] G. B. Chavhan, P. S. Babyn, B. Thomas, M. M. Shroff, and E. M. Haacke, "Principles, techniques, and applications of T2*-based MR imaging and its special applications.", *Radiographics : a review publication of the Radiological Society of North America, Inc*, vol. 29, no. 62983, pp. 1433–1449, 2009, ISSN: 0271-5333. DOI: `10.1148/rg.295095034`.

[83] E. M. Haacke, S. Mittal, Z. Wu, J. Neelavalli, and Y. C. N. Cheng, "Susceptibility-weighted imaging: Technical aspects and clinical applications, part 1", *American Journal of Neuroradiology*, vol. 30, no. 1, pp. 19–30, 2009, ISSN: 01956108. DOI: `10.3174/ajnr.A1400`.

[84] J. Wen, A. H. Cross, and D. A. Yablonskiy, "On the role of physiological fluctuations in quantitative gradient echo MRI: Implications for GEPCI, QSM, and SWI", *Magnetic Resonance in Medicine*, vol. 73, no. 1, pp. 195–203, 2015, ISSN: 15222594. DOI: `10.1002/mrm.25114`.

[85] P.-F. Van de Moortele, J. Pfeuffer, G. H. Glover, K. Ugurbil, and X. Hu, "Respiration-induced B0 fluctuations and their spatial distribution in the human brain at 7 Tesla.", *Magnetic resonance in medicine*, vol. 47, no. 5, pp. 888–95, 2002, ISSN: 0740-3194. DOI: `10.1002/mrm.10145`. [Online]. Available: `http://doi.wiley.com/10.1002/mrm.10145http://www.ncbi.nlm.nih.gov/pubmed/11979567`.

[86] D Raj, D. P. Paley, a. W. Anderson, R. P. Kennan, and J. C. Gore, "A model for susceptibility artefacts from respiration in functional echo-planar magnetic resonance imaging.", *Physics in medicine and biology*, vol. 45, no. 12, pp. 3809–3820, 2000, ISSN: 0031-9155. DOI: `10.1088/0031-9155/45/12/321`.

[87] P. J. Bolan, P.-G. Henry, E. H. Baker, S. Meisamy, and M. Garwood, "Measurement and correction of respiration-Inducedb0 variations in breast1h mrs at 4 tesla", *Magnetic Resonance in Medicine*, vol. 52, no. 6, pp. 1239–1245, 2004. DOI: `10.1002/mrm.00000`.

[88] B. Zahneisen, J. Assländer, P. Levan, T. Hugger, M. Reisert, T. Ernst, and J. Hennig, "Quantification and correction of respiration induced dynamic field map changes in fMRI using 3D single shot techniques", *Magnetic Resonance in Medicine*, vol. 71, no. 3, pp. 1093–1102, 2014, ISSN: 07403194. DOI: `10.1002/mrm.24771`.

[89] P. G. Henry, P. F. Van De Moortele, E. Giacomini, A. Nauerth, and G. Bloch, "Field-frequency locked in vivo proton MRS on a whole-body spectrometer", *Magnetic Resonance in Medicine*, vol. 42, no. 4, pp. 636–642, 1999, ISSN: 07403194. DOI: `10.1002/(SICI)1522-2594(199910)42:4<636::AID-MRM4>3.0.CO;2-I`.

[90] Y. Duerst, B. J. Wilm, M. Wyss, B. E. Dietrich, S. Gross, T. Schmid, D. O. Brunner, and K. P. Pruessmann, "Utility of real-time field control in T2 *-Weighted head MRI at 7T.", *Magnetic resonance in medicine*, vol. 22, no. April, p. 0312, 2015, ISSN: 1522-2594. DOI: `10.1002/mrm.25838`. [Online]. Available: `http://www.ncbi.nlm.nih.gov/pubmed/26307944`.

[91] Y. Duerst, B. J. Wilm, B. E. Dietrich, S. J. Vannesjo, C. Barmet, T. Schmid, D. O. Brunner, and K. P. Pruessmann, "Real-time feedback for spatiotemporal field stabilization in MR systems", *Magnetic Resonance in Medicine*, vol. 73, no. 2, pp. 884–893, 2015, ISSN: 15222594. DOI: `10.1002/mrm.25167`.

[92] P. Van Gelderen, J. A. De Zwart, P. Starewicz, R. S. Hinks, and J. H. Duyn, "Real-time shimming to compensate for respiration-induced B0 fluctuations", *Magnetic Resonance in Medicine*, vol. 57, no. 2, pp. 362–368, 2007, ISSN: 07403194. DOI: `10.1002/mrm.21136`.

[93] S. J. Vannesjo, B. J. Wilm, Y. Duerst, S. Gross, D. O. Brunner, B. E. Dietrich, T. Schmid, C. Barmet, and K. P. Pruessmann, "Retrospective correction of physiological field fluctuations in high-field brain MRI using concurrent field monitoring.", *Magnetic resonance in medicine*, vol. 73, no. 5, pp. 1833–43, 2015, ISSN: 1522-2594. DOI: `10.1002/mrm.25303`. [Online]. Available: `http://www.ncbi.nlm.nih.gov/pubmed/24903278`.

[94] M. J. Versluis, B. P. Sutton, P. W. de Bruin, P. Börnert, A. G. Webb, and M. J. van Osch, "Retrospective image correction in the presence of nonlinear temporal magnetic field changes using multichannel navigator echoes", *Magnetic Resonance in Medicine*, vol. 68, no. 6, pp. 1836–1845, 2012, ISSN: 07403194. DOI: `10.1002/mrm.24202`. [Online]. Available: `http://doi.wiley.com/10.1002/mrm.24202`.

[95] J. P. Marques and R. Bowtell, "Application of a fourier-based method for rapid calculation of field inhomogeneity due to spatial variation of magnetic susceptibility", *Concepts in Magnetic Resonance Part B: Magnetic Resonance Engineering*, vol. 25, no. 1, pp. 65–78, 2005, ISSN: 10437347. DOI: `10.1002/cmr.b.20034`.

[96] V. Avbelj, J.-M. Kalisnik, R. Trobec, and B. Gersak, "Breathing rates and heart rate spectrograms regarding body position in normal subjects.", *Computers in biology and medicine*, vol. 33, no. 3, pp. 259–66, 2003, ISSN: 0010-4825. DOI: `10.1016/S0010-4825(02)00092-6`. [Online]. Available: `http://www.ncbi.nlm.nih.gov/pubmed/12726804`.

[97] M. Versluis, J. Peeters, S. van Rooden, J. van der Grond, M. van Buchem, A. Webb, and M. van Osch, "Origin and reduction of motion and f0 artifacts in high resolution T2*-weighted magnetic resonance imaging: Application in Alzheimer's disease patients", *NeuroImage*, vol. 51, no. 3, pp. 1082–1088, 2010, ISSN: 10538119. DOI: `10.1016/j.neuroimage.2010.03.048`. [Online]. Available: `http://dx.doi.org/10.1016/j.neuroimage.2010.03.048http://linkinghub.elsevier.com/retrieve/pii/S1053811910003356`.

[98] B. J. Wilm, C. Barmet, M. Pavan, and K. P. Pruessmann, "Higher order reconstruction for MRI in the presence of spatiotemporal field perturbations", *Magnetic Resonance in Medicine*, vol. 65, no. 6, pp. 1690–1701, 2011, ISSN: 07403194. DOI: `10.1002/mrm.22767`.

[99] W. Jiang, P. E. Larson, and M. Lustig, "Simultaneous auto-calibration and gradient delays estimation (SAGE) in non-Cartesian parallel MRI using low-rank constraints", *Magnetic Resonance in Medicine*, vol. 80, no. 5, pp. 2006–2016, 2018, ISSN: 15222594. DOI: `10.1002/mrm.27168`.

[100] P. J. Koopmans, R. Manniesing, W. J. Niessen, M. A. Viergever, and M. Barth, "MR venography of the human brain using susceptibility weighted imaging at very high field strength", *Magnetic Resonance Materials in Physics, Biology and Medicine*, vol. 21, no. 1-2, pp. 149–158, 2008, ISSN: 09685243. DOI: `10.1007/s10334-007-0101-3`.

[101] R. Watts, Y. Wang, and M. R. Prince, "Method and apparatus for anatomically tailored k-space sampling and recessed elliptical view ordering for bolus-enhanced 3D MR angiography", *US patent 7003343B2*, 2006.

[102] D Atkinson, M Brant-Zawadzki, G. Gillan, D Purdy, and G Laub, "Improved MR angiography: magnetization transfer suppression with variable flip angle excitation and increased resolution.", *Radiology*, vol. 190, no. 3, pp. 890–4, 1994, ISSN: 0033-8419. DOI: `10.1148/radiology.190.3.8115646`. [Online]. Available: `http://www.ncbi.nlm.nih.gov/pubmed/8115646`.

[103] B. A. Hargreaves, C. H. Cunningham, D. G. Nishimura, and S. M. Conolly, "Variable-rate selective excitation for rapid MRI sequences", *Magnetic Resonance in Medicine*, vol. 52, no. 3, pp. 590–597, 2004, ISSN: 07403194. DOI: `10.1002/mrm.20168`.

[104] S. Schmitter, X. Wu, G. Adriany, E. J. Auerbach, K. U??urbil, and P. F. Van De Moortele, "Cerebral TOF angiography at 7T: Impact of B1+ shimming with a 16-channel transceiver array", *Magnetic Resonance in Medicine*, vol. 71, no. 3, pp. 966–977, 2014, ISSN: 07403194. DOI: `10.1002/mrm.24749`.

[105] G. B. Pike, B. S. Hu, G. H. Glover, and D. R. Enzmann, “Magnetization transfer time-of-flight magnetic resonance angiography.”, *Magnetic resonance in medicine : official journal of the Society of Magnetic Resonance in Medicine / Society of Magnetic Resonance in Medicine*, vol. 25, no. 2, pp. 372–379, 1992, ISSN: 0740-3194.

[106] M. Babayeva, T. Kober, B. Knowles, M. Herbst, R. Meuli, M. Zaitsev, and G. Krueger, “Accuracy and Precision of Head Motion Information in Multi-Channel Free Induction Decay Navigators for Magnetic Resonance Imaging”, *IEEE Transactions on Medical Imaging*, vol. 34, no. 9, pp. 1879–1889, 2015, ISSN: 1558254X. DOI: `10.1109/TMI.2015.2413211`.

[107] T. E. Wallace, O. Afacan, M. Waszak, T. Kober, and S. K. Warfield, “Head Motion Measurement and Correction using FID Navigators”, *Magnetic Resonance in Medicine*, no. April, 2018, ISSN: 07403194. DOI: `10.1002/mrm.27381`.

[108] D. Zacà, U. Hasson, L. Minati, and J. Jovicich, “Method for retrospective estimation of natural head movement during structural MRI”, *Journal of Magnetic Resonance Imaging*, pp. 1–11, 2018, ISSN: 15222586. DOI: `10.1002/jmri.25959`.

[109] J. Meineke and T. Nielsen, “Data consistency-driven determination of B 0 -fluctuations in gradient-echo MRI”, *Magnetic Resonance in Medicine*, no. November, pp. 1–10, 2018, ISSN: 07403194. DOI: `10.1002/mrm.27630`. [Online]. Available: `http://doi.wiley.com/10.1002/mrm.27630`.

[110] A. Loktyushin, P. Ehses, B. Schölkopf, and K. Scheffler, “Autofocusing-based phase correction”, *Magnetic Resonance in Medicine*, vol. 00, pp. 1–11, 2018, ISSN: 07403194. DOI: `10.1002/mrm.27092`. [Online]. Available: `http://doi.wiley.com/10.1002/mrm.27092`.

[111] F. Gretsch, H. Mattern, D. Gallichan, and O. Speck, “Fat navigators and Moiré phase tracking comparison for motion estimation and retrospective correction”, *Magnetic Resonance in Medicine*, vol. 83, no. 1, pp. 83–93, 2020, ISSN: 0740-3194. DOI: `10.1002/mrm.27908`. [Online]. Available: `https://onlinelibrary.wiley.com/doi/abs/10.1002/mrm.27908`.

[112] J. Jorge, F. Gretsch, D. Gallichan, and J. P. Marques, “Tracking discrete off-resonance markers with three spokes (trackDOTS) for compensation of head motion and B0 perturbations: Accuracy and performance in anatomical imaging”, *Magnetic Resonance in Medicine*, vol. 79, no. 1, pp. 160–171, 2018, ISSN: 15222594. DOI: `10.1002/mrm.26654`. [Online]. Available: `http://doi.wiley.com/10.1002/mrm.26654`.

[113] F. Gretsch, H. Mattern, D. Gallichan, and O. Speck, “Direct comparison of fat navigators and Moiré phase tracking for retrospective brain motion correction at 7T”, in *Proc. Intl. Soc. Mag. Reson. Med. 27*, 2019, p. 440.

[114] F. Gretsch and D. Gallichan, “Segmented 3D fat navigators for faster brain motion tracking at 7T”, in *Proc. Intl. Soc. Mag. Reson. Med. 26*, 2018, p. 4084.

[115] ——, “Motion corrected high resolution time-of-flight angiography at 7T using Segmented FatNavs”, in *Proc. Intl. Soc. Mag. Reson. Med. 25*, 2017, p. 0780.

[116] F. Gretsch, T. Kober, M. Waszak, J. P. Marques, and D. Gallichan, “High temporal resolution retrospective motion and B0 correction using FIDNavs and segmented FatNavs at 7T”, in *Int. Soc. Magn. Res. Med.*, 2016, p. 4251.

[117] F. Gretsch, J. P. Marques, R. Gruetter, and D. Gallichan, “Investigating the potential of highly accelerated FatNavs for dynamic shimming”, *Proc. Intl. Soc. Mag. Reson. Med. 23*, vol. 23, no. 205321, p. 205 321, 2015.

# Contribution to publications

## Papers

F. Gretsch, H. Mattern, D. Gallichan, and O. Speck, “Fat navigators and Moiré phase tracking comparison for motion estimation and retrospective correction”, *Magnetic Resonance in Medicine*, vol. 83, no. 1, pp. 83–93, 2020, ISSN: 0740-3194. DOI: `10.1002/mrm.27908`. [Online]. Available: `https://onlinelibrary.wiley.com/doi/abs/10.1002/mrm.27908`

F. Gretsch, J. P. Marques, and D. Gallichan, “Investigating the accuracy of FatNav-derived estimates of temporal B0 changes and their application to retrospective correction of high-resolution 3D GRE of the human brain at 7T”, *Magnetic Resonance in Medicine*, vol. 80, no. 2, pp. 585–597, 2018, ISSN: 07403194. DOI: `10.1002/mrm.27063`. [Online]. Available: `http://doi.wiley.com/10.1002/mrm.27063`

J. Jorge, F. Gretsch, D. Gallichan, and J. P. Marques, “Tracking discrete off-resonance markers with three spokes (trackDOTS) for compensation of head motion and B0 perturbations: Accuracy and performance in anatomical imaging”, *Magnetic Resonance in Medicine*, vol. 79, no. 1, pp. 160–171, 2018, ISSN: 15222594. DOI: `10.1002/mrm.26654`. [Online]. Available: `http://doi.wiley.com/10.1002/mrm.26654`

## Conference proceedings

F. Gretsch, H. Mattern, D. Gallichan, and O. Speck, “Direct comparison of fat navigators and Moiré phase tracking for retrospective brain motion correction at 7T”, in *Proc. Intl. Soc. Mag. Reson. Med. 27*, 2019, p. 440

F. Gretsch and D. Gallichan, “Segmented 3D fat navigators for faster brain motion tracking at 7T”, in *Proc. Intl. Soc. Mag. Reson. Med. 26*, 2018, p. 4084

F. Gretsch and D. Gallichan, “Motion corrected high resolution time-of-flight angiography at 7T using Segmented FatNavs”, in *Proc. Intl. Soc. Mag. Reson. Med. 25*, 2017, p. 0780

F. Gretsch, T. Kober, M. Waszak, J. P. Marques, and D. Gallichan, “High temporal resolution retrospective motion and B0 correction using FIDNavs and segmented FatNavs at 7T”, in *Int. Soc. Magn. Res. Med.*, 2016, p. 4251

F. Gretsch, J. P. Marques, R. Gruetter, and D. Gallichan, “Investigating the potential of highly accelerated FatNavs for dynamic shimming”, *Proc. Intl. Soc. Mag. Reson. Med. 23*, vol. 23, no. 205321, p. 205 321, 2015

# Curriculum Vitae

Frédéric GRETSCH
Route Neuve 81
1024 Ecublens
Switzerland
Mobile: +41 79 547 90 81
E-mail :
`frederic.gretsch@gmail.com`

## Education

| | |
|---|---|
| Oct. 2014 - Present | **PhD Studies in Physics** at LIFMET, EPFL, Switzerland.<br>Thesis: Motion correction in brain magnetic resonance imaging using fat navigators. |
| Oct. 2013 - March 2014 | **Language Stay in Tokyo** at ISI Language School, Takadanobaba. |
| 2011-2013 | **Master of Science MSc in Physics** at EPFL, Switzerland.<br>Thesis: Effective field theories with spontaneous breaking of conformal invariance in perturbative expansion.<br>Final Master Grade: 5.87/6. |
| 2007-2010 | **Bachelor of Science MSc in Physics** at EPFL, Switzerland. |

## Language skills

| | |
|---|---|
| French | Native |
| English | Full professional proficiency |
| German | Fair |
| Japanese | JLPT N3-N4 |

## Professional experience

| | |
|---|---|
| March-May 2013 | **Assistant researcher** for the laboratory of particle physics and cosmology at EPFL, Switzerland. |
| September-December 2010 | **Teaching Assistant** at EPFL: Support for classical mechanics courses. |
| Summer 2008 & 2009 | Internship at the Nestlé Research Center (inventory duties),<br>Vers-chez-les-Blanc, Switzerland. |